



UNIVERSITAT POLITÈCNICA
DE CATALUNYA
BARCELONATECH

Integrated solutions for the energy and seismic retrofit of existing buildings

Camilla Lops

ADVERTIMENT La consulta d'aquesta tesi queda condicionada a l'acceptació de les següents condicions d'ús: La difusió d'aquesta tesi per mitjà del repositori institucional UPCommons (<http://upcommons.upc.edu/tesis>) i el repositori cooperatiu TDX (<http://www.tdx.cat/>) ha estat autoritzada pels titulars dels drets de propietat intel·lectual **únicament per a usos privats** emmarcats en activitats d'investigació i docència. No s'autoritza la seva reproducció amb finalitats de lucre ni la seva difusió i posada a disposició des d'un lloc aliè al servei UPCommons o TDX. No s'autoritza la presentació del seu contingut en una finestra o marc aliè a UPCommons (*framing*). Aquesta reserva de drets afecta tant al resum de presentació de la tesi com als seus continguts. En la utilització o cita de parts de la tesi és obligat indicar el nom de la persona autora.

ADVERTENCIA La consulta de esta tesis queda condicionada a la aceptación de las siguientes condiciones de uso: La difusión de esta tesis por medio del repositorio institucional UPCommons (<http://upcommons.upc.edu/tesis>) y el repositorio cooperativo TDR (<http://www.tdx.cat/?locale-attribute=es>) ha sido autorizada por los titulares de los derechos de propiedad intelectual **únicamente para usos privados enmarcados** en actividades de investigación y docencia. No se autoriza su reproducción con finalidades de lucro ni su difusión y puesta a disposición desde un sitio ajeno al servicio UPCommons No se autoriza la presentación de su contenido en una ventana o marco ajeno a UPCommons (*framing*). Esta reserva de derechos afecta tanto al resumen de presentación de la tesis como a sus contenidos. En la utilización o cita de partes de la tesis es obligado indicar el nombre de la persona autora.

WARNING On having consulted this thesis you're accepting the following use conditions: Spreading this thesis by the institutional repository UPCommons (<http://upcommons.upc.edu/tesis>) and the cooperative repository TDX (<http://www.tdx.cat/?locale-attribute=en>) has been authorized by the titular of the intellectual property rights **only for private uses** placed in investigation and teaching activities. Reproduction with lucrative aims is not authorized neither its spreading nor availability from a site foreign to the UPCommons service. Introducing its content in a window or frame foreign to the UPCommons service is not authorized (*framing*). These rights affect to the presentation summary of the thesis as well as to its contents. In the using or citation of parts of the thesis it's obliged to indicate the name of the author.



UNIONE EUROPEA
Fondo Sociale Europeo



Earth Systems and Built Environments (UNICH)

Ingeniería de la Construcción (UPC)

XXXII Cycle - PON

ING-IND/11

INTEGRATED SOLUTIONS FOR THE ENERGY AND SEISMIC RETROFIT OF EXISTING BUILDINGS

Thesis by Camilla Lops

Supervisor: Prof. Sergio Montelpare

Co-Supervisor: Prof. Luca Pelà

Prof. Guido Camata

PhD Coordinators: Prof. Isabella Raffi (UNICH)

Prof. Joan Ramon Casas Rius (UPC)

Academic year 2019/2020

Synopsis

European building stock is characterised by low energy efficiency and high structural vulnerability with respect to earthquakes, especially in seismic prone areas like Italy. In fact, the vast majority of buildings has been designed before the introduction of modern energy and seismic codes. Faced with the need for energy and structural retrofit, an integrated approach becomes a suitable choice, with benefits in terms of reduced construction time and costs.

The present work proposes a framework for the holistic renovation of existing buildings, improving their structural and energy performance with low environmental impact. A “holistic renovation” approach aims to concurrently tackle all building’s deficiencies, increasing the structural design service life, and achieving higher levels of safety, sustainability and ultimately resilience.

The aforementioned holistic approach is applied to a real case study: a multi-storey reinforced concrete building located in Pescara (Central Italy) retrofitted with an Engineered Double Skin Façade. The proposed retrofit is chosen based on the great variety of possible configurations it may assume and its applicability on the building’s envelope. Applying this retrofit provides the building with a so-called “filter zone” which guarantees better comfort conditions in the indoor spaces, as well as higher seismic performances. In addition, occupants’ relocation is prevented and therefore, any potential downtime.

In order to assess the effects of the Engineered Double Skin Façade on the case study, multisectoral simulations are performed, including energy, computational fluid dynamics, life cycle assessment and structural analyses. Obtained results are used to discuss the multiple benefits of the proposed retrofit from the structural and the energy efficiency point of view.

Resumen

El parque de edificios europeo se caracteriza por poseer una baja eficiencia energética y una alta vulnerabilidad frente a los terremotos, especialmente en áreas de elevada actividad sísmica como Italia. La gran mayoría de edificios existentes se diseñaron antes de la aparición de los modernos códigos sísmicos y energéticos. Debido a la necesidad de la modernización energética y estructural del parque de edificios existentes, un enfoque integral se convierte en una solución adecuada, presentando múltiples beneficios en términos de reducción del tiempo de construcción y costes.

La presente tesis propone una metodología para la rehabilitación integral del parque de edificios existentes, consiguiendo mejorar su rendimiento estructural y energético con un bajo impacto ambiental. El enfoque integral planteado tiene como objetivo abordar de forma simultánea todas las deficiencias que presentan los edificios, aumentando de esta manera su vida útil desde el punto de vista estructural y logrando aumentar los niveles de seguridad, sostenibilidad y resiliencia.

La metodología de rehabilitación integral mencionada anteriormente es aplicada al estudio de un caso real, correspondiente a un edificio construido en hormigón armado situado en Pescara (centro de Italia), sobre el cual se ha realizado el montaje y aplicación de una Double Skin Façade de carácter ingenieril con el objetivo de modificar su comportamiento estructural y energético. La implementación de esta modificación dota al edificio de una zona que mejora el confort térmico del interior y su comportamiento frente a sismos. Además, la modernización y mejora de los edificios existentes evita la necesidad de reubicar a sus ocupantes y, por lo tanto, la inactividad de la estructura.

Los efectos de la implementación de una Double Skin Façade de carácter ingenieril sobre el caso de estudio son evaluados previamente, realizándose simulaciones multisectoriales que incluyen diversos enfoques: energía, dinámica de fluidos computacional, ciclo de vida y análisis estructurales. Los resultados obtenidos a través de las simulaciones realizadas son empleados para discutir los múltiples beneficios que presenta su implementación y, por lo tanto, la modernización propuesta, siempre desde el punto de vista estructural y de eficiencia energética.

Sommario

Il patrimonio europeo esistente si caratterizza per avere scarsa efficienza energetica ed elevata vulnerabilità strutturale, elemento particolarmente evidenziato nelle zone a rischio sismico come l'Italia. Un alto numero di edifici, infatti, è stato progettato ed edificato prima dell'emanazione di normative energetiche e sismiche. Un approccio integrato, capace di far fronte alla necessità di riqualificazione energetica e strutturale degli edifici esistenti, diventa dunque la scelta auspicabile in grado di garantire molteplici benefici, come ad esempio la riduzione dei tempi e costi di costruzione.

La presente tesi propone una metodologia per la riqualificazione olistica degli edifici esistenti, atta al migliorarne le prestazioni strutturali ed energetiche, garantendo al contempo un basso impatto ambientale. L'applicazione di un approccio olistico permette di far fronte a tutte le carenze dell'edificio, incrementandone la vita utile e assicurando il raggiungimento di più elevati livelli di sicurezza, sostenibilità e resilienza.

Il suddetto approccio è applicato ad un caso studio reale: un edificio multipiano in cemento armato situato in Pescara (centro Italia), riqualificato mediante l'inserimento di una Double Skin Façade ingegnerizzata. Si è scelto un tale intervento di riqualificazione per la varietà delle configurazioni possibili che può assumere e data la sua localizzazione, esterna alle superfici perimetrali dell'edificio. L'applicazione di una tale soluzione permette la creazione di una zona filtro, capace di garantire migliori condizioni di comfort all'interno degli ambienti occupati e, al contempo, elevate prestazioni sismiche. In aggiunta, intervenendo esternamente, viene evitato lo spostamento degli abitanti e l'eventuale cessazione d'uso dell'edificio.

Al fine di valutare gli effetti migliorativi raggiungibili con l'inserimento della Double Skin Façade al caso studio, si ricorre ad analisi multisettoriali, includenti simulazioni energetiche, di fluidodinamica computazionale, strutturali e del ciclo di vita. I risultati ottenuti sono utilizzati per commentare i molteplici benefici inerenti al comportamento strutturale e all'efficienza energetica della soluzione proposta.

Acknowledgements

First and foremost, I would like to thank my supervisor, Prof. Sergio Montelpare for spotting my potential, for believing in me and for always being by my side along this journey. I will be forever thankful for your teachings, your counsels, and for having transmitted to me your passion for physics. You have been my main mentor along this journey, and you have always treated me as a colleague rather than as a subordinate, accepting my limits and blunting my edges. For all of this, I will be forever grateful.

Furthermore, I would like to thank Prof. Luca Pelà and Prof. Guido Camata for having shared with me their knowledge structural engineering expertise and for guiding me towards the full completion of this thesis. Finally, a special thanks goes to PhD. Marco Terrenzi for easing my struggle with the most complicated structural concepts always with patience, humour, and encouragement.

A profound thank you goes to all the PhD students of UNICH and UPC that shared with me this adventure and ended up being much more than simple colleagues, they became a second family. Thank you so much for your support, especially in those moments half up the mountain when I was unable to see its top. In particular, special thanks go to Nicola, my adventure/misadventure companion, with whom I have shared this university journey since its first day.

Last but not least, I would like to express my gratitude to my boyfriend Sergio, for having been so close to me despite the distance that separates us, for having been a lighthouse in my hardest times and a best friend in the leisure ones. Thank you for having kept my pace while walking by my side despite my life's frenzy without pretence or request. Your helping hand and your constant fuelling of my determination are amongst the factors that most helped me achieving this goal. You always believed in me, even in those moments when I stopped doing so.

Contents

Introduction	1
1. The Holistic Approach in Building Restoration	5
1.1. Introduction	5
1.2. The Holistic Renovation of Existing Buildings	10
1.3. Conclusions	12
2. The Double Skin Façade	14
2.1. Introduction	14
2.2. DSF Definition.....	14
2.3. DSF Classification.....	16
2.4. Advantages and Disadvantages of the DSF.....	21
2.5. DSF Origin and Evolution	22
2.6. DSF Innovation	32
2.7. Examples of Engineered DSFs.....	40
2.8. DSF Modelling: Between Difficulties and Limitations.....	46
3. Case Study	52
3.1. Introduction	52
3.2. Reference Building: Structural and Energy Properties	52
3.3. Preliminary Considerations	57
4. Dynamic Energy Simulations	58
4.1. Introduction	58
4.2. Weather Data Files for Energy Simulations	60
4.2.1. Correlation Models for Estimating Solar Radiation	67
4.2.2. Weather File Comparisons	71
4.3. Energy Modelling of the Reference Building.....	79

4.3.1. Model Calibration and Results.....	84
4.4. DSF Modelling and Results.....	90
4.5. The Impact of Climate Change on Buildings	106
4.5.1. Generation of Future Climatic Files.....	109
4.5.2. The Impact of Climate Change on the Reference Building	114
4.6. Conclusions	120
5. Computational Fluid Dynamics Simulations	123
5.1. Introduction	123
5.2. Modelling of the Reference Building	125
5.3. Modelling of the Double Skin Façade	128
5.3.1. Modelling of the Multi-Storey DSF and Preliminary Simulations	128
5.3.2. The Multi-Storey DSF Performance under Several Wind Directions	139
5.3.3. Modelling of the Corridor DSF	142
5.3.4. Modelling of the Shaft-Box DSF.....	144
5.3.5. DSF Performance Comparisons.....	149
5.4. Modelling of the Reference Building with DSF on Two Elevations.....	154
5.5. Evaluation of Optimised DSF Shapes	159
5.6. Conclusions	171
6. Structural Simulations	173
6.1. Introduction	173
6.2. Modelling of the Reference Building	175
6.3. Modelling of the Engineered DSF.....	190
6.3.1. Dissipative Braces: Main Aspects and Design Procedures	192
6.3.2. Static and Dynamic Nonlinear Analyses of the Engineered DSF	202
6.4. Conclusions	210
7. Life Cycle Analyses	212
7.1. Introduction.....	212

7.2. LCA and Buildings	216
7.3. LCA and Double Skin Façades	217
7.4. LCA Applied to the Engineered Double Skin Façade.....	218
7.5. Conclusions	222
8. Conclusions.....	224
8.1. Major Contributions and Significant Results.....	224
8.2. Future Directions	225
References	227
List of Figures	241
List of Tables	261
Appendix A.....	263
Appendix B.....	282
Appendix C.....	300
Appendix D.....	308
Appendix E	312
Appendix F	323

Glossary

EEA	European Environment Agency
EPBD	Energy Performance of Buildings Directive
BPIE	Building Performance Institute Europe
EPC	Energy Performance Certificate
DSF	Double Skin Façade
NV	Natural Ventilation
MV	Mechanical Ventilation
HV	Hybrid Ventilation
BW	Box-Window
C	Corridor
SB	Shaft-Box
MS	Multi-Storey
OAC	Outdoor Air Curtain
IAC	Indoor Air Curtain
SA	Supply Air
EA	Exhaust Air
BF	Static Air Buffer
IF	Intelligent Façade
ETFE	Ethylene Tetrafluoroethylene
PTFE	Polytetrafluoroethylene
HVAC	Heating Ventilation and Air Conditioning
PCM	Phase Changing Materials
PV	Photovoltaic
TMD	Tuned Mass Damper

BRB	Buckling Restrained Braces
BRAD	Buckling-Restrained Axial Dampers
SMA	Shape Memory Alloy
DLS	Damage Limit State
LSLS	Safety Limit State
CFD	Computational Fluid Dynamics
ES	Energy Simulation
$h_{i,conv}$	Heat Transfer Coefficient
T_{wall}	Surface Temperature
$\Delta T_{i,r}$	Room Temperature
Q	Heat Flux
ATER	Regional Enterprise for Social Housing
RC	Reinforced Concrete
BES	Building Energy Simulations
RCM	Regional Climate Model
TMY	Typical Meteorological Year
R	Correlation Coefficient
RMSD	Centred Root-Mean-Square Difference
σ	Standard Deviation
MM5	Mesoscale Model Fifth Generation
IWEC	International Weather for Energy Calculations
CTI	Italian Thermo-Technical Committee
PVGIS	Photovoltaic Geographical Information System
ARTA	Regional Environmental Protection Agency
DB	DesignBuilder

PSU	Penn State University
NCAR	National Center for Atmospheric Research
PBL	Planetary Boundary Layer
LSM	Land Surface Model
BK	Blackadar (MM5 Regional Climate Model)
MRF	Medium-Range Forecast (MM5 Regional Climate Model)
T	Temperature
P	Atmospheric Pressure
RH	Relative Humidity
m	Optical Air Mass Number
P_0	Atmospheric Pressure at Sea Level
α_s	Solar Altitude Angle of the Sun
τ	Atmospheric Transmittance Coefficient
I_p	Direct Radiation on a Surface Perpendicular to the Beam
G_{sc}	Global Solar Constant
I_{dir}	Direct Radiation
I_{diff}	Diffused Radiation on a Horizontal Surface
θ_s	Solar Zenith Angle
I_{gl}	Global Solar Radiation
k_t	Hourly Clearness Index
k_d	Diffuse Fraction Component
a	Solar Altitude
REF	Reference Data
U	Transmittance
s	Layer Depth

λ	Material Heat Conductivity
COP	Coefficient of Performance
$T_{\text{operative}}$	Operative Temperature
CC	Climate Change
IPCC	Intergovernmental Panel on Climate Change
UNEP	United Nations Environment Programme
WMO	World Meteorological Organization
NASA	National Aeronautics and Space Administration
GHG	Greenhouse Gases
SRES	Special Report on Emissions Scenarios
RCP	Representative Concentration Pathway
CORDEX	Climate Downscaling Experiment
WCRP	World Climate Research Program
RCD	Regional Climate Downscaling
TLC	Top Left Corner
TRC	Top Right Corner
BLC	Bottom Left Corner
BRC	Bottom Right Corner
ALADIN	Aire Limitée Adaptation Dynamique Développement InterNational
ECMWF	European Centre for Medium-Range Weather Forecasts
CNRM	Centre National de Recherches Météorologiques
p	Climatic Parameter
mt	Month
y	Year
$K_{(i)}$	Rank Order of the i th Day

N	Total Number of Days for a Month over all Years
U-RANS	Unsteady Reynolds-Averaged Navier-Stokes
K	Kinetic Energy
ε	Dissipation Rate
RSE	Replaceable Structural Elements
F_c	Concrete Compressive Strength
F_y	Yield Strength of Steel
V_{\max}	Ultimate Shear Resistance
ξ_{\max}	Shear Deformation
M_{cr}	Cracking Bending Moment
θ_{cr}	Cracking Rotation
M_y	Yielding Bending Moment
θ_y	Yielding Rotation
M_u	Ultimate Bending Moment
θ_u	Ultimate Rotation
M_{res}	Residual Bending Moment
θ_{res}	Residual Rotation
σ_{br}	Fictitious Failure Compressive Stress
$\sigma_{br(1)}$	Diagonal Tension
$\sigma_{br(2)}$	Sliding Shear along Horizontal Joints
$\sigma_{br(3)}$	Crushing in the Corners in Contact with the Frame
$\sigma_{br(4)}$	Diagonal Compression
σ_{m0}	Vertical Compression Strength Measured on the Masonry Specimens
τ_{m0}	Shear Strength Recorded by Means of the Diagonal Compression Test

u	Sliding Resistance in the Joints
σ_0	Vertical Stress Due to Working Loads
$\sigma_{br,min}$	Minimum Value of Infill Failure Modes
H_{mfc}	Ultimate Lateral Strength
ω	Width of the Strut
e	Thickness of the Masonry Panel
θ	Angle Between the Strut and the Horizontal Axis
d	Diagonal Length of the Masonry Panel
λh	Non-Dimensional Parameter
K_1	Coefficient for the Equivalent Strut Model
K_2	Coefficient for the Equivalent Strut Model
E_m	Elastic Equivalent Modulus
E_c	Elastic Modulus of Concrete
h	Height of the storey
h_m	Height of the Masonry Panel
I	Momentum of Inertia
K_{mfc}	Stiffness of the Equivalent Strut
f_{wh}	Compression Strength for the Horizontal Direction
f_{wv}	Compression Strength for the Vertical Direction
f_{wu}	Sliding Shear Resistance of Mortar Joints
f_{ws}	Shear Resistance Under Diagonal Compression
E_{wh}	Secant Modulus of Elasticity for Horizontal Direction
E_{wv}	Secant Modulus of Elasticity for Vertical Direction
G	Shear Modulus
W	Unit Weight of the Infills

MDOF	Multi Degree of Freedom
SDOF	Single Degree of Freedom
ADRS	Acceleration Displacement Response Spectrum
CLS	Collapse Limit State
Sd	Spectrum Displacement
Sa	Spectrum Acceleration
Sd _(CLS)	Displacement Demand for the SODF System (CLS)
Sd _(LSLS)	Displacement Demand for the SODF System (LSLS)
Sd _(DLS)	Displacement Demand for the SODF System (DLS)
FRP	Fiber Reinforced Polymers
f	Effectiveness Factor of Dissipative Braces
F _y [*]	Yield Force
d _y [*]	Yield Displacement
k _F [*]	Elastic Stiffness of the Equivalent Bare Structure
d _u [*]	Ultimate Displacement
d _{Bm} [*]	Maximum Displacement of the Equivalent SDOF System of the Braced Structure
μ _{DB}	Ductility Factor of the Equivalent Bracing System
d _{DBu}	Ultimate Displacement of the Equivalent Bracing
d _{DBy}	Yielding Displacement of the Bracing System
k _{DB} ^j	Elastic Stiffness of the Bracing System at the jth Step
F _{DB} ^j	Yield Force of the Damped Bracing System
k _{DB,i}	Stiffness of the Equivalent Bracing at the Storey i
k _{F,i}	Single Storey Existing Frame Stiffness
r _k	Ratio Between the Elastic Stiffness of the Equivalent Bare Structure and Elastic Stiffness of the Bracing Systems

k_{DB}	Elastic Stiffness of the Bracing Systems
Δ_{si}	Inter-Storey Displacement Obtained by Means of Linear Static Analyses
$F_{DB,i}$	Yield Force of the Equivalent Bracing at the Storey i
r_F	Ratio Between the Strength of the Equivalent Bare Structure and Bracing System
$F_{y,i}$	Yield Force of the Storey i
$d_{y,i}$	Displacement at the Elastic State of the i^{th} Floor
S_{TOT}	Total Building Displacement Defined by Means of Linear Analyses
$k_{DB,i,s}$	Elastic Stiffness of the Single Dissipative Brace
$F_{DB,i,s}$	Strength of the Single Dissipative Brace
$n_{DB,i}$	Number of Braces
ϕ_s	Angle with the Horizontal
PO	Pushover
LCSA	Life Cycle Sustainability Assessment
LCT	Life Cycle Thinking
LCP	Life Cycle Perspective
LCA	Life Cycle Analysis
ELCA	Environmental Life Cycle Assessment
LCC	Life Cycle Costing
SLCA	Social Life Cycle Assessment

Introduction

In recent years, the need of making the built environment more resilient, i.e. more resistant and adaptable, has become increasingly evident. In Europe, this aspect concerns the vast majority of existing buildings, which present several deficiencies from the structural and the energy-efficiency point of view. In particular, the structural inadequacy has been highlighted by recent seismic events, which caused a high loss of lives. Moreover, several buildings are beyond their design service life, as they date back to the 1960s, and were designed using techniques and materials that are now considered obsolete.

Nowadays, it is possible to retrofit existing buildings using advanced and high-efficient technologies. However, most of the time, the retrofit addresses either the structural or the energy-efficiency deficiency, without a comprehensive approach. To overcome this limitation, a new holistic renovation approach has been recently introduced. This approach aims to concurrently tackle all building's deficiencies, extending the design service life while pursuing safety, sustainability, and resilience.

Following the aforementioned holistic approach, the aim of this dissertation is to propose and evaluate a building's retrofit through an Engineered Double Skin Façade (DSF). This retrofit is designed to increase both structural and energy performance. Expected benefits of the holistic approach are reduced construction time and costs as well as reduced use of raw materials and energy, thus lowering the environmental impact. In addition, being the DSF installed along the building's exterior, it is not necessary to relocate occupants, and the continuity of operations is guaranteed.

The DSF was already investigated, along other structural and energy-efficiency retrofit solutions, by Scholars of the University of Bergamo (Italy) and the University of Brescia (Italy) in previous Doctoral dissertations. Main innovative aspects of the current work are the highly detailed energy assessments and the Computational Fluid Dynamics (CFD) analyses, the latter of which was never considered before.

Chapter 1 describes in detail the holistic approach used for retrofitting existing buildings. Then, the characteristics of the European built environment are

discussed. More specifically, the environmental impact of buildings and the Construction Industry sector, in general, is highlighted, in terms of energy consumption and CO₂ emission. In addition, few examples of combined structural and energy retrofit are presented.

Chapter 2 describes the origin, evolution and developments of the DSF systems, classifying them according to the configurations currently available. Then, innovative solutions aimed to increase the energy efficiency of the aforementioned DSF systems are discussed. Moreover, the concept of Engineered DSF is presented, providing examples of how the retrofit solution may be used to improve also the buildings' structural safety.

Chapter 3 describes the case study, an existing reinforced concrete (RC) building in Pescara, Central Italy, along with the multisectoral simulations used to assess its performance before and after the introduction of the DSF system.

Chapter 4 describes the energy modelling of the case study. Energy consumptions and comfort conditions are assessed before and after the introduction of the DSF system. More specifically, several configurations of DSF are tested (Box-Window, Corridor, Shaft-Box and Multi-Storey DSF). Then, the impact of climate change on the chosen outputs is investigated in order to define long-term optimal solutions. Additional details on the energy modelling may be found in Appendix A and B.

Chapter 5 describes the CFD simulations performed on the case study. At first, a simplified model (i.e. a rectangular prism) is adopted to assess the accuracy of the simulations. Then, additional elements such as the pitched roof and balconies are introduced in order to evaluate possible variations on the predicted air fluxes. As for the energy modelling of Chapter 4, also in this case, several configurations of DSF are used (Corridor, Shaft-Box and Multi-Storey DSF). Each typology is tested for different incoming wind directions to define the most efficient solution. Moreover, different shapes of adopted DSF configurations are analysed to improve the fluid dynamic behaviour of the retrofitted building. Additional details on the simulations may be found in Appendix E.

Chapter 6 describes the structural analyses performed on the case study. The vulnerability and seismic performance are investigated before and after the introduction of the Engineered DSF system, through linear and nonlinear static and

dynamic analyses. Obtained results are used to discuss the effectiveness of the Engineered DSF system on improving structural performance.

Chapter 7 describes the Life Cycle Analyses (LCA) performed on the case study for the different configurations of DSF also used in Chapter 4 and 5 (Box-Window, Corridor, Shaft-Box and Multi-Storey DSF). For each configuration, the Embodied and Equivalent Carbon is assessed as well as their impact on climate change.

Chapter 8 draws the main conclusions of the current work and discuss possible future developments.

Appendix A and B provide additional details on the climatic files used as input for the dynamic energy simulations. Indeed, these files may significantly affect the accuracy of simulations and therefore have to be carefully selected. For this reason, a previously validated methodology on a case study located in Asunción (Paraguay) for comparing and defining eventually missing climatic parameters is presented in Appendix A. Moreover, Appendix B includes all settings for the DSF modelling, which are established on the base of simplified simulations. These analyses focused on various aspects which may lead to increase the effectiveness of the DSF, such as its correct orientation or the most suitable shading system.

Appendix C shows architectural and structural details of the RC building chosen as case study.

Appendix D reports, in detail, the output, expressed in building heating and cooling consumption, obtained from the dynamic energy simulations performed in Chapter 4.

Appendix E lists the CFD analysis settings adopted as well as previously conducted studies used to validate the model presented in Chapter 5.

Appendix F shows the couples of accelerograms selected for the nonlinear analyses performed in Chapter 6.

This dissertation was carried out under a Co-tutoring Agreement among the “G. d’Annunzio” University of Chieti-Pescara (Italy) and the Universitat Politècnica de Catalunya (Spain) within a Double Degree Industrial PhD Programme. The

Introduction

proposed framework is meant to allow the combination and contamination of research skills from Academia with the user-oriented and business skills of Industry.

1. The Holistic Approach in Building Restoration

1.1. Introduction

In the last decades, the economy centred on general reduction of energy consumption and CO₂ emissions has dictated important changes in every sector and especially in the world of construction. Buildings are, in fact, one of the key consumers of energy in Europe, and a generally rising trend in energy use has been recorded in the last twenty years [1]. According to the European Environment Agency (EEA), in 2017 the transport sector accounted for 31% of total final energy consumption in the EU Member States, followed by the households (27%), industry (25%) and services (15%) sectors [2], as depicted in Figure 1.1.

The energy use in households is mainly related to space and water heating, which together are responsible for 80% of the total building energy consumption [3] (see Figure 1.2). The high percentage is mostly due to the use of less-efficient heating equipment, traditionally present in existing buildings, that are mainly fossil fuel-based, and poorly insulated envelopes, unable to avoid heat losses through the outer surfaces.

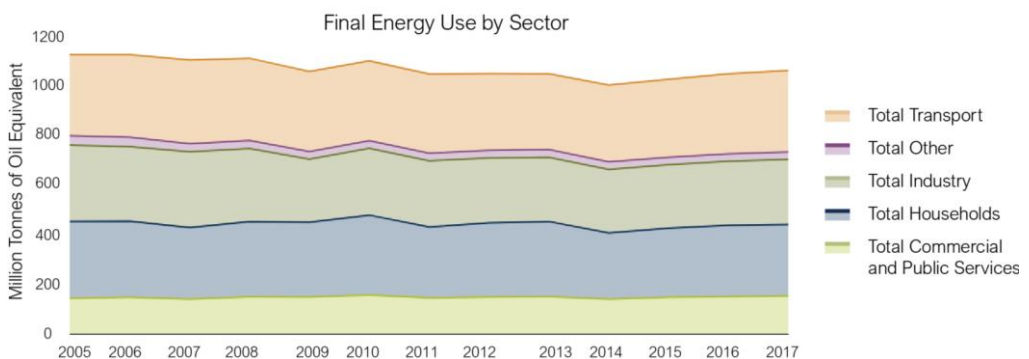


Figure 1.1. The final energy use by fuel and sector for the EU Member States [2].

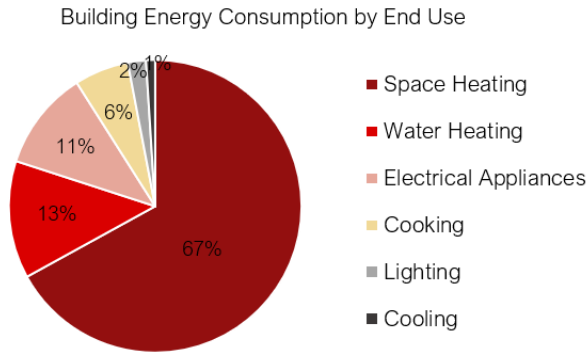


Figure 1.2. Breakdown of the energy consumption by end-use for EU households.

The significant impact of this sector related to the energy consumption is also estimated for the greenhouse gas emissions of which buildings and construction together account for the 36% of global final energy use and 39% of energy-related CO₂ emissions when upstream power generation is included [4]. Considering the so high potential for cost-effective energy savings, the building sector has become a priority area for the European Commission that has promoted various actions for reducing the building requirement and promoting their renovation. The prominent examples of this effort are the Directive 2002/91/EC [5] and the Directive 2010/31/EU [6], commonly known as the EPBD (from its full name Energy Performance of Buildings Directive) and its recasting. The first is mainly centred on the definition of a standardised methodology more oriented to new buildings. The second, instead, aims to deal with existing building not only when they are subjected to a major renovation, but also in case of replacement and retrofitting of few elements or technical systems [1]. After the EBPDs, the EU Member States have shown a growing interest in the building energy improvement and, as main results, a specific article centred on building renovation was introduced in the new Energy Efficiency Directive 2012/27/EU [7].

The great attention to the existing building stock is due to the consciousness that the European heritage has been mainly erected before the 1960s when the sustainable problem was in a preliminary phase, and energy building regulations were minimal. According to the Building Performance Institute Europe (BPIE) survey, reported in Figure 1.3, in fact, the 35% - 42% of the building is dated before the 1960s, and another consistent part was erected between 1961 and 1990 for the effect of the massive boom in the construction sector.

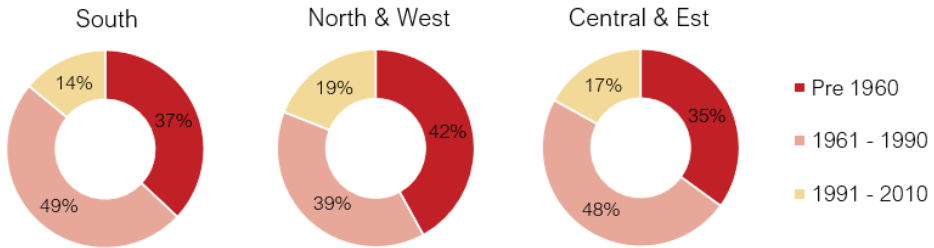


Figure 1.3. The categorisation of the construction period of the EU Housing stock [3].

The need of building energy upgrading is also confirmed by the information coming from the Energy Performance Certificate (EPC), according to which less than 3% of the European heritage presents an A-EPC label [8]. Figure 1.4 depicts the distribution of the building stock in Europe subdivided per country and EPC class. The comparison excludes Germany and Poland, for the absence of a central database, and those countries for which the extrapolation of the label from the limited/skewed population is not possible (e.g., Romania and Slovakia). As can be seen, for the quasi totality of the countries involved in the sample, higher percentages are referred to the presence of dwellings with low energy labels (from D to G). Thus, looking at the whole Europe situation, approximately 75% of buildings does not ensure good energy performances, presenting D and inferior labels, as depicted in Figure 1.5.

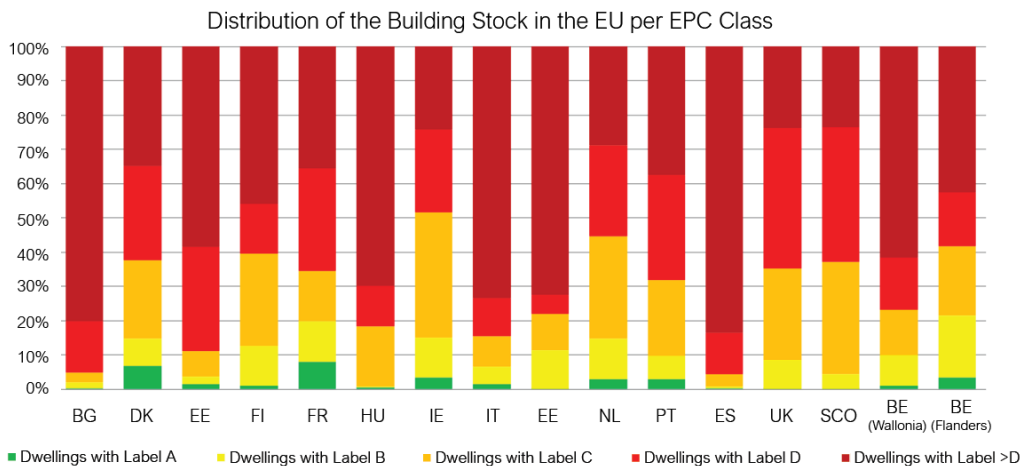


Figure 1.4. Subdivision of the European building stock per country and EPC class (the sample covers half of the EU Member States) [8].

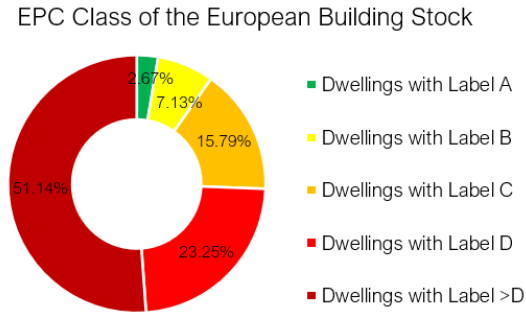


Figure 1.5. Classification of the European building stock according to the dwelling's EPC data (Elaborated from [8]).

Besides the energy problem, a second aspect that should be taken into account involves the high structural unsuitableness and seismic vulnerability of the existing heritage. A large percentage of buildings, in fact, has been built before the introduction of national anti-seismic codes or the enforcement of the modern ones, and the updating of the seismic classification of Europe [9]. The main consequence of this aspect is a vast number of buildings not designed or adequately verified for horizontal actions. In addition, a lot of them have exhausted the estimated life that is around 50-60 years, as suggested by current building codes. All of these features have been underlined by the recent earthquakes, mostly occurred in Italy, which have caused various damages to residential constructions, monumental buildings and industrial facilities, some of which previously restored for being more energy-efficient [9].

According to these aspects, a holistic approach, able to combine the improvement of the energy and structural performance and overcome the above-mentioned lacks, could be a successful choice. In fact, coupling structural retrofit interventions with energy-saving measures entails further benefits like a more significant reduction of the building environmental impact or the possibility of taking advantage of national subsidies established for each sector [10]. Various investigations support the holistic renovation of the existing heritage, and the most comprehensive work is the one carried on by Marini et al. [9], centred on the application of the Life Cycle Thinking for the energy and seismic upgrading of buildings. The cited investigation analyses the possible scenarios which could be adopted in case of energy retrofit of existing buildings. The first evaluates the

demolition and the reconstruction of the building stock. Even if extensively practiced, this choice has a high environmental impact, in terms of raw material depletion, energy consumption and waste production. For this reason, it is not taken into account in the following comparisons.

The second option considers the sole energy restoration. Thus, the seismic behaviour of the main structure remains unchanged and, in case of earthquakes, an extra cost should be added for the building repair. The last scenario, instead, adopts a combined approach, and improves, at the same time, the energy and structural building performance. The two possible solutions are depicted in Figure 1.6, where the energy consumption, operational cost and carbon emission are expressed as a function of the design building life. The charts represent the seismic event as an expected loss, expressed in terms of annual energy consumption, considering the uncertainty of the event. It is interesting to note that, in case of the sole building energy intervention (Figure 1.6a), the service life of the main structure is not extended. Thus, after a seismic event (the X-point in the chart), the whole building could be damaged, and the obtained improvements may be lost. On the contrary, the application of a combined retrofit intervention (Figure 1.6b) ensures, from one side, the extension of the building life and the reduction of its seismic vulnerability, and, on the other, confers better energy performances. By adopting this approach, in case of earthquakes, the building repair costs, both environmental and economic, would be lower than the previous option.

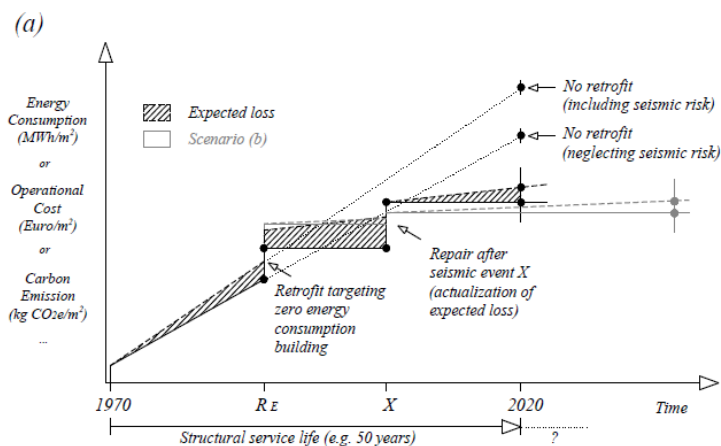


Figure 1.6. Evaluation of energy consumption, operational cost and carbon emission during the building life cycle, considering, the energy (a) and the energy + seismic (b) retrofit [9].

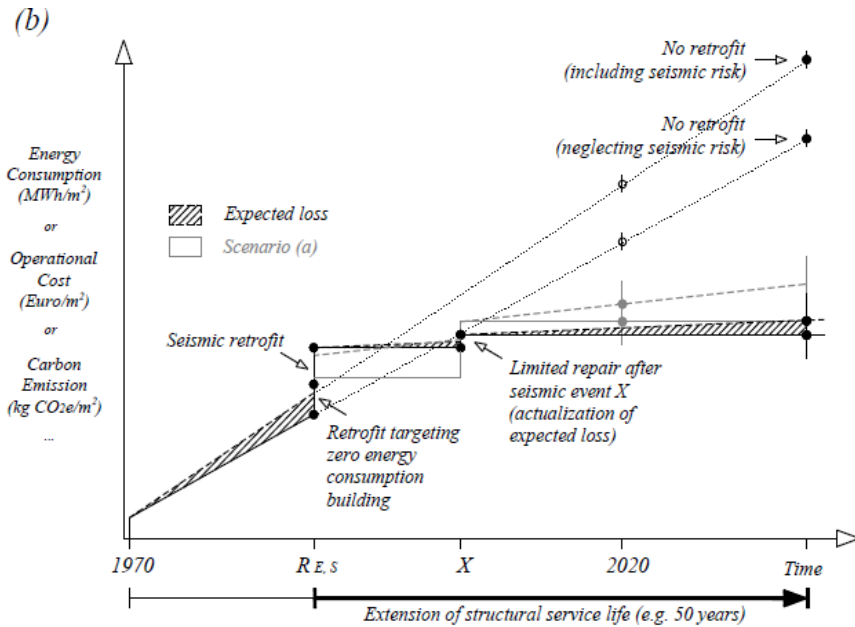


Figure 1.6. (Continued).

1.2. The Holistic Renovation of Existing Buildings

In light of evident structural, energetical and architectural deficiencies, the general tendency is solving each set of problems working in a sectorial way and without joint coordination among different disciplines. The analysis of state of the art, in fact, underlines that the suggested solutions generally define options that are episodic and limited to the resolution of isolated and temporary matters, although they are, in some cases, technologically advanced.

There are only a few examples which adopt the holistic approach in the renovation of existing buildings and the most interesting ones consider the insertion of technologies externally to the building, placed either on the perimeter (Structural Coating) or connected to the structure (Double Skin Façades). Figure 1.7 depicts a simplified scheme of possible integrated solutions.

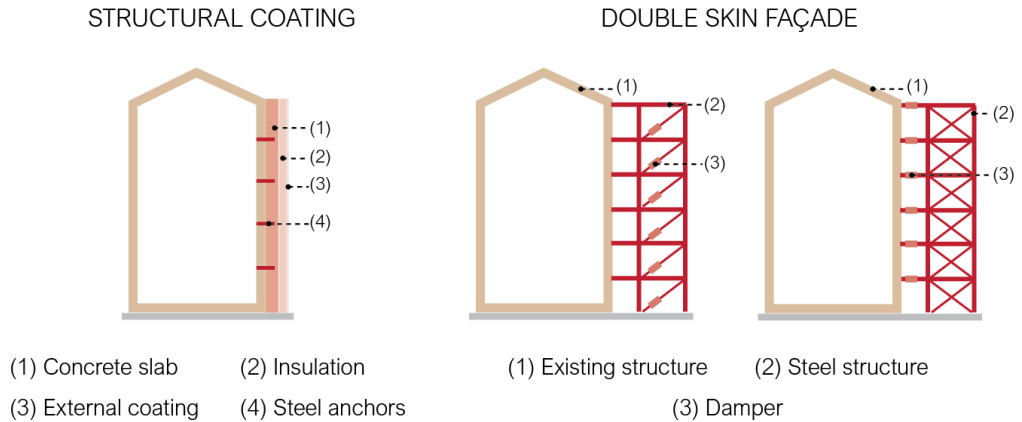


Figure 1.7. Restorative intervention solutions which adopt the holistic approach.

The Structural Coating (or Seismic Coat) is a reinforced concrete layer with a depth equal to 12-15 cm, placed on the external perimeter of the existing building and connected to it through metal anchors [11] [12] [13]. It creates a self-bearing structure able to contrast horizontal forces by realising a sort of strength and rigid “box”, which is able to keep internal stresses as small as possible, even in the presence of a rare earthquake. It is designed for remaining in the elastic field, creating a not dissipative solution which determines the definition of two systems: the existing building for gravitational loads and the seismic coat for the horizontal forces. The possibility of inserting an insulation layer in the stratigraphy allows the improvement of the energy performance of the building, reducing the transmittance and the heat losses through the perimeter (Figure 1.8).

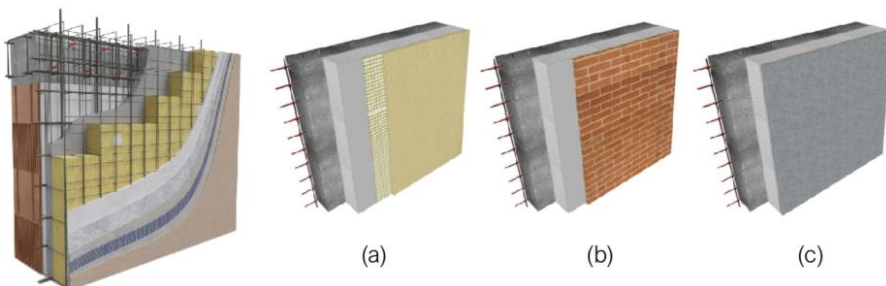


Figure 1.8. Schematisation of the Seismic Coat (left) and possible external coatings, (a) Plaster, (b) Brick, and (c) Metal [12].

The solution can be designed for reaching different seismic safety and energy efficiency levels according to the layer thickness and the used material. Therefore, the Seismic Coat could represent the right choice for integrated building restoration, as shown in Figure 1.9.



Figure 1.9. Example of the retrofitted building with the ECOSISM Seismic Coat before (a) and after (b) the restoration [12].

In alternative to the Seismic Coat, more interesting solutions consider the insertion of new structures made of steel and glass, the Double Skin Façade, which assume not only an architectural and energetic aspect but also improve the structural performance of the building. Considering the multiple features and configurations that these systems can assume, they are detailed presented and described in Chapter 2.

1.3. Conclusions

The assessment of the European building stock underlines the following considerations:

- A significant percentage of existing buildings is characterised by high seismic vulnerability, mainly due to their age and structural design. Most of them, in fact, were constructed before the introduction of the first seismic codes and are not designed or verified for withstanding horizontal forces. Moreover, they have also exhausted their design service life, and they should be retrofitted for complying to current seismic standards and guaranteeing an acceptable safety level.

- Buildings and the construction sector have together a massive environmental impact with high energy consumptions and CO₂ emissions. The presence, in fact, of low efficient equipment and poorly insulated envelopes affect the building performance. High energy requirement and inhabitants' discomfort conditions are the main results of these deficiencies.
- In light of evident structural and energetical deficiencies of existing buildings, an integrated retrofit intervention addressing both problems may be the optimum choice, with consequent benefits in terms of money and time.
- Among the various options, currently available for the structural and energetic upgrading of existing buildings, there are only a few examples which adopt a combined approach, and they are the Seismic Coat and the Engineered Double Skin Façade. Both are conceived for being placed on the outer surfaces of the building, avoiding the occupants' dislocation.

On the base of these findings, an Engineered Double Façade version is suggested and evaluated in the present work for the holistic renovation of the building adopted as a case study. The choice of centred the analysis on multi-layer façades and not on Structural Coatings is mainly due to their higher versatility from a structural, energetic, and fluid dynamic point of view.

2. The Double Skin Façade

2.1. Introduction

To better understand the main aspects of the retrofit solution investigated in the present research, a brief description of Double Skin Façade (DSF) systems is necessary. For this reason, various considerations which should be taken into account in the design of a multi-layer façade are described in the following lines.

Starting from its definition, several classification criteria are analysed, explaining the fundamental differences and peculiarities of each of them. Moreover, a focus on the main advantages and disadvantages of DSF systems is inserted for underlining negative aspects connected to such solution which need to be mitigated.

From its introduction, DSF has been profoundly improved, assuming more articulate and complex shapes for ensuring better energy performances and combining advanced technologies as the insertion of new materials or systems.

The innovation does not involve only the energy efficiency, and various works are centred on the analysis of Engineered DSFs, with a structural and energy function, which could be used for the design of new buildings or the restoration of the existing ones.

The last part of the chapter makes a review of principle approaches, currently available, for the energy modelling of these systems, exploring their limitations and opportunities. This is a crucial aspect that must be considered since the first stages of the DSF design, believing that their thermal performances, if wrongly investigated, can lead to inaccurate results.

2.2. DSF Definition

The Double Skin Façade is a European architectural trend mainly driven by the aesthetic desire for all glass façade buildings, the need of a consistent reduction of the energy consumption linked to the occupation stage and the parallel increase of the indoor comfort conditions, both acoustic and thermic [14].

The essential concept of the Double Skin Façade appears in the early 20th century in the northern European countries. In the preliminary version, the multi-layered façade is conceived and designed for reducing the heating consumption thanks to the air buffer enclosed in the cavity, which acts as a barrier for the heat losses and as a filter for the exchanges through the external envelope.

Uuttu (2001) describes this technology as “a pair of glass skins separated by an air corridor (also called cavity or intermediate space) ranging in width from 20 cm to several meters. The main layer of glass, usually insulating serves as part of the conventional structural wall or a curtain wall, while the additional layer, usually single glazing, is placed either in front of or behind the main glazing. The layers make the air space between them work to the building’s advantage primarily as insulation against temperature extremes and sound” [15].

Saelens (2002) defines the multiple skin façade as “an envelope construction, which consists of two transparent surfaces separated by a cavity, which is used as an air channel” [16].

In both definitions, three main elements can be identified:

- The DSF is defined as an envelope construction, selecting the borders for considering what is or not involved in this category (atria, ventilated greenhouses and glazed corridors are excluded).
- The presence of two glass skins able to ensure the transparency of the building surfaces.
- The insertion of the air corridor for the mitigation of extreme temperatures and noises.

To these main aspects, a new important element is introduced in the definition offered by Ding et al. (2005) who talks about an adjustable sunshade device, such as blinds, usually installed in the intermediate space to protect the interior rooms from high cooling loads caused by insulation [17].

2.3. DSF Classification

The extreme variety of the possible typologies of DSFs can be classified according to different criteria which are independent of one another and based not only on the geometric characteristics of the façade but also on its mode of working [18]. These are:

- The ventilation mode (Natural, mechanical and hybrid Ventilation).
- The compartmentalisation of the façade (Multi-Storey, Shaft-Box, Corridor and Box-Window DSF).
- The airflow type (Exhaust Air, Supply Air, Static Air Buffer, External Air Curtain, Internal Air Curtain).

Classifying the DSF according to the ventilation mode means defining the primary operation of the cavity, which can be naturally or mechanically ventilated. In a natural ventilated DSF (NV), the ventilation of the cavity is only due to the pressure difference generated by the stack effect and/or by the wind action. It does not present any mechanical components which help the air movements. This typology of DSF is the most common thanks to its simplicity of execution and maintenance. On the other side, it has some limitations considering that its performance is strictly connected to the external environmental conditions of the site (solar radiation, wind inflow and outflow pressure).

In a mechanically ventilated Double Skin Façade (MV) the ventilation is ensured by mechanical components that allow a constant and always efficient cavity airflow. The use of external elements could increase the operation and maintenance costs of the system. For this reason, the mechanically ventilated DSF is not highly recommended.

The last typology, the hybrid one (HV), combines the two systems previously described: the cavity is naturally ventilated when the climatic conditions are able to guarantee the selected airflow rate, otherwise the mechanical components start working as driven forces.

The second classification considers the presence or not of cavity partitions, and the possible subcategories are:

- The Box-Window DSF (BW): the façade is both horizontally and vertically fragmented, creating boxes with the same height of the storeys. The inflow and outflow vents are located in each module, and the ventilation of the cavity takes place inside the cell, defining weak fluxes limited to the specific box. The presence of vertical and horizontal partitions avoids the risk of acoustic bridges along the cavity height whereas, from an architectural point of view, this solution is the most fixed, most of the time not applicable in retrofit interventions but only for new buildings.



Figure 2.1. Box-Window DSF schematisation and examples.

- The Corridor DSF (C): the cavity is limited only by horizontal partitions, placed at the storey height. In this version, the ventilation is not continued from one level to the other, and the vents for the airflows are placed at the bottom and the top of each corridor.



Figure 2.2. Corridor DSF schematisation and examples.

- The Shaft-Box DSF (SB): the cavity is divided by vertical partitions, and the ventilated channel extends along the total building height. This type of façade is adopted only in case of a naturally ventilated cavity, considering that the driven force is the stuck effect. It is more applicable to new buildings than for the

restoration of the existing ones considering that its conformation or the anchors to the existing façade are not always compatible. From the economic point of view, the Shaft-Box configuration is highly profitable for the elevate prefabrication of its components and for having low maintenance costs, considering the absence of horizontal obstacles.



Figure 2.3. Shaft-Box DSF schematisation and examples.

- Multi-Storey DSF (MS): the façade is entirely open, without any horizontal or vertical partitions. The unique volume is only interrupted by perforated metal walkways inserted for the maintenance of the system. It is the most flexible option if compared to the others and, for this reason, it can be used both in case of restoration and new building design. The consistent air volume that enters and passes through the whole elevation if positively affects the ventilation with benefits, especially on the cooling side, increase the risk of acoustic bridges and fire propagation inside the cavity.



Figure 2.4. Multi-Storey DSF schematisation and examples.

The last criteria for classifying the DSFs is according to the direction of the air fluxes, and they are divided in:

- Outdoor Air Curtain (OAC): the air enters and exits the cavity from and to the outside.
- Indoor Air Curtain (IAC): the air enters and exits the cavity from and to the inside.
- Supply Air (SA): the air enters the cavity from the outside and is introduced inside the building.
- Exhaust Air (EA): the air comes from the inner spaces and is ejected outside.
- Static Air Buffer (BF): the cavity is sealed and acts as a filter for mitigating the thermal variations.

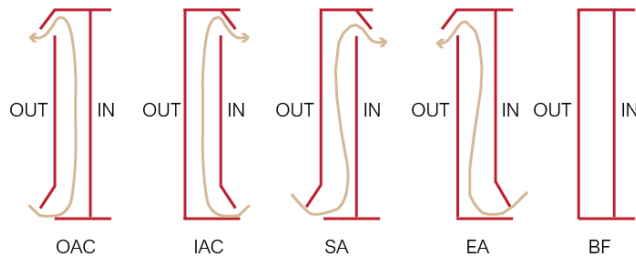


Figure 2.5. Air fluxes classification method.

The various ventilation modes can coexist in the same DSF, and they can be combined in an elevate number of options. The most common types, summarised in Table 2.1, are:

- Passive Façade: this is the most common solution in Europe, especially for commercial buildings. It is designed for being sealed during the wintertime for acting as an additional layer with benefits for the transmittance values. When the cavity is overheated, in summer, for example, the natural ventilation is activated.
- Active Façade: the cavity is sealed and designed for not communicating with the external environment and the air enters mechanically.
- Interactive Façade: this typology is very close to the main idea of naturally ventilated DSF, presenting only one difference. The ventilation is not only conferred to the stuck effect, but mechanical components are inserted.

Table 2.1. Main DSF ventilation modes.

Ventilation Type	Name of the Façade Typology
Natural	Passive Façade
Mechanical	Active Façade
	Interactive Façade

Figure 2.6 depicts the schematisation of the amount of each typology according to the classification criteria here described. The data come from the analyses conducted over 200 buildings all over the world [19].

The configuration with the highest percentage is Multi-Storey DSF (58%). Bow-Window and Corridor types show the same rate (17%) and the less common is the Shaft-Box configuration (7%). According to the ventilation type, naturally ventilated DSFs are the most diffuse (58%), while hybrid ventilation proved to be the least common solution (9%). Regarding the airflow path, the most common answer is the outdoor air curtain (45%). All other airflow path options fall within the same magnitude (11-16%). It should be noted that a significant number of buildings present more than one possible solution concerning airflow path.

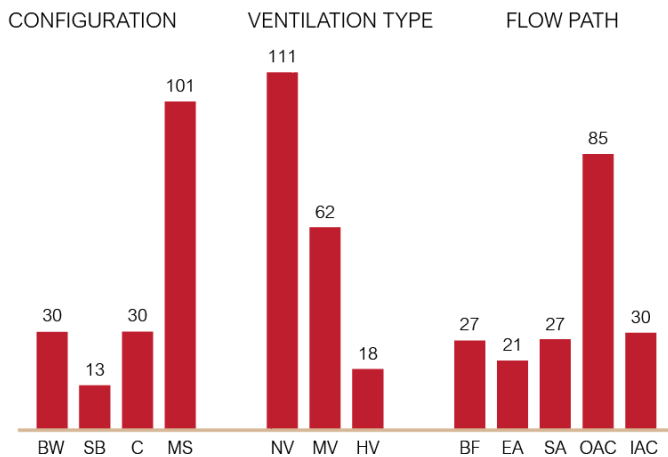


Figure 2.6. Number of DSF classified according to the analysed criteria.

In addition to the classification mentioned above methods, a more general and less standardised way for subdividing the multi-layer façade appears when the

idea of “intelligence” started to be included on DSF by the introduction of intelligent skin/façade/glass-façade concept [19].

An Intelligent Façade (IF) is, according to Wigginton and Harris (2002), “a composition of construction elements confined to the outer, weather-protecting zone of a building, which performs functions that can be individually or cumulatively adjusted to respond predictably to environment variations, to maintain comfort with the least use of energy”.

In other words, when the DSF associates to its main aspects the capability of being changeable, adapting to changes in outdoor conditions for achieving indoor comfort requirements and reduce energy consumption, it becomes an IF.

2.4. Advantages and Disadvantages of the DSF

The environmental benefits of DSFs have been deeply investigated by researchers for establishing the real feasibility of this technology. The main advantages can be summarised as energy consumption reduction, ventilation and thermal comfort enhancement, daylighting and glare control, sound insulation and noise mitigation [20] [21].

The reduction of energy consumption is the primary benefit, evaluated adopting different types of simulations, modelling systems and experimental approaches. For ensuring good performances, a Double Skin Façade must be designed considering climatic conditions, cavity ventilation and depth, and blind position. If thought as a combination of different typologies and adjustable systems, its efficiency could positively affect both cooling and heating needs. As the literature review underlines, an adequately designed Double Skin Façade can lead to consistent energy savings, up to 50% if compared to a single glazed skin [21].

Another remarkable peculiarity of DSFs which contributes to obtaining good performances of these technologies, especially in case of hot and subtropical climates, is the improvement of the ventilation, airflow and thermal comfort. The insertion of the air channel, naturally or mechanically ventilated, can replace contaminated air with fresh air. The result is the natural cooling phenomenon with the improvement of the human comfort condition.

The DSF accounts among the other advantages also the increase of the daylighting of the inner spaces thanks to its transparency. By the insertion of a shading system, inside or outside the cavity and adjustable according to the sunlight angles, the glare issue can be controlled and avoided, and the natural lighting can be uniformly distributed inside the building. For being effective, the shading system should be accurately designed and validated by means of computer simulations for ensuring that the indoor daylight illuminance value does not adversely impact the occupants.

The last benefit involves acoustic insulation and noise mitigation. The outer skin, in fact, acts as a barrier against the noise, obstructing its propagation. This aspect could become very useful when the Double Skin Façade is located inside noisy environments such as high traffic urban areas.

As analysed in the previous lines, the benefits of the Double Skin Façades involve both the comfort and energy-saving area. The disadvantages, instead, mainly affect the costs. If compared to a conventional façade, in fact, the DSF has higher construction costs because of the presence of the outer layer and the cavity. Moreover, extra charges are also associated with the accurate and detailed design phase, for ensuring the effectiveness of the system. Additional money should also be considered for the maintenance and operation of the DSF, related to the cleaning, inspection and servicing of the system. However, life cycle analysis confirms that DSFs can have long-term economic benefits [21].

2.5. DSF Origin and Evolution

Several books, articles and reports describe the history of the Double Skin façade. The first rudimental, as mentioned by Saelens [16], appears in 1849 when the director of the Industrial Museum in Brussels describes a mechanically ventilated multiple skin façade. This embryonal version of DSF was designed for allowing the circulation of hot and cold air, respectively in summer or wintertime, between the two layers.

A more defined concept of Double Skin Façade appears in first decades of the 20th century, following the influence of the new architectural tendencies based on the use of steel and glass and spread all over the world after the Great Exhibition held in Chicago in 1893.

The first real DSF example is the Steiff Toy Factory, built in 1903 in Giengen, Germany (Figure 2.7). The central aspect of the project was the maximisation of the natural lighting of the inner spaces, as expressly required by the client. The Double Skin extends over the whole height, and a 25 cm cavity depth improves the thermal properties of the external envelope.

For avoiding the overheating of the cavity and the general discomfort during the summer period, the cross-ventilation system was introduced, and low solar factor value glasses were selected for the outer layer.



Figure 2.7. Main elevations and a section of the Steiff Toy Factory.

The building was a success, and two additions were constructed in 1904 and 1908 with the same Double Skin system but using a timber structure, instead of the steel one, for budget reasons [18]. In the following years, because of the temperature increase, large ventilators were inserted on the façade for reducing the thermal discomfort recorded during the hottest months.

This example of Double Skin Façade never became famous, maybe because the building was far away from the main economic and cultural cities like Frankfurt and Berlin.

Later on, between 1926 and 1933, the famous architect Le Corbusier theorised the essential concept of DSF with his “Mur neutralisant” and the “Respiration exacte” [22]. The two solutions should be considered as complementary and based on the same three main aspects:

- A high airtightness through the envelopes for avoiding air and heat fluxes from inside to outside (wintertime) and vice versa (summertime).

- Mechanical and controlled ventilation for regulating, if necessary, indoor humidity and temperature.
- The conception of the façade as an active device able to neutralise energy flows through glazed surfaces. The idea is transforming the building envelope as a barrier for avoiding or, at least, mitigating heat fluxes from and to the inner spaces. For this reason, air pipes around the sealed double-glazed cavity are inserted. The air is thought for being warm in winter and cold in summer for collaborating to the heating and cooling needs of the building.

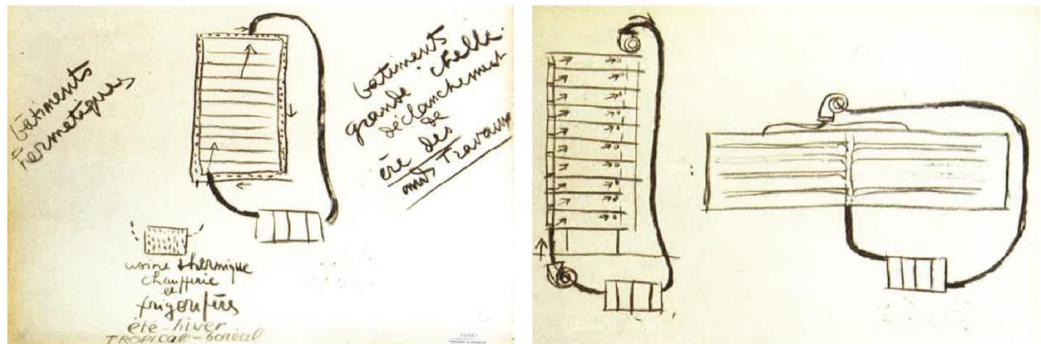


Figure 2.8. “Mur neutralisant” and the “Respiration exacte” sketches by Le Corbusier.

The DSF concept was firstly used in Italy in 1939, with the restoration of the ICO Center 3, in Ivrea (Figure 2.9). In this case, the use of an external skin was due to the designers’ intuition and not supported by any theory regarding its functionality. Attention to the cavity overheating was the critical point of the design and, for this reason, the inner layer presents manually adjustable blinds. Moreover, the south façade offers two different design choices for solar radiation control. Deep reinforced concrete overhangs and metallic slats are placed for being more effective in the solar shading. A cross-ventilation strategy is adopted to avoid discomfort conditions during the hottest months [23].



Figure 2.9. Main elevations of the ICO Center 3.

In the early 70s, the idea of the multi-layer façade was exported to North America and, in 1980, the Occidental Chemical Center in New York became the first building with this technology (Figure 2.10) [24]. It was primarily sponsored, becoming one of the best examples of possible energy efficiency solutions.



Figure 2.10. Main elevations of the Occidental Chemical Center and the focus on the cavity with the internal blinds.

The cavity, with a depth equal to 1.2 m, is designed for acting as a buffer zone and extends over the total elevation. It is ventilated thanks to the insertion of two systems: one for the extraction of the air from the cavity and the other for the conditioning of the inner spaces. An internal shading system, manually controlled, is inserted on the inner surface.

Since these first and simple examples, the Double Skin Façade concept becomes deeply investigated, exploring new configurations to improve the building

energy efficiency. This is the case of the RWE AG Headquarters (1996), the Agbar Tower (1999) and the Aurora Place (2000).



Figure 2.11. The RWE AG Headquarters (a), the Agbar Tower (b) and the Aurora Place (c).

The RWE AG Headquarters in Essen (Figure 2.11a) underlines the effectiveness of a well-designed DSF. The cavity is though for being sealed and acting as buffer area during the coldest months and opened for increasing the air fluxes and avoiding the overheating of the inner spaces. Thanks to this system, the building can be occupied without any conditioning (both cooling and heating) for 70% of the year.

The Barcelona Agbar Tower (Figure 2.11b) explores the biomimetic approach. The façade, with its ellipsoidal shape, acts as a human skin capable of operating as a filter for the external conditions. The windows are asymmetrically located according to the solar exposition and present external metallic brise-soleils, different for each orientation. In addition, photovoltaic panels are inserted on the south façade.

The Aurora Place in Sydney (Figure 2.11c) presents, on the external skin, screen-printed glasses for the sunlight reflection and the glare control. An internal

Chapter 2

shading system is also inserted for avoiding the overheating risk of the cavity, and additional metallic slats are placed on the façade mainly exposed to the sun.

The Jean-Marie Tjibao Cultural Center in New Caledonia (Figure 2.12), designed by Renzo Piano in 1998, reflects the adaptation and the contamination of the DSF system with the traditional wooden shells called “Kanakas”. The building is composed of two concentric rings. The main structure is made of wooden beams connected to the inner layer through metal anchors.



Figure 2.12. The Jean-Marie Tjibao Cultural Center and a focus on the metal anchors.

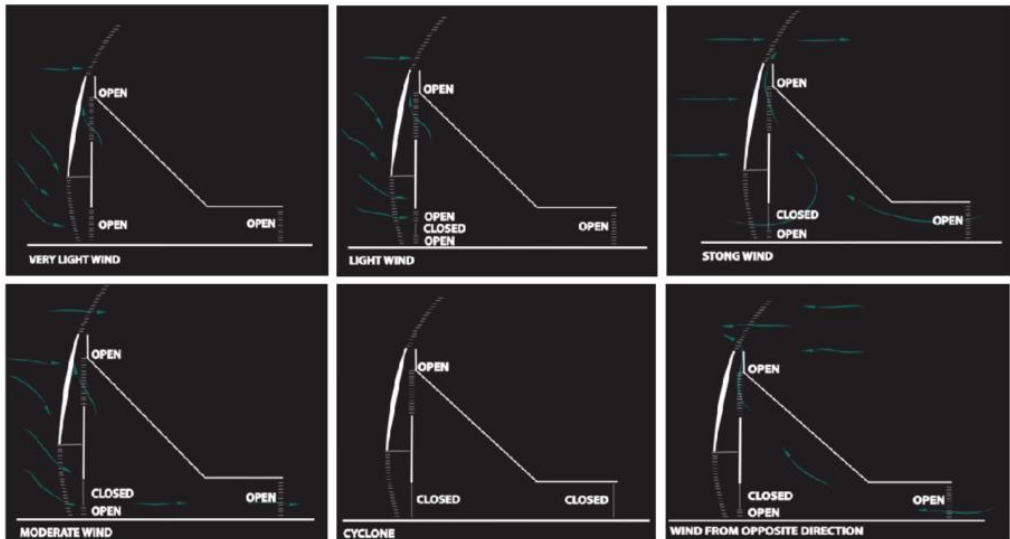


Figure 2.13. Possible configurations of the external skin in response to wind conditions.

The high building performances allow the absence of the conditioning system. The DSF, in fact, is designed for reacting according to the climate conditions. The façade openings are oriented, considering the main wind directions. They are thought of being variable and adjustable with the variation of the meteorological conditions. The external skin is able to regulate the air fluxes and ventilation of the cavity and protects the inner spaces in case of adverse phenomena. Figure 2.13 shows the possible configurations that the external layer can assume.

The DSF becomes also conceived as Active Wall, and interesting examples in this sense are the One Peking Road in Hong Kong (2003) (Figure 2.14a) and the Moor House in London (2004) (Figure 2.14b). The sensors, installed on the façade, measure light and temperature values and, according to the recorded conditions, activate or deactivate the external blinds. Thanks to this electronic control, the façade solar shading and the cavity ventilation ensure the maximum comfort for the occupants and energy savings.

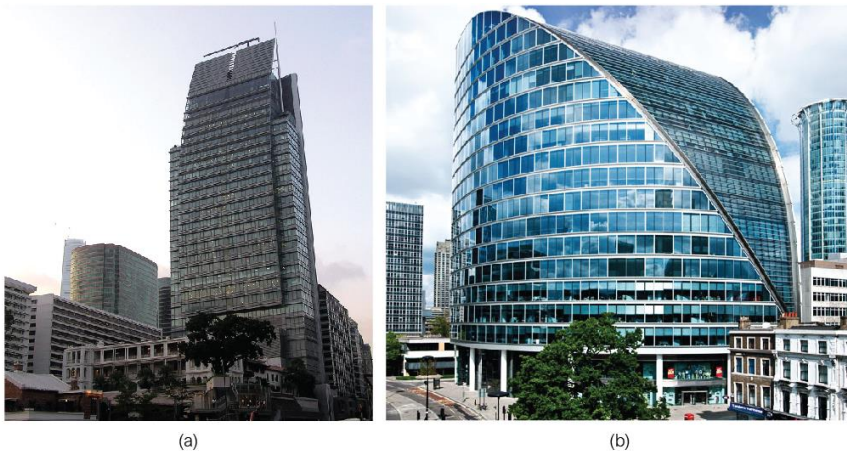


Figure 2.14. The One Peking Road (a) and the Moor House (b).

A highly innovative DSF is the MEDIA-Tic in Barcelona (Figure 2.15). Realised in 2009, the building replaces the ordinary glass, commonly used for the skins of the façade, with a new material: the Ethylene Tetrafluoroethylene (ETFE). This material is conceived for assuming two different configurations. The ETFE Diaphragm lays on the south-east elevation and incorporates three layers: the first layer is transparent, whereas the other two have a reverse-pattern that, if inflated

Chapter 2

or deflated, transforms the façade from transparent to opaque, avoiding solar penetration (Figure 2.16).



Figure 2.15. North-eastern (left) and south-eastern (right) elevations.

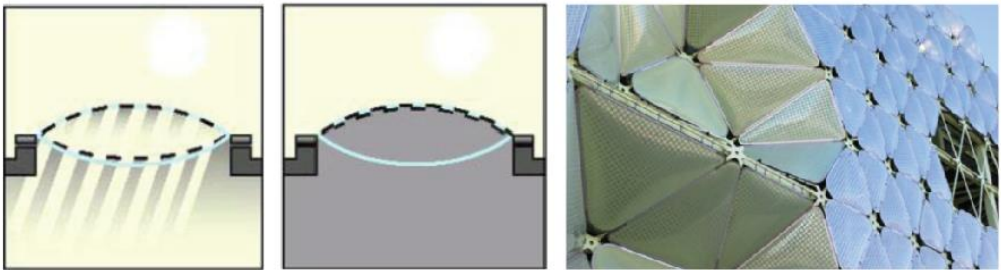


Figure 2.16. Schematisation of the ETFE Diaphragm operation.



Figure 2.17. South-western elevation with the shading system off (a) and on (b).

The south-western elevation is even more advanced, considering the presence of the ETFE lenticular configuration. Once the sun rays reach the sensors, the automated system injects dense nitrogen gas inside the pillow to instantly diffuse the solar radiation [25]. Figure 2.17 shows the two options of the façade: when the ETFE lenticular configuration is active (b) or not (a).

Thanks to the characteristics of the responsive façade, the building accounts a reduction in terms of energy consumption due to the cooling needs equal to 20% and avoids the emission of 114 tons of CO₂ [26].

Since the second decade of the 21st century, the exploration of new DSF shapes became an essential and universal aspect among engineers and architects, causing the introduction of more articulate and sophisticated systems. Figure 2.18 and Figure 2.19 show some of the famous buildings with advanced DSF technologies.



Figure 2.18. Pictures of the Canton Tower (a), the Capital Gate (b) and the Pearl River (c).

The Canton Tower in Guangzhou (2010) is one of the first buildings centred on the exploration of new configurations, marking a clear breakdown with the simple rectangular ones. Its form, volume and structures are generated by two ellipses rotated relative to another. This rotation confers the idea of a twisting tower. For ensuring the expected performances, wind tunnel tests have been performed on the scaled model of the building. Moreover, the parametric design has been

conducted for adopting the minimum amount of material needed to meet the criteria set for the tower [27].

The Abu Dhabi Capital Gate (2011) presents a more articulate configuration for improving building energy performance. The structure is composed of two diagrids: one external which defines the shape of the building and an inner one connected to the central reinforced concrete core. The internal layer has single glazed windows, whereas the external one is made of double glasses for improving the thermal insulation of the façade. The cavity, used as a buffer zone, avoids that the heated air coming from the outside enters the inner spaces. Façade reinforced panels, with diamond shapes, are designed to resist intense winds coming from various directions. The tower presents an external shading system, made of light metallic meshes that flexibly adapt to the façade line. This system is able to remove 30% of the solar heat [28].

The Pearl River in Guangdong (2011) is the best example of the integration of renewable energy on technologically advanced DSF. The tower, in fact, is oriented for intercepting the prevalent winds and led to apposite openings, where vertical axis turbines are located for the electrical energy generation. On the east and west façade, the shading system incorporates photovoltaic panels.

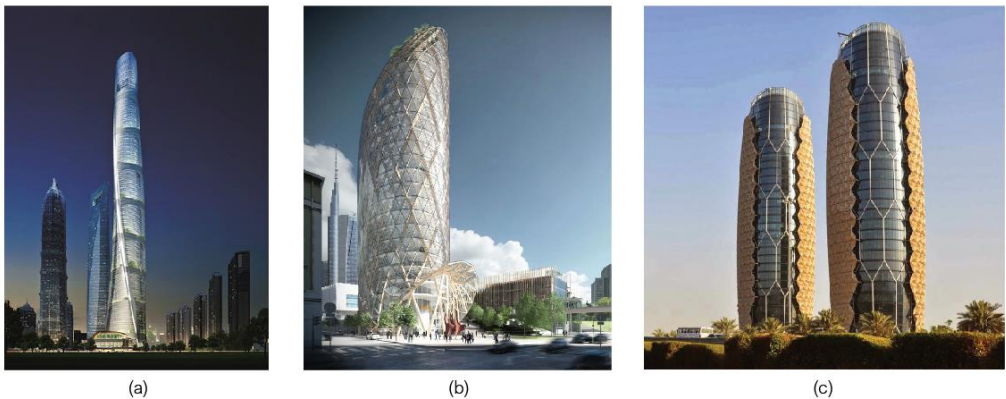


Figure 2.19. Pictures of the Shanghai Tower (a), the UnipolSai Tower (b) and the Al Bahar Towers (c).

The Shanghai Tower (2015) assumes a specific configuration due to the central design concept: a reduction equal to 24% of the wind load on the façade.

The shape is conceived as a vertical spiral and the horizontal envelope, which assumes the configuration of an equilateral triangle, is extended to the top of the building with a specific rotational angle different floor by floor. For ensuring good performances of the Double Skin Façade, fluid dynamics analyses have been performed during the design phase, investigating the air fluxes generated by different shapes inside the cavity.

The UnipolSai Tower in Milan (under construction-2021) is designed for optimising the façade components and surfaces, ensuring a lower environmental and cost impact. The external skin is intended for being adjustable and adaptable to external climate variations, minimising building heating and cooling needs.

Abu Dhabi Al Bahar Towers (2012) are preliminary examples of dynamic buildings. The façade, in fact, presents an external shading system that, according to the solar radiation and ventilation recorded by sensors, controls and changes the configuration of the outer layer. Inner spaces are shaded by a series of transparent umbrella-like components, able to open or close according to the sun path, as depicted in Figure 2.20. Polytetrafluoroethylene (PTFE) is the material adopted for these panels, driven by linear actuators.

The insertion of such intelligent systems allows the reduction of building cooling needs. In addition, solar and photovoltaic panels are inserted on the façade. The main result due to the combination of these technologies is the decrease of CO₂ emission by 1750 tonnes per year [29].



Figure 2.20. Detail of the operation modes of the external shading system.

2.6. DSF Innovation

The analysis of solutions for improving the energy performance of Double Skin Façade is a topic quite explored by researchers all over the world. Detailed

investigations are conducted for evaluating the DSF efficiency associated with different glazing options and shading systems.

According to the literature review [30], the use of the single clear glass for the inner pane and double reflective glazing for the outer surface guarantees the best option. By adopting this configuration, a saving in annual cooling energy up to 26% can be reached in comparison with a base case building with a traditional external wall and single absorptive window glazing. The obtained result is in contrast with the common European practice, which usually adopts single hardened glazing for the outer surface and an insulated double one for the inner layer.

Another essential and widely analysed aspect involves the shading system and evaluates the main parameters responsible for better solar protection. According to Gratia et al. [31], in fact, building cooling consumption can decrease up to 23% by paying attention to three main aspects:

- The location of the blinds.
- The colour of the blinds.
- The opening of the Double Skin.

According to the authors, the impact of the opening of the Double Skin Façade influences energy reduction from 7.4% to 12.6%. Instead, the characteristic of the blind system (both colour and localisation) can lead to an even more significant cut.

The most effective sun protection is generally ensured by using external blinds [32]. In case of DSF, the shading devices can be inserted inside the cavity (behind the outer skin, in the middle of the cavity or in front of the inner layer) for being protected from the bad weather and pollution. The authors select as the best configuration the localisation in the middle of the cavity because it allows a higher reduction of the temperature on the inner surface. Moreover, the light-coloured blinds (0.17 solar absorptance and 0.65 solar reflection) can induce higher cooling reduction than the mean-coloured ones (0.42 solar absorptance and 0.40 solar reflection).

Other investigations involve possible connections of DSF to the HVAC system, its use as a solar chimney or the insertion of new elements like Photovoltaic cells, vegetation, or Phase Changing Materials.

The University of Seoul suggests the use of a Multi-Storey Double Skin Façade in which the air fluxes are regulated by the conditioning system [33]. In detail, three are the investigated models, depicted in Figure 2.21. Case 1 represents the basic model of the case study, to which no control strategies are applied. In Case 2, the air heated by the solar radiation and exceeded 21°C is introduced to inside through openable windows located on the inner layer. Case 3 explores the option in which the cavity is combined with the HVAC system and used as a preheating space. In all cases, the DSF is placed on the south elevation and simulations are performed for evaluating the heating energy requirement associated with each model.

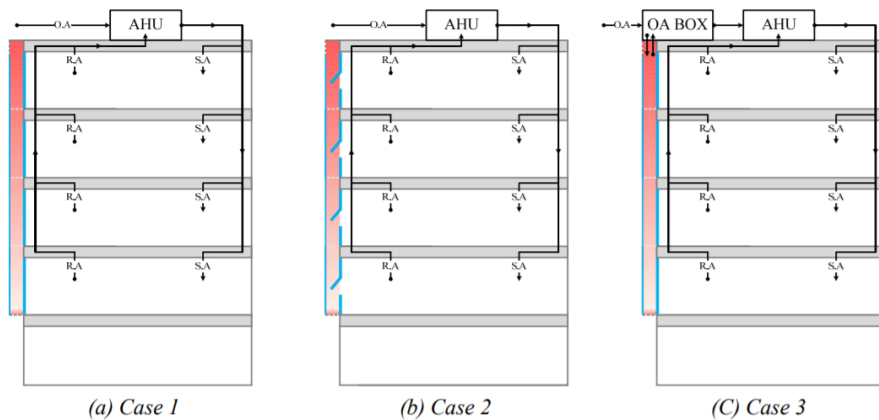


Figure 2.21. Schematic illustration of the simulation cases [18].

According to the obtained results, both Case 2 and 3 are more efficient than the basic configuration in terms of heating need reduction. Moreover, Case 3 confirms to be the best option, allowing, on the other side, a cooling energy reduction of 38%.

Other investigations analyse the performance of Double Skin Façades conceived as a solar chimney, evaluating its feasibility, and defining the main parameters which mostly affect the efficiency. Solar chimneys are passive

elements that use solar energy to induce buoyancy-driven airflow and naturally ventilate the building. Figure 2.22 shows the schematisation of the main suggested solutions.

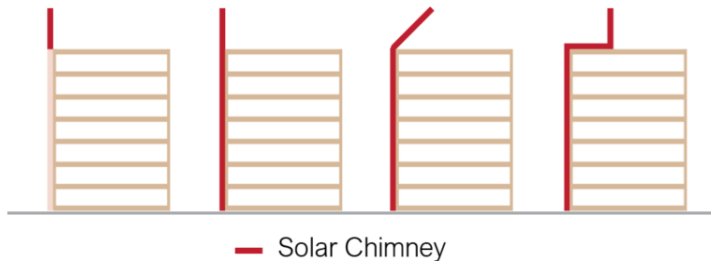


Figure 2.22. Possible configurations of solar chimney integrated into DSF systems.

Comparing with conventional Double Skin Façades, the insertion of the solar chimney is able to strengthen the stack effect, occurring in the intermediate space. Thanks to this aspect, stable natural ventilation is guaranteed through the building. The analysis underlines that the effectiveness of the solution depends on the height of the chimney: increasing this parameter, in fact, more ventilation rate and favourable pressure difference distribution are recorded [17] [34].

Moreover, the inclination of the chimney influences the thermal performance of the building. Vertical solar chimneys induce better airflow into the room if compared to the horizontal or sloped ones [35].

Stec et al. [36] analyse the application of vegetation inside the Double Skin Façade cavity, as shown in Figure 2.23. The primary considerations that should be taken into account are flowerpots, adequate spacings and the selection of the plants that shed in winter. According to the authors, the insertion of plants reduces the temperature on the DSF inner layer with benefits on the cooling side. A such conceived system, in fact, can reduce the building cooling capacity by almost 20%. Moreover, this solution would bring additional benefits like:

- The thermal insulation improvement.
- The acoustic condition improvement.
- The air filtering from dust and chemicals.
- The oxygen production and CO₂ reduction.

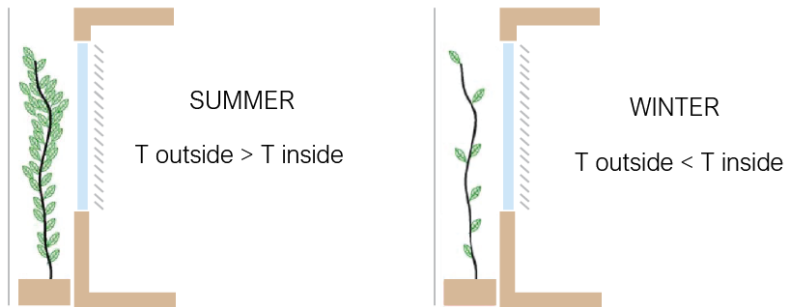


Figure 2.23. Summer (left) and winter (right) performance of the façade with plants [23].

Possible synergies among the Double Skin Façades and smart materials are also investigated, adding Phase Changing Materials (PCM) inside the system. The study conducted by de Gracia et al. [37] considers the introduction of microencapsulated PCM in the air chamber of a ventilated DSF. The addition of PCM has a double function: they absorb solar radiation for heating purposes during the winter season and become a cold storage system during the summer period. The analysed solution guarantees three main aspects: free cooling, cold storage, and prevention of solar radiation incidence. Figure 2.24 shows the operation modes of the system.

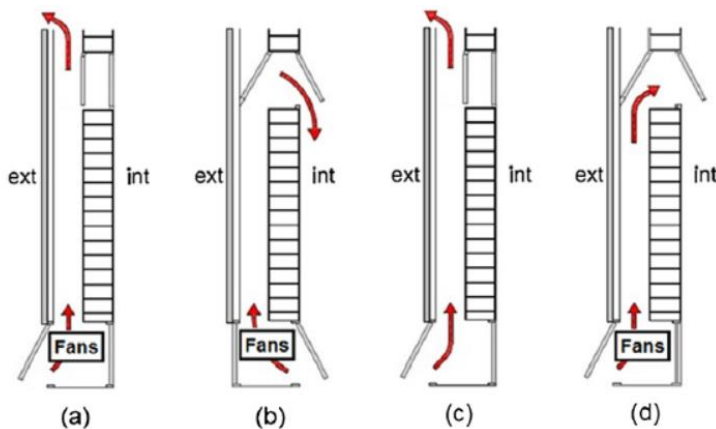


Figure 2.24. PCMs operation: (a) Charge process, (b) discharge process, (c) overheating prevention, (d) free cooling [22].

According to the obtained results, adding PCM to DSFs positively affects the free cooling. However, the cold storage sequence is able to provide during 3-4 hours at the peak cooling demand period of the building.

The application of PCMs is also investigated as incorporated on the outer surface of the DSF [38]. The focus of the research is evaluating the DSF cavity and inner skin surface temperatures, and the impact of PCMs on the annual building cooling demand. The analysis demonstrates that such a solution is able to reduce cooling needs up to 50% drastically.

The last topic recently investigated involves the efficient implementation of solar energy system barred by transparent Photovoltaic (PV) cells inside the cavity or on the outer surface of active DSFs [39] [40] [41] [42].

The analysis carried out by Gaillard et al. [39] evaluates the insertion of solar PV cells into a significant portion of the outer glazed surface and openings at the bottom and the top, for allowing natural ventilation by stuck or wind effect. The outer layer of the DSF is conceived with a prismatic configuration (Figure 2.25) for compensating the façade azimuth and improving the electrical performance by a more favourable orientation of solar cells.

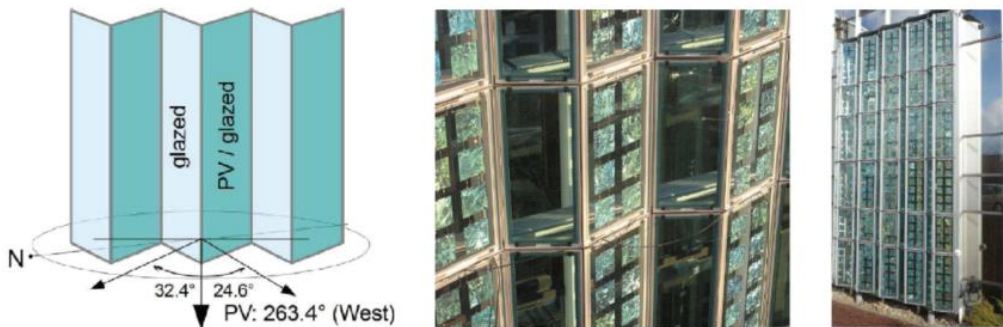


Figure 2.25. Design concept and pictures of the PV façade prototype [24].

During the summer configuration, the optimisation of the stack effect and heat transfer by natural convection is mainly sought to maintain the nominal efficiency of PV cells, which depends on the temperature. For a winter operating configuration, the system may be used for heat recovery as well as electricity production.

The analysis underlines that considering the building energy requirements, the performance during spring and autumn is encouraging and the longer daylight hours during summer allow a more significant cumulated electrical and power generation. Moreover, the natural ventilation of the cavity ensures, with specific wind conditions, the favourable cooling of the PV façade via the heat transfer to the exterior.

The insertion of PV modules on the building façade is also investigated by Athienitis et al. [40]. The proposed system consists of semi-transparent and opaque PV modules, placed on the outer layer for the generation of the solar electricity and thermal energy. Such designed technology allows the transformation of the façade from a simple external envelope to an active and energy-positive one.

For increasing the efficiency of the PV panels, the buoyancy-driven airflow within the cavity may be assisted by a fan (natural /hybrid ventilation). Figure 2.26 depicts the sketch and the operation of the PV façade. The numerical models of the solution are performed localising the PV Double Skin Façade in two different weather zones, Naples (Italy) and Montreal (Canada). The analysis underlines that the system can provide a high percentage of the electricity demand for building energy uses, and this improvement is particularly intense in the case of the Mediterranean climate.

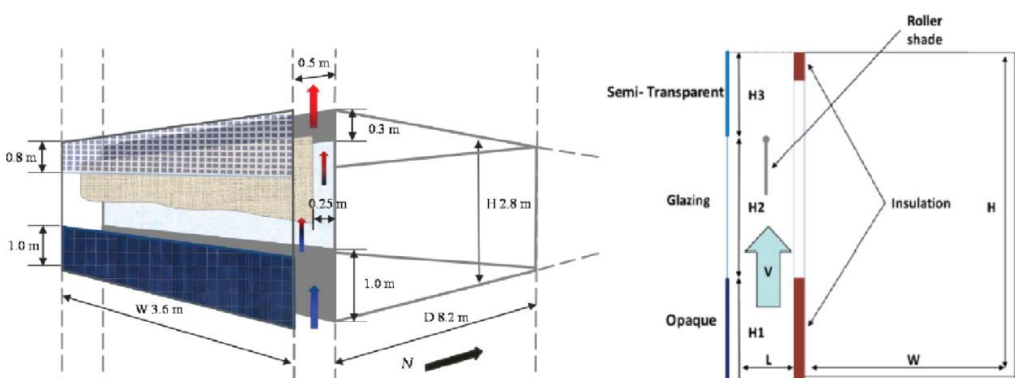


Figure 2.26. Sketch (left) and operation (right) of the PV façade [25].

The Hunan University in China [41] analyses the insertion of PV blinds in the DSF cavity. The central concept of the study is pursuing the façade solar shading while parts of radiation are converted into electricity. The innovation of this research stays in the localisation of the photovoltaic cells placed directly on the blinds.

A dynamic photovoltaic shading system is also investigated by Jayathissa et al. [42]. The suggested solution is designed for improving the building energy performance by controlling solar heat gains and natural lighting and, in the meanwhile, generating electricity on-site. In comparison to the previous research, the shading system is dynamic. The primary purpose of the façade is to guarantee satisfactory protection from solar radiation, the electricity generation, the inner free cooling, and the view (Figure 2.27).

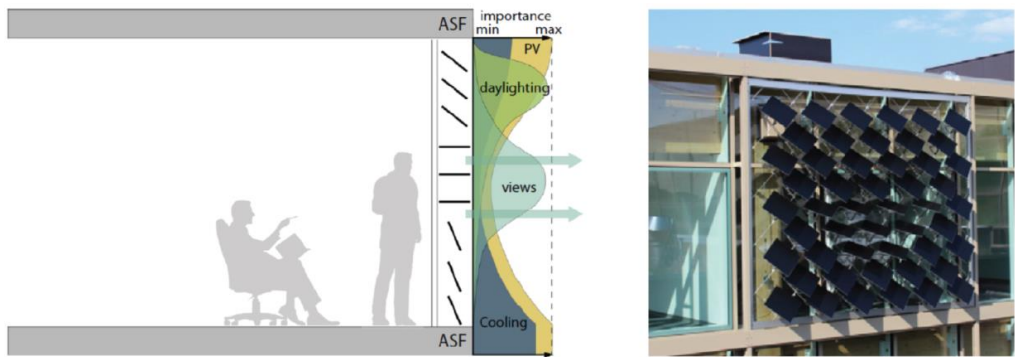


Figure 2.27. Active solar façade concept (left) and dynamic shading system (right) [27].

The analysis underlines that the suggested solution can save a 20-80% net energy if compared to an equivalent static PV shading system, depending on the efficiency of the building. On a typical sunny winter day, the PV generation is able to compensate for 62% of the energy demand, whereas on a sunny summer day, this rises to 270%. Over the year, including cloudy days, the PV supply compensates for 61% of the annual energy demand. This can reach 95% in the case of very efficient heating and cooling systems.

2.7. Examples of Engineered DSFs

The DSF innovation does not involve only energy efficiency aspects, promoting its combination with new and advanced technologies or materials. A novel focus consists of the insertion of structural elements able to confer an extra function, the seismic one, to the so-called Engineered Double Skin Façade. A such conceived façade becomes a mass damper system or an exoskeleton which, in case of restoration, can reduce the seismic vulnerability of existing buildings.

While mass dampers and DSFs are not new technologies individually, their combination is innovative and effective. Moon and Zhang et al. investigate the potential of the DSFs designed as structural motion control systems.

In detail, Moon [43] evaluates two DSF configurations: the first considers the DSF anchored to the primary structure by low axial stiffness connectors, the second suggests the insertion of distributed multiple tuned mass damper (TMDs) within the cavity. The main difference between the two options is the consideration of the outer skin of the DSF: flexible in the first case and fixed in the second one. Figure 2.28 depicts a schematisation of the explored solutions.

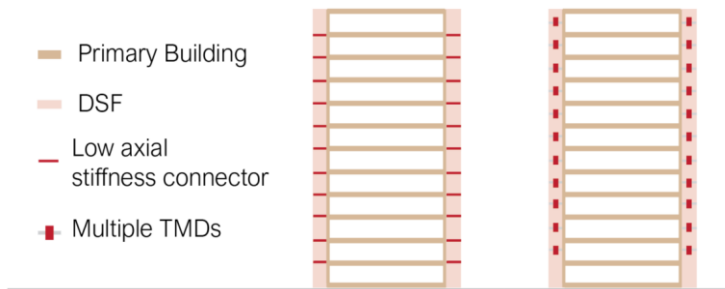


Figure 2.28. Concept diagram of DSF with low axial stiffness connectors (left) and multiple TMDs inside the cavity (right) (elaborated from [28]).

According to the first design strategy, the DSF is, in fact, conceived for moving back and forth, whereas the vibration of the primary structure is significantly reduced. The second scheme, instead, considers a rigidly anchored DSF, as it conventionally happens, and the movement of the fundamental structure is controlled by the insertion of vertically distributed multiple small TMDs placed inside the cavity. The results underline the effectiveness of both solutions for managing

building movement due to dynamic forces. Moreover, the eventual excessive motion of the outer skin in the first configuration represents a design challenge which could affect the practical application of the system.

Zhang et al. [44], starting from the preliminary analyses elaborated by Moon, investigate various options for DSF damper systems. In detail, three main configurations are evaluated, and they are schematised in Figure 2.29 and Figure 2.30. The common element for all schemes is the presence of multiple dampers and actuators placed in the connection between the inner and outer layer of the DSF (Figure 2.29).

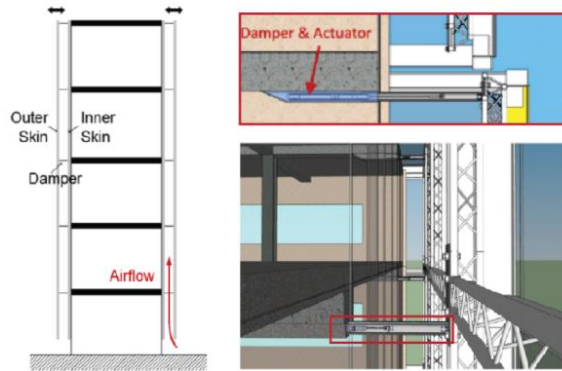


Figure 2.29. DSF damper concept and focus on the connection between the primary building and movable façade [29].

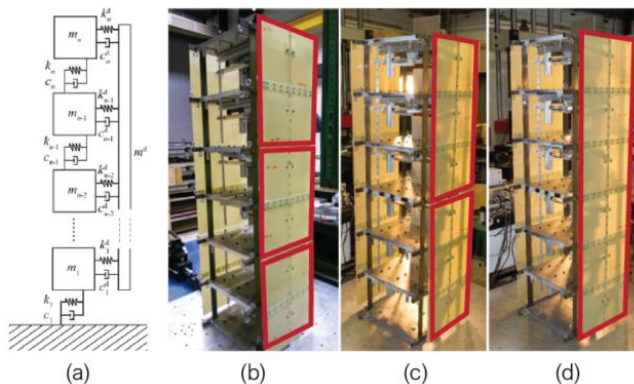


Figure 2.30. DSF damper rheological model (a) and analysed configurations: three dampers (b), two dampers (c) and one damper (d) [29].

The one damper configuration (Figure 2.30d) considers the façade spanned and connected to all six floors, moving as an entire piece. In the two and three damper configurations (respectively Figure 2.30c and b), each of the DSF dampers spanned respectively three or two floors. The obtained results show the effectiveness of the explored solutions estimating in terms of inter-story drifts. Among the DSF configurations, the one damper option ensures better performances than the others with a 42.73% decrease of the inter-story drift and a 53.67% decrease of the floor acceleration compared to the uncontrolled structure.

The Integrated DSF proposed by Takeuchi et al. [45] considers the insertion of seismic energy dissipation devices for conferring the additional structural function. Buckling Restrained Braces (BRBs) are inserted on the inner layer and protected by the external skin made of glass and louvre. Figure 2.31 depicts the schematisation of the investigated solution and its structural concept.

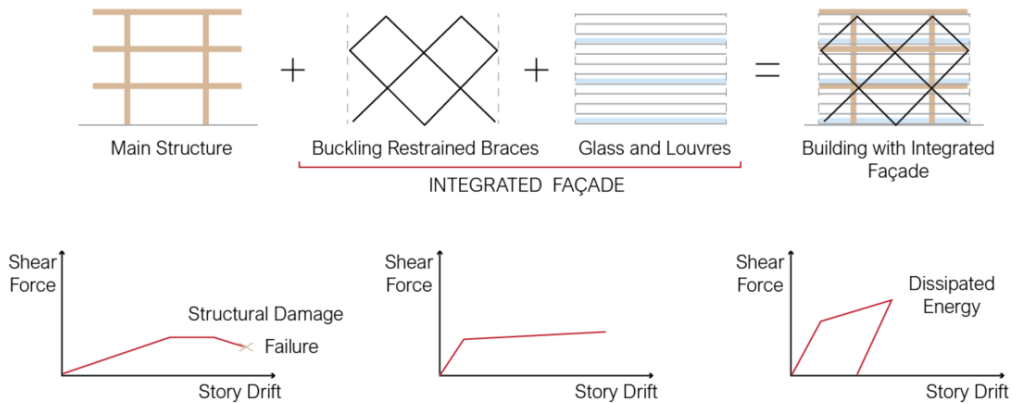


Figure 2.31. Main elements of the Integrated Façade and its structural concept (elaborated from [30]).

The proposed DSF is applied for the retrofit of an existing building, the Tokyo Institute of Technology. The seismic performance is improved by the insertion of BRADs, whereas the energy efficiency is ensured by the presence of the DSF cavity, designed for being open or closed according to climatic conditions. A detailed analysis is also carried out by the authors for defining the best shading system and glazing type in order to avoid discomfort situations in the occupied spaces.

Figure 2.32a and b show the 6-storey reinforced concrete building, respectively, in the pre and post-intervention configurations.



Figure 2.32. The Tokyo Institute of Technology before (a) and after (b) the restoration.

The adaptive building exoskeleton suggested by Scuderi [46] comes from the application of the biomimicry approach for the restoration of existing buildings. Starting from the animal exoskeleton with protective functions against temperature, sunlight or impacts and attacks, the “building exoskeleton” is conceived for enclosing the primary structure introducing higher stiffness and new dissipative capacity (Figure 2.33).

The exoskeleton more than being changeable in size, extension, typology and technology, can be designed for having an adaptive behaviour. This means that it can be, in a static condition, structurally independent to the existing building and collaborate when load cases require additional strength, as it happens during an earthquake.

Passive dissipative devices, strategically located and used as connectors between the new and the existing structure, decrease the horizontal displacements during seismic events. Shape memory alloys materials (SMAs) are selected to implement the dissipative dampers, thanks to their intrinsic properties: recentring and energy dissipation capabilities, excellent corrosion and fatigue resistance, large elastic strain capacity, and hysteretic damping.

Two different dissipative devices are selected for connecting the exoskeleton to the original building: the first is the one designed by Krumme and uses SMA wires for always working in tension, the second by Dolce and Marnetto in which the

recentring capabilities of NiTi wires, are coupled with the energy dissipation properties of steel elements.

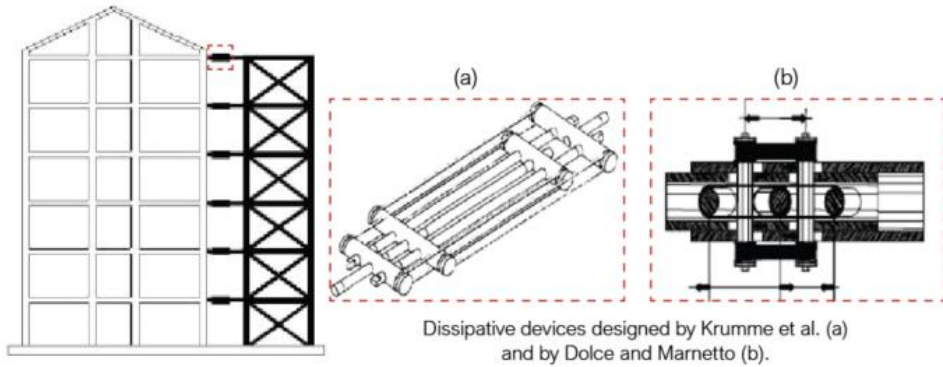


Figure 2.33. Schematisation of the adaptive exoskeleton [47].

Recently, significant progress in the field of DSFs for the energy and structural retrofit of existing buildings has been made by the Department of Engineering and Applied Sciences at the University of Bergamo. Various are the works which have explored this topic. For the sake of the brevity, only a few of them are reported in the following lines.

Several Engineered Double Skin Façades are analysed by Passoni et al. [48], and they take into account two different configurations thanks to the possibility to consider the exoskeleton made of shear walls or exploring a shell behaviour for the new façade (Figure 2.34).

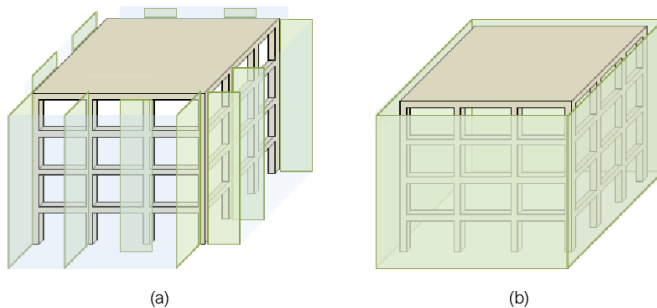


Figure 2.34. Shear walls (a) and shell structure (b) analysed by the University of Bergamo [47].

Chapter 2

In the first solution, the structural improvement is totally entrusted to shear walls, and the reduction of the energy requirement is ensured by the thermal insulation that covers the walls. Reinforced concrete or steel plate walls and steel braced frames are some of the shear wall technologies which can be adopted.

In the shell solution, instead, the shape and the extension of the new façade are analysed in order to decrease the area of every single structural component, loading as little as possible the foundations and the thinner parts of the exoskeleton.

Both the shear walls and the shell solution can be designed in contact with the existing structure or can be jutting. In the second case, new closed spaces are created for residences or opened areas, such as loggias and greenhouses, on one or more than one sides and with variable length. Both solutions, in addition, can be designed as either dissipative or not, inserting new devices or overstrength elements.

The solution analysed by Labò et al. [49] suggests the insertion of an external diagrid able to improve, at the same time, the energy and structural performance of existing buildings. The diagrid is conceived for assuming different strengthening solutions: elastic, dissipative and passive-responsive.

In the case of elastic diagrid, the required performance is achieved by adding a stiff and over-resistant exoskeleton able to limit the existing building displacement and protect the main structure from any possible damage condition.

The dissipative diagrid is designed for dissipating the horizontal forces due to earthquakes, and seismic devices are placed inside the connection of the diagrid with the primary structure or along the façade.

The last option, the smartest among the others, is conceived for adapting its behaviour according to the seismic intensity by changing its static scheme. For low-intensity earthquakes, in fact, the diagrid is designed for remaining in the elastic field, whereas it becomes adaptive to severe seismic events, thus protecting the primary building.

Figure 2.35 schematises the main configurations herein evaluated. The first two options, which consider elastic or dissipative diagrids, are involved in the standard strengthening solution, whereas the responsive one considers a sliding

operation, acting as a stiff system at the Damage Limit State, and as a dissipative one for the Life Safety Limit State. Thanks to this adaptability, low-intensity earthquakes do not cause any damages to the primary structure and intense loads transferred to floor diaphragms and foundations due to strong seismic events are reduced.

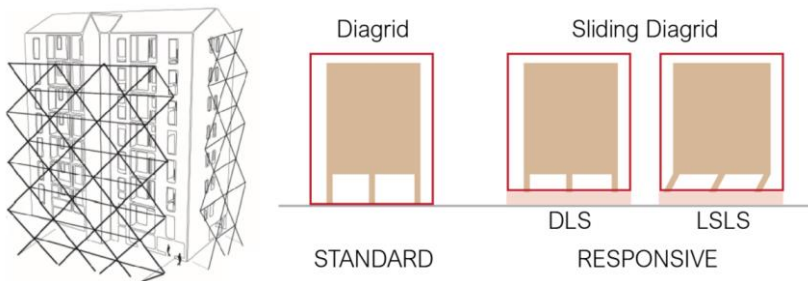


Figure 2.35. Axonometry of the Diagrid solution and schematisation of the retrofitted building with a standard or responsive exoskeleton [33].

2.8. DSF Modelling: Between Difficulties and Limitations

Since its introduction, DSF has been assuming different configurations. This improvement has influenced the development of numerical methods used to predict the thermal performance of DSF systems. Analytical and lumped models, network models, control volume models, zonal models and computational fluid dynamics (CFD) are, in fact, some of the possible approaches currently available for the numerical modelling of DSF systems. Each of them is based on different assumptions and complexity grade with consequences in the accuracy of results.

The first numerical models to be developed for studying the thermal behaviour of DSFs are the **analytical and lumped models**. Both can be adopted for obtaining useful information during the design stage, and several hypotheses affect the accuracy of results. The physical principles are solved introducing empirical correlations, available from the literature review, and used to calculate convection and radiation heat transfer coefficients.

The **airflow network modelling** considers each building component as a network of nodes and applies the conservation of mass for inlet and outlet fluxes associated with every node. It can be integrated with a thermal network model

which solves the heat balance at each node, fundamental in case of DSF simulations. This approach can provide fast and useful information, even if less precise if compared to CFD analyses, and it is mainly used by building energy simulation programs.

In the **control volume approach**, each layer of the façade is subdivided into various control volumes, connected to the others by the presence of the air channel. This method is based on the consideration that the mass flow rate associated with every volume is equal to the mass flow rate at the inlet. It provides a good compromise between computational resources and accuracy.

The **zonal approach** represents an intermediate method between the lumped and the CFD modelling since the DSF is subdivided into several control volumes, both 2D and 3D, more significant than the CFD meshes, with a lower computational cost.

The last and most accurate method for evaluating the thermal behaviour of DSFs involves **Computational Fluid Dynamics** techniques. CFD analyses apply a system of partial differential equations which govern the flow field and are derived from the principles of conservation of mass, momentum and energy. Outputs as temperature, velocity or pressure are calculated for each cell enclosed inside the solution domain. The equation usually solved is the Reynolds-Averaged Navier-Stokes that predicts averaged values for turbulent flows.

The literature review [50] underlines that the simulation approach drastically affects the capacity of the model in the prediction of the thermal behaviour of these systems and several studies evaluate [51] the limits and difficulties of Energy Simulation (ES) programs in the estimation of temperatures and airflow rates inside the cavity, suggesting new methods which combine them with CFD modelling.

The coupling approach, more accurate and reliable, has to bridge some discontinuities between the ES and CFD programs, due to different time scales, space models and speed patterns. Zahi et al. [47] describe some efficient strategies for integrated ES and CFD simulations for ensuring better estimations.

The common aspect among various coupling procedures is the consideration that, from one side, the ES program needs thermal exchange coefficients which should be accurate, and, on the other side, CFD analysis

requires internal superficial temperatures obtainable from building energy simulations. Figure 2.36 summarises various phases of the coupling procedure, underlining the circularity of the process.

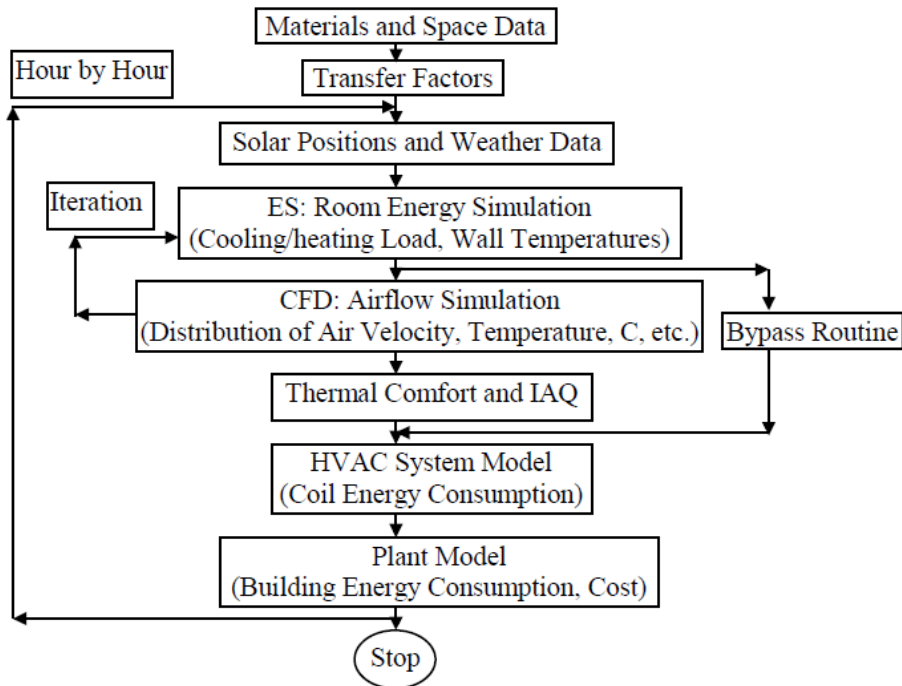


Figure 2.36. Main phases of a possible coupling procedure [47].

Coupling procedures can be classified according to the performance of the process. The dynamic process performs continuous information exchange between ES and CFD programs, while the static one has occasional information exchange for a simulation. The choice among one approach and the other depends on the user's accuracy requirement solution (Figure 2.37).

The static coupling approach involves one step or two-step exchange of information, whereas the dynamic strategies can assume various configurations according to the iterations that need to be performed. In the one-time step dynamic procedure and the full dynamic one, iterations between ES and CFD are performed until convergence, with a high computational cost.

Quasi dynamic coupling processes require less computational effort, and they should be adopted in case of small time-step simulations. For analyses performed over the whole year, the suitable coupling procedure is the virtual dynamic one which is able to generate, after various interactions between Es and CFD simulations, a function database to be implemented for the building energy investigation.

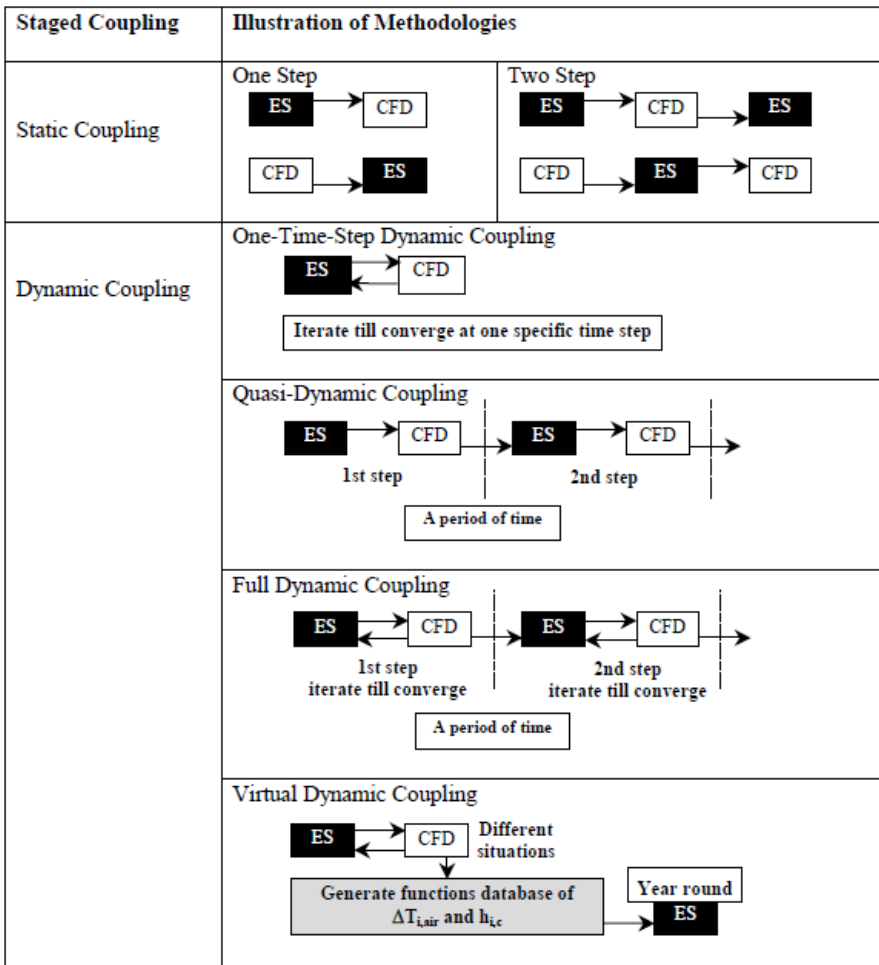


Figure 2.37. Schematisation of the coupling strategies herein described [47].

To underline how the coupling procedure can improve the accuracy of DSF building simulations, results obtained by the Massachusetts Institute of Technology are reported in the following lines [47].

A quasi dynamic coupling strategy is selected, and it starts from energy simulations, performed for calculating surface temperatures used as boundary conditions for CFD analyses. Flow and temperature distributions for each time step are main outputs obtained from CFD simulations, and they are inserted as input in the ES program for estimating new and more accurate surface temperatures and building energy requirement.

Table 2.2 shows the comparison among the day-averaged convective heat transfer coefficient ($h_{i,conv}$), the surface temperature (T_{wall}) of the building south wall where the DSF is placed, and its difference with the room temperature ($\Delta T_{i,r}$), calculated with and without the ES-CFD coupling.

Table 2.2. Comparison between heat transfer coefficients, surface temperatures and energy requirement calculated with and without the coupling procedure [47].

South wall	$h_{i,conv}$ (W/m ² K)	$\Delta T_{i,r}$ (°C)	T_{wall} (°C)	Q (W)
Without CFD	2.41	0	9.62	583
With CFD	4.37	-0.1077	11.65	638

The convective heat transfer coefficient estimated with the CFD analysis is almost twice the one obtained from the simple ES simulation. The new value allows the increase of the heat flux (Q) and the surface temperature.

Evaluating all heat transfer mechanisms for the same building component (Figure 2.38), it is clear that the increase of the heat transfer coefficient and surface temperature affects conduction, convection and radiation fluxes. Performing ES without any coupling strategy with CFD analyses tends to underestimate both conduction and convection mechanisms, whereas the radiation is slightly overcalculated.

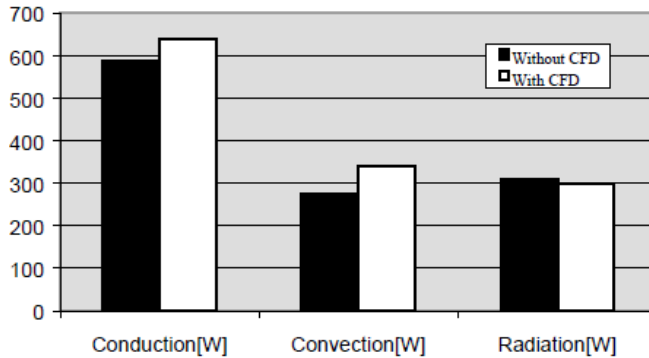


Figure 2.38. Heat transfer mechanism estimated on the building south wall [47].

The research here reported demonstrates the effects that boundary conditions have on the accuracy of estimations in case of DSF buildings. For this reason, they must be carefully set for avoiding wrong results which could affect the design of the whole system and the expected performance. Moreover, even if not precise as CFD analyses, ES simulations give a general idea of the DSF efficiency and, for this reason, more suitable in early design phases considering their low accuracy in the airflow patterns and temperature distributions.

3. Case Study

3.1. Introduction

The chapter is centred on the definition of basilar information about the reference building selected for the application of the Engineered Double Skin Façade. The attention has been focused on a building belonged to the social housing stock because representative of the typical construction practice of the past, reflecting any attention to seismic or energy problems.

In this sense, the building becomes typical of an existing heritage without architectural quality but mostly present on the territory and its conversion into a more eco-efficient and resilient one could be essential, nowadays and in the following years.

The Directive 2002/91/EU and its review 2010/31/EU indicate existing building heritage as a critical sector to obtain the reduction of energy consumption and atmospheric pollution. For this reason, new technical and technological standards for social housing buildings characterised by low energy performances, wicked technical devices and inappropriate comfort conditions are a primary requirement. Moreover, essential deficiencies can be easily identified also on the structural side, defining the holistic approach as the winning strategy for the rehabilitation of existing buildings.

Main features and structural details reported in the following lines are derived by the original structural, and architectural construction documents of the whole complex, presented in detail in Appendix C. Only general aspects are here reported, whereas specific information about energy or structural properties is inserted respectively in Chapter 4 and Chapter 6.

3.2. Reference Building: Structural and Energy Properties

The reference structure is a reinforced concrete building located in San Donato district in Pescara, Central Italy. The area is known for the Mediterranean climate, with mild winters and hot, sunny summers.



Figure 3.1. The localisation of Pescara (left and middle) and the reference building (right).

Owned by ATER (regional enterprise for social housing), it was built in 1983 according to the regulation codes and the construction techniques of the time. The building, identified with a red rectangle in Figure 3.2, is part of a residential area composed of three buildings, erected in the same moment and presenting common aspects.



Figure 3.2. Location of the reference building (red rectangle).

The selected case study is inadequate from a seismic and energetic point of view and with minor architectural value, as it can be seen from the views presented

in Figure 3.3. It hosts 48 apartments of which 12 with a total surface equal to 50 m² (A apartment) and 36 of 70 m² (B Apartment). The A apartments, two at every level, are located at the heads of the structure.



Figure 3.3. Views of the reference building. South-east (left) and north-west (right).

Figure 3.4 to Figure 3.8 show, respectively, architectural plans and elevations of the case study. The building has seven stories, a total height equal to 21.5 m, and a rectangular shape with 60 m and 12 m as main dimensions. The inter-story height is 2.7 m except for the ground floor, higher than the others (3.5 m). The garages and the entrance are located on the ground floor, while residential apartments are placed on the upper levels.

It is composed of two constructions, separated by a thermal joint. For this reason, only one construction is evaluated in the structural analyses, supposing that each building structurally behaves independently. The whole building is, instead, modelled for performing dynamic energy and CFD simulations because of the influence that the orientation or local fluxes can have on the estimations.



Figure 3.4. The architectural plan of the ground floor.



Figure 3.5. The architectural plan of the typical floor.



Figure 3.6. South-east elevation.



Figure 3.7. North-west elevation.

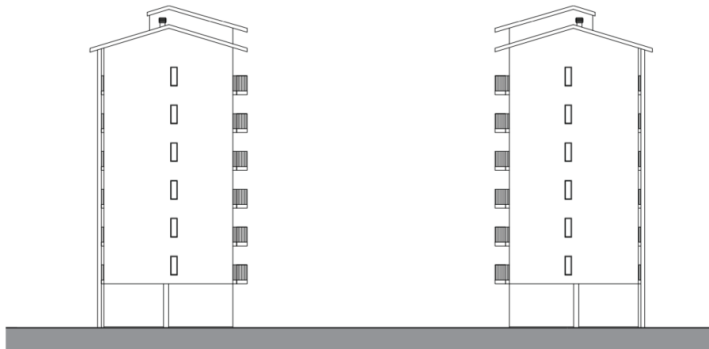


Figure 3.8. North-east (left) and South-west (right) elevations.

The building has an RC frame structure with infills made of hollow bricks. Hollow-core concrete slabs are present. The used concrete has a strain class equal to C25/30, and the steel of reinforcements is FeB38k. The structural details, reported in Appendix C, show the presence of bent rebars, as commonly designed according to the '80s Italian constructive technique. The bent rebar, traditionally inserted for collaborating with stirrups in the shear strength of structural elements, is effective for gravitational loads and becomes inactive in seismic conditions after reversal of the shear forces. The main consequence of this aspect is the high vulnerability to shear failure mechanisms.

From the energetic side, the building envelope does not comply to the current standard in the sector. The perimeter walls, in fact, does not present any insulation materials, but only an air gap enclosed by two brickwork layers, with a total transmittance value equal to $1.46 \text{ W/m}^2\text{K}$. Moreover, single glass windows contribute to the building inadequate performance, especially during the coldest months.

A preliminary phase for the modelling of the case study is the definition of the missed information, necessary for the structural and energy simulations. Flexural and shear reinforcements of beams are present only for a few structural components (see Appendix C) and, for this reason, their design is made according to the 80's Italian Code and hypothesising the constructive technique used at that time. For the energy modelling, essential parameters as the HVAC systems, the type of window glasses and the transmittance values for the opaque surfaces are assumed from data from the literature review.

3.3. Preliminary Considerations

The analysis of the technical documentation highlights primary deficiencies of the reference building, on both structural and energy side. They can be identified as:

- The presence of vertical irregularities. The ground floor is higher than the upper floors and does not have infill panels. Such configuration may lead to a possible soft-story mechanism.
- The presence of in-plan irregularities. The building centre of masses and the centre of rigidities do not overlap each other. This eccentricity can cause torsional modes in case of horizontal forces and the increase of displacement in localised parts of the structure.
- The structural design has been made only considering gravitational loads. This means that structural components do not have been verified to horizontal forces with a consequent high seismic vulnerability in case of earthquakes.
- The absence of proper insulation, combined to low-efficiency HVAC systems, confers low thermal performances of the building which does not satisfy current energy-efficiency standards.

4. Dynamic Energy Simulations

4.1. Introduction

The present chapter is focused on dynamic energy simulations carried on for evaluating the energy performance, expressed in terms of energy consumption and thermal comfort, of the reference building in its original state and with various DSF configurations. The choice of performing dynamic analyses stands in more accuracy and better-quality estimations than static or quasi-static simulations. The creation of a reliable model for these analyses needs the specification of several parameters such as building envelope details, thermal properties of materials and operational schedules. All these aspects must be coupled with the choice of suitable dataset, which better represents the climate surrounding the building.

Several scientific investigations have been developed to analyse the impact of weather data files in building energy simulations, as well as to calibrate and assess the accuracy of different weather data sources [52] [53]. The use of reliable climatic data, in fact, is an important issue both for the correct estimation of the building energy performance and the design of retrofit interventions. According to Bhandari et al., the predicted annual and monthly building energy consumption can vary, respectively, by $\pm 7\%$ and $\pm 40\%$ as a function of the provided location's weather data [54]. Thus, the proper selection of the climatic data becomes a crucial point especially when different building technological options are compared, by using dynamic simulation programs to optimise the energy performance and cost-effectiveness in various locations and climate zones. Besides, a better fit of simulation output to a real building context could help architects and engineers for designing more energy-efficient buildings and contributing to the global warming mitigation [55].

Unfortunately, not every site has recorded weather data, and it becomes necessary to use estimation models or software for their generation. However, it is essential to note that the prediction of climatological models is always subjected to uncertainty due to limitations of knowledge on the climate system, pollution and available computing sources [56]. A second aspect referred to measured or

estimated weather data is the possible absence of some climatic parameters, as it commonly happens with the solar radiation.

Global solar radiation or its direct and diffused components are not always available, but they have a significant impact on dynamic simulations. For this reason, a robust investigation sector is centred on the definition and evaluation of models for estimating the global radiation from other climatic parameters or for its decomposition into direct and diffuse solar components. The literature review underlines that the choice of solar radiation models can affect the reliability of dynamic simulations in the calculation of the hourly building energy demand and its effect is much more rooted in case of building with large windows, as it happens with DSFs [57]. The comparative analyses carried on by Lupato et al. [58] demonstrates that the selection of the correlation model can influence the heating and cooling energy prediction with an error, respectively, equal to 3.6% and 3.9%.

All these aspects should be taken into account, especially in the case of Double Skin Façade buildings. The application of multi-layer façades, in fact, is profoundly affected by the climatic conditions of the building locations and southern European countries are characterised by relevant solar gains that play a significant role in the performance of DSFs [59]. Moreover, the here adopted methodology for the generation and assessment of climatic files and the estimation of solar variables by using empirical models and correlations have been already tested and validated by performing various analyses, published on scientific Journals (Energy & Buildings and Building Simulation) and summarised in Appendix A. Preliminary simulations have also been carried on for evaluating the improvement achievable with the insertion of various typologies of passive and active Double Skin Façades, applied to a simple case study and detailed reported in Appendix B.

This chapter is addressed to a comparative analysis of weather datasets obtained with various sources (both real and virtual) and the evaluation of their effects on building energy performances through dynamic simulations, resourcing EnergyPlus software (Version 8.9) and DesignBuilder interface (Version 6.1.3). The chapter has three main stages briefly described below. The first stage involves the comparison between climatic datasets coming from real weather stations and regional climate models. The investigated parameters are temperature, global solar radiation, atmospheric pressure, relative humidity, wind speed and direction, and they are compared by plotting Taylor diagrams. In addition, a subsection is centred

on the decomposition of global solar radiation by adopting an empirical correlation model, solving the problem of missing data. This stage aims to figure out the accuracy of regional models in describing the pattern of the selected weather parameters and to define the climatology of the city under analysis.

In the second stage, the created weather data files are used in the building simulation software for quantifying the influence of various climatic data on the prediction of its energy performance, considering both the original state and with multiple DSF configurations. The last step, instead, evaluates the impact of climate change on the case study, before and after the insertion of the Double Façade, for estimating the building energy consumption and thermal comfort conditions due to future meteorological data.

This chapter is structured as follows. After this introduction, the weather data files generation and comparison are described in section 4.2. Subsequently, Section 4.3 presents the energy modelling and calibration of the case study, whereas Section 4.4 is centred on the description of the input parameters and setting referred to the modelling of DSF systems. It also presents the improvement due to the insertion of the Double Façade, compared with those related to the building original state. Section 4.5 describes the methodology followed for the generation of future climatic data and their effect on the case study with and without the DSF. Finally, Section 4.6 draws the main conclusions.

4.2. Weather Data Files for Energy Simulations

In recent years, the use of computational tools for the energy assessment of buildings has significantly increased, becoming a crucial point during the design stage. Building energy simulations (BES) are carried on assuming, as a general object, the achievement of the best indoor thermal comfort with the minimum energy requirement. Results of dynamic energy simulations are affected by many uncertainties, and the reliability depends on the accuracy of the inputs. For this reason, the model calibration is an essential preliminary phase, as suggested by the ASHRAE Guideline 14-2002 [60].

According to Radhi [61], the main factors which impact on a building energy use are the climate, design and people. Among these inputs, the most influence is the climate surrounding the building, as demonstrated by various researchers all

over the world. Weather data can generally be obtained by meteorological stations, which, unfortunately, are not always available for every location of interest. When real data are not present, Regional Climate Models (RCMs) can be used for generating estimated meteorological values for the investigated site. In general, RCMs use statistical methods to create detailed weather files on actual or past measured databases derived from a long period of recordings (usually 20-30 years). The main output of these models is the so-called “Typical Meteorological Year” (TMY).

On the basis of these evaluations, the reference building, selected as the case study, is dynamically simulated considering climatic files coming from real and virtual anemometers, adopting, in the second case, various RCMs obtained from the Fifth Mesoscale Model and the Coordinated Regional Downscaling Experiment.

The analysed building is located in the city of Pescara which has, according to the climate classification system developed by Köppen-Geiger [62], a humid subtropical climate denominated *Cfa*. The *C* group corresponds to “Warm Temperate” climates, the small letter *f* means “fully humid” and indicates the lack of a dry season. The letter *a* corresponds to a “hot summer”. Figure 4.1 depicts the Köppen-Geiger classification for the European continent.

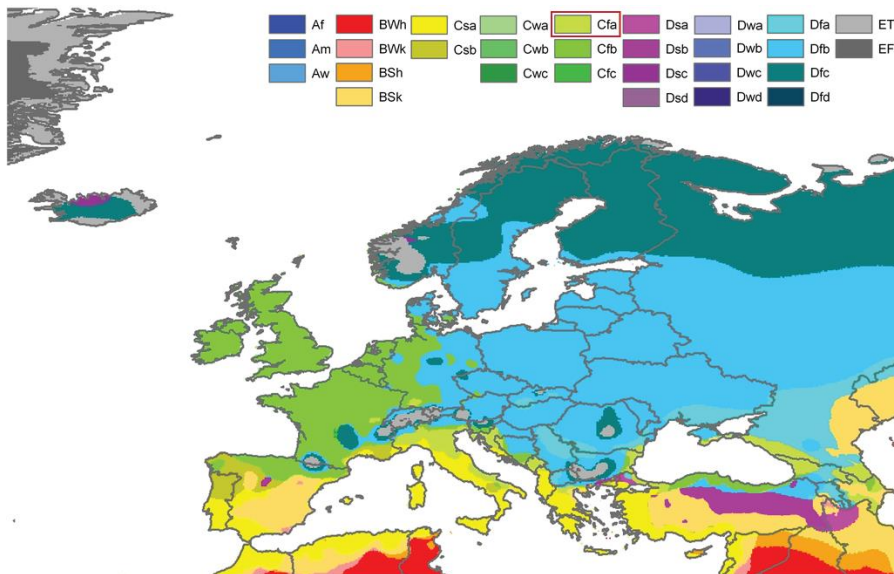


Figure 4.1. Köppen-Geiger climate type map of Europe [62].

In addition, the Italian national territory is subdivided into climatic zones, independent from their geographical location [63]. Each climatic zone, classified with a letter from A to F, presents a specific amount of degree-day. The degree-day unit is the sum, extended to all days in a conventional annual heating period, of positive differences between interior temperature (conventionally fixed at 20°C) and the mean daily external temperature. Pescara is classified as Zone D with a range of degree-days from 1400 to 2100 [64].

Various are the weather datasets coming from different sources and compared in the following lines. The investigated climate parameters are temperature, atmospheric pressure, relative humidity, wind speed and wind direction. Moreover, some standard methodologies are used to estimate the diffused and direct component of the global solar radiation, aiming to solve the problem of missing separated components and to evaluate the accuracy of the selected correlation models. In both cases, the evaluation is made through Taylor diagrams which consider the correlation coefficient (R), the centred root-mean-square difference (RMSD) and the standard deviation (σ).

The used weather data sources correspond to the Fifth Mesoscale Model (MM5), the International Weather for Energy Calculations (IWEC), the Italian Thermo-Technical Committee (CTI by its Italian initials) and observed data obtained from the Photovoltaic Geographical Information System (PVGIS), the Climate Network of the Osservatorio Meteorologico Milano Duomo Foundation, and the Regional Environmental Protection Agency (ARTA by its Italian initials). The recorded data are referred to the year 2017, selected as the reference year for the calibration of the model. Table 4.1 summarises the weather datasets used in the present analysis, reporting the name and a brief description of the data source for each climatic file.

Table 4.1. Weather datasets used in the energy simulations.

Weather dataset	Description
Climate Network_2017	Dataset for the year 2017, collected from the Climate Network weather station in Pescara
ARTA_2017	Dataset for the year 2017, collected from the ARTA weather station in Pescara
PVGIS_2017	Dataset for the year 2017, collected from PVGIS weather station in Pescara
DB-IWEC	Default dataset available in DB for Pescara obtained from IWEC
CTI	Dataset available for Pescara obtained from Italian Thermo-Technical Committee
MM5-MRF-LSM	Dataset for the year 2017, extracted with the MRF PBL developed by Hong & Pan, combined with the NOAA LSM
MM5-PLEIM-XIU	Dataset for the year 2017, extracted with the PBL developed by Pleim & Chang, combined with the LSM developed by Pleim & Xiu
MM5-BK	Dataset for the year 2009, extracted with the PBL developed by Blackadar

International Weather for Energy Calculations (IWEC)

DesignBuilder (DB) uses EnergyPlus format hourly weather data (*.epw) to define external conditions during simulations. Each location has a separate file describing the external weather parameters for every hour of the year at that location. These hourly weather data are typical data derived from hourly observations. Many of these weather files correspond to a record of multiple years, where each selected month is representative of that month for the period of record; the data describe the general patterns for that month and is not intended to be the average. The selection of months is usually based on a weighing of temperature, humidity, wind, and solar radiation.

The weather datasets used for this work correspond to the default weather file available in DB for Pescara, which has hourly weather data obtained from the International Weather for Energy Calculations [65]. The dataset is collected over an 11-year period (1959-1970). As this weather data source may represent the

most used for building energy simulations, it is included in the present analysis to determine its reliability against single year weather data, especially in the case of model calibrations. Measured data come from the meteorological station located at 42°85'00" northern latitude and 14°20'00" eastern longitude.

The Italian Thermo-Technical Committee (CTI)

Since 2016, updated databases for the generation of the Typical Meteorological Year for all Italian locations have been published by the Italian Thermo-Technical Committee [66]. These data are referred to measurements carried on for the city of Pescara, from 2007 to 2010. The TMY is generated on the basis of prescriptions defined by the European Standard (EN ISO 15927-4 "Hygrothermal performance of buildings - Calculation and presentation of climatic data - Part 4: Hourly data for assessing the annual energy use for heating and cooling") [67]. Measured data are referred to the meteorological station located at 42°28'00" northern latitude and 14°13'00" eastern longitude.

Fifth Mesoscale Model (MM5)

MM5 is the PSU/NCAR Mesoscale Model Fifth Generation (MM5), developed by the Penn State University (PSU) and the National Center for Atmospheric Research (NCAR). It is a model system able to simulate or predict mesoscale and regional-scale atmospheric circulation. Initially, this model was only hydrostatic, but after some further releases, it has definitively become non-hydrostatic. It is based on the momentum and energy conservation equations and adopts a tendency equation for the perturbation pressure (model prognostic on the pressure variable). The model employs a σ pressure coordinate system, based on the hydrostatic pressure reference, and uses finite difference numerical schemes (Arakawa B staggering). Further information can be found in Grell et al. [68].

The spatial configuration of the MM5 used in the present thesis consists of five nested domains (Figure 4.2a). The coarser domain has a horizontal resolution of 32.4 km; the next one has 10.8 km, the third 3.6 km, the fourth is set to 1.2 km grid spacing, and the inner domain has a 0.4 km resolution. Grid points for each domain are in total 31 (yellow rings), and the centre of all domains coincides with the reference building location (red circle), as it can be seen in Figure 4.2b.

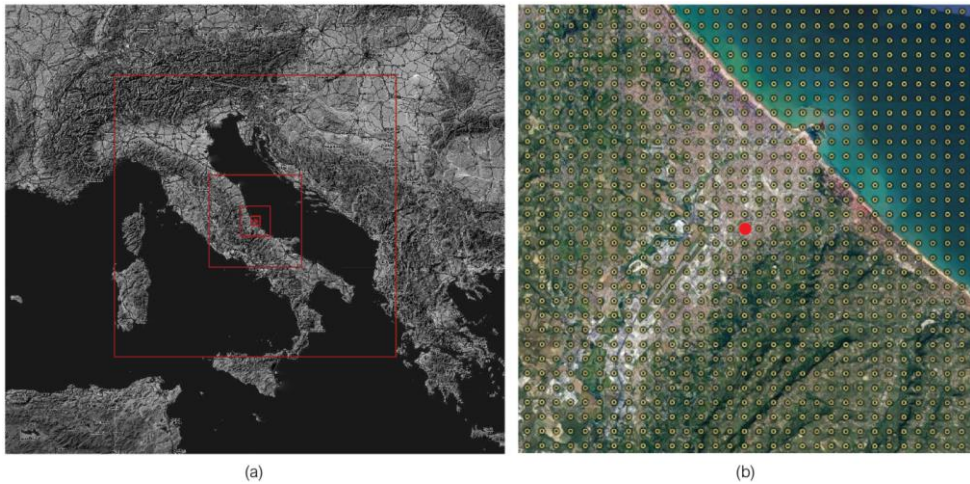


Figure 4.2. MM5 nested domains (red squares) (a) and the grid of the inner domain (b).

In the present work, the simulating features of the MM5 surface meteorological parameters are evaluated using three different combinations of the planetary boundary layer (PBL) and land surface model (LSM) parameterisation schemes. The first one corresponds to the PBL of Medium-Range Forecast model (MRF) developed by Hong & Pan [69] combined with the NOAH LSM (hereafter referred as MM5-MRF-LSM). The second combination comprises the PBL developed by Pleim & Chang [70] coupled with the LSM developed by Pleim & Xiu [71] (hereafter referred as MM5-PLEIM-XIU). The third and last model here evaluated is the one created by Blackadar [72] (hereafter referred as MM5-BK).

The collection of datasets for Pescara adopts simulations which cover one year from January 1st, 2017 to December 31st, 2017 and the chosen hindcasting procedure creates output values with 4-minute interval, converted into 1-hour variables for the intercomparisons and energy simulations. The database is extracted for the virtual anemometer localised at 42°26'34" northern latitude and 14°12'26" eastern longitude.

Observed data (Climate Network, ARTA and PVGIS)

Observed data are recorded from various sources for the year 2017 and compared with TMYs or estimated values. Figure 4.3 localises each real weather station and shows their position in comparison to the reference building.

Climate Network is a private and professional network of urban meteorological stations in Italy, developed in 2010. It consists of almost 50 weather stations located in several cities. The selected meteorological station is placed at the University of Pescara (42°27'07" northern latitude and 14°13'29" eastern longitude), and data with hourly timestep are recorded for all climatic parameters [<https://www.fondazioneomd.it/climate-network>].

The ARTA meteorological station is, instead, placed in the city centre of Pescara (42°28'06" northern latitude and 14°12'40" eastern longitude) and hourly data referred to the selected year are directly downloaded by the website [<https://www.artaabruzzo.it>].

The last database which involves measured values is composed of PVGIS data, a web application that allows the user to get information on climatic parameters. It is an entirely free and open access system with values for location in Europe and Africa, as well as a large part of Asia and America. Data can be downloaded from its website [https://re.jrc.ec.europa.eu/pvg_tools] where TMY are present for various year ranges. It is mainly used for obtaining information about solar radiation and photovoltaic system energy production. In the current work, the TMY generated from measured values referred to the recording period from 2007 to 2016 is selected. The data are extracted from the meteorological station located at 42°27'50" northern latitude and 14°12'50" eastern longitude.



Figure 4.3. The localisation of weather stations selected for the comparison.

4.2.1. Correlation Models for Estimating Solar Radiation

Climatic files, necessary for dynamic energy simulations, involve information about solar radiation and its components. Unfortunately, continuous measurements of solar variables are rare due to the high cost of the equipment which is not always installed in meteorological stations. In this sense, a critical investigated sector is the evaluation of empirical correlations for estimating, from other climatic variables, the global solar radiation, or its decomposition into direct and diffuse components.

A large number of correlations or methods based on the use of more readily meteorological data for predicting global solar radiation can be subdivided, considering the following factors [73]:

- Astronomical factors (solar constant, earth-sun distance, solar declination, and hour angle).
- Geographical factors (latitude, longitude, and elevation of the site).
- Geometrical factors (azimuth angle of the surface, tilt angle of the surface, sun elevation or azimuth angle).
- Physical factors (scattering of air molecules, water vapour content, scattering of dust and other atmospheric constituents such as O₂, N₂, CO₂, etc.).
- Meteorological factors (extra-terrestrial solar radiation, sunshine duration, temperature, precipitation, relative humidity, effects of cloudiness, soil temperature, evaporation, reflection of the environs, etc.).

Among various methods, the approach developed by Al Riza [74], on the basis of the work of Campbell and Norman [75] (hereafter just referred as Campbell and Norman), is commonly adopted for estimating the hourly global solar radiation. The selected methodology calculates the hourly global radiation from meteorological parameters like temperature (T), atmospheric pressure (P) and relative humidity (RH).

The first step consists in calculating the optical air mass number (m), which expresses the ratio of slant path length through the atmosphere to zenith path

length, according to Equation 4.1, where P_0 is the atmospheric pressure at sea level and α_s is the solar altitude angle of the sun.

$$m = \frac{P/P_0}{\sin \alpha_s + 0.50572 * (\alpha_s + 6.07995) \cdot 1.6364} \quad (4.1)$$

The second step is the definition of the atmospheric transmittance coefficient (τ). Beam atmospheric transmittance is the percentage of the beam (direct) radiation that penetrates the atmosphere without being scattered. Its calculation can be defined by the decision matrix, reported in Table 4.2, which considers the concept that water vapour through relative humidity reduces incoming radiation.

Table 4.2. Decision matrix for determining the atmospheric transmittance.

N°	RH condition (%)	τ value
1	RH \leq 40	0.69
2	40 < RH \leq 45	0.67
3	45 < RH \leq 55	0.57
4	55 < RH \leq 65	0.47
5	65 < RH \leq 75	0.41
6	75 < RH \leq 80	0.30
7	RH > 80	0.20

Once the τ value is known, it is possible to calculate the direct radiation on a surface perpendicular to the beam (I_p), which is a function of the global solar constant ($G_{sc} = 1367 \text{ W} \cdot \text{m}^{-2}$) and the optical air mass number (m) (see Equation 4.2). Then, the direct radiation (I_{dir}) and the diffused radiation on a horizontal surface (I_{diff}) can be calculated, respectively, with Equation 4.3 and 4.4, both expressed as a function of the solar zenith angle (θ_s). The last step allows the estimation of global solar radiation (I_{gl}) with Equation 4.5.

$$I_p = G_{sc} * \tau^m \quad (4.2)$$

$$I_{dir} = I_p * \cos \theta_s \quad (4.3)$$

$$I_{diff} = 0.30 * (1 - \tau^m) * G_{sc} * \cos \theta_s \quad (4.4)$$

$$I_{gl} = I_{dir} + I_{diff} \quad (4.5)$$

When the global radiation is measured or estimated, and the unknown values are, instead, its components, various empirical correlations can be adopted. Many investigations allow the estimation of global solar radiation components, correlating the fraction of the hourly radiation on a horizontal plane which is diffused (I_{diff}/I_{gl}) with the hourly clearness index (k_t). An interesting literature review of the empirical correlation models commonly used is presented by Tapakis et al. [76] and summarised in Table 4.3.

Table 4.3. Empirical correlation models suggested by various authors.

References	Location	Date	Constrains	k_t
Orgill and Hollands	Toronto, Canada	1967-1971	$k_t \leq 0.35$	$1-0.249k_t$
			$0.35 < k_t \leq 0.75$	$1.557-1.84k_t$
			$0.75 < k_t$	0.177
Erbs et al.	Highett, Australia	1966-1969	$k_t \leq 0.22$	$1-0.09k_t$
			$0.22 < k_t \leq 0.8$	$0.9511-0.1604k_t+4.388k_t^2-$ $6.638k_t^3+12.336k_t^4$
			$0.8 < k_t$	0.165
Bugler	Highett, Australia	1966-1970	$k_t \leq 0.4$	0.94
			$0.4 < k_t$	$(1.29-1.19k_t)/(1-0.334k_t)$
Hawladar	Paya Lebar, Singapore	1962	$k_t \leq 0.225$	0.915
			$0.225 < k_t < 0.775$ $0.775 \leq k_t$	$1.135-0.9422k_t+0.3878k_t^2$ 0.215
De Miguel et al.	Mediterranean Area	1978-1996	$k_t \leq 0.21$	$0.995-0.081k_t$
			$0.21 < k_t \leq 0.76$ $0.76 < k_t$	$0.724+2.738k_t-8.32k_t^2+4.967k_t^3$ 0.18
Karatasou et al.	Athens, Greece	1996-1998	$0 < k_t \leq 0.78$	$0.995-0.05k_t-2.4156k_t^2+1.4926k_t^3$
			$0.78 < k_t$	0.2
Chandrasekaran and Kumar	Madras, India	1983-1987	$k_t \leq 0.24$	$1-0.178k_t$
			$0.24 < k_t \leq 0.8$	$0.9686+0.1325k_t-1.4183k_t^2-$ $10.1860k_t^3+8.3733k_t^4$
			$0.8 < k_t$	0.197
Soares et al.	Sao Paulo City, Brazil	1998-2001	$k_t \leq 0.17$	1
			$0.17 < k_t < 0.75$ $0.75 \leq k_t$	$0.9+1.1k_t-4.5k_t^2+0.01k_t^3+3.14k_t^4$ 0.18
Oliveira et al.	Sao Paulo City, Brazil	1994-1999	$k_t \leq 0.17$	1
			$0.17 < k_t < 0.75$ $0.75 \leq k_t$	$0.97+0.8k_t-3k_t^2-3.11k_t^3+5.2k_t^4$ 0.18

Table 4.3. (Continued).

References	Location	Date	Constrains	k_d
Jacovides et al.	Athalassa, Cyprus	1998-2002	$k_t \leq 0.1$ $0.1 < k_t \leq 0.8$ $0.8 < k_t$	0.987 $0.94+0.937k_t-5.01 k_t^2+3.32k_t^3$ 0.177
Reindl et al.	5 European and North American Locations	1979-1982	$k_t \leq 0.3$ $0.3 < k_t < 0.78$ $0.78 \leq k_t$	1.020-0.248 k_t 1.45-1.67 k_t 0.147
Boland et al.	Victoria, Australia	67 days	-	$1/(1+\exp(7.997*(k_t-0.586)))$
Boland et al.	Adelaide, Australia	67 days	-	$1/(1+\exp(-5.00+8.60k_t))$
Lam and Li	Hong Kong	1991-1994	$k_t \leq 0.15$ $0.15 < k_t \leq 0.70$ $0.70 < k_t$	0.977 1.237-1.36 k_t 0.273
Collares-Pereira and Rabl	Five location in United States	1961-1976	$k_t \leq 0.17$ $0.17 < k_t < 0.80$	0.99 $1.188-2.272k_t+9.473k_t^2-21.586k_t^3+14.648k_t^4$
Al Riahi et al.	Fudhaliyah, Iraq	1984-1987	$k_t < 0.25$ $0.25 \leq k_t \leq 0.7$ $0.7 < k_t$	0.932 1.293-1.631 k_t 0.151
Torres et al.	Pamplona, Spain	2006-2008	$k_t \leq 0.225$ $0.225 < k_t \leq 0.755$ $0.755 < k_t$	0.9943-0.1165 k_t $1.4101-2.9918k_t+6.4599k_t^2-10.329k_t^3+5.514k_t^4$ 0.18
Chikh et al.	3 locations in Algeria	1990-1992	$k_t \leq 0.175$ $0.175 < k_t < 0.87$ $0.87 \leq k_t$	1-0.232 k_t 1.17-1.23 k_t 0.203
Elminir et al.	3 locations in Egypt	1999-2002	$k_t \leq 0.22$ $0.22 < k_t \leq 0.8$ $0.8 < k_t$	0.8526-1.1778 k_t $0.814-1.106k_t+0.366k_t^2-0.997k_t^3+1.221k_t^4$ 0.213
Ulgen and Hepbasli	Izmir, Turkey	1994-1998	$k_t \leq 0.32$ $0.32 < k_t \leq 0.62$ $0.62 < k_t$	0.68 $0.0743-19.343k_t+206.91k_t^2-719.72k_t^3+1053.4k_t^4-562.69 k_t^5$ 0.30
Lee et al.	22 locations in South Korea	1986-2005	$k_t \leq 0.2$ $0.2 < k_t < 1$	0.92 $0.691+2.4306k_t-7.3371k_t^2+4.7002k_t^3$
Ruiz-Arias et al.	Albacete, Spain	2002-2006	-	$0.086+0.88\exp(-\exp(-3.877+6.138k_t))$
Macagnan et al.	Madrid, Spain	1975-1991	$k_t < 0.2$ $0.2 \leq k_t < 0.7$ $0.7 \leq k_t$	0.996+0.424 $k_t-0.586k_t^2$ $1.11-0.203k_t-2.52k_t^2+0.617k_t^3+1.063k_t^4$ $-0.0169-0.99 k_t+1.63k_t^2$

As can be seen, the correlations are tested in different cities located, both in the north and south hemisphere. The common element among all correlations is the definition of the diffuse fraction component (k_d) from only a single predictor which is the clearness index, ignoring important aspects as solar altitude (a), persistence of global radiation level, long-wave atmospheric emission air mass, relative humidity, apparent solar time and temperature.

Starting from the evaluated limits of all these correlations, Tapakis et al. have introduced a new correlation model in which the solar altitude, expressed in radiant, is also taken into account. The correlation suggested by the authors is represented by Equation 4.6, where p_1 , p_2 , p_3 , p_4 , p_5 , p_6 and p_7 are empirical coefficients, shown in Table 4.4:

$$k_d = \frac{p_1}{[p_2 + \exp(p_3 + p_4 k_t + p_5 k_t^2 + p_6 \alpha_s + p_7 k_t \alpha_s)]} \quad (4.6)$$

Table 4.4. Coefficient of the correlation model for each constrain.

Constrains	p_1	p_2	p_3	p_4	p_5	p_6	p_7
$0 \leq k_t < 0.32$	7.37	7.52	-13.57	64.94	-71.73	6.97	-22.06
$0.32 \leq k_t < 0.63$	5.11	3.91	-0.07	1.67	2.9	-0.5	0.94
$0.63 \leq k_t < 1$	11.7	29.85	-83.28	241.32	-168.56	-14.84	21.06

This correlation has been tested and validated on the Cyprus island, and comparisons with the other models applied to the northern hemisphere underline that the introduction of the α parameter into the calculation slightly improves the accuracy of results. For this reason, the decomposition of the global solar radiation in the present thesis is made adopting the Tapakis et al. empirical correlation model.

4.2.2. Weather File Comparisons

The above-mentioned weather datasets are compared by means of Taylor diagrams in order to estimate the quality of the sources, referred to specific years or selected periods, as in the case of TMYs. Moreover, the comparisons aim to underline the importance of using the correct database in case of building modelling and calibration.

The Taylor diagram [77] is widely used to investigate climate models, considering its ability to compare datasets and evaluating various skills at the same time. Each point in the two-dimensional Taylor diagram can represent simultaneously three statistics (R , $RMSD$ and σ). The correlation coefficient R is a number between -1 and +1, which measures the strength or consistency of the

relationship between two variables (x and y). If $R=0$, the two variables are uncorrelated. A positive correlation means that x and y vary in the same direction. For a negative R , x and y go in opposite directions (a larger x will imply a smaller y). If $R=1$ then x and y are completely correlated, indicating an entirely consistent relationship. The centred root-mean-square difference (RMSD) is the most widely used statistic to quantify differences between two variables and tends to zero when they become more alike. The standard deviation σ is the standard distance between a variable and the mean of the dataset, and it measures the fluctuations of the error around this mean.

In Taylor diagrams, the RMSD between the simulated and observed patterns is proportional to the distance to the point on the x-axis identified as "REF", which is the reference data. The dashed arcs indicate the RMSD. The standard deviation of the simulated pattern is proportional to the radial distance from the origin (dotted arc). The solid arc indicates the standard deviation of the reference. Simulated or estimated patterns that agree well with observations lie nearest the point marked "REF" on the x-axis. These models will have a relatively high correlation (dot-dash line) and low RMS errors. Models lying on the solid arc will have the correct standard deviation, which indicates that the pattern variations are of the right amplitude [27].

The climatic files obtained from the selected sources are translated into hourly datasets before plotting Taylor diagrams. Comparisons are made both on annual and seasonal range period to evaluate the accuracy of each model for general and specific conditions. Seasons are defined according to the meteorological seasons in Italy: spring from 01/03 to 31/05, summer from 01/06 to 31/08, autumn from 01/09 to 30/10 and winter from 01/12 to 28 (29)/02.

Two series of Taylor diagrams, normalised by dividing the values by the standard deviation of the correspondent observed quantity, are plotted in the following lines (Figure 4.4 to Figure 4.10). First, general climatic parameters (temperature, atmospheric pressure, relative humidity, wind speed and direction) are compared; then, a focus is made on the solar radiation (both global and direct component) for dealing with the ability of various models in its estimations. Climate Network is selected as the reference dataset for the first type of diagrams, for being the most reliable and with high quality measured data. PVGIS is, instead, chosen

for the other charts considering its accuracy in solar data predictions due to the main application for the photovoltaic system design.

The annual Taylor diagram (Figure 4.4) depicts a different accuracy and variability of the chosen sources according to the selected parameter. The results outline that all sources are able to describe the temperature variable (red markers) both in terms of RMSD and R. In fact, all of them lie close to the reference point with a minimum correlation equal to 0.8 and the highest centred root-mean-square difference of 0.75. ARTA and PVGIS datasets (real anemometers) have both a standard deviation equal to 1 but with various correlation coefficients, 0.92 for the first and 0.85 for the second, and RMSD that are, respectively, 0.30 and 0.55. This means that even if both have recorded data, there is a variation in comparison to the measured data obtained from a source with a different location.

Among the other anemometers, the estimated values coming from the MM5 models can represent with reasonable accuracy the temperature parameter. The MM5-BK model (ring marker), the MM5-MRF-LSM model (x marker) and the MM5-PLEIM-XIU (square marker) perform the investigated parameter with high correlation coefficient (from 0.88 to 0.95), right standard deviation (from 0.78 to 0.90) and low RMSD (from 0.30 to 0.45). Moreover, the virtual anemometers allow better estimation than the typical year values of the DB (diamond marker) and the CTI (triangle marker) datasets.

A more significant variation is obtained with the atmospheric pressure parameter (yellow markers) which assumes more variability among the considered sources. The CTI dataset does not present this data, and, for this reason, there is not a yellow triangle marker in the graph. The MM5-PLEIM-XIU, with 0.23 RMSD, 1σ and 0.97 R, is the best model in the prediction of the atmospheric pressure, and it performs better than the measured data. This trend is also confirmed with the MM5-MFR-LSM and BK models but with a lower correlation coefficient, 0.90 for the first and 0.75 for the second, and higher RMSD respectively equal to 0.50 and 0.75. The DB source, with constant values of atmospheric pressure set at 101.13 kPa, shows the weakest performance in comparison to the others. Also, PVGIS has low accuracy, recording high values of RMSD, low correlation and standard deviation.

The relative humidity (blue markers) is measured or estimated with high variability. This parameter is not present in the DB dataset. The ARTA database describes better than the others its variability with RMSD, R and σ respectively equal to 0.80, 0.50 and 0.80. MM5 models, in all cases, perform better than the CTI and PVGIS datasets. A similar trend is also recorded for the wind speed and direction parameters plotted, respectively, with green and purple markers. In both cases, low correlation coefficients are registered, and MM5-MRF-LSM and MM5-PLEIM-XIU models show the best performance if compared to the others, except for the ARTA dataset, which has lower RMSD and higher R values. The DB source confirms to be less accurate in comparison to the others.

The general trend obtained with the annual datasets is also confirmed, recording slight variations, on the seasonal scale (Figure 4.5 to Figure 4.8). The DB database shows the lowest accuracy in the prediction of all parameters, whereas the MM5 models are able to estimate them with better accuracy. In detail, both MM5-MRF-LSM and MM5-PLEIM-XIU models confirm to be more liable than the MM5-BK model, which has, among the three, the highest RMSD and lowest correlation coefficient. Evaluating the performance of real anemometers, the ARTA dataset is more accurate than the PVGIS one, as obtained for the annual diagram.

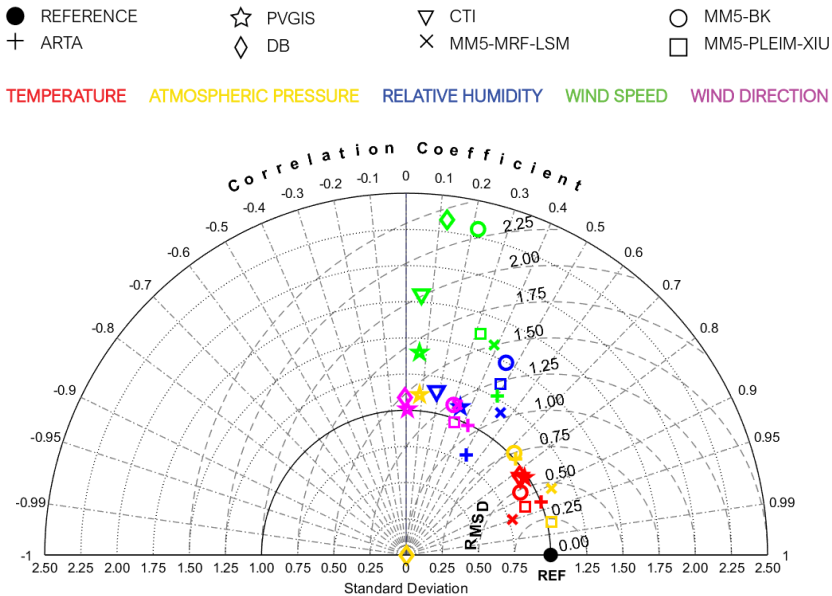


Figure 4.4. Normalised Taylor diagram based on annual datasets.

Chapter 4

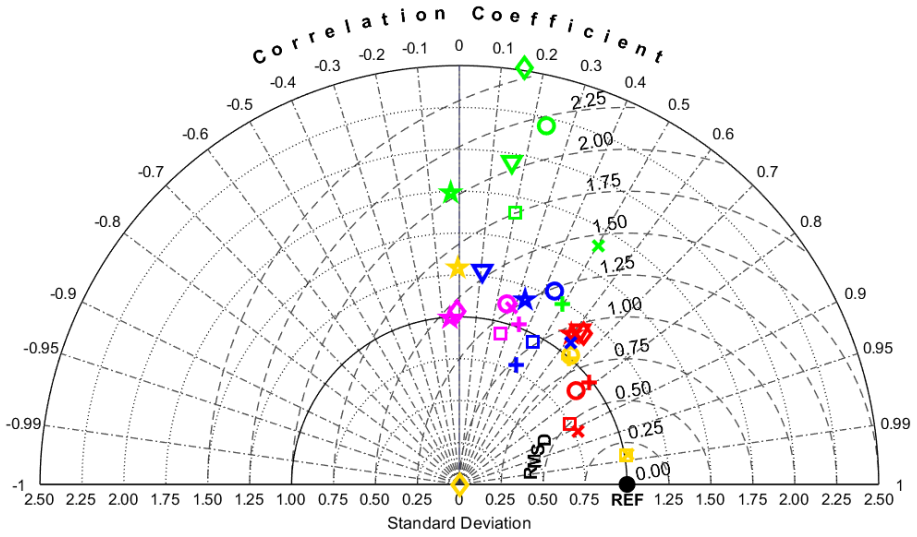
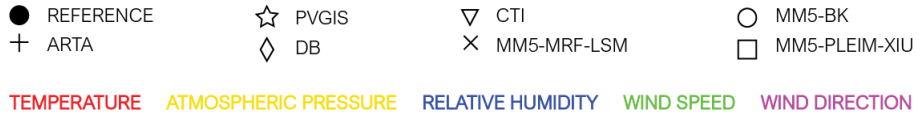


Figure 4.5. Normalised Taylor diagram for the spring season.

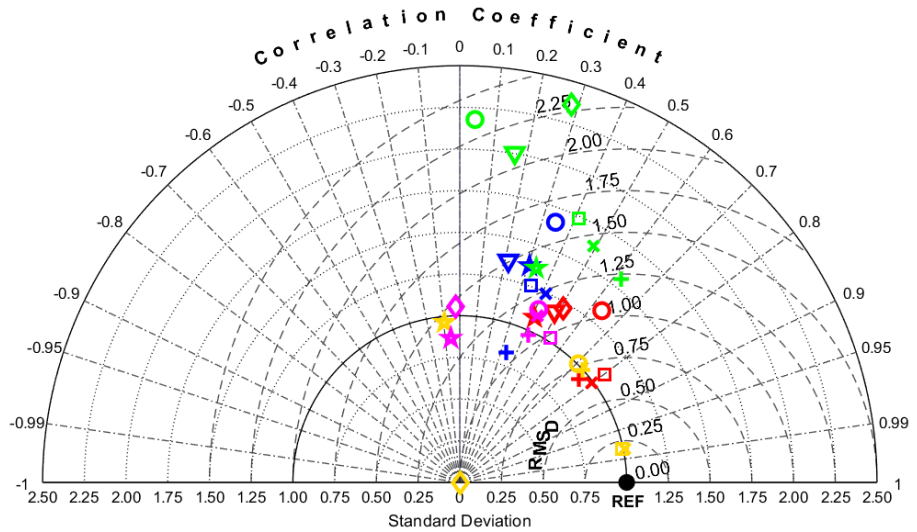


Figure 4.6. Normalised Taylor diagram for the summer season.

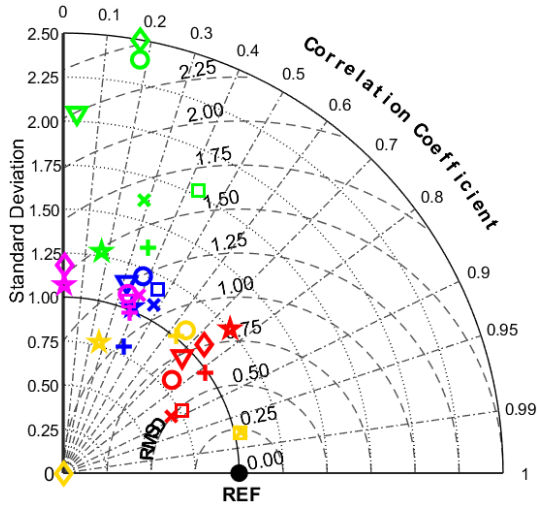


Figure 4.7. Normalised Taylor diagram for the autumn season.

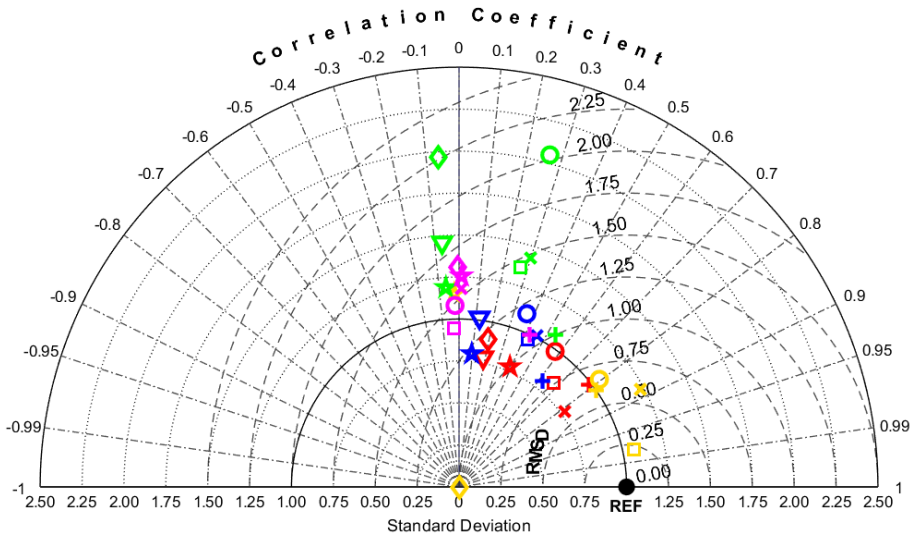


Figure 4.8. Normalised Taylor diagram for the winter season.

The second sequence of Taylor diagrams is focused on the solar radiation parameter, both global and direct. In this case, the reference dataset is the PVGIS one. Green markers describe the performance of sources in the estimation of the global radiation, whereas the brown markers represent the direct radiation calculated for all datasets adopting the Tapakis et al. empirical correlation.

In the estimation of the global radiation on an annual time step (Figure 4.9), all datasets show good accordance in terms of RMSD, R and σ with the reference. The DB and CTI data have a high correlation coefficient (equal to 0.85) and centred root-mean-square difference (equal to 0.55). Reasonable estimations are also obtained with data coming from MM5 models. In detail, the MM5-PLEIM-XIU and MM5-BK models perform better than the MM5-MRF-LSM one, with R, RMSD and σ values respectively equal to 0.88, 0.52 and 1.10. Good accuracy is also ensured by climatic stations, especially with the ARTA dataset, which shows high correlation coefficient and RMSD, respectively 0.88 and 0.51, and a 1.10 standard deviation value. Evaluating the direct solar radiation component, less accuracy can be seen and, in general, the same trend referred to the global parameter is confirmed. The DB and CTI datasets have, also in this case, low RMSD and σ values and high correlation coefficients. The MM5 models which better describe this parameter are the MM5-BK and the MM5-MRF-LSM, whereas the MM5-PLEIM-XIU tends to underestimate the direct solar radiation slightly. This variation pattern is also confirmed by the seasonal time step for which the same considerations can be done (Figure 4.10).

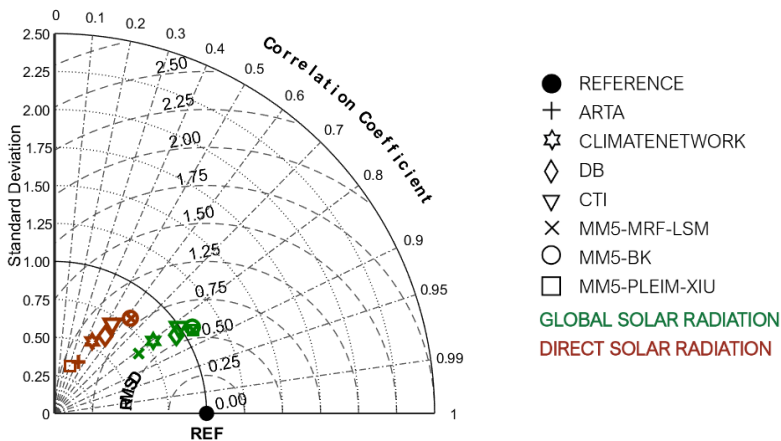


Figure 4.9. Normalised Taylor diagram based on annual datasets for solar radiation.

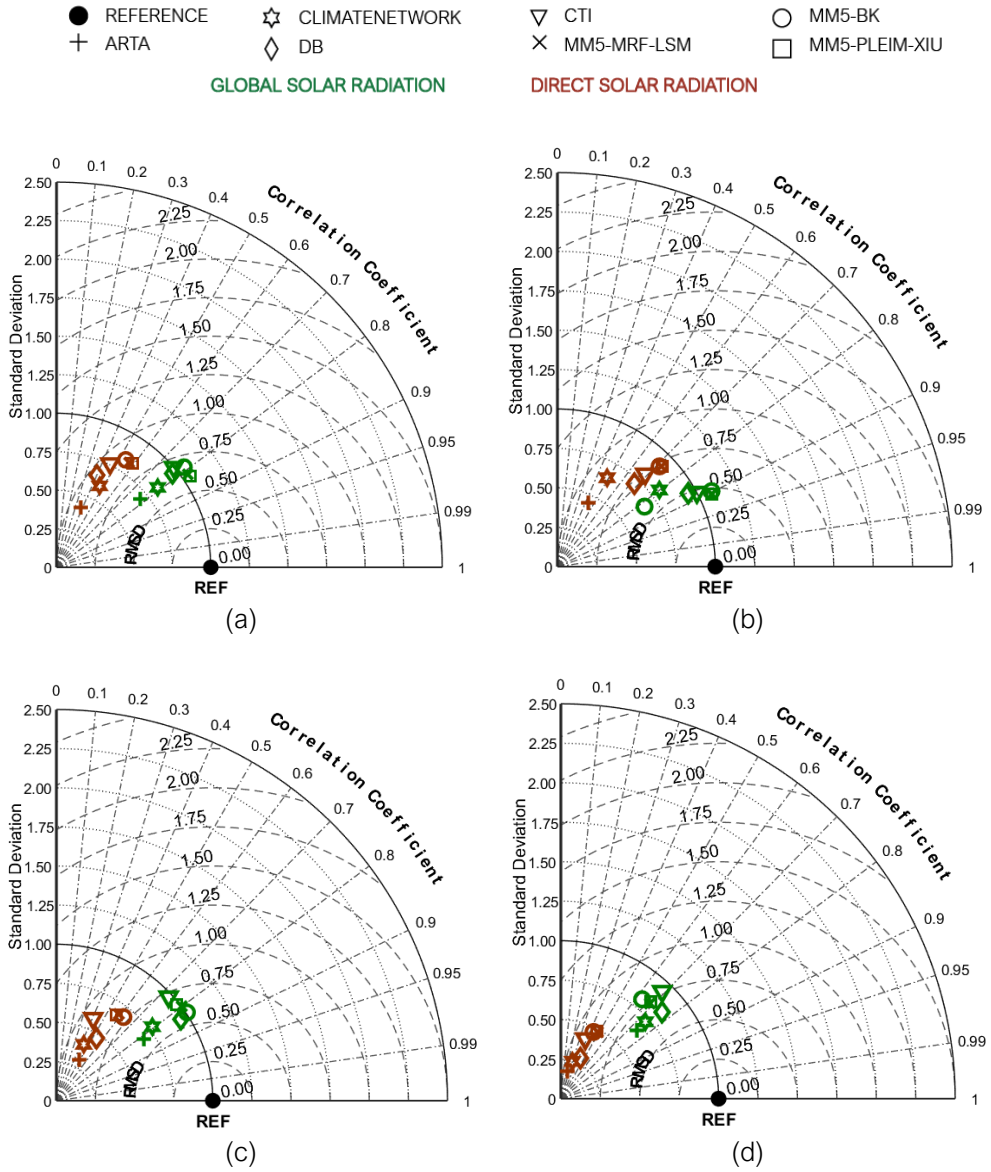


Figure 4.10. Normalised Taylor diagrams for seasonal datasets for solar radiation: (a) spring, (b) summer, (c) autumn and (d) winter.

As underlined by the Taylor diagrams, climatic data coming from various sources may show high variability in the characterisation of a specific weather parameter. This variability can also be recorded between data obtained from real anemometers because of a different measurement period or accuracy of the

records. When recorded data are absent, the regional climate models represent a good option in the estimation of almost all climatic variables, becoming a reliable alternative for the generation of input file adopted in energy simulations. Moreover, the use of empirical correlations for the decomposition of the global solar radiation, opportunely tested and validated, can lead to reasonable estimations, solving the problem of missing data.

4.3. Energy Modelling of the Reference Building

As mentioned in Chapter 3, the selected case study is a social housing building which consists of a 7-story structure and located in a residential suburb of Pescara. The ground floor has four staircases. Each staircase is made of two thermal zones: one for the staircase itself, and the other for a storage room. Therefore, the ground floor has eight thermal zones in total. On the other storeys, eight apartments at each level of which two are A-type (50 m²) and six B-type (70 m²). The A apartment is composed of five thermal zones: kitchen (5.90 m²), dining room (15.78 m²), bedroom (16.09 m²), bathroom (4.76 m²) and circulation area (6.90 m²). The B apartment, instead, has seven thermal zones: kitchen (8.19 m²), dining room (23.86 m²), bedroom 1 (12.92 m²), bedroom 2 (17.30 m²), bathroom (7.08 m²), a storage room (2.27 m²), and circulation area (10.29 m²). Figure 4.11 depicts the thermal zone localisation for the typical floor.

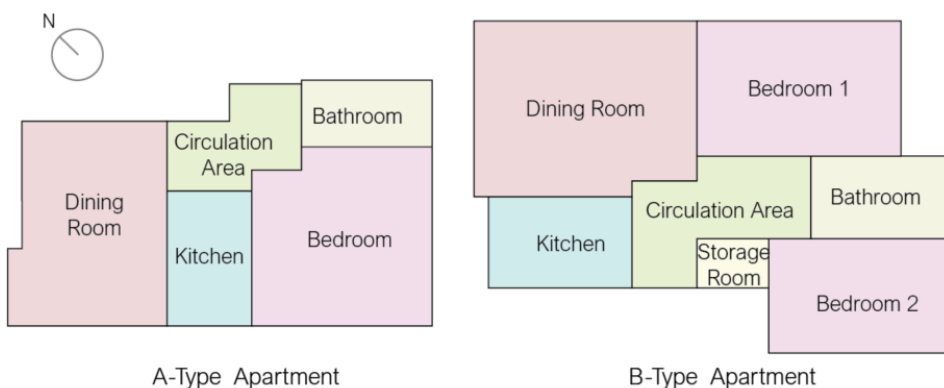


Figure 4.11. The localisation of Thermal zones on the typical floor.

On the basis of the architectural maps and stratigraphies reported in Appendix C, the external walls, with a depth equal to 33 cm, do not present any insulation layer. There are also 23 cm thick walls placed for delimiting the apartment from the staircase, and partitions (with 11 cm depth) to subdivide each apartment into various thermal zones. About glazed surfaces, no detailed information is inserted in the building technical documentation, and single glazing windows with transmittance (U) value equal to 3.78 W/ m²K are selected on the basis of the analysis of the literature review [78]. Table 4.5 summarises the thermal properties of the building envelope.

Table 4.5. Description of building envelope components.

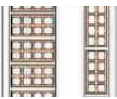
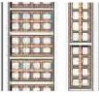





Building component	Material (outer to inner)	s [m]	λ [W/mK]	U [W/m ² K]
33cm External Wall 	(a) Lime plaster	0.02	0.80	1.46
	(b) Brickwork	0.13	0.84	
	(c) Air gap	0.08	0.30	
	(d) Brickwork	0.08	0.62	
	(e) Lime plaster	0.02	0.80	
23cm Semi-External Wall 	(a) Lime plaster	0.02	0.80	1.60
	(b) Brickwork	0.13	0.84	
	(c) Air gap	0.03	0.30	
	(d) Brickwork	0.08	0.62	
	(e) Lime plaster	0.02	0.80	
11cm Partitions 	(a) Plaster	0.02	0.16	1.27
	(b) Plasterboard	0.07	0.25	
	(c) Plaster	0.02	0.16	
Glazing 	Single clear glazing	0.006	-	3.78
Interstorey roof 	(a) Cast concrete	0.02	1.13	0.78
	(b) Concrete slab	0.16	0.16	
	(c) Plaster	0.02	0.16	

Table 4.5. (Continued).

Building component	Material (outer to inner)	s [m]	λ [W/mK]	U [W/m ² K]
External roof 	(a) Ceiling tiles	0.02	0.06	0.61
	(b) Cast concrete	0.02	1.13	
	(c) Concrete slab	0.16	0.16	
	(d) Plaster	0.02	0.16	
Pavement 	(a) Cast concrete	0.02	1.40	3.37
	(b) Ceramic	0.02	1.30	


No information is present about the building heating and cooling system that is defined according to data coming from buildings similar to the case study for the construction period and typology. The building heating involves the use of radiators with a seasonal Coefficient of Performance (COP) equal to 0.84 and natural gas as source. For improving the inhabitants' comfort condition, splits are installed for the cooling of the inner spaces. The cooling COP is set equal to 1.4, and the source is electricity.

The temperature setpoints for heating and cooling for all thermal zones are, respectively, 22°C (with 20°C as set-back temperature) and 28°C. The metabolic factor is set to 0.90 for the whole building, as well as for the clothing insulations, which is 0.50 clo for the summer season and 1.00 for the winter season. The model infiltration is considered constant and fixed at 0.70 ac/h. Table 4.6 depicts the input parameters which vary according to the activity of the thermal zone.

Table 4.6. Input parameters used for simulations. For each thermal zone, the occupation density (people/m²), the minimum fresh air (l/s-person), the target illuminance (Lux), and the occupation schedule are shown.

Thermal Zone	Occupation	Fresh Air	Illuminance	Schedule
Bedroom	0.0229	10	100	<p>All Days</p>
Bathroom	0.0187	12	150	<p>All Days</p>
Kitchen	0.0237	12	300	<p>All Days</p>
Storage Room	0.0243	12	100	<p>All Days</p>
Dining Room	0.0169	10	150	<p>All Days</p>

Table 4.6. (Continued).

Thermal Zone	Occupation	Fresh Air	Illuminance	Schedule
Circulation area	0.0196	10	100	 <p>The graph shows the Occupation Factor over a 24-hour period. The y-axis ranges from 0 to 1.0, and the x-axis shows time from 00:00 to 00:00. There are two distinct peaks: one at 08:00 reaching a factor of 1.0, and a second, broader peak starting at 16:00, reaching a maximum of approximately 0.95 around 19:00 before declining to 0.5 at 00:00.</p>

The influence of neighbouring buildings is taken into account by inserting, as block components, the closest structures which could shade the case study and, for the same reason, the presence of the balconies on the north-west façade is considered placing external profiles, as it can be seen in Figure 4.12.

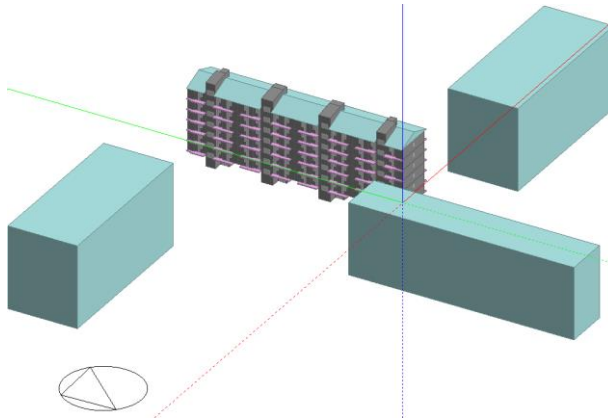


Figure 4.12. The energy model of the case study with balconies (pink elements) and neighbouring buildings (cyan elements).

Dynamic energy simulations are performed for evaluating the building energy performance, considering the above mentioned climatic files, opportunely converted in *.epw files using Elements (Version 1.0.6) by Big Ladder Software, which is a free, open-source, cross-platform software tool for creating and editing custom weather files [79].

4.3.1. Model Calibration and Results

Once the Case study has been modelled, a crucial phase is its calibration. A double calibration is here adopted for better quality analyses. First, dynamic simulations are carried on for estimating the building natural gas consumption to be compared with data collected from a building, similar to the case study for, typology, localisation and construction period (Figure 4.13). Then, the comparison is made between the obtained results and the typical heating consumption of buildings with the same characteristics and age, collected from the TABULA webtool [80].

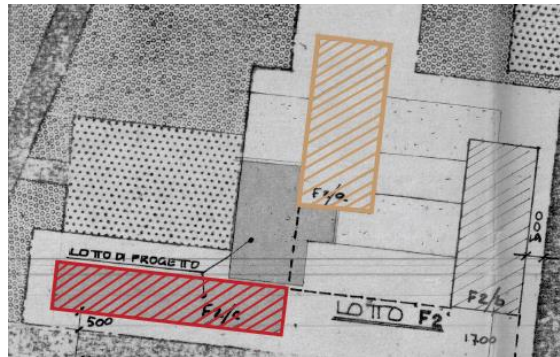


Figure 4.13. The localisation of the case study (red box) and the building selected for the calibration (light brown box).

The collected bills are referred to the year 2017, and the heating period (1st October-31stMarch) is considered for the calibration. The case study is rotated for ensuring the same orientation of the reference building, identified with the light brown rectangle in Figure 4.13. Monthly simulations are performed setting as a key output the natural gas consumption (heating + cooking), expressed in kWh/m². Three different climatic files are considered for the comparisons: the ARTA and Climate Network datasets (PVGIS is not involved because of its inaccuracy in the prediction of the general weather parameters as seen with Taylor diagrams) and the DB climatic file. The natural gas consumption is defined on a two-month range, except for January and December, in accordance with the recorded data. Error bars, set at 5%, are inserted as inferior and superior limits for the comparisons.

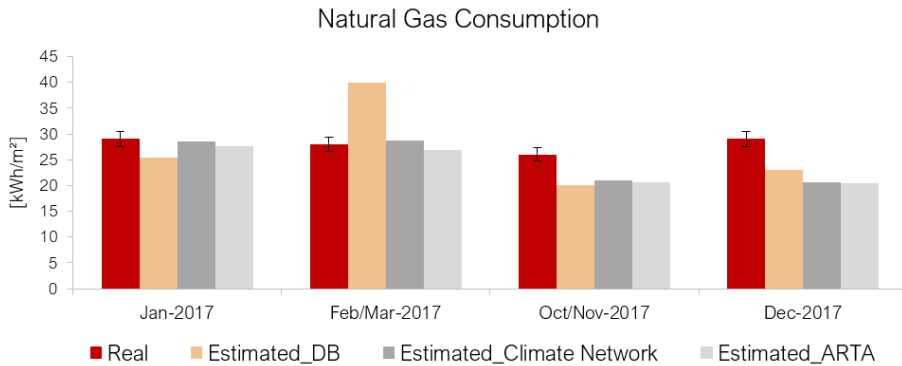


Figure 4.14. Comparison among estimated and collected values for the model calibration.

The comparison, depicted in Figure 4.14, shows general accordance between estimated and measured values. The highest accuracy is recorded with the ARTA and Climate Network climatic files. They, in fact, are able to predict within the acceptable range the energy consumption for January and February/March bimester better than the DB dataset which, instead, tends to under/overestimate the selected output. More significant differences are calculated for December for which the estimated values are, with all climatic data, out of the acceptable range. The possible explanation of such behaviour can be due to the measured data, considering that the available bill is referred to December 2017-January 2018 and the estimation of the consumption for a single month is done by dividing the total amount by two. For this reason, the December data are not strictly taken into account for the calibration.

The same inaccuracy can also be seen for the October-November bimester but, in this case, the principle reason stands in the limitations of predictions for transitory months, because deeply influenced by the inhabitants' comfort condition and their use of occupied spaces. In fact, as underlined by various works previously carried on in the field of energy simulations, the building requirement/consumption for mild periods could vary, more than the rest of the year, according to the human behaviour (inhabitants' age, habits, etc.).

Considering the total natural gas consumption for the selected months, the obtained values are also in accordance with data coming from the survey on the energy performance of the existing building stock presented in the literature [78]. An apartment building erected between the 1976 and 1990 year and located in a

mild climatic zone (most of the selected case study are placed in the E zone) consumes for the heating and generation of domestic hot water 120 kWh/m^2 , while the model estimated values are 109, 100 and 96 kWh/m^2 with, respectively the DB, Climate Network and ARTA dataset. On the basis of the comparisons and assuming these data as representative values for having a general idea about the building requirement referred to various construction ages, the model can be considered calibrated and able to describe the real behaviour of the case study.

The energy performance of the reference building is evaluated both in terms of energy consumption, and thermal comfort condition. In the first case, the results are referred to the annual building heating and cooling use, whereas the thermal comfort is investigated considering a weekly timestep, simulating alternatively the typical summer (August, from 17th to 23rd) and winter (January, from 20^h to 26th) conditions. Moreover, for defining comfort/discomfort rates, the operative temperature is estimated for two different building thermal zones, selected for their orientation. North and south exposed thermal zones (see Figure 4.15) are chosen for investigated, respectively, the winter and summer thermal comfort. This choice is made considering the building dimensions and for avoiding averaged values which could be not representative of the real conditions.



Figure 4.15. The localisation of the thermal zones selected for the winter (blue rectangle) and summer (red box) comfort.

For better understanding the obtained results, monthly mean temperatures for each climatic file are plotted in Figure 4.16. The ARTA and Climate Network outputs describe a similar trend, especially in terms of building heating consumption. Evaluating the temperature distribution, ARTA and Climate Network show good accordance with each other. Variations can be, instead, identified with the PVGIS dataset and this happens because, even if made of recorded data, it is a typical meteorological year and it does not match with single-year measurements. The difference underlined between the temperature values does not profoundly

affect energy consumption, which shows only little variations. The DB results emphasise a higher heating consumption and a lower cooling requirement, as expected, considering that it records the most moderate monthly mean temperatures (blue line in Figure 4.16). Considering the CTI heating consumption, the estimated value is lower than the DB, whereas the cooling need increases. This happens because of the higher temperatures that, from one side, allow the heating reduction and from the other raise the cooling need.

The last comparison involves the energy performance estimated with the MM5 regional climate models. The MM5-MRF-LSM model tends to overestimate temperatures during the coldest months with the lowest heating load, whereas the summer values are moderate with a consequent small cooling need. The MM5-PLEIM-XIU, instead, tends to underestimate temperatures during the whole year, affecting the building energy consumption on both cooling and heating side. The BK model shows a similar temperature distribution of the MRF-LSM during the summer period and low values for the wintertime with a consequent increment of the heating consumption.

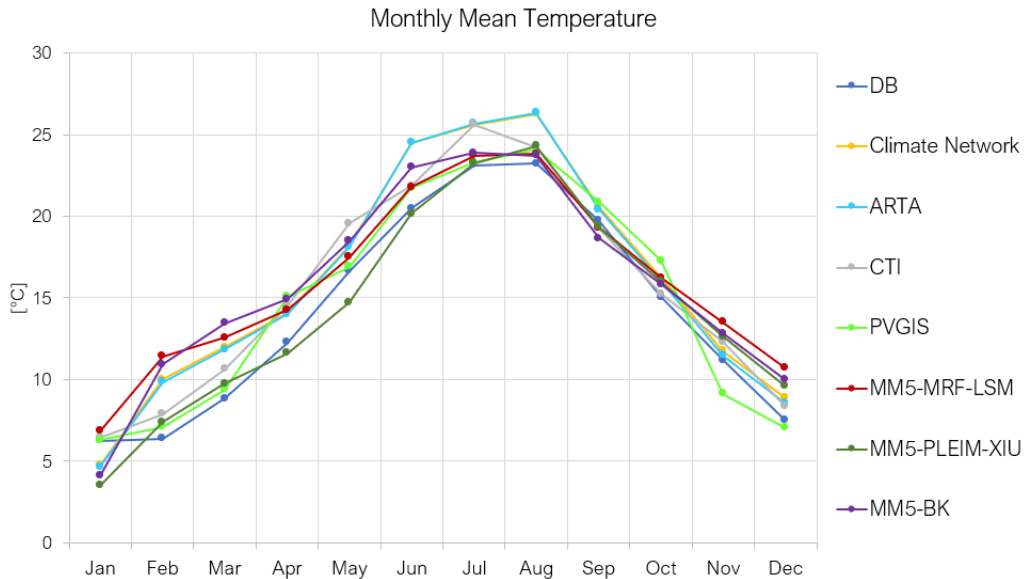


Figure 4.16. Monthly mean values referred to the temperature for each climatic dataset.

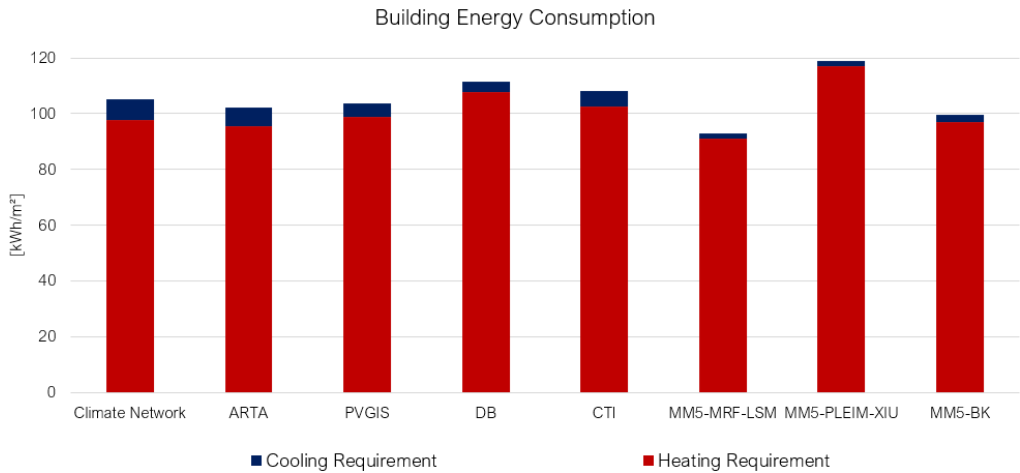


Figure 4.17. Annual energy consumption estimated for the reference building.

The evaluation of the thermal comfort is done according to the UNI EN 15251:2008 (CEN 2014) [81], which associates comfort/discomfort rates to four categories. Category I has a high level of expectation, and it is recommended for spaces occupied by very sensitive people. Category II is for normal levels of expectations, suitable in case of new buildings or renovations. Category III represents a moderate, acceptable level of expectation and could be used for existing buildings, whereas the last, Category IV, involves the other conditions not referred to the previous cases.

The standard establishes for each comfort category a temperature interval, suggesting recommended indoor operative temperatures for the design of heating and cooling systems. These limits are used, in the present analysis, for defining the upper and lower limit for each category. It is essential to underline that the here investigated parameter is referred to a building with a heating and cooling system. Thus, the performed analyses aim to evaluate its effectiveness in guaranteeing acceptable comfort rates inside the occupied spaces.

Table 4.7. Operative Temperature range for comfort categories.

Category	Winter Operative Temperature Range	Summer Operative Temperature Range
I	$T_{\text{operative}} > 21^{\circ}\text{C}$	$T_{\text{operative}} \leq 25.5^{\circ}\text{C}$
II	$20^{\circ}\text{C} < T_{\text{operative}} \leq 21^{\circ}\text{C}$	$25.5^{\circ}\text{C} < T_{\text{operative}} \leq 26^{\circ}\text{C}$
III	$18^{\circ}\text{C} < T_{\text{operative}} \leq 20^{\circ}\text{C}$	$26^{\circ}\text{C} < T_{\text{operative}} \leq 27^{\circ}\text{C}$
IV	$T_{\text{operative}} < 18^{\circ}\text{C}$	$T_{\text{operative}} > 27^{\circ}\text{C}$

Figure 4.18 and Figure 4.19 show thermal comfort results referred, respectively, to summer and winter weeks. Starting from the summer comfort rates, the results obtained with the ARTA and Climate Network datasets are similar, due to quasi-identical temperature distribution. Little variations are due to different values of global solar radiation which has, like temperature, a more decisive influence than the other climatic variables in dynamic simulations. The PVGIS results tend, instead to show a more significant fluctuation if compared to the other real data, as obtained for the building energy requirement. The DB dataset, recording the lowest temperatures, ensures, in 77% of cases, the best comfort level, whereas this amount is reduced for simulations performed with the CTI database, due to its general increase of the measured temperatures. The MM5 models show various comfort/discomfort ranges. According to the MM5-MRF-LSM, a high level of expectation is estimated for almost all the time, and a similar circumstance is obtained with the MM5-PLIEM-XIU model, even if with a lower intensity. The MM5-BK dataset, instead, performs the worst comfort conditions, predicting the Category IV for 11%.

Evaluating the winter comfort (Figure 4.19), the poorest conditions are estimated with MM5-PLIEM-XIU and MM5-BK models, considering that they show the lowest monthly mean temperatures for the selected month (January). They predict, for the quasi-totality of the time, a moderate level of expectation and a similar trend is also obtained with the CTI file. It ensures the Category II condition only for 10% of the time, whereas, in general, a moderate comfort condition is obtained. MM5-MRF-LSM, DB and PVGIS datasets, having the same temperature trend, show a similar subdivision between Category II and III. The last two databases, ARTA and Climate Network, show the same behaviour in the prediction of the winter thermal comfort as already obtained for the summer period.

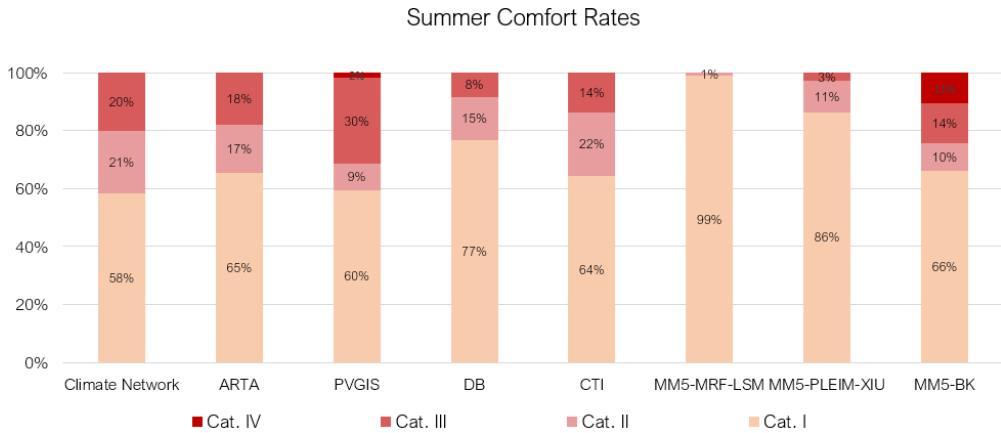


Figure 4.18. Summer comfort rates for the reference building in the original state.

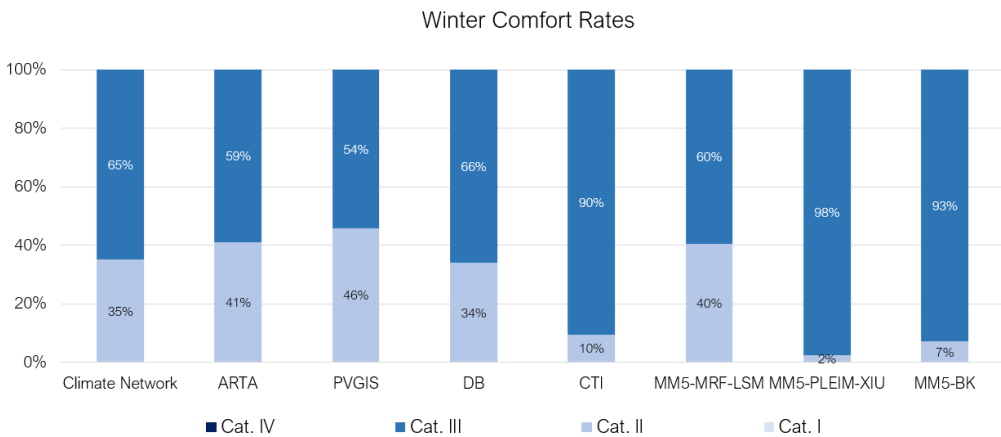


Figure 4.19. Winter comfort rates for the reference building in the original state.

4.4. DSF Modelling and Results

According to the main findings obtained from preliminary analyses reported in Appendix B, the insertion of the DSF on west and east elevations does not have a significant impact on the reduction of building energy loads. The localisation of DSFs on the north and south façade, instead, can drastically improve the building performance. In addition, according to the results, a 1 m cavity depth performs better than dipper sizes, if used both as a buffer zone or a ventilated area, and external blinds with low reflectivity slots ensure the most effective shading of the inner spaces, extremely important during the summer period. The last finding

involves some considerations referred to the simulation settings that should be introduced when these systems are modelled using DesignBuilder. Firstly, the Zone type on the Activity tab is set to “Cavity”, and this means that the zone is considered as unoccupied with no HVAC or lighting template data. Moreover, the internal convection algorithm is activated to model the cavity air space correctly, and a full interior and exterior solar distribution algorithm is switched on, allowing solar radiation to be accurately transmitted through the interior glazing in the partition.

Considering all these aspects, 1 m cavity DSFs are placed on the north-west and south-east elevations, and a shading system with external blinds is inserted and designed for being operable only during the summertime. Such configuration avoids the overheating of the cavity with consequent discomfort conditions during the hottest months, without reducing the effectiveness of the solution in the wintertime.

The DSF is conceived for being naturally ventilated. External and internal grills are located, respectively, on the outer skin and the inner layer, represented by the existing building envelope. External grills are active, allowing the air to enter the Double Façade, during the hottest months, whereas they are closed for the winter period, creating a buffer area. Internal grills, instead, are designed for being adjusted by users, according to the inner temperature distribution. The natural ventilation of the building is controlled by inserting the outdoor maximum temperature control. This set avoids that the overheated air inside the cavity enters the building with adverse effects on the cooling side.

The outer skin is made of a steel structure and high-performance windows (triple glass) with low U value and solar heat gain coefficient, respectively, equal to 0.78 W/m²K and 0.474. For evaluating the effectiveness of DSF systems, various configurations are modelled and tested. Multi-Storey, Shaft-Box, Corridor and Box Window DSFs are investigated, both in terms of energy consumption and thermal comfort conditions. For the Corridor type, two different cases are studied: when the outer grills are inserted on the principal elevation of the façade or when they are on the lateral envelope. The inner partitions, eventually inserted inside the cavity according to the selected category, present single glazed windows enclosed in the steel structure. Figure 4.20 schematises the chosen options, identifying the air fluxes which enter/exit for each DSF typology. Figure 4.20a and b represents, respectively, the Multi-Storey and Shaft-Box configurations, whereas Figure 4.20c

and d the two versions of the Corridor DSF. Finally, the Box-Window typology is schematised in Figure 4.20e.

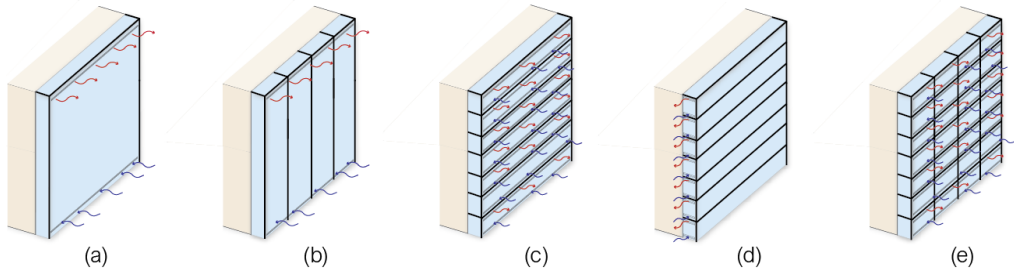


Figure 4.20. Schematisation of the investigated DSFs selected for energy simulations.

Dynamic energy simulations are performed considering the selected climatic files in order to evaluate the effectiveness of the suggested solution with various input data. Moreover, for each comparison, the heating and cooling requirement estimated for the original state is reported, in order to underline benefits and achievements obtainable with the analysed DSF configurations.

Building heating and cooling loads estimated with various climatic files are shown from Figure 4.21 to Figure 4.28. According to the results, the building heating requirement is much higher than the cooling need, and this is recorded for both the original state and after the DSF insertion. Even if a smaller reduction can be seen on the cooling side, it is pretty clear that a naturally ventilated DSF, opportunely shaded, is able to improve the building energy efficiency and reduce its total consumption. This is confirmed with all climatic files. Multi-Storey DSF represents the best option being able to reduce from 37% up to 54% the energy load, respectively estimated with the MM5-PLIEM-XIU and PVGIS dataset, in comparison to the original state. This configuration seems to be effective, especially on the heating side, ensuring higher reductions than the other typologies. A such conceived Double Façade does not present any cavity separations and, consequently, it reduces more than the alternatives, the risk of thermal bridges. On the cooling side, the ventilation of the cavity affects the building cooling requirement positively, even if, compared to the other configurations, the estimated cavity air fluxes are less intense and with minor benefits on the cooling side. The Shaft-Box DSF, instead, represent an excellent compromise among the cooling and heating reduction. It, in fact, improves building performance with a

decrement of up to 41%. Even if less efficient than the MS configuration on the heating side due to the presence of more anchors between the external building envelope and the DSF system, the stuck effect improves the ventilation of the cavity ensuring a higher reduction of the cooling load. The other two configurations show similar performances for both heating and cooling consumption. The insertion of external grills at every floor affects the cooling need positively, and this is estimated in the case of Corridor and Bow-Window DSFs. The total energy consumption can be reduced up to 39% and 36% respectively for the Corridor and Box-Window DSF. It is interesting to note that, for the Corridor configuration, the insertion of inflow grills on the principal elevation of the façade or its lateral envelope does not significantly affect the DSF cooling performance. Tables with cooling and heating consumption estimated for each DSF configuration and climatic files are detailed reported in Appendix D.

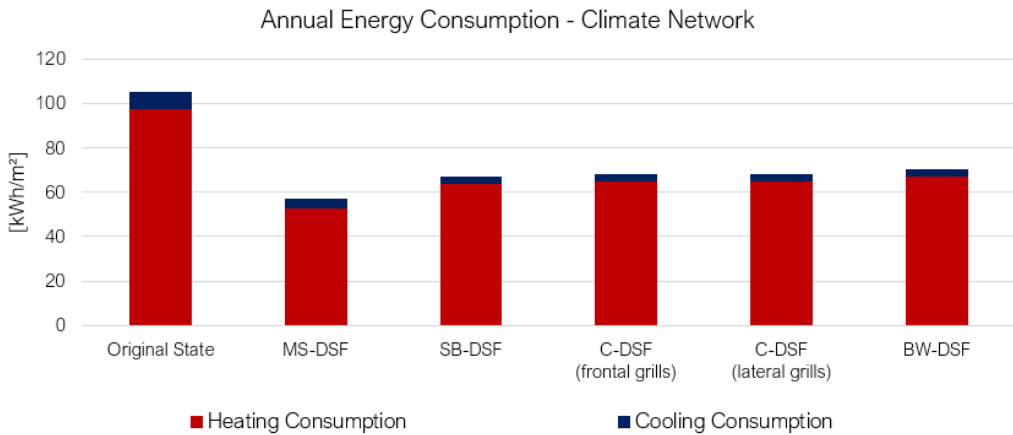


Figure 4.21. Building annual energy consumption estimated with the Climate Network climatic file.

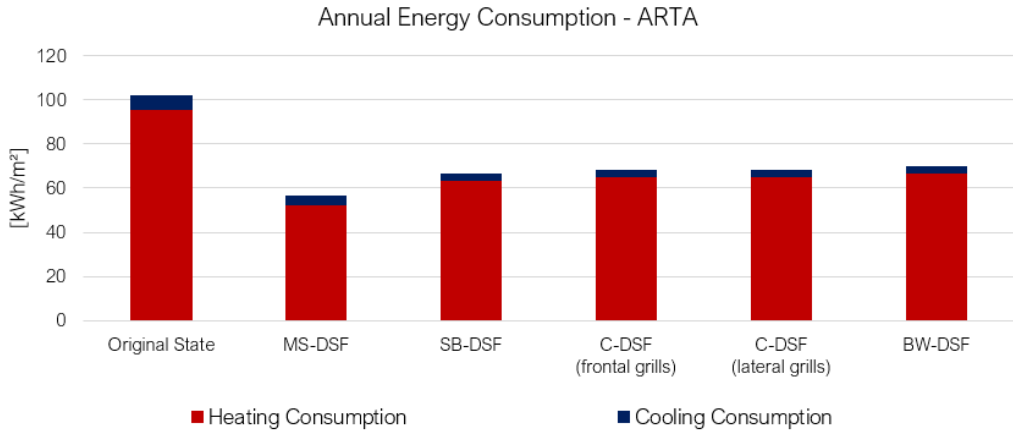


Figure 4.22. Building annual energy consumption estimated with the ARTA climatic file.

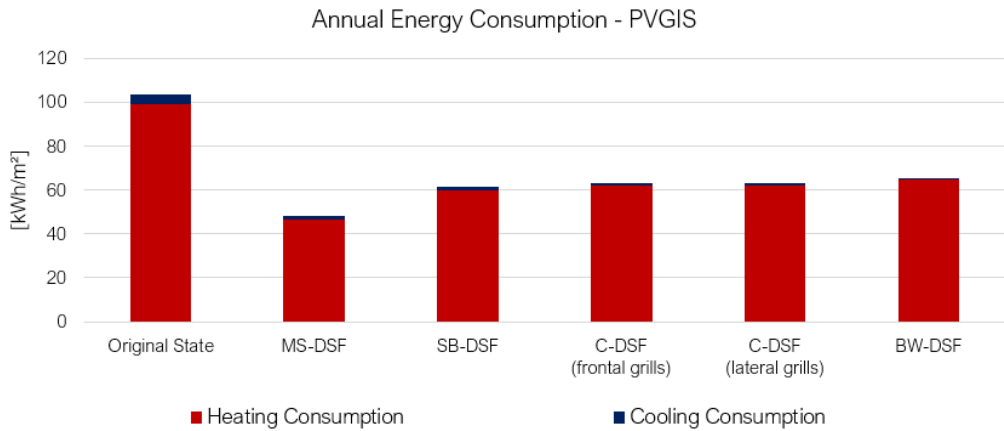


Figure 4.23. Building annual energy consumption estimated with the PVGIS climatic file.

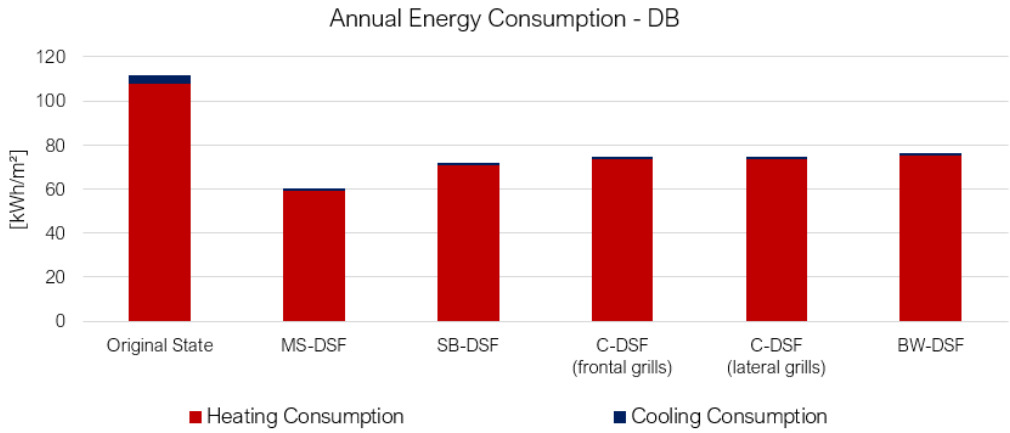


Figure 4.24. Building annual energy consumption estimated with the DB climatic file.

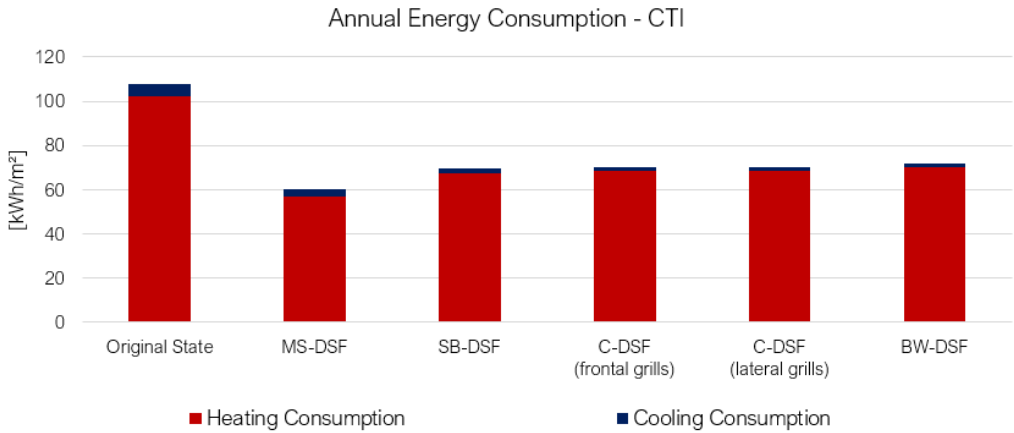


Figure 4.25. Building annual energy consumption estimated with the CTI climatic file.

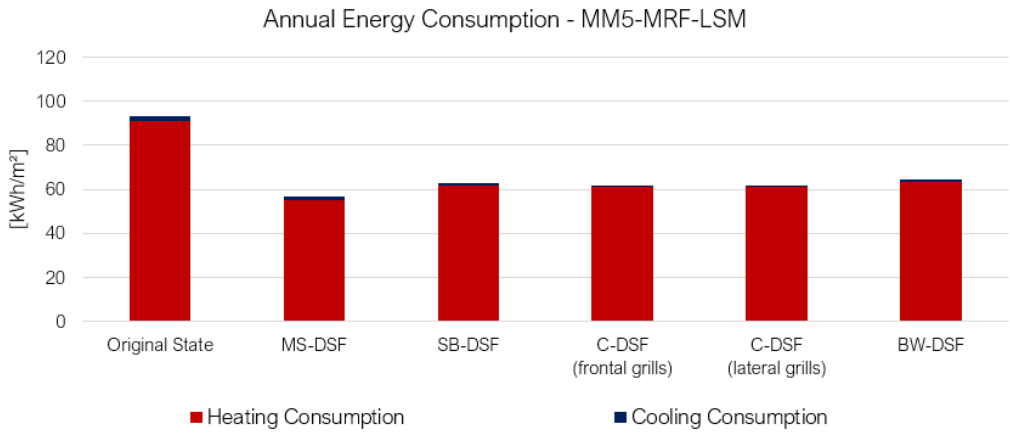


Figure 4.26. Building annual energy consumption estimated with the MM5-MRF-LSM climatic file.

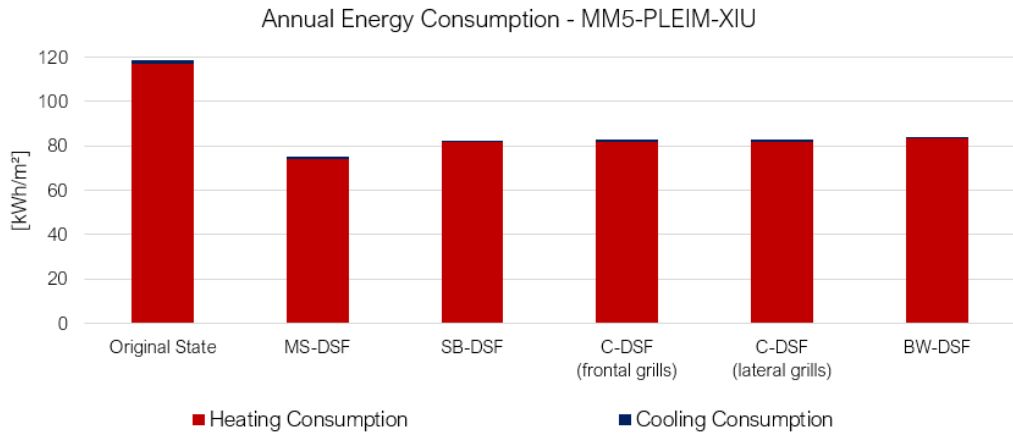


Figure 4.27. Building annual energy consumption estimated with the MM5-PLiM-XIU climatic file.

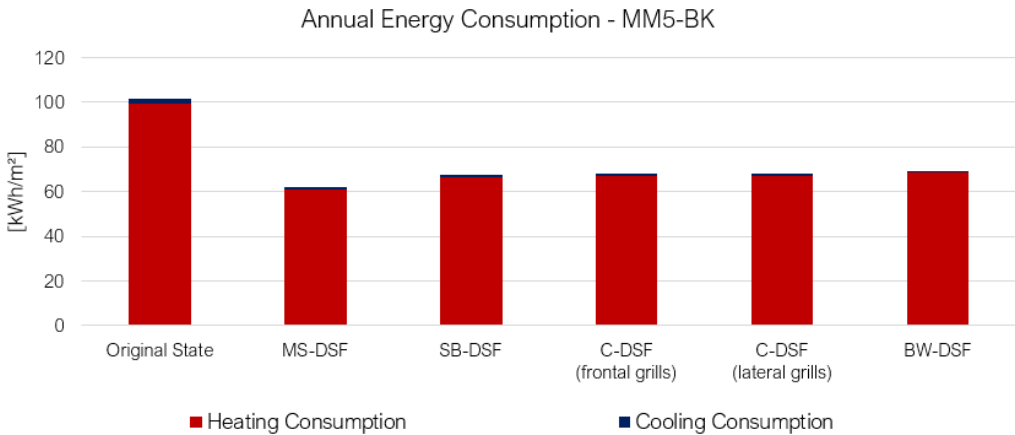


Figure 4.28. Building annual energy consumption estimated with the MM5-BK climatic file.

Evaluating the outputs referred to the thermal comfort (from Figure 4.29 to Figure 4.44), the effectiveness of the DSF estimated on the consumption side is confirmed. Moreover, better performances are ensured with all typologies of Double Façade and for both summer and winter conditions. According to summer simulations, higher quality conditions are obtained if compared to the original state, and this is guaranteed for all climatic files. In detail, introducing a Shaft-Box DSF ensures better indoor environmental conditions, allowing a higher reduction of the inner operative temperature. Improvements are also estimated with the other typologies, and these are less appreciable in case of the Corridor type, which has the worst performance among the others.

The results referred to the MM5 climatic files show how the insertion of the multi-layer façade allows having, always, the high level of expectation, ensuring comfort conditions even for more sensitive people. The same trend is also estimated for the wintertime, for which the insertion of the DSF, augmenting the operative temperature of the occupied spaces, increments the indoor comfort. In this case, the best configurations seem to be the Multi-Storey and the Corridor façade, that, for all climatic files guarantee a higher increment of the better comfort categories.

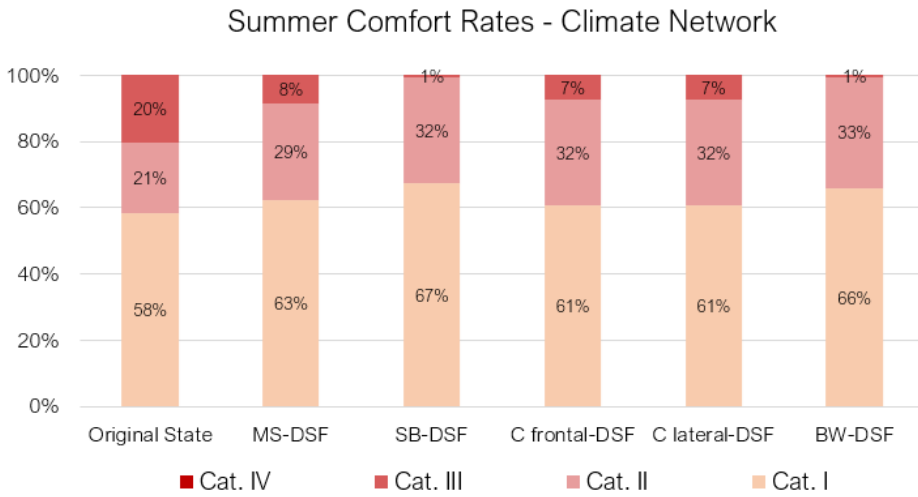


Figure 4.29. Comfort rates for the typical summer week according to Climate Network climatic file.

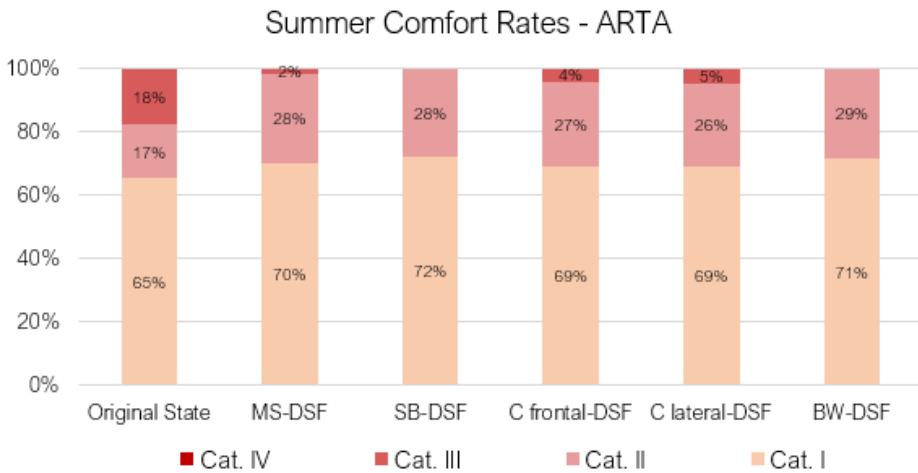


Figure 4.30. Comfort rates for the typical summer week according to ARTA climatic file.

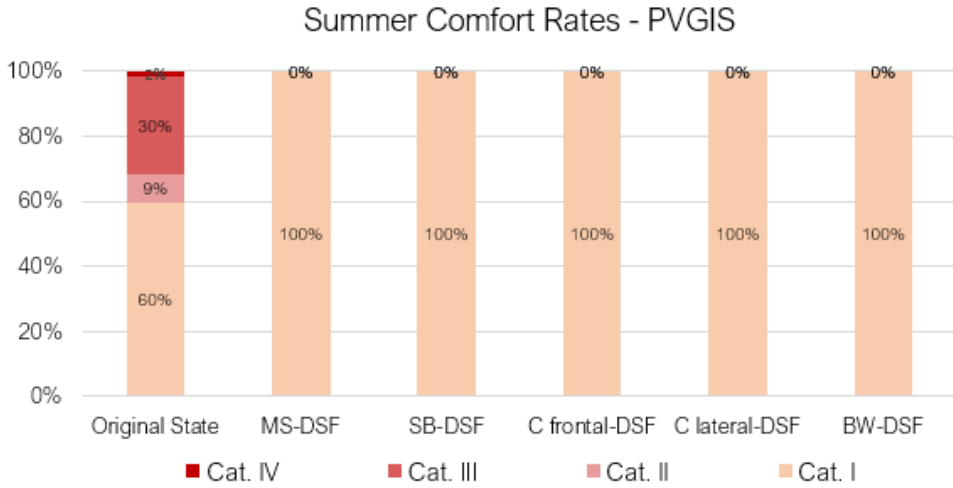


Figure 4.31. Comfort rates for the typical summer week according to PVGIS climatic file.

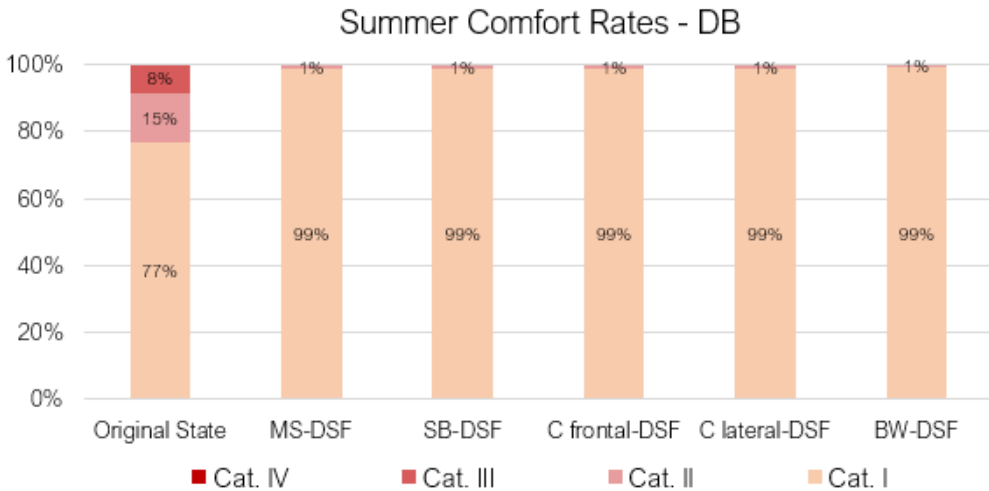


Figure 4.32. Comfort rates for the typical summer week according to DB climatic file.

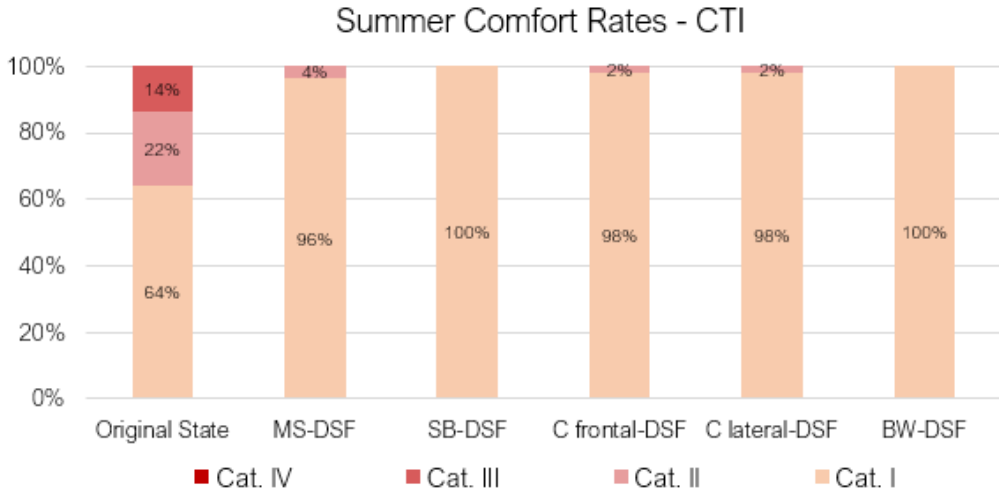


Figure 4.33. Comfort rates for the typical summer week according to CTI climatic file.

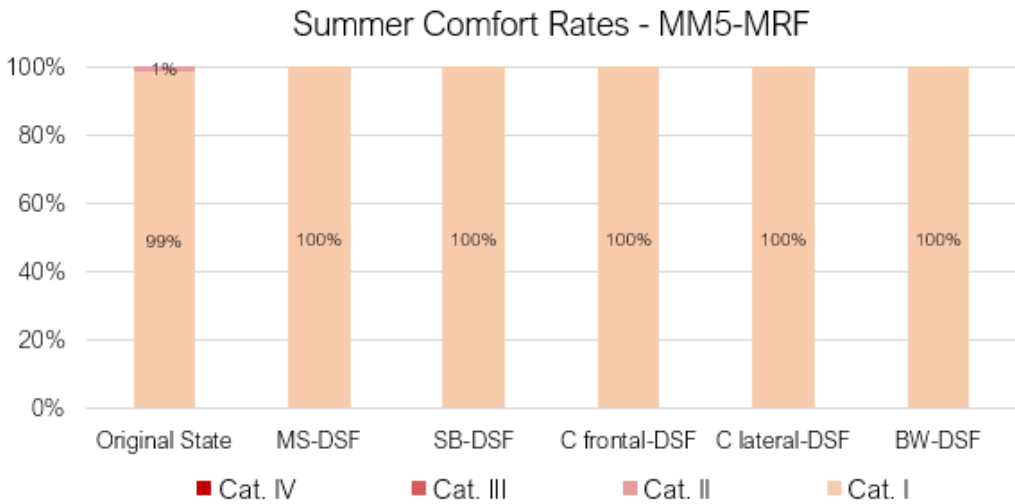


Figure 4.34. Comfort rates for the typical summer week according to MM5-MRF-LSM climatic file.

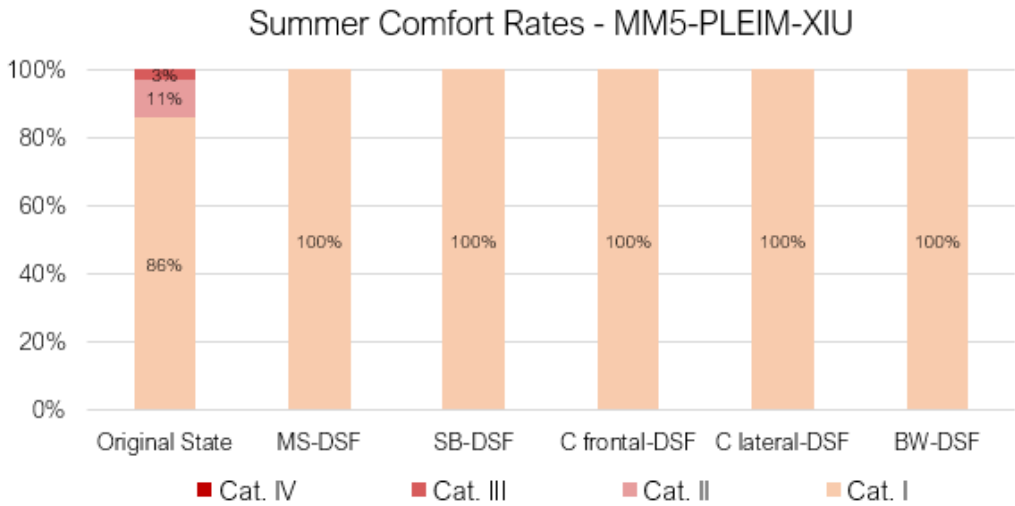


Figure 4.35. Comfort rates for the typical summer week according to MM5-PLEIM-XIU climatic file.

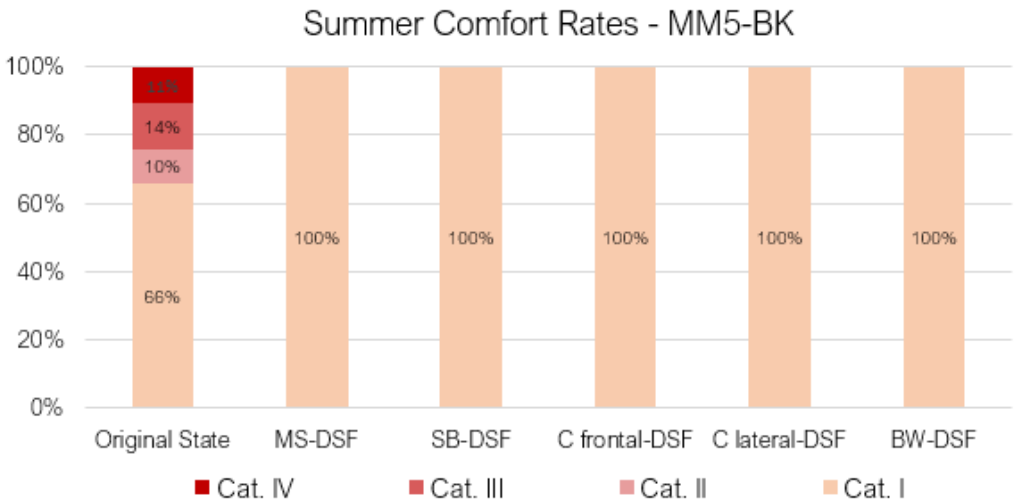


Figure 4.36. Comfort rates for the typical summer week according to MM5-BK climatic file.

Winter Comfort Rates - Climate Network

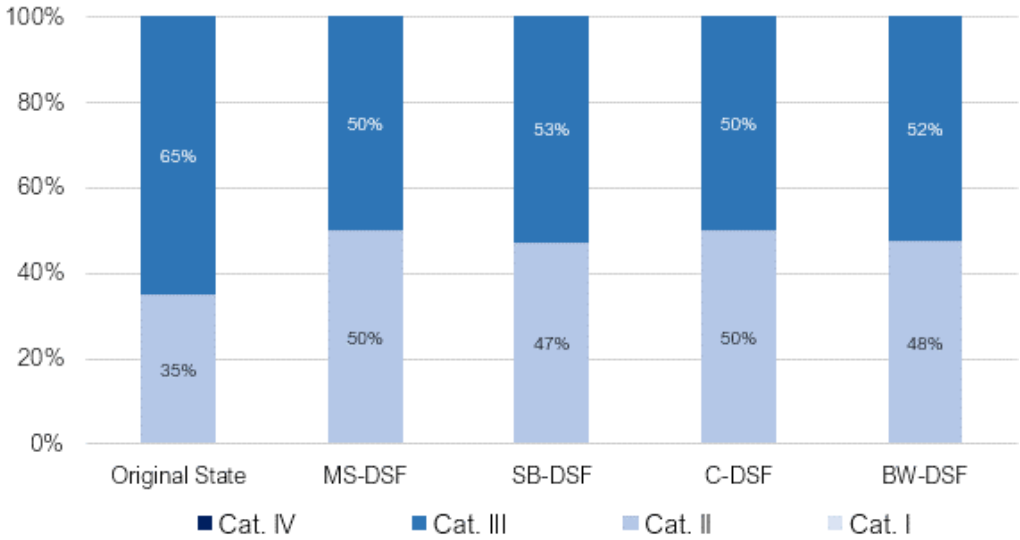


Figure 4.37. Comfort rates for the typical winter week according to Climate Network climatic file.

Winter Comfort Rates - ARTA

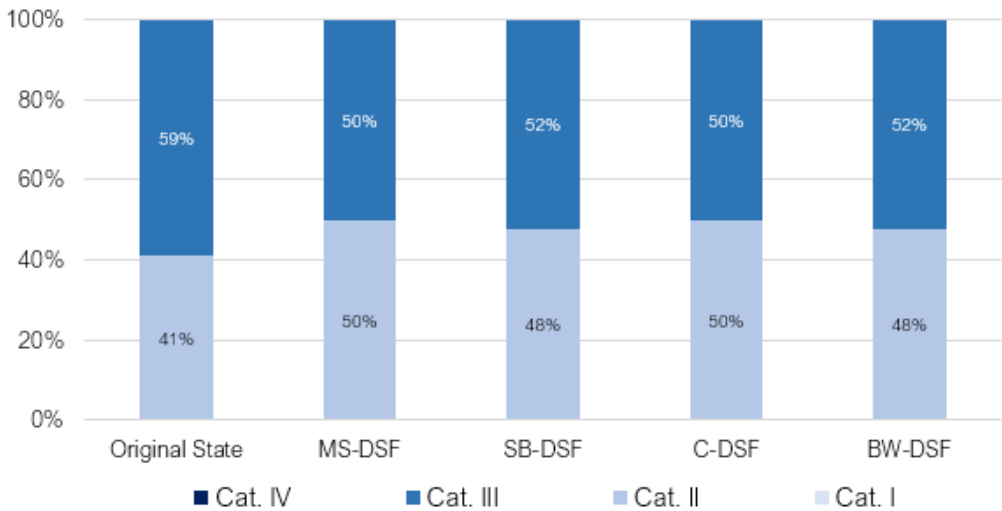


Figure 4.38. Comfort rates for the typical winter week according to ARTA climatic file.

Winter Comfort Rates - PVGIS

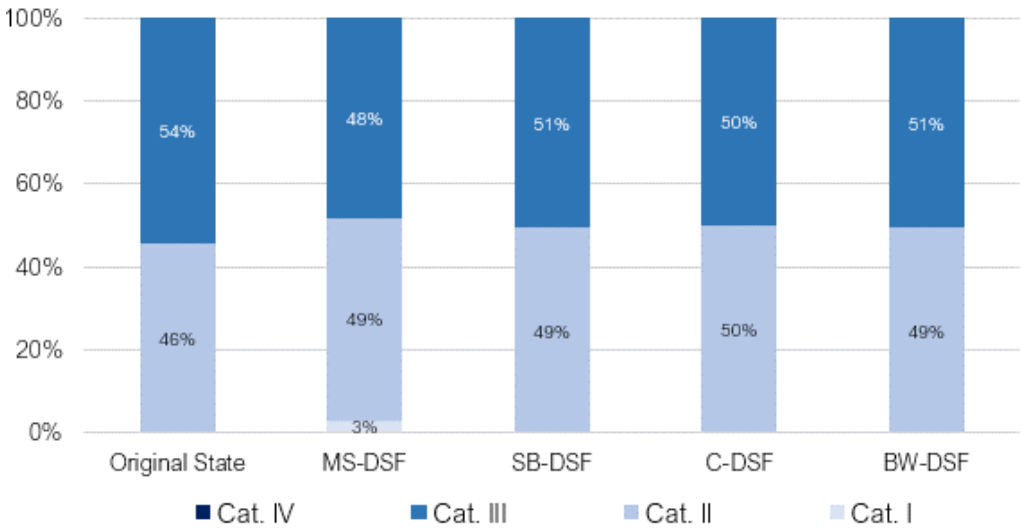


Figure 4.39. Comfort rates for the typical winter week according to PVGIS climatic file.

Winter Comfort Rates - DB

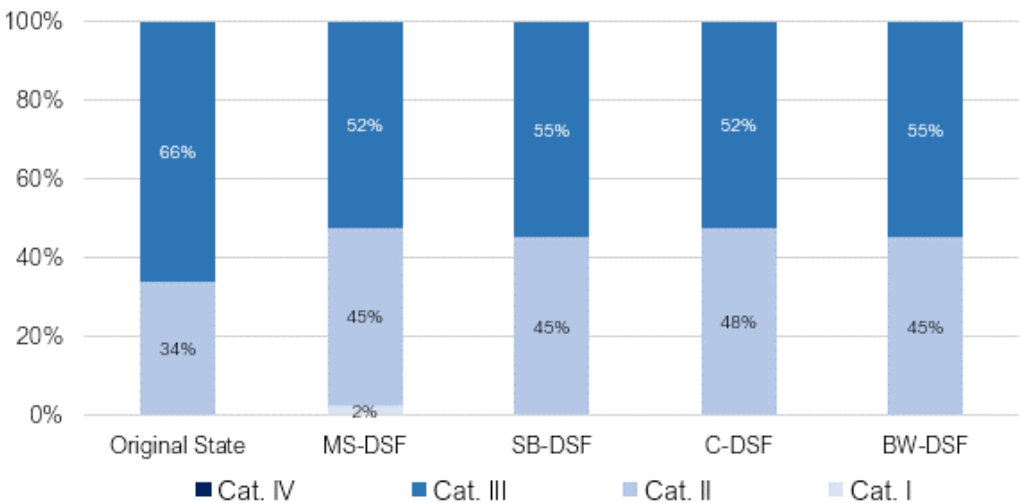


Figure 4.40. Comfort rates for the typical winter week according to DB climatic file.

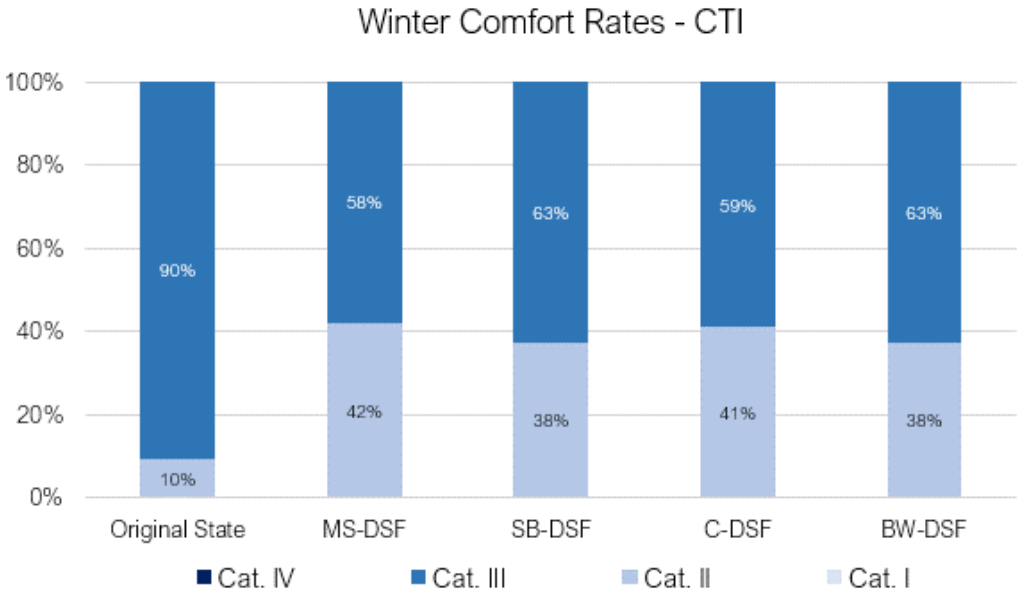


Figure 4.41. Comfort rates for the typical winter week according to CTI climatic file.

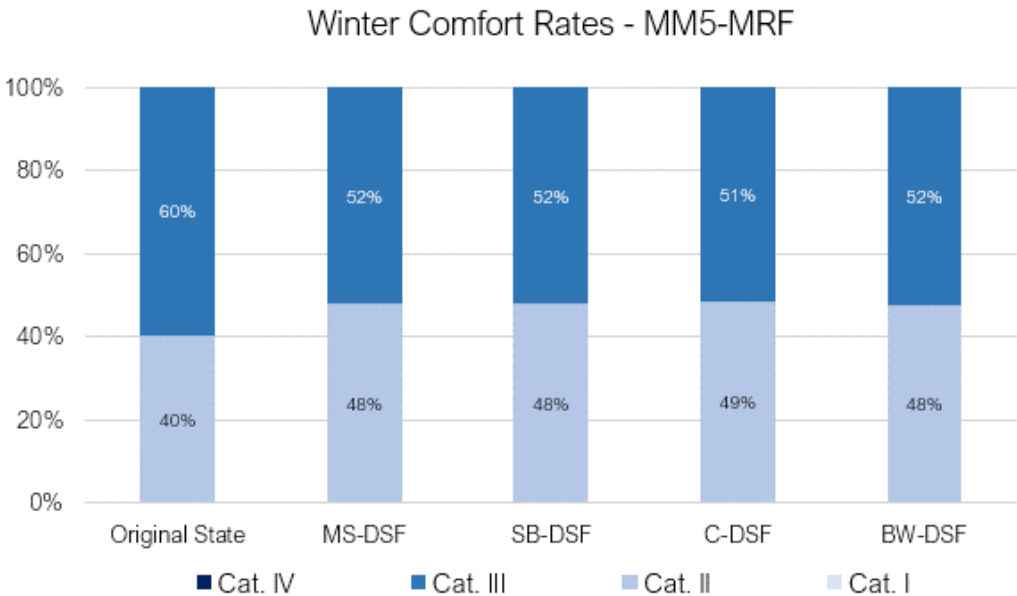


Figure 4.42. Comfort rates for the typical winter week according to MM5-MRF-LSM climatic file.

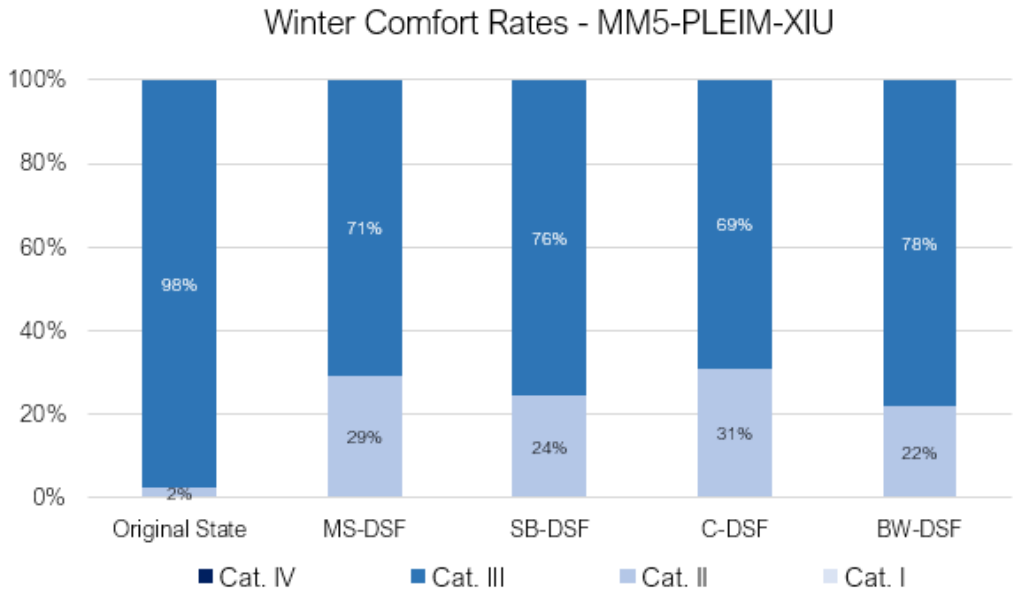


Figure 4.43. Comfort rates for the typical winter week according to MM5-PLEIM-XIU climatic file.

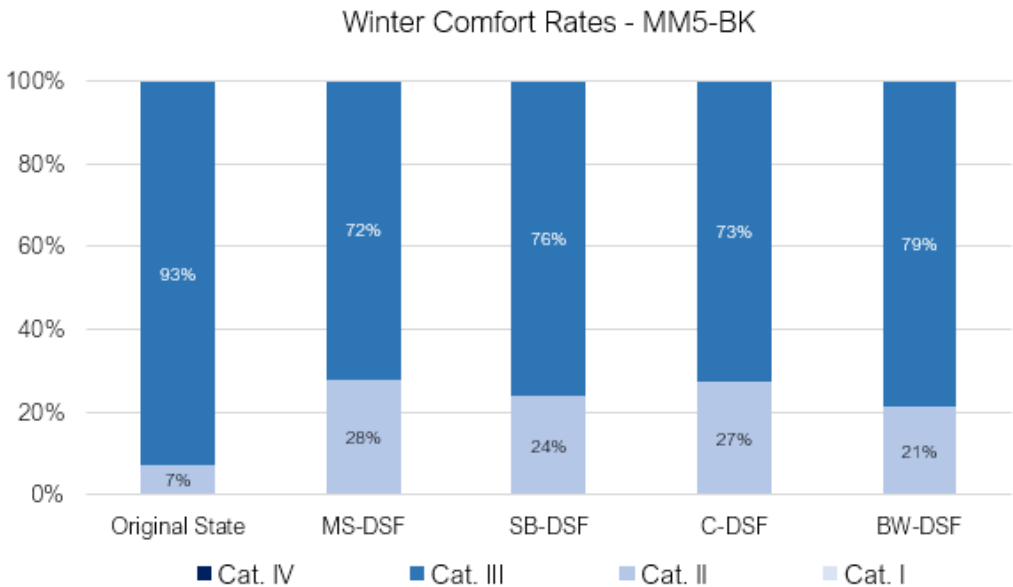


Figure 4.44. Comfort rates for the typical winter week according to MM5-BK climatic file.

4.5. The Impact of Climate Change on Buildings

Nowadays, Climate Change (CC) is one of the biggest challenges that the world is facing and trying to control. One of the first and principal organisations involved in this sector is the Intergovernmental Panel on Climate Change (IPCC), a United Nations body for assessing the science related to climate change. Established by the United Nations Environment Programme (UNEP) and the World Meteorological Organization (WMO) in 1988, it aims to provide policymakers with regular scientific assessments about climate change, identifying adaptation and mitigation strategies [82]. The IPCC assessments record scientific information that can be used to develop climate policies by governments. Since its creation, the IPCC has published five assessment reports about climate change, besides several technical articles and methodological guidelines. According to the fifth assessment report, the CC is inexorable and irreversible due to the past, present and future CO₂ emissions. The most alarming aspect is that its consequences will persist for several centuries, even after a drastically CO₂ emissions reduction [83]. Some of the CC long-term effects, according to the IPCC, are the global warming, frost-free seasons, precipitation pattern changes, a higher number of droughts and heatwaves, the increase of the sea-level and the ice-free conversion of the Arctic Ocean.

For better understanding the intensity of the problem, data coming from the National Aeronautics and Space Administration (NASA) are reported in Figure 4.45. The graph compares the global surface temperature (red line) and the total solar irradiance (yellow line) since 1880. The lighter dotted lines represent the yearly levels, whereas the heavier and solid lines the 11-years average trends.

As it is clear in the picture, while the Sun's energy output has caused in the past the climate change, being the fundamental energy source of the whole climate system, after 1960 the global warming started to be not anymore influenced and driven by the solar irradiance, considering that since 1750 its average amount remained constant, recording slight fluctuations. Moreover, as observed by various scientists, the temperature increase is measured only in the lower atmospheric layers, whereas cooling phenomena are noted in the upper levels. This happens because the heat is trapped by greenhouse gases (GHG) in the lower atmosphere [82].

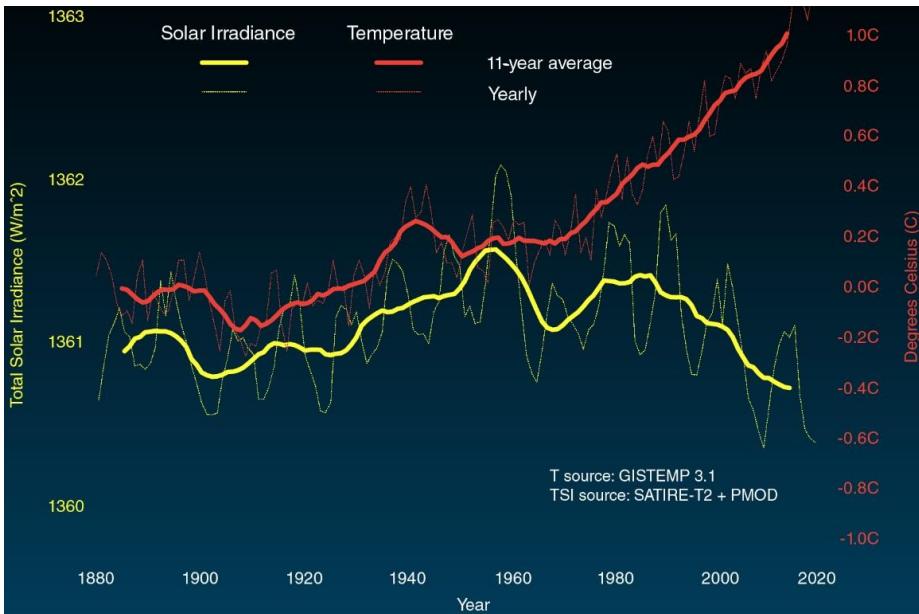


Figure 4.45. Temperature and Solar Activity trends over the years [82].

Since the IPCC identified the CC as an urgent global problem, several climate scenarios have been developed considering different factors to predict climate variability. The main objective is to detect and analyse the likely climate change to subsequently estimate their impacts, for developing adequate mitigation and adaptation strategies. The defined possible future climate scenarios have been updated several times, considering variations in the conducted political developments, protocols, and international agreements in this sector.

The last two sets of scenarios launched by the IPCC correspond to the Special Report on Emissions Scenarios (SRES) and the Representative Concentration Pathways (RCPs). Being the last one, they are the most recommended since they were updated and expanded in scope (regarding the SRES). They cover a range of radiative forcing levels examined in the open literature and containing relevant information for climate model runs. These scenarios are not a complete package of socio-economic, emission and climate projections since the expression “concentration pathway” refers to internally consistent sets of projections of the components of radiative forcing, where concentrations are used as the primary product of the RCPs, designed as input to

climate models. With these conditions, a set of four pathways were created that lead to radiative forcing levels of 8.5, 6.0, 4.5 and 2.6 W/m² by the end of the century, where each of the RCPs covers the 1850-2100 period [84] [85]. Figure 4.46 depicts the projected trends in global CO₂ emissions under the RCP scenarios.

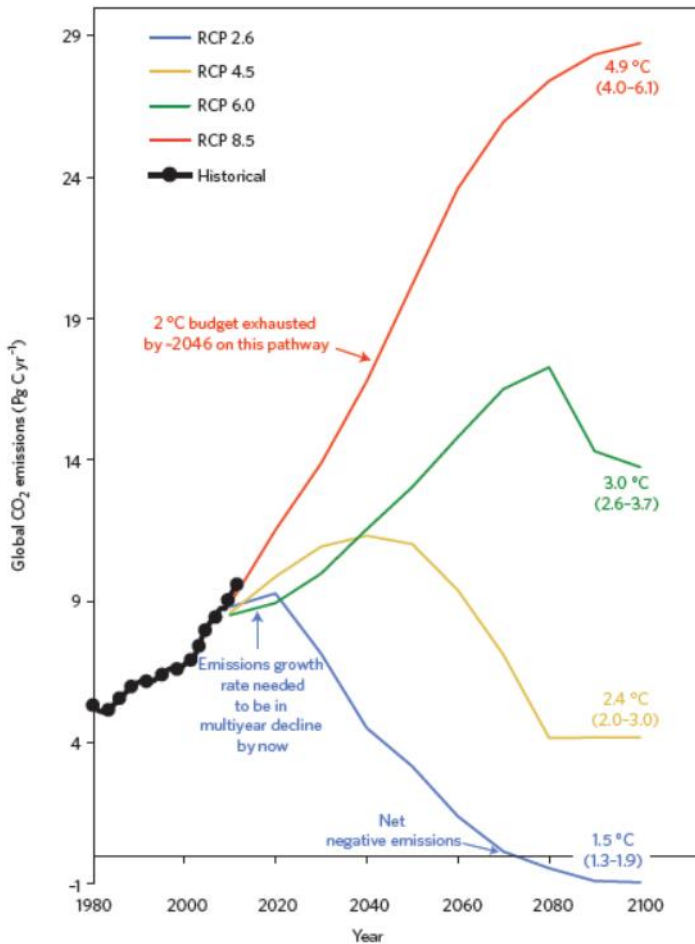


Figure 4.46. Projected trends of global CO₂ emissions under various RCP scenarios [85].

The creation of climate projections scenarios represents key tools for the development of adaptation and mitigation strategies facing Climate Change threats. The climate scenarios analyse how anthropogenic activities might

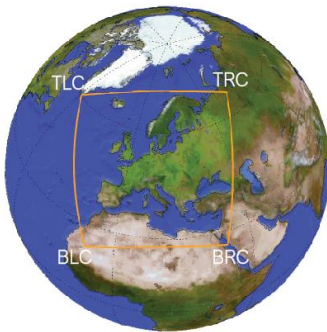
influence the concentrations of greenhouse gases in the atmosphere, and they predict how it will affect the climate system. Currently, the use of climate models to generate weather datasets for building energy simulations represents a robust strategy to evaluate their thermal performance under future climate conditions, having a crucial role for the updating or the creation of construction standards.

The uncertainties involved in the use of projections for future weather data since the climate models and scenarios are clear and their limitations, regarding the level of confidence in the predictions, are currently investigated. However, the climate scenarios and the weather datasets, obtained by simulations with climate models, represent the sole decision-making tool, currently available, to predict the impact of climate change on buildings and, subsequently, to develop different adaptation initiatives and mitigation strategies. The long-term changes in the outdoor climate conditions, in fact, have substantial influences on the building energy performance and their impact should be carefully evaluated. The external temperature increase affects the indoor environment and leads to higher energy loads for HVAC systems, especially on the cooling side [86]. Moreover, these variations can profoundly alter the thermal comfort of the occupied spaces that have to cope with conditions for which they were not initially designed [87].

On the basis of these considerations, the effectiveness of the analysed Double Façade is also tested by elaborating future climatic data, referred to three different TMYs that represent meteorological parameters referred to a near, medium and far future.

4.5.1. Generation of Future Climatic Files

Future climatic files are generated by using the Coordinated Regional Climate Downscaling Experiment (CORDEX). It is a program sponsored by the World Climate Research Program (WCRP) to develop a coordinated framework for evaluating and improving Regional Climate Downscaling (RCD) techniques and producing a new generation of RCD-based fine-scale climate projections for identified regions worldwide [88]. The CORDEX results are assumed as a baseline by the Intergovernmental Panel on Climate Change (IPCC) for defining climate change impact and adaptation studies. Its various domains allow the estimation of climatic variables for all over the world, and the Euro-CORDEX is its European branch (Figure 4.47).



Non-Rotated Coordinates of Domain Corners

Top Left Corner (TLC): 315.86; 60.21

Top Right Corner (TRC): 64.4; 66.65

Bottom Left Corner (BLC): 350.01; 22.20

Bottom Right Corner (BRC): 36.30; 25.36

Figure 4.47. Euro-CORDEX Domain and the coordinates of its corners.

The Aire Limitée Adaptation dynamique Développement InterNational (ALADIN) is a limited area bi-spectral model, developed at the beginning of the 1990s within a large consortium gathering numerous weather centres in Europe [89]. The main peculiarity is that, contrary to most of the available RCMs which are “grid-point” models, it has been designed as a spectral model with the exception that all physical parameterisation computations are performed in the conventional grid-point space. This approach also requires the employment of effective direct and inverse spectral transformations between spectral and grid-point spaces [90]. Its first version was based on the physics of the ARPEGE-Climat model version 4 [91], established by the Météo-France in collaboration with the European Centre for Medium-Range Weather Forecasts (ECMWF). Since the beginning of the 2000s, the ALADIN model is used at the Centre National de Recherches Météorologiques (CNRM) with the name CNRM-ALADIN. Various works, centred on the evaluation of the accuracy and effectiveness of this model over differently sized domains, underline the good capability in the estimation of climatic parameters on both spatial and temporal scales, inside the European area [90] [92] [93].

The CNRM-ALDIN, available in Euro-CORDEX is selected for elaborating future climatic files to be adopted as inputs in dynamic simulations. Data with a 3hs-time frequency are extracted from the nearest grid point to Pescara (yellow point in Figure 4.48), which is 7.5 km far from the case study and placed at 42°28'57” northern latitude and 14°08'07” eastern longitude. The selected RCP is 4.5, which is consistent with a future with relatively ambitious emission reductions,

and this scenario is chosen for being in accordance with national policies in the reduction of greenhouse gas emissions.



Main CORDEX Dataset Information

Domain: EUR-11

Institute: CNRM

RCM Model: ALADIN63

IPCC Scenario: RCP4.5

Time-Frequency: 3 hrs

Figure 4.48. CORDEX primary information and grid-points with localisation of the selected virtual anemometer (yellow ring) and the reference building (red circle).

The available weather variables are relative humidity, atmospheric pressure, global solar radiation, wind velocity and temperature. Multiple years are extracted for obtaining various typical years. The definition of the reference year is conducted according to the method described in the technical standard EN ISO 15927-4:2005 and following its suggestions [67] [94].

The first step involves the calculation of the daily averaged value for each climatic parameter (p), month (mt) and year (y) of the datasets. Then, the averaged values for a specific month of all the available years are sorted in increasing order to calculate the cumulative function $\phi_{(p,mt,i)}$ for each parameter and i^{th} day.

$$\phi_{(p,mt,i)} = k(i) / N + 1 \quad (4.7)$$

where $K_{(i)}$ is the rank order of the i^{th} day and N is the total number of days for a month over all years. The following step consists in sorting the averaged values for a specific month and year in increasing order for obtaining the cumulative distribution function $F_{(p,y,mt,i)}$ for each parameter and i^{th} day.

$$F_{(p,y,mt,i)} = J(i) / n + 1 \quad (4.8)$$

Then, for each month and year, the statistics by Finkelstein-Schafer are defined according to Equation 4.9. The last two steps involve the sorting of months, for which the rank is calculated for every parameter and summed for obtaining the total ranking and for each month, among the first three months with the lowest ranking sum, the one with the lower absolute deviation is chosen as representative for the TMY generation.

$$FS_{(p,y,mt)} = \sum_{i=1}^n |F_{(p,y,mt,i)} - \phi_{(p,mt,i)}| \quad (4.9)$$

For improving the quality of the generated TMY, weighting meteorological parameters are inserted in the Finkelstein–Schafer, as suggested by Cebecauer et al. [95]. The stronger influence of some variables than the others is taken into account by increasing the weight of those parameters. Higher impact factors are attributed to surface temperature and solar radiation (8/24), whereas a lower value (4/24) is assigned to relative humidity and wind speed that slightly affect energy simulations. A twenty-year range is selected for generating the typical year. Thus, data from 2020 to 2040, from 2040 to 2060 and from 2060 to 2080, are used for elaborating, respectively, 2030, 2050 and 2070 TMYs. Once the selected years are generated, a cubic spline function is used to obtain interpolated values and transforming the time-frequency of the investigated parameters from 3hs to 1hr.

Figure 4.49 and Figure 4.50 depict comparisons of monthly mean values for temperature and global solar radiation between historical (DB dataset), new (ARTA and Climate Network database) and future (2030, 2050 and 2070 TMYs) data. The historical dataset (solid blue line) shows the lowest monthly mean temperatures. In contrast, the future data (dotted lines) tend, in general, to assume similar values and trend of those referred to the year 2017. According to the predictions, higher temperatures are attended for the coldest months (from November to February), while a little reduction is estimated for the summer period. More profound variations are expected, instead, for the global solar radiation, as it can be seen in Figure 4.50. In this case, the picks estimated by the CORDEX data are much higher than those recorded in the past and the present, reaching up to 330 W/m².

Comparing these parameters on early averaged values (Figure 4.51), the same trend is confirmed. On the temperature side, from past to future conditions, the increment is gradual, reaching a 2°C delta between the years 2017 and 2070,

Chapter 4

whereas a higher variation is expected for the solar radiation. It is essential to underline that these comparisons involve projections referred to a specific scenario which considers the adaptation of policies for the CO₂ emission containment.

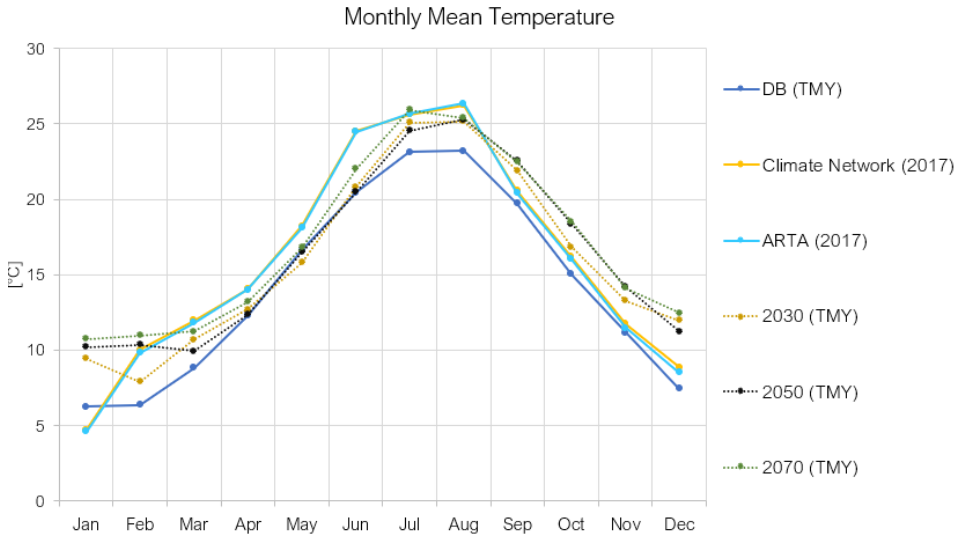


Figure 4.49. Monthly mean values referred to the temperature.

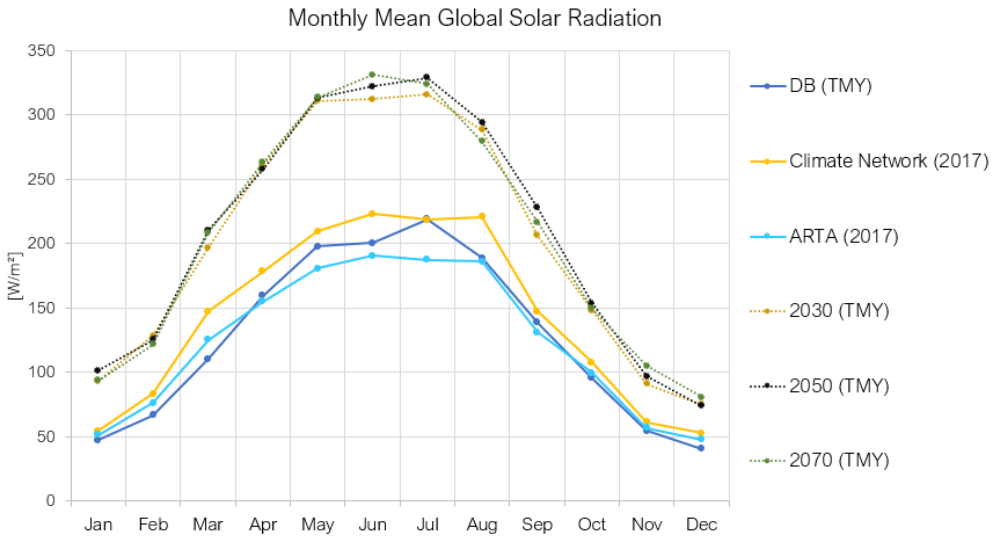


Figure 4.50. Monthly mean values referred to global solar radiation.

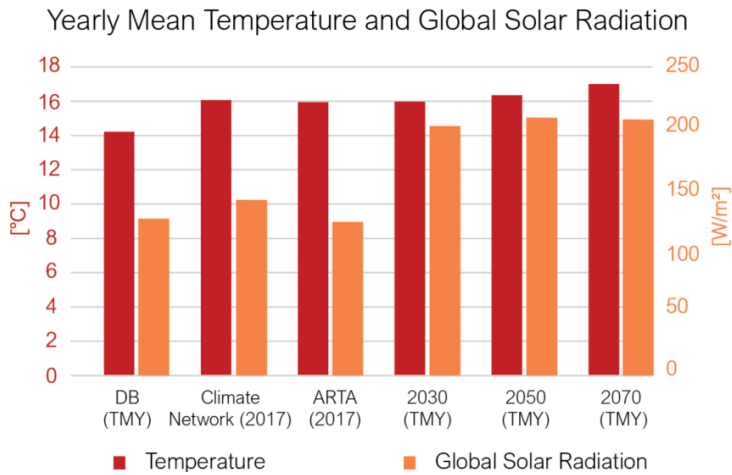


Figure 4.51. Yearly mean values referred to temperature and global solar radiation.

4.5.2. The Impact of Climate Change on the Reference Building

The impact of climate change is here analysed, evaluating the effect that future outdoor conditions could have on the building consumption and thermal comfort. Energy simulations are carried out for estimating the investigated outputs, considering future climatic files referred to the years 2030, 2050 and 2070. The results underline a constant increase of the building cooling load and a similar decrement of the heating need, and this happens for both the original state and with DSF configurations. Also for future conditions, the best typology is represented by the Multi-Storey DSF which allows, at the same time, a good cooling reduction and a more intense heating decrement. The trend estimated for the other typologies with the previously analysed climatic files is validated and, even if with similar values, the insertion of multiple grills for the ventilation of the cavity, as it happens in the Corridor and Box-Window configurations, ensures higher energy savings for the summer period.

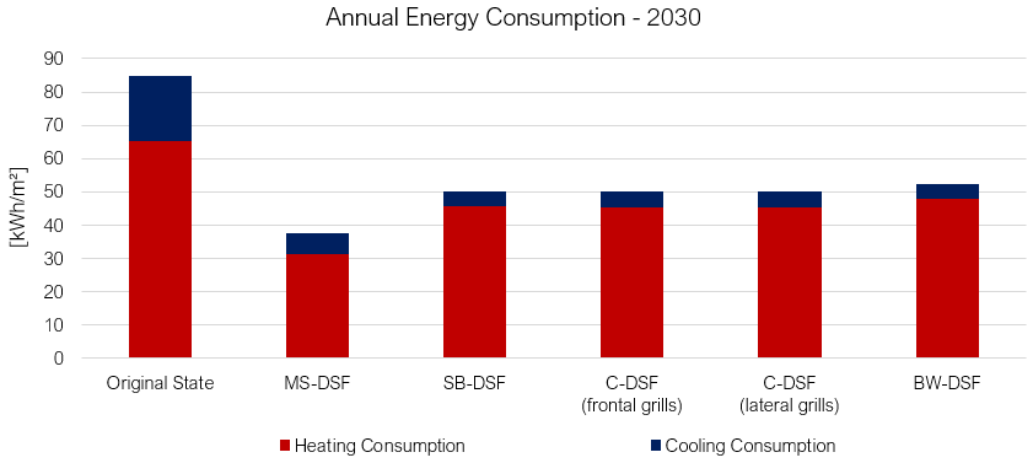


Figure 4.52. Building annual energy consumption estimated for the year 2030.

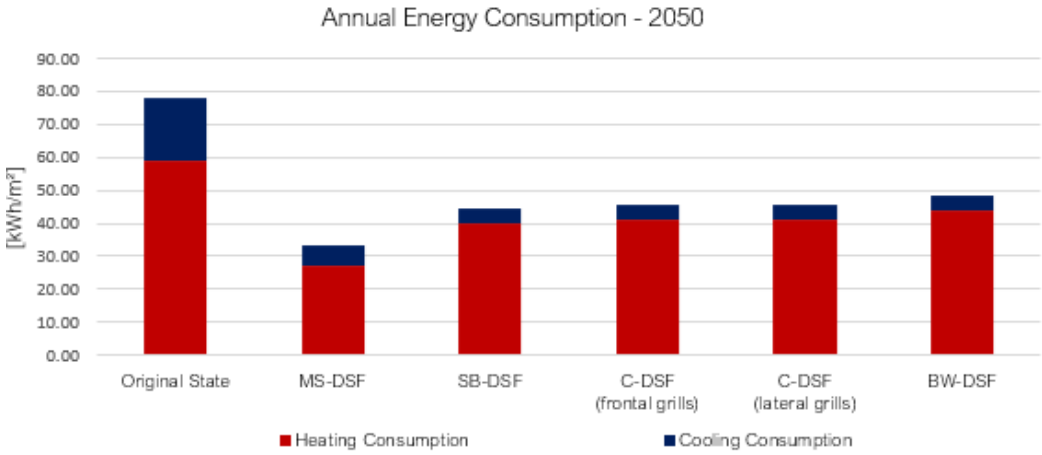


Figure 4.53. Building annual energy consumption estimated for the year 2050.

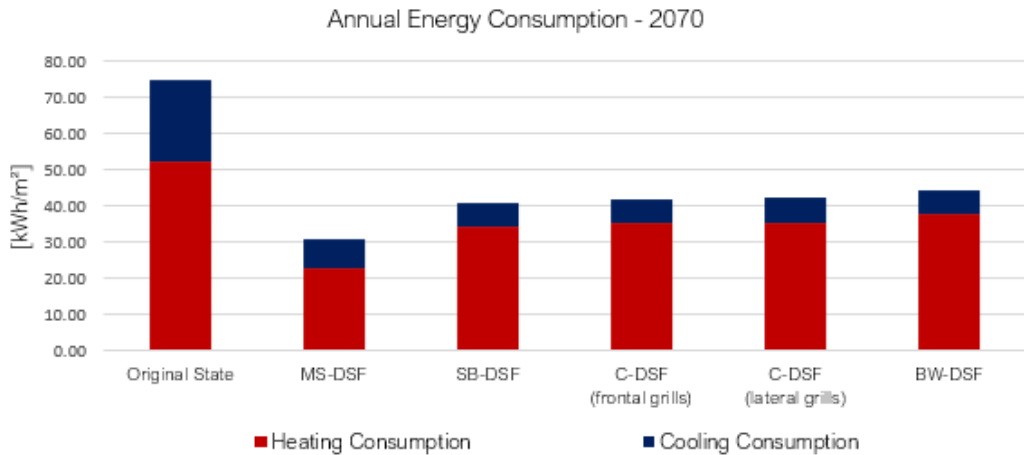


Figure 4.54. Building annual energy consumption estimated for the year 2070.

The analysis of the thermal comfort, predicted for future conditions, is plotted from Figure 4.55 to Figure 4.60. It underlines several variations which should be taken into account for farther considerations about the effectiveness of DSF systems. The estimated summer performance of Double Façades could lead to a different distribution of future comfort levels, due to higher picks reachable by the global solar radiation. As it can be seen in Figure 4.50, the amount of monthly mean radiation expected for the years 2030, 2050 and 2070 is much more significant than the present and past conditions, and this can generate worst comfort rates for various DSF typologies. Due to a high solar load, the Double Façade, in fact, becomes a heated element, which continually emits the accumulated heat. This element is much more sensitive to this phenomenon than the original building envelope because it is entirely made of glazed surfaces. If from one side the DSF acts as a heat damper, reducing the effect of solar picks on the inner operative temperature, it also tends to enlarge the number of hours for which higher temperatures are estimated and, consequently, lower level of comfort. A mechanical system should be introduced to improve the summer indoor environment and to help natural ventilation in case of extra loads, converting the DSF into hybrid technology.

Evaluating winter comfort rates (Figure 4.58 to Figure 4.60), the general temperature increase predicted for the coldest months allows the increment of best levels of expectation and this is estimated for both the building original state and

after the DSF insertion. The discomfort rates referred to future conditions tend, in fact, to decrease, and this reduction assumes more significant values for DSF systems that ensure better performances than those reachable by the reference building in its original state. As obtained with the past and present climatic data, the DSF that allows the best indoor environment is the Multi-Storey, which is capable of guaranteeing the highest percentage with a better level of expectations. Moreover, it is interesting to note that the winter comfort referred to the year 2050 shows better values than the year 2070. The explanation of this phenomenon stands in the higher temperatures and solar radiation predicted for the investigated period (January), which positively affect the heating side, reducing its load.

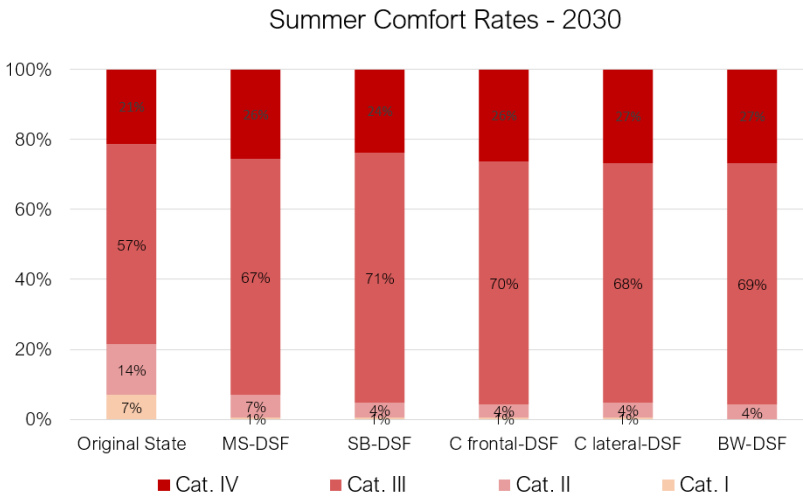


Figure 4.55. Comfort rates for the typical summer week according to the 2030 climatic file.

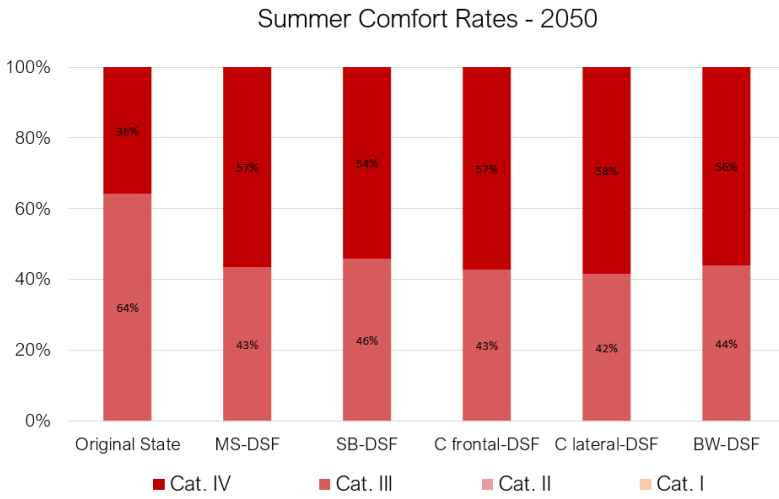


Figure 4.56. Comfort rates for the typical summer week according to the 2050 climatic file.

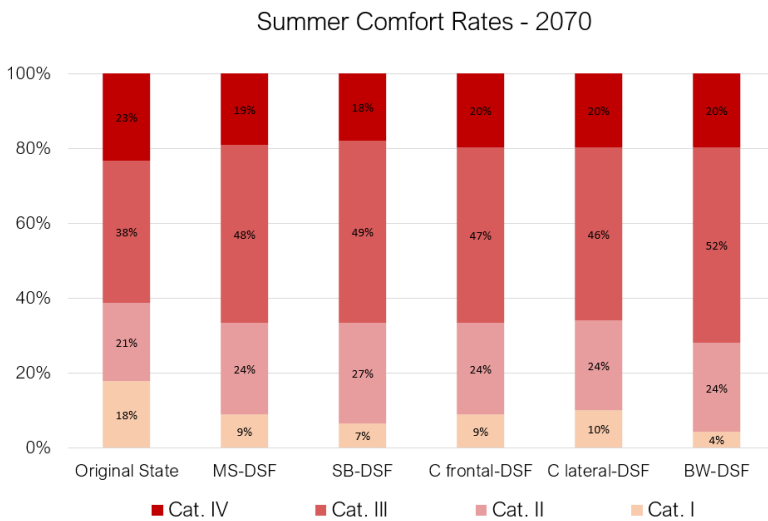


Figure 4.57. Comfort rates for the typical summer week according to the 2070 climatic file.

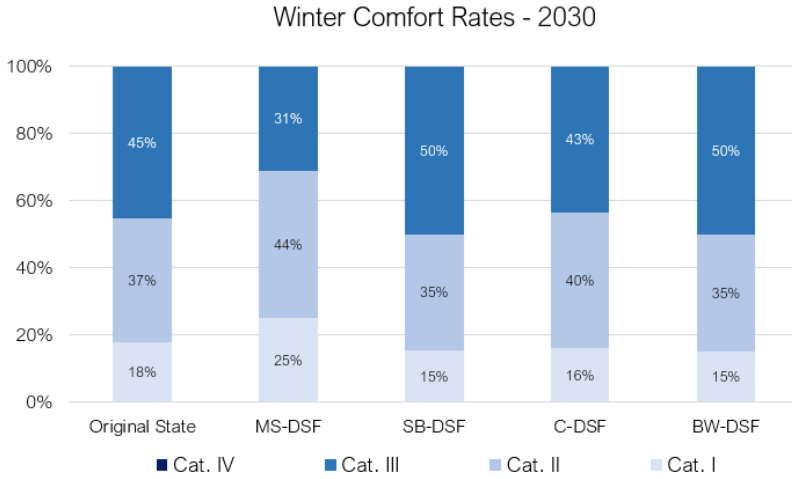


Figure 4.58. Comfort rates for the typical winter week according to the 2030 climatic file.

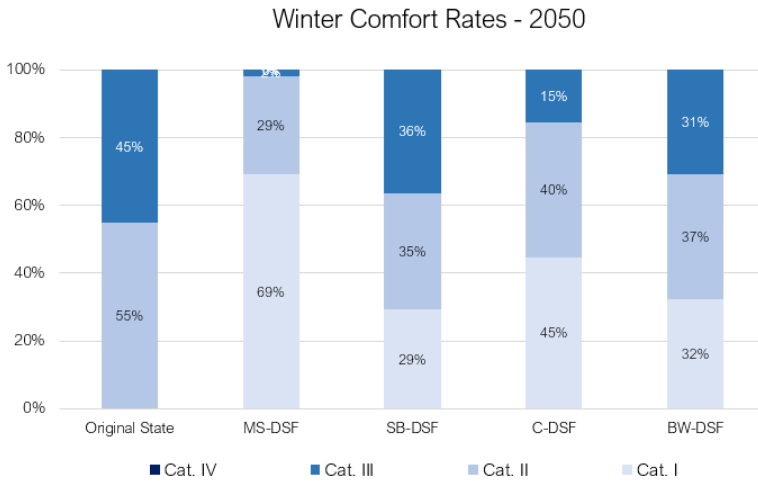


Figure 4.59. Comfort rates for the typical winter week according to the 2050 climatic file.

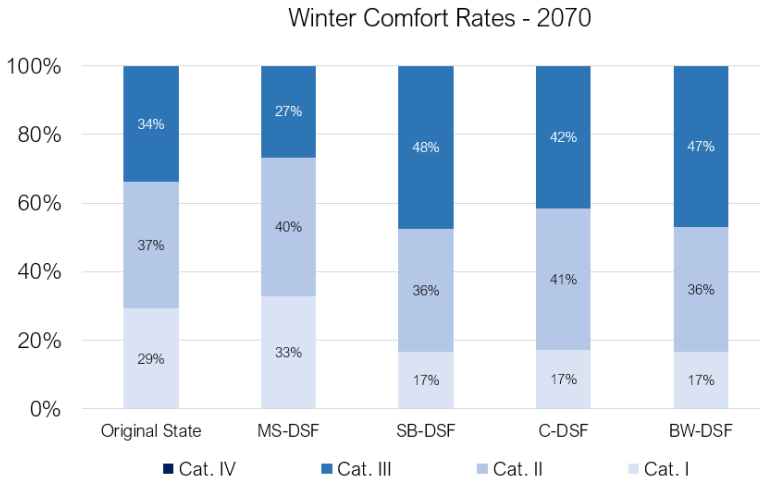


Figure 4.60. Comfort rates for the typical winter week according to the 2070 climatic file.

4.6. Conclusions

The performed dynamic energy simulations underline several findings that can be summarised as follows:

- Not all weather databases show the same level of data accuracy. Varying results, in fact, could be obtained comparing the climatic files among each other or the outputs coming from building energy simulations. Moreover, evident variations between the weather data can be slightly reflected on energy use prediction since building envelope and environmental control systems mitigate climate parameters fluctuations over time.
- The DB dataset, which is commonly used for dynamic simulations, shows a great variation and poor correlations if compared to a specific year. Its use for the model calibration can affect the reliability of the outputs. In addition, the DB climatic file represents a TMY obtained from a recorded period referred to various decays ago. For this reason, the weather parameters are not representative of the current climatology of the site and tend to affect the accuracy of predictions.
- Regional Climate Models can be considered a good option for generating predicted climatic data when observed values are unavailable. Thus, the use of RCMs to build a typical meteorological year, simulating a

considerable period, could represent a reliable strategy to be implemented in the dynamic energy modelling of buildings. Moreover, the options of combining various regional climate models, on the basis of their capability in estimating specific seasons, could increase the accuracy of predictions. In the particular case, for example, the MM5-MRF-LSM seems to perform better the wintertime, whereas the MM5-BK shows higher accuracy for the summer period. Good performances could be ensured for the whole year by creating only one TMY from their combination.

- The use of empirical correlations and models for the decomposition of the global solar radiation into its direct and diffuse contribution is an excellent option to overcome the problem of missing data without reducing the weather database accuracy. The essential aspect involves the selection of the right correlation, which, better than others, allows higher quality estimations.
- Dynamic simulations of the case study underline that the highest energy consumption is due to heating loads and the insertion of various DSF configurations, acting as a buffer zone, can profoundly mitigate and reduce the energy consumptions estimated for the wintertime. Moreover, the addition of a multi-layer façade, opportunely ventilated and shaded, can also ensure better performances during the summer period, allowing a consequent reduction of the cooling requirement of the inner spaces. The general improvement in terms of energy consumption can also be seen on comfort rates.
- All the investigated Double Skin Façades confirm to be a useful option for the improvement of the energy performance of existing buildings. The best configuration which allows the highest energy consumption is the Multi-Storey typology thanks to its drastically decrease of the heating load. In addition, it also ensures considerable benefits on the cooling side, even if reduced in comparison to the Box-Window and Corridor option.
- The evaluation of the impact of climate change on the reference building, by elaborating future climatic conditions, underlines that the general increase of temperatures and solar radiations could affect the building energy performance with the rise of the cooling requirement and a

consequent reduction of the heating loads. The insertion of DSF can mitigate the CC effects, reducing the predicted energy consumption and ensuring better performances than the building in its original state would have. On the comfort side, a proper investigation should be done for avoiding the overheating of the DSF cavity due to extreme levels of solar radiation and coupling the natural ventilation with mechanical systems could be the useful option.

The main findings here presented confirm the effectiveness of the Double Skin Façade, which can be considered a reliable option for the conversion of existing buildings into more energy-efficient systems. It is essential to bear in mind the limitations of dynamic simulations in case of DSF modelling. Various works, in fact, analyse the difficulties from energy software in the prediction of the cavity airflows and the exact temperature distributions along the DSF height [96] [97]. For better estimations, more accurate Computational Fluid Dynamics simulations are performed in the following chapter.

5. Computational Fluid Dynamics Simulations

5.1. Introduction

The chapter aims to evaluate the fluid dynamic behaviour of Double Skin Façade systems by means of Computational Fluid Dynamics analyses. As underlined in Chapter 4 and confirmed by several investigations, building energy simulations have various limitations in the correct estimation of air fluxes and temperature stratification inside the DSF cavity. Thus, the CFD approach can play an essential role in evaluating and improving the thermal performance of these systems.

CFD simulations have been implemented increasingly over the last two decades, thanks to the diffusion of advanced computing sources able to reduce times and costs [98]. According to Papakonstantinou et al. [99], computer analyses are able to describe the natural ventilation of occupied spaces, offering predictions that are in good agreement with experimental values of air velocity, temperature and pressure. Moreover, Liddament [100] underlines how the estimations obtained by numerical methods have enabled the concepts of ventilation efficiency to be applied at the design stage, while the value of the experimental method has been restricted to the evaluation of existing structures.

The literature review about the CFD modelling of DSFs suggests its capability in predicting results, which are not only physically plausible but also in good agreement with available experimental campaigns. As confirmed by Dama et al. [101], in fact, the CFD approach is able to give a qualitative picture of the realistic flows which characterise the DSF cavity. Spiking about the quantitative scale, CFD estimations could be deeply affected by the selection of wrong turbulence models or boundary conditions, that represent the essential core of the simulation. For this reason, the validation and verification of the model is a fundamental step, as suggested by Chen and Srebric [102].

Xu and Ojima [103] confirm the reliability of CFD simulations applied to Double Façades and estimate as minimal and maximal error in the comparisons between measured and predicted values, respectively, 2.5% and 12%. Other investigations are, instead, centred on the evaluation and definition of the best settings to be used for performing CFD analyses, as the study led by Pasut and De Carli [104]. The research is focused on defining a scientifically validated strategy for carried out CFD simulations in case of naturally ventilated DSF buildings. Moreover, the work intends to identify those factors which are essential in the simulation and the others that increase the model complexity without improving the prediction capacity.

Despite the above-mentioned benefits that the CFD introduces into the design process, the user must be aware of the common downfalls and limitations specific to the analysis model. In fact, for performing correct CFD simulations, the full comprehension of the fundamental aspects which govern the fluid dynamic problem, as the conservation equations (conservation of mass, momentum and energy) or the adopted turbulence model (Reynolds-Averaged Navier-Stokes, Large Eddy Simulation and Detached Eddy Simulation) is fundamental.

This chapter is structured as follows. After this introduction, the modelling of the reference building in its original configuration is described in Section 5.2. Subsequently, Section 5.3 is centred on the elaboration of various Double Façade models for estimating their fluid dynamic performances. This section also presents sensitivity analyses which assume as key points the mesh size, the DSF cavity depth and the use of bi or three-dimensional models. Section 5.4 offers a more detailed model of the case study (with pitched roof and balconies) in which the DSF is placed on two elevations. Then, optimised DSF shapes are investigated and described in Section 5.5. Finally, Section 5.6 draws the main conclusions.

The simulations here presented are referred to the summer period when the ventilation of the cavity is allowed for improving the building free cooling. The models are elaborated on the basis of considerations and findings coming from preliminary analyses performed on a simpler case study, opportunely calibrated, reported in Appendix E. The commercial software used for the analysis is Star CCM+ (version 13) [105].

5.2. Modelling of the Reference Building

CFD analyses are performed for evaluating the wind pressure and velocity around the reference building. The case study is modelled as a simple prismatic shape, with main dimensions equal to 60 m x 12 m and 21.5 m tall. For these preliminary simulations, the pitched roof and balconies are not modelled, both added in the second stage of the study. Moreover, the building volume is completely closed at the ground floor where, instead, the original configuration presents pilotis. The main model components are the domain and the building. The domain size is carefully defined for ensuring good accuracy in the predictions and adequate processing times. For this reason, the cylindrical domain has a diameter of 150 m and a height of 100 m. These values are chosen for allowing the wind to enclose the building entirely. The vertical surface of the domain is horizontally subdivided into three regions, whereas the base is composed of two concentric rings. Figure 5.1 shows the main components and subdivisions of the domain and building.

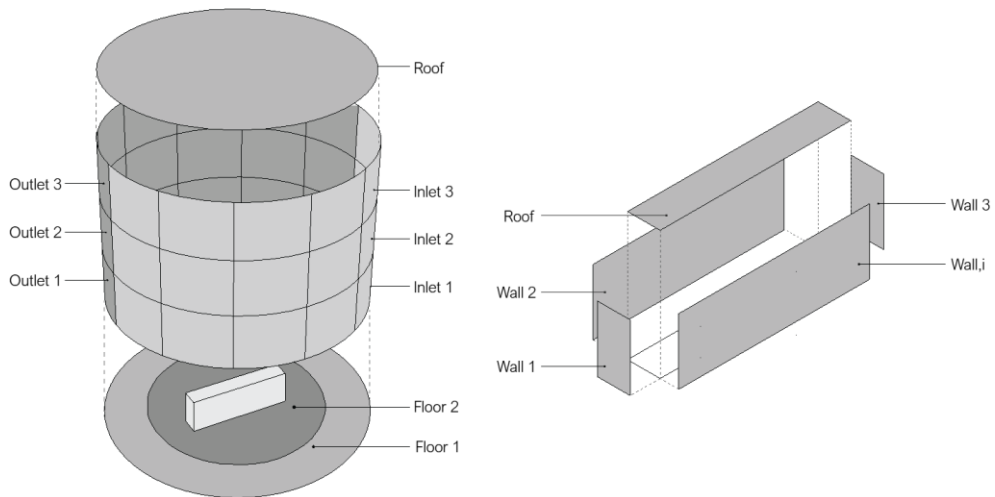


Figure 5.1. Domain and building components of the modelled case study.

Velocity inlet and pressure outlet are the settings assigned respectively to the frontal domain surfaces where the wind velocity is defined as an input, and the rear ones for which pressure levels are fixed. Polyhedral and prism layer meshes are used for discretising the domain and the building (see Figure 5.2). After various

attempts for obtaining a good quality mesh, the data inserted for the meshing step are as follows:

- Base Size = 0.4 m
- Number of Prism Layer = 5
- Prism Layer Stretching = 1.2
- Prism Layer Thickness = 0.1 m

The total number of model cells is 133860, and the unsteady Reynolds-Averaged Navier-Stokes (U-RANS) model is selected for the numerical simulations. In detail, the turbulence is considered by means of the two-equation k - ϵ model, in which transport equations are solved for the turbulent kinetic energy k and its dissipation rate ϵ . The initial conditions are 0.0 Pa for pressure and 0.4 m/s for wind velocity along the x-axis towards the negative direction. The simulation time step is set equal to 0.01 s for avoiding convergence problems. The here-defined inputs are subsequently adopted also for the modelling of the selected DSF configurations.

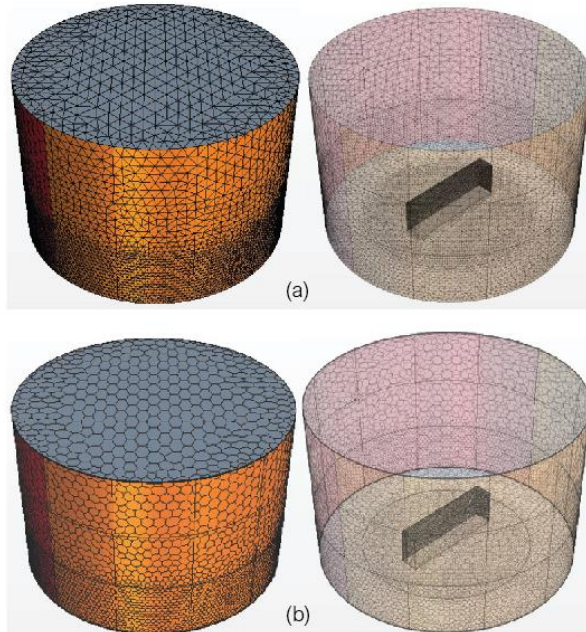


Figure 5.2. Surface (a) and Volume (b) meshes of the case study model.

Pressure conditions and velocity magnitude are the investigated outputs, plotted respectively, in Figure 5.3 and Figure 5.4. According to the results, on the south-east elevation of the building in its pre-intervention configuration, the pressure reaches the maximum values because of the generation of stagnation points. Thus, inside this area, the velocity magnitude is zero.

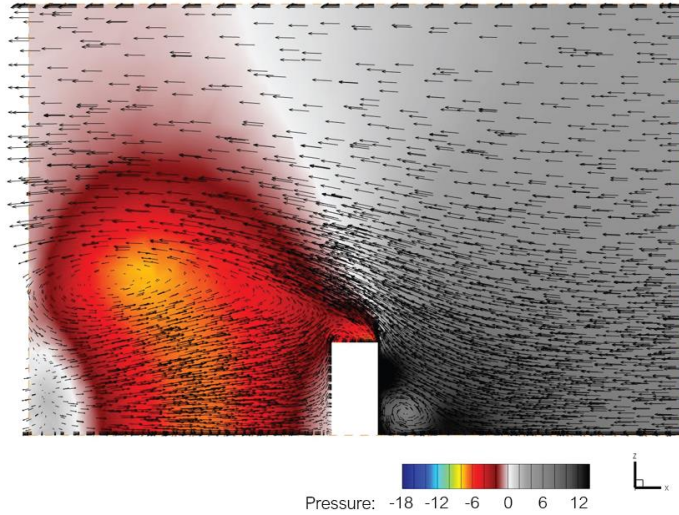


Figure 5.3. Pressure levels estimated for the reference building before the DSF insertion.

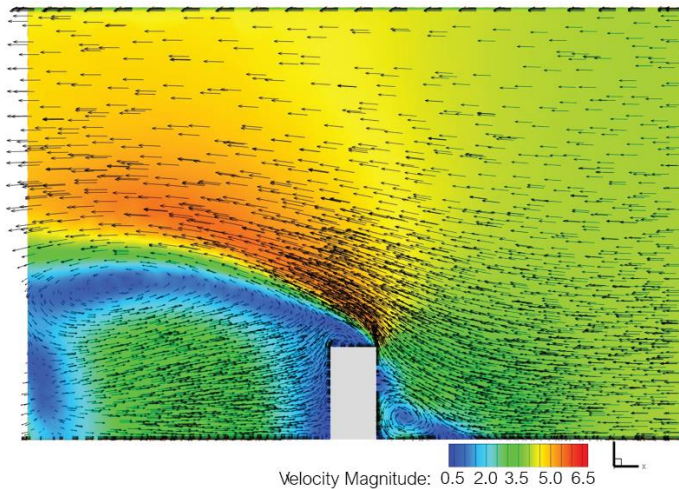


Figure 5.4. Velocity magnitudes estimated for the reference building before the DSF insertion.

5.3. Modelling of the Double Skin Façade

After evaluating the fluid dynamic behaviour of the reference building in the existing configuration, several simulations are carried on for testing the effectiveness of various DSF options. In detail, the Multi-Storey, Shaft-Box and Corridor typologies are selected for CFD analyses. The choice of not modelling the Box-Window Double Façade stands in the fact that, among all typologies, it is the less interesting from a fluid dynamic point of view due to the presence of small cells, characterised by weak air fluxes. Moreover, its performance can be compared, even if with less intensity, with the estimations referred to a Corridor DSF.

The analyses here presented adopt different wind directions in order to investigate the performance variation of these systems. The twelve sectors into which the domain is subdivided are thus characterised as incoming wind (six sectors) or pressure outlet (six sectors), according to the selected direction, whereas the domain mesh remains unchanged. First, the Multi-Storey DSF is tested by performing sensitivity analyses for estimating the influence of the mesh size on the predictions. Then, various cavity depths are evaluated for selecting the one able to ensure the best ventilation, thus having a more significant impact on the building free cooling. Finally, comparisons are made considering the performance of the Multi-Storey configuration with the Shaft-Box and Corridor DSF.

5.3.1. Modelling of the Multi-Storey DSF and Preliminary Simulations

The first Double Façade to be investigated is the Multi-Storey configuration, selected for performing preliminary analyses referred to the mesh size and cavity depth. It is essential to underline that, for this stage, the Double Façade is inserted only on the south-east elevation, chosen for being the most interesting from the energetic point of view, as underlined in the previous chapter. The hypotheses assumed for modelling the reference building (e.g., mesher type, turbulence model, solver criteria) are also used in this case. The sensitivity analysis is carried on for defining the best mesh dimension able to ensure, at the same time, the accuracy of the results and affordable processing time. Three different mesh sizes (0.5 m, 0.25 m and 0.1 m) are evaluated for the discretisation of the DSF cavity. For the present stage, the DSF is 1 m depth, and it is modelled as a layer which encloses the building elevation for the whole length, starting from the first floor (not covering

the ground floor). The domain and building surfaces, including those referred to the DSF system, are shown in Figure 5.5.

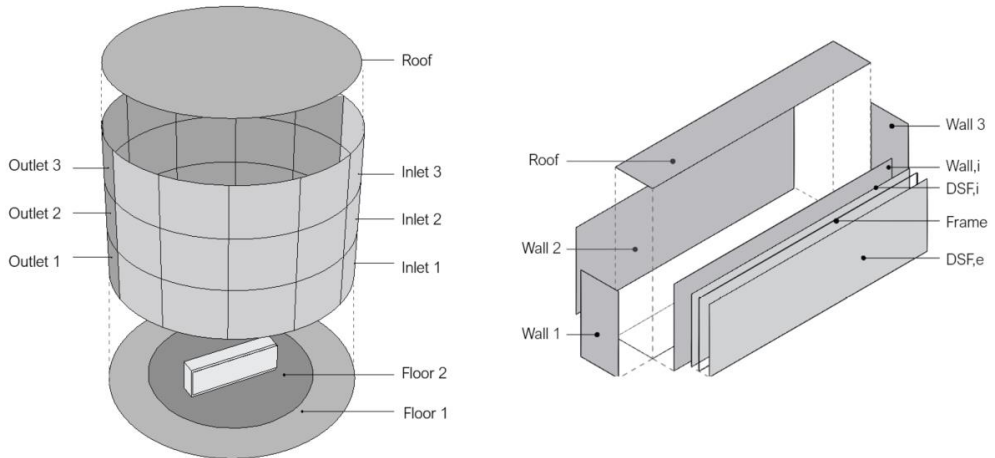


Figure 5.5. Components of the domain (left) and DSF Building (right).

Polyhedral and prism layer meshes are chosen for both surface and volume meshing, as depicted, respectively, in Figure 5.6 and Figure 5.7. As boundary conditions, the velocity vector is set to 4 m/s along the x-axis, with negative direction, whereas the pressure value defined for the outlet surfaces is 0 Pa. The physical settings as the turbulence model or the definition of the analysis parameters are presented in Section 5.2. For investigating the flux variation inside the DSF cavity, probe lines are inserted at different heights, as shown in Figure 5.8.

Table 5.1 summarises the basic information about the here presented models. It is important to bear in mind that a smaller mesh size involves a higher processing time. In the specific case, the solving time related to the simulation with a 0.1 m mesh model can be up to four times longer than the one necessary for the calculation with 0.5 m meshes.

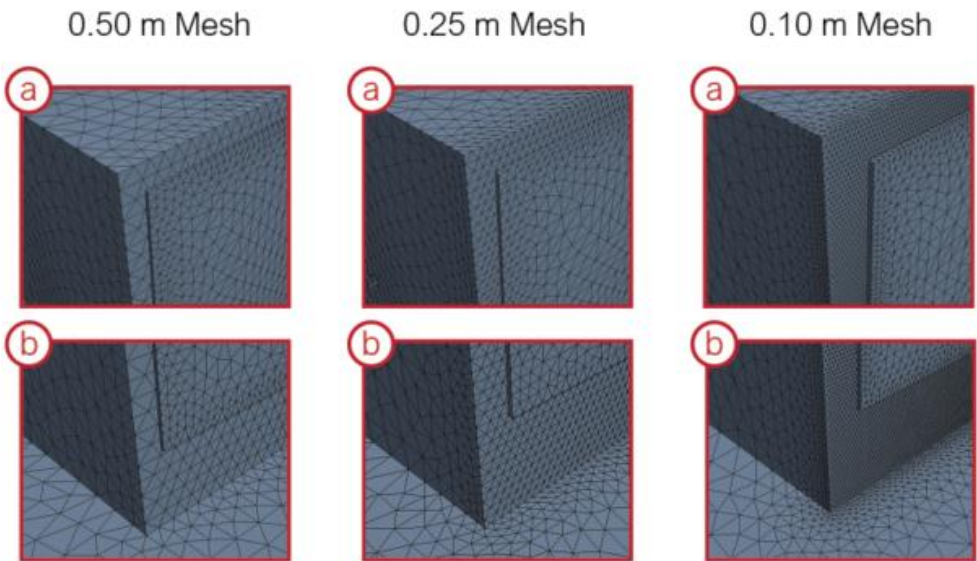
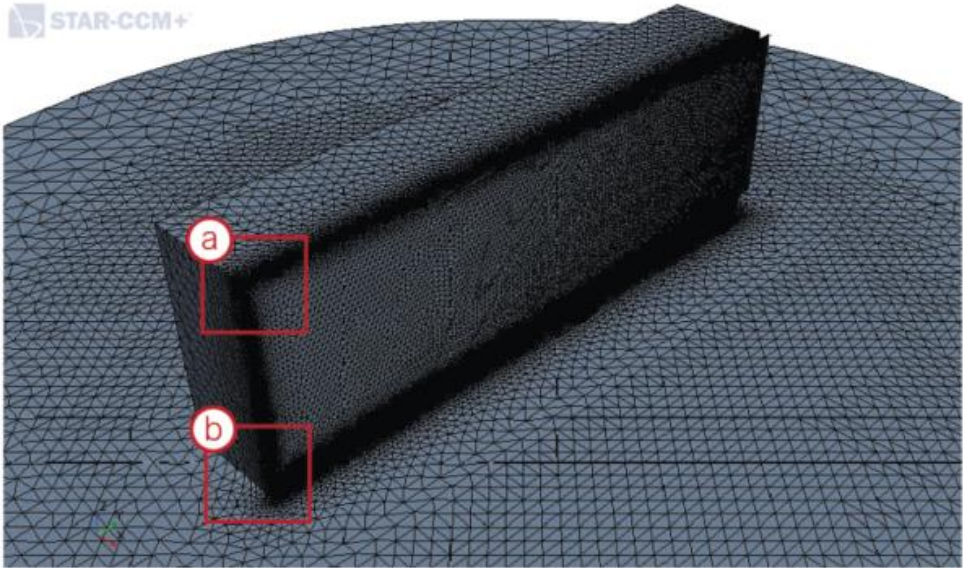
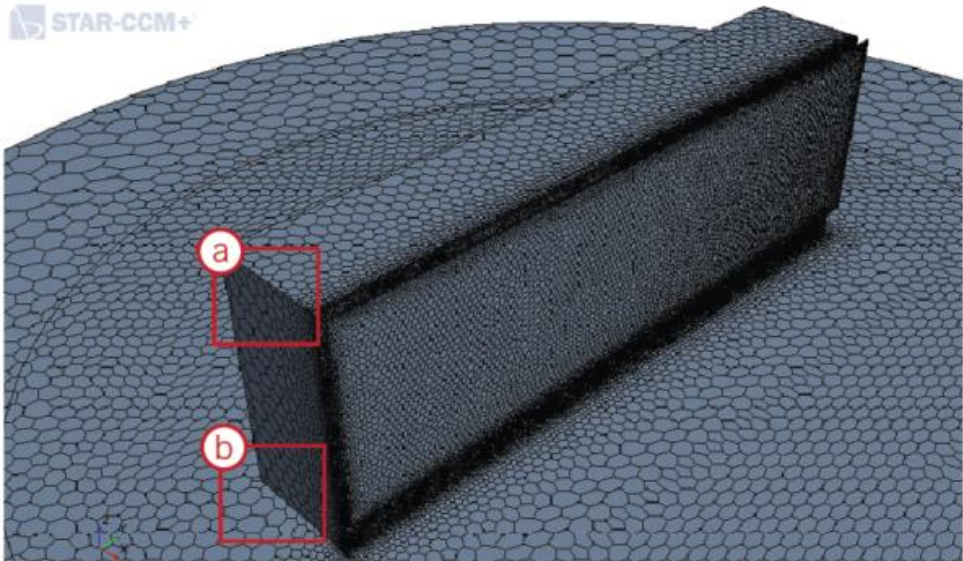


Figure 5.6. Surface meshes referred to different mesh sizes.



0.50 m Mesh

0.25 m Mesh

0.10 m Mesh

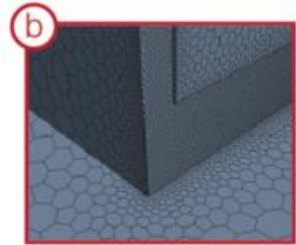
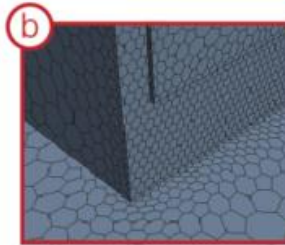
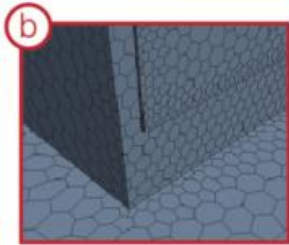
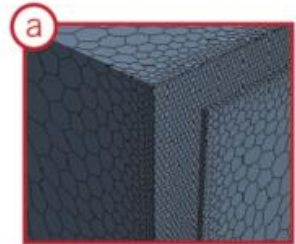
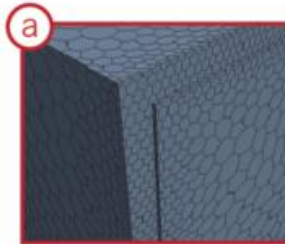
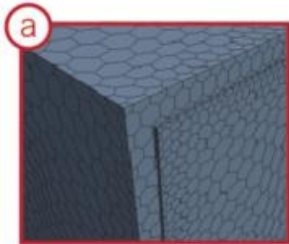


Figure 5.7. Volume meshes referred to different mesh sizes.

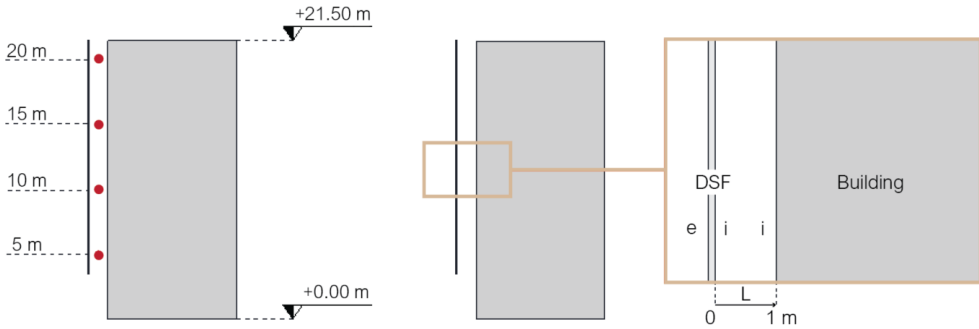


Figure 5.8. The localisation of the probe lines inserted inside the DSF cavity.

Table 5.1. Synthesis of the main settings adopted for the investigated models.

Parameter	0.1 Mesh Size	0.25 Mesh Size	0.5 Mesh Size
Mesh Size	0.10 m	0.25 m	0.50 m
Number of Cells	1568311	475410	313439
Time Step	0.01 s	0.01 s	0.01 s
Physical Time	160 s	150 s	150 s
Processing Time	19 dd	8 dd	5 dd

The velocity profile estimated for the above-mentioned probe lines and for each mesh size is plotted in Figure 5.9. Looking at the obtained results, there is not an evident variation between one model and the others, and all options perform well the DSF behaviour. The only difference can be seen at the base of the Double Façade where, in correspondence to the probe line at 5 m, the smallest mesh is able to describe the flux separation better than the others.

To confirm this finding, the velocity magnitude and pressure level inside the cavity are plotted in Figure 5.10 and Figure 5.11. For both cases, the 0.5 m mesh is not able to predict the values at the bottom of the DSF where the air enters the cavity that are, instead, well calculated by the 0.1 m size. Considering the processing time referred to each simulation, the choice of an interim solution, as it is the 0.25 m mesh, allows obtaining acceptable results with reasonable solving times. On the basis of these considerations, the mesh adopted for the following simulations is the 0.25 m size.

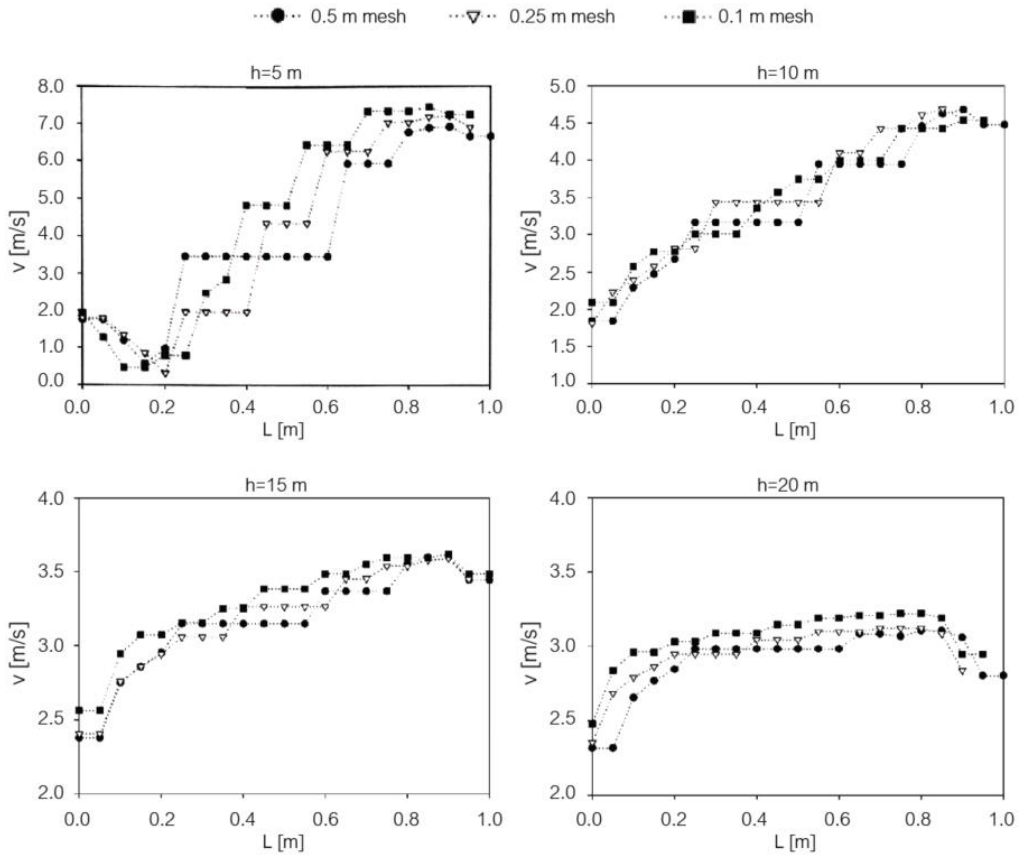


Figure 5.9. Velocity profile comparisons for each probe line and mesh size model.

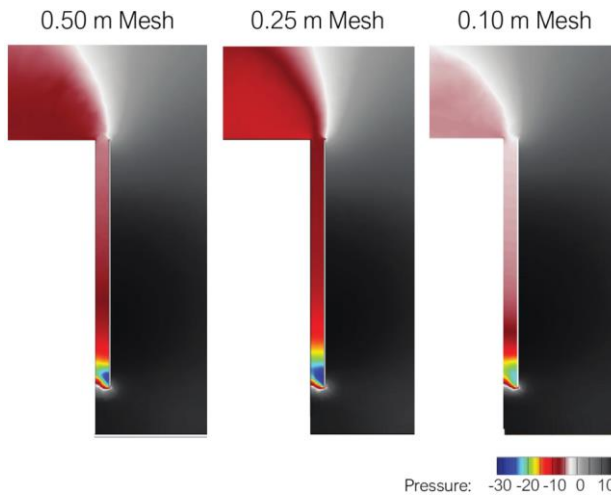


Figure 5.10. Pressure levels inside the DSF cavity estimated for various mesh sizes.

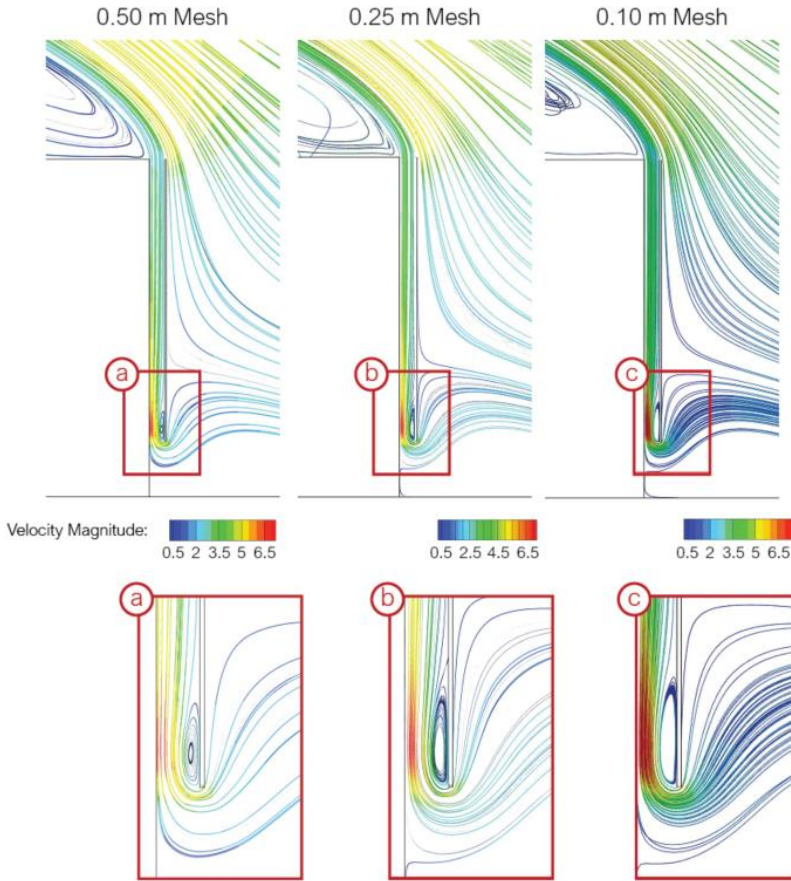


Figure 5.11. Velocity magnitudes inside the DSF cavity estimated for various mesh sizes.

After the sensitivity analysis, the second stage involves the evaluation of DSF with deeper cavities. Two different models are elaborated with, respectively, a 1.5 m and 2 m cavity depth. The hypotheses assumed for the previous simulations are also confirmed in this case. Figure 5.12 underlines the different cavity dimensions selected for the comparisons. Moreover, considering the good convergence of the simulation, the time step is incremented from 0.01 s to 0.05 s. The total number of cells for the two models are 517265, for the 1.5 m cavity depth, and 534032, for the 2 m cavity option.

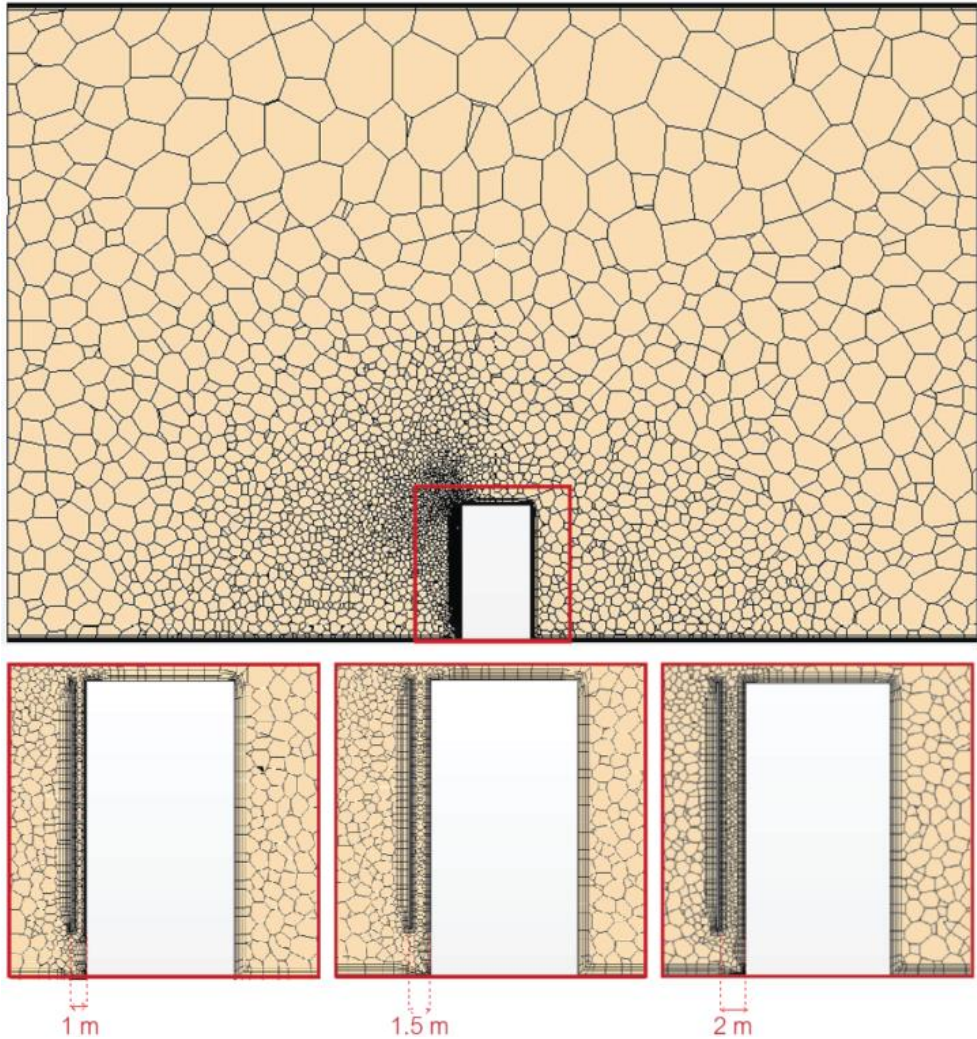


Figure 5.12. Comparison of the selected DSF cavity depth.

Figure 5.13 shows comparisons between the velocity values estimated for various DSF cavity dimensions (1 m, 1.5 m, and 2 m) and those referred to the building in its existing configuration. The absence of the DSF, as it can be seen for the existing building, does not encourage the ventilation of the façade, predicting low and constant velocity values. Putting the attention on the performance of DSFs, it is clear that thinner cavities ensure higher velocities inside the layers closer to the external skin, thus collaborating in the reduction of the glazed surface temperature.

On the contrary, increasing the cavity depth, better ventilation reaches the existing façade, with consequent benefits on the building cooling.

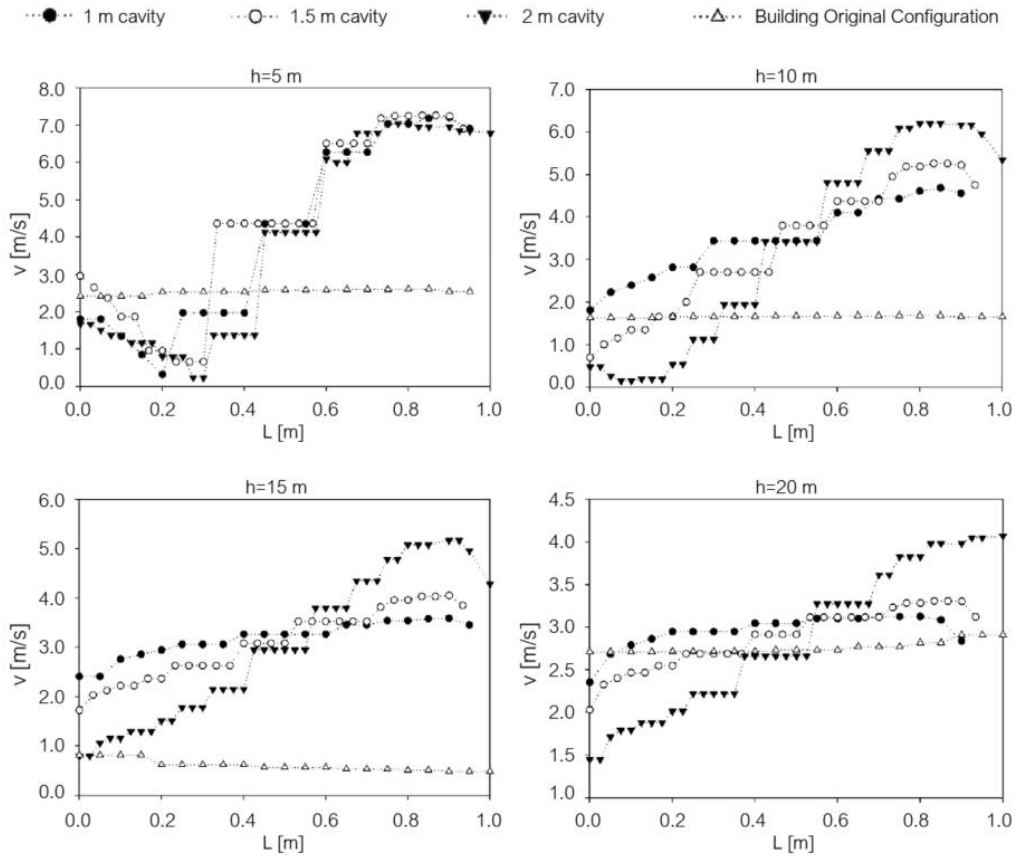


Figure 5.13. Velocity profile comparisons for each probe line and DSF cavity.

The benefits which could be ensured by inserting the DSF on the existing building are highlighted by comparing the velocity profiles with the pressure levels and the velocity magnitudes, respectively plotted in Figure 5.14 and Figure 5.15. The most efficient solution appears to be the 1 m cavity DSF which generally ensures reasonable ventilation rates. Besides, the insertion of an external shading system able to reduce the solar load on the façade would collaborate to natural ventilation and avoid the overheating risk of the cavity.

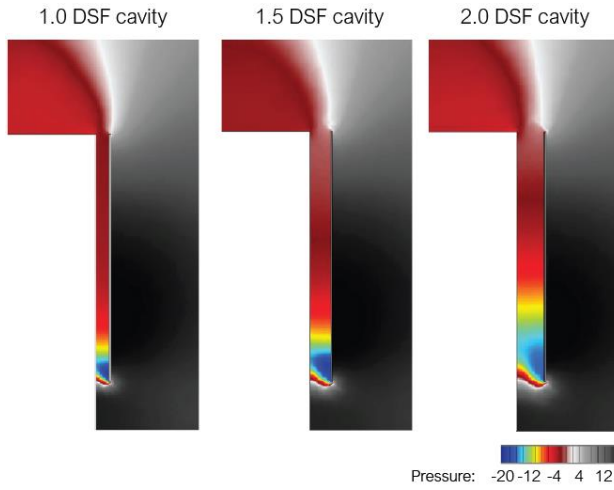


Figure 5.14. Pressure levels inside the DSF for the investigated cavity depths.

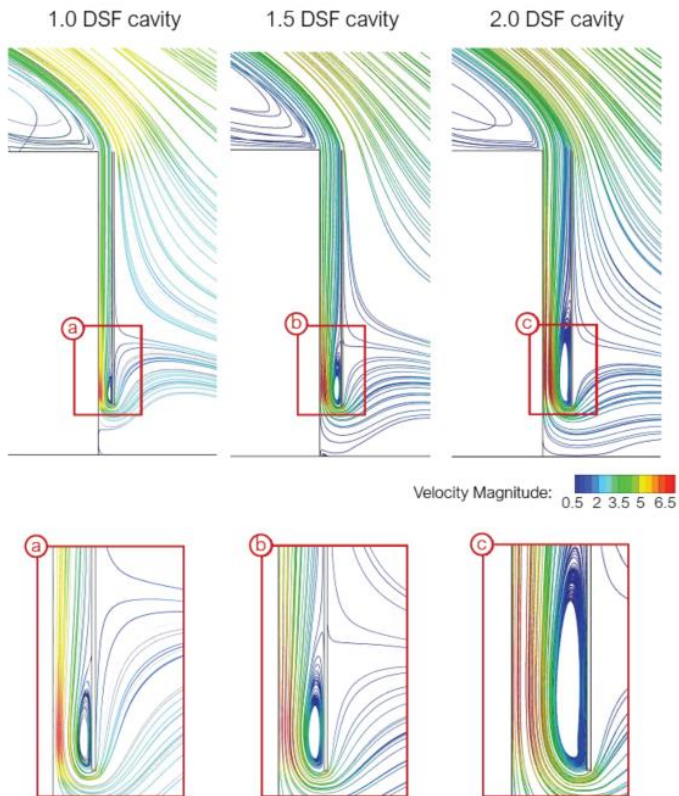


Figure 5.15. Velocity magnitudes inside the DSF for the investigated cavity depths.

The last set of preliminary simulations intends to evaluate the model sensitivity to the use of a three or bi-dimensional domain. Thus, the already elaborated model is converted into a bi-dimensional setup, as schematised in Figure 5.16. Moreover, the comparisons aim also to quantify the impact that the ratio between the two main building dimensions (length and depth) has on the results. In detail, starting from the real building extension for which one façade is six times larger than the other (6:1), two more options are evaluated. The first case considers one dimension three times larger than the other (3:1), whereas the last assumes that both façades have the same extension (1:1).

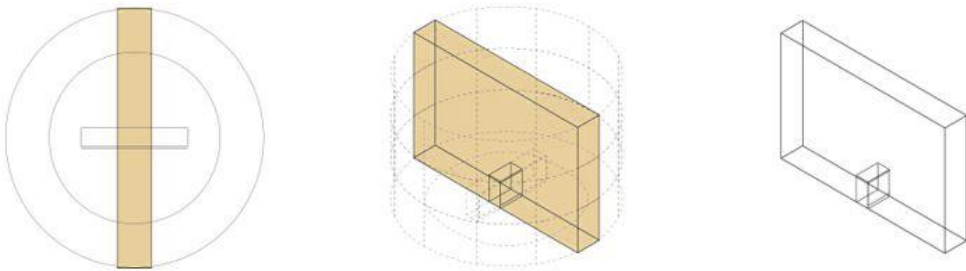


Figure 5.16. Followed steps for the conversion of the model from 3D to 2D.

Velocity profiles referred to each probe lines for the here-analysed models are plotted in Figure 5.17. They underline that the bi-dimensional model, considering the building infinitely vast, estimates the highest velocity values inside the DSF cavity. Moreover, it is interesting to observe that reducing the ratio between the two main building dimensions the velocity profile decreases inside the cavity. This happens because the fluxes can, in the bidimensional case, completely enclose the building, ensuring better performances.

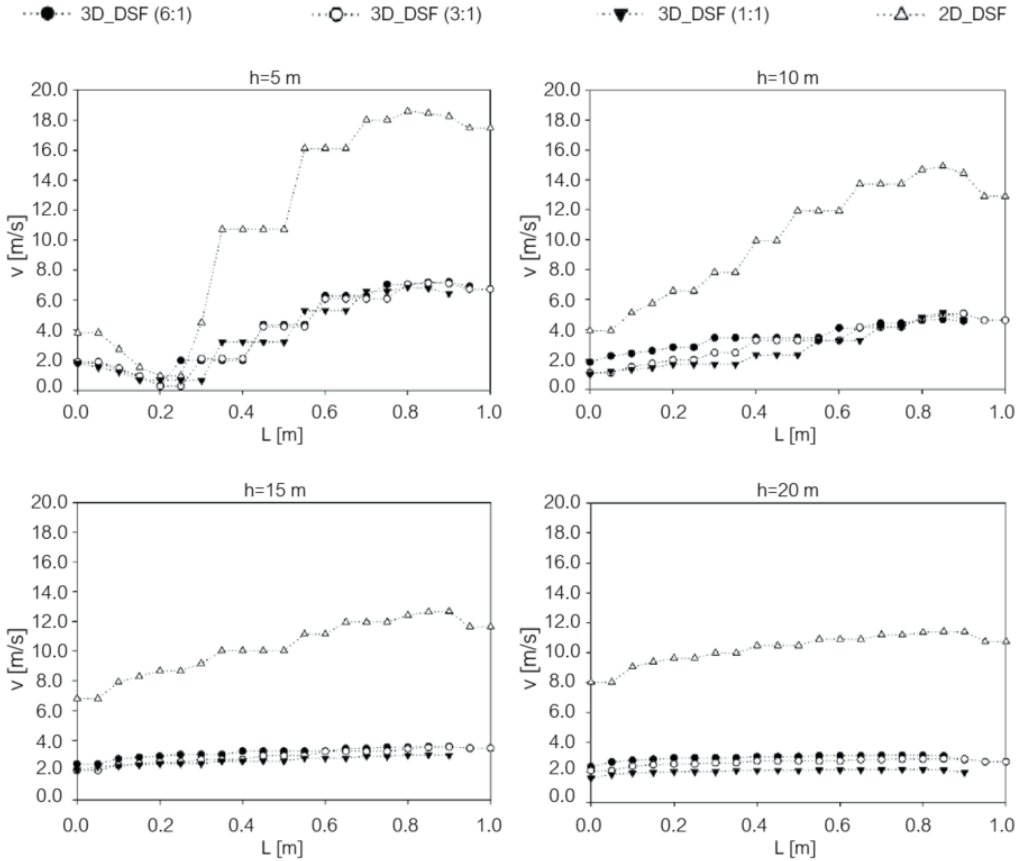


Figure 5.17. Velocity profile comparisons for each probe line and DSF model.

5.3.2. The Multi-Storey DSF Performance under Several Wind Directions

Further investigations are carried on for estimating the effects on the DSF performance due to various wind directions. The analyses conducted in the previous section, in fact, assume as boundary condition the wind coming from the south-east and impacting directly on the principal elevation of the Double Façade. The following evaluations, instead, consider the south (45°) and south-west (90°) wind, as schematised in Figure 5.18.

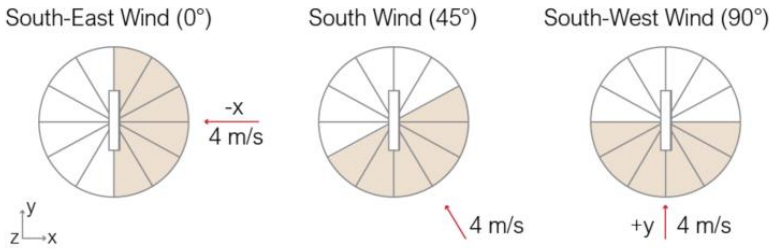


Figure 5.18. Wind directions evaluated for the here presented analyses.

The velocity profile estimated for each probe line and wind direction is plotted in Figure 5.19. According to the outputs, the highest velocities are reached inside the cavity when the wind diagonally impacts on the DSF. In fact, the 45° wind generates more intense ventilation of the cavity than the other two directions. The main reason for this phenomenon is related to its horizontal and upward components that are both strong. By comparing these contributions, respectively j and k , with the 45° and 0° wind (see Figure 5.20) it can be seen that the k -component is much more intense than the others for almost all probe lines. This finding also suggests that using only one wind profile could be not representative of the full condition.

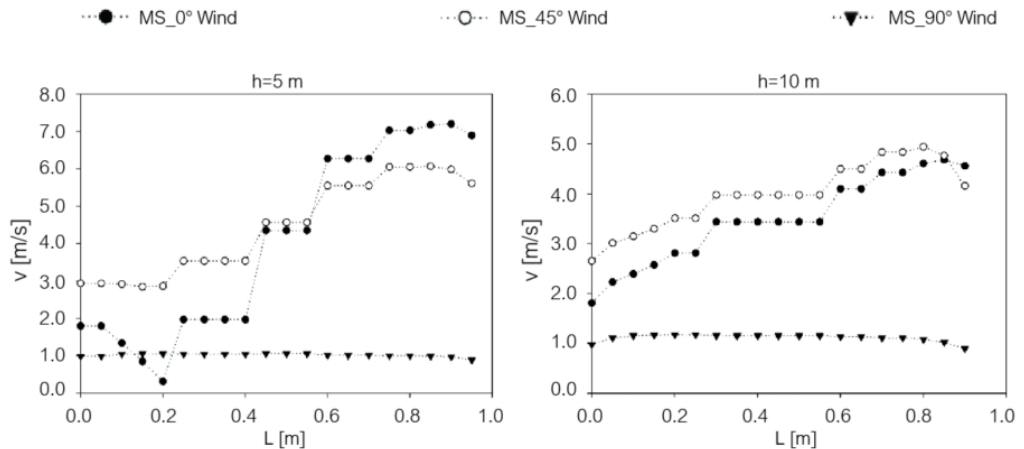


Figure 5.19. Velocity profile comparisons for each probe line and various wind directions.

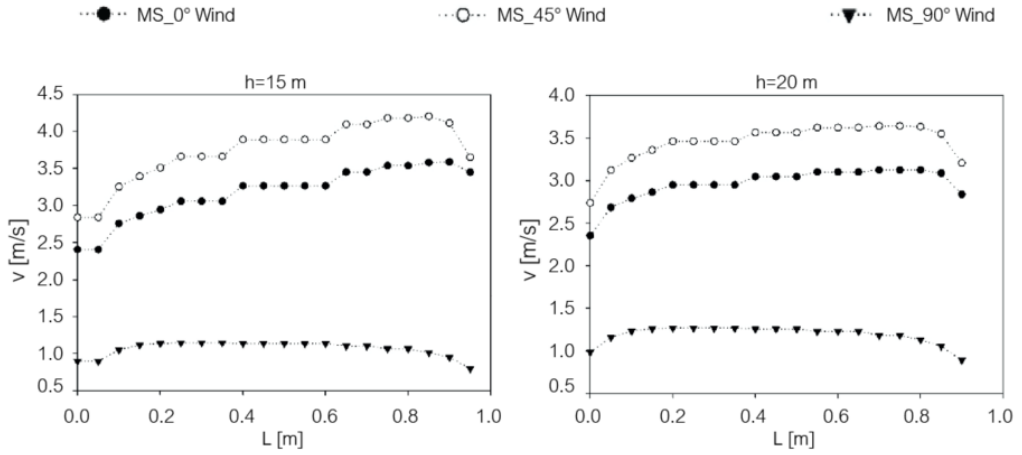


Figure 5.19. (Continued).

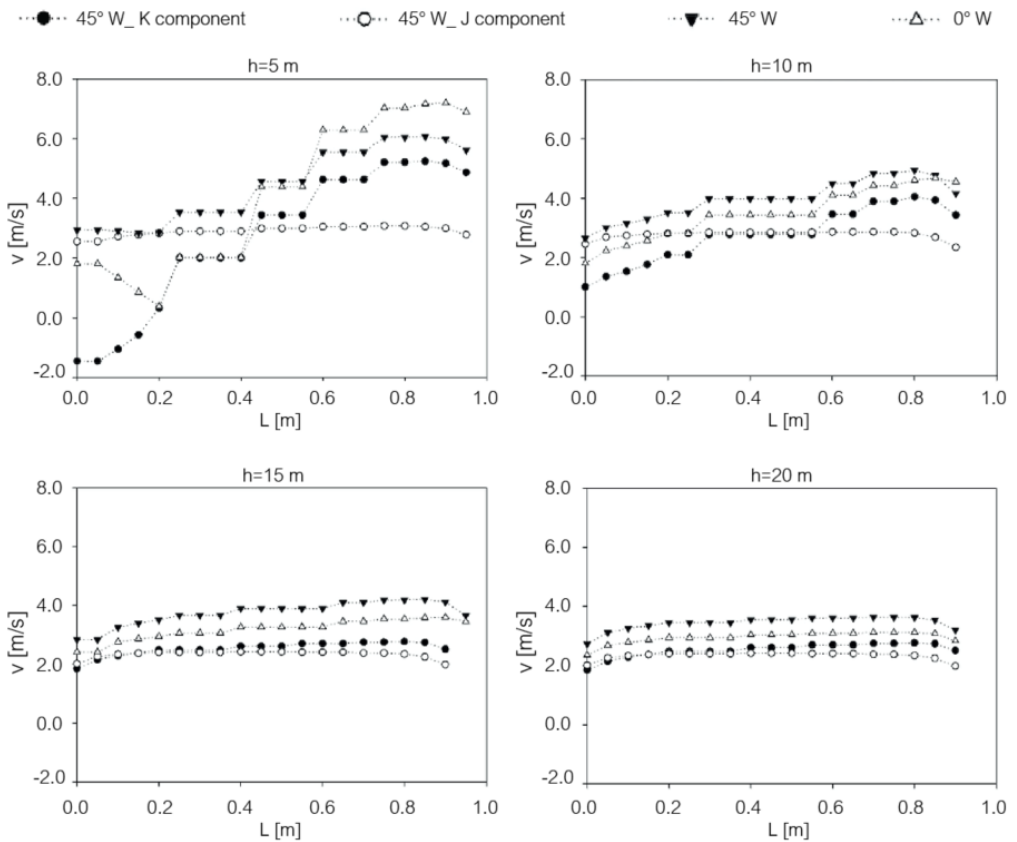


Figure 5.20. Velocity profile comparisons for each probe line and various wind directions with a focus on the k and j component for the 45° wind.

5.3.3. Modelling of the Corridor DSF

On the basis of the primary considerations and findings obtained from the Multi-Storey DSF model, more complex configurations are tested, and horizontal partitions are inserted at each floor for subdividing the cavity. The ventilation inside the DSF is ensured by the air which enters and exits the lateral surface of the outer skin. The modelled surfaces for both the domain and the building with the DSF system are plotted in Figure 5.21, whereas the surface and volume mesh generation are shown, respectively, in Figure 5.22 and Figure 5.23. The model is thus composed of 523398 cells with dimension equal to 0.25 m, chosen for being a good compromise between reduced analysis solving time and accuracy in the estimations.

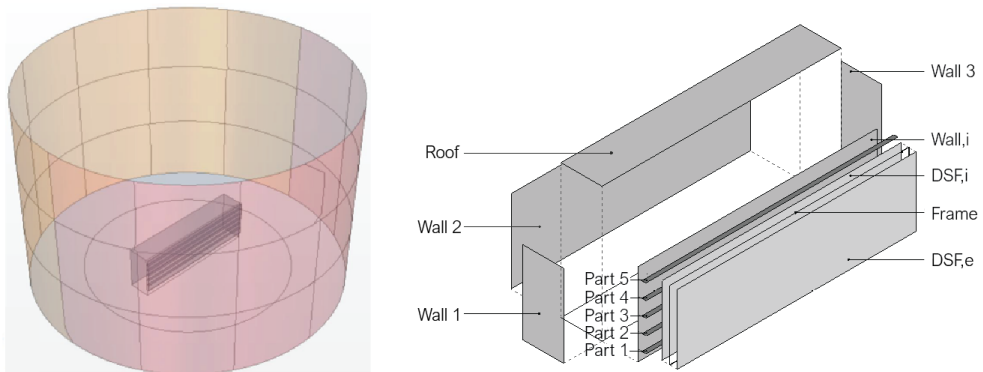


Figure 5.21. Components of the domain (left) and Corridor DSF Building (right).

The outputs plotted in Figure 5.24 represent the velocity profile, predicted for the previously described probe lines and referred to the chosen wind directions (0° , 45° and 90°). It is interesting to note that, as seen for the Multi-Storey configuration, the best ventilation rate is ensured by a wind which impacts with a specific angle on the DSF (45°). The worst ventilation is, instead, obtained with a south-east wind for which lower velocity values are estimated at different heights. The reason for such weak ventilation is the localisation of the inlet and outlet grills on the lateral elevation of the DSF, which is not directly invested by the wind action.

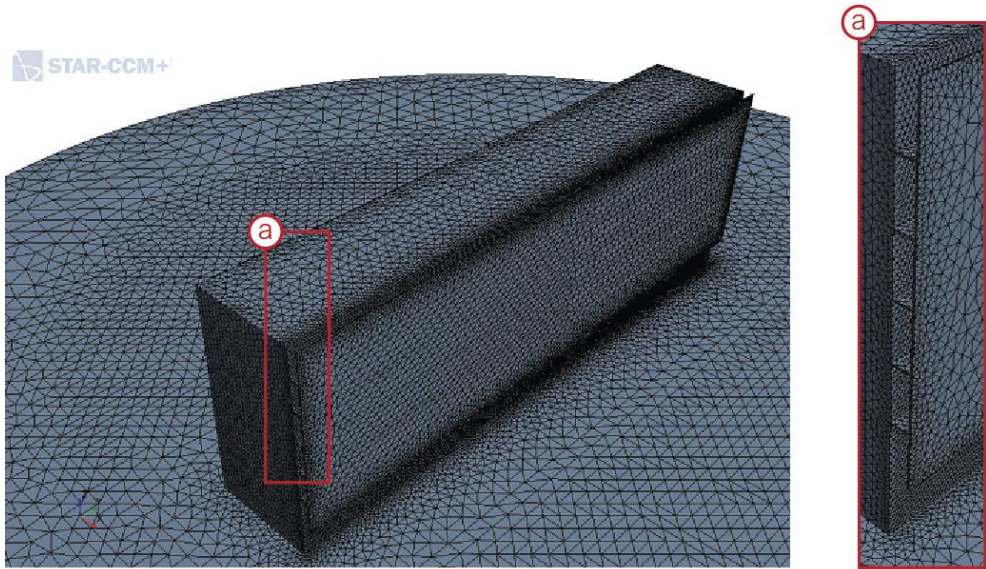


Figure 5.22. Surface meshes referred to the Corridor DSF configuration.

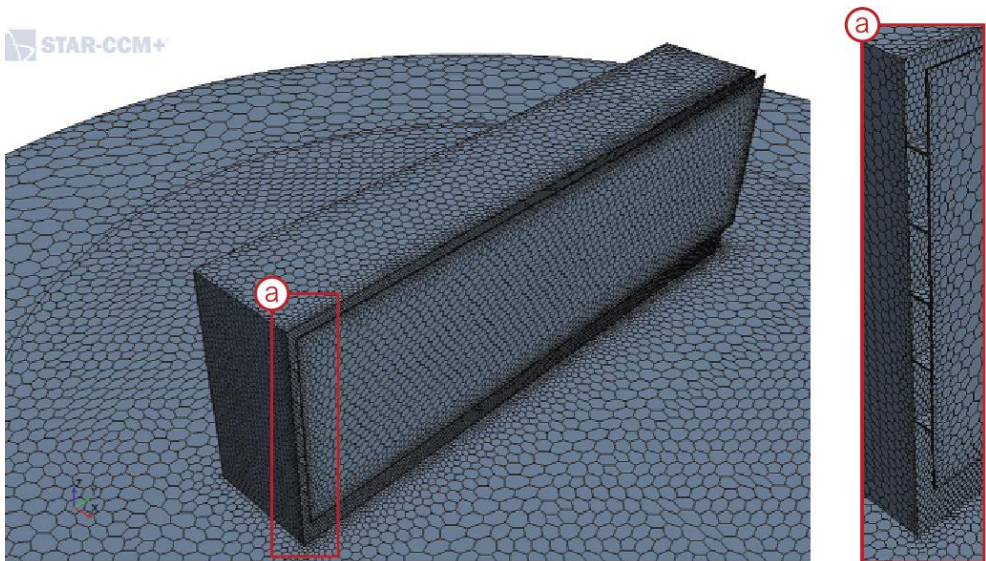


Figure 5.23. Volume meshes referred to the Corridor DSF configuration.

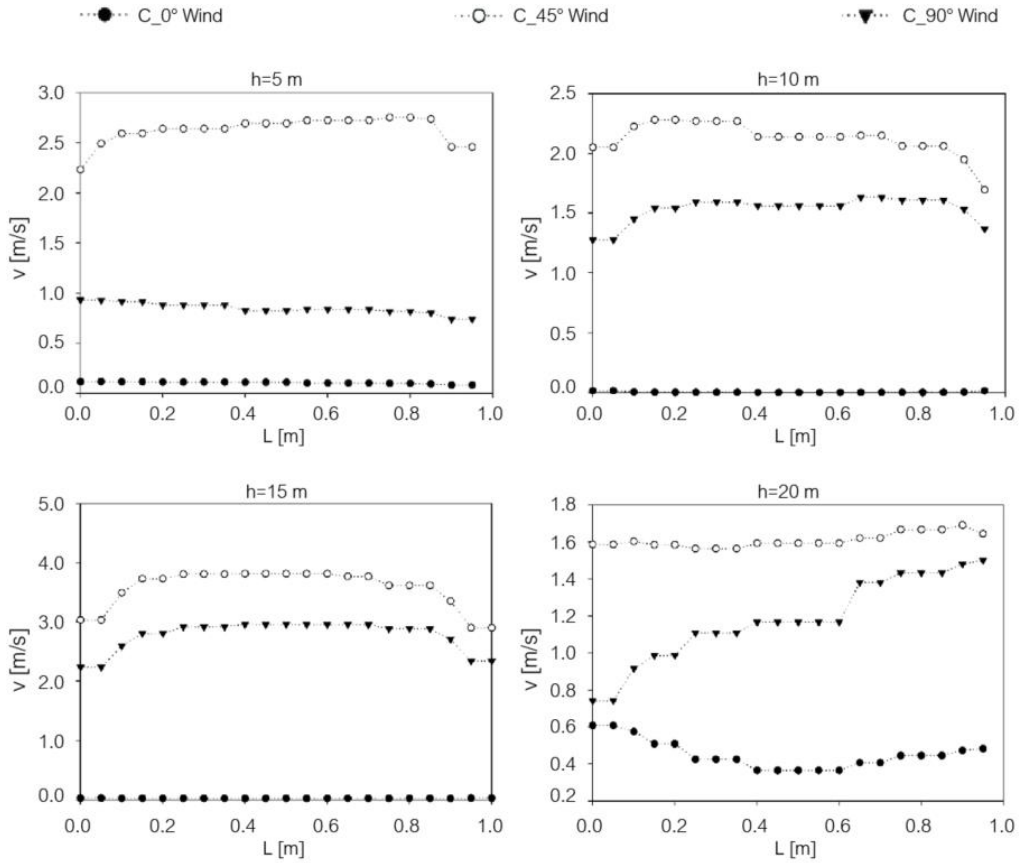


Figure 5.24. Velocity profile comparisons for each probe line and various wind directions estimated for the Corridor DSF.

5.3.4. Modelling of the Shaft-Box DSF

The third DSF to be evaluated is the Shaft-Box configuration. In this case, the cavity is subdivided into various air channels by inserting vertical partitions. The domain and building surfaces are schematised in Figure 5.25, whereas the surface and volume meshes are plotted, respectively, in Figure 5.26 and Figure 5.27. Also in this case, the mesh size is set equal to 0.25 m, thus obtaining a model made of 591785 cells.

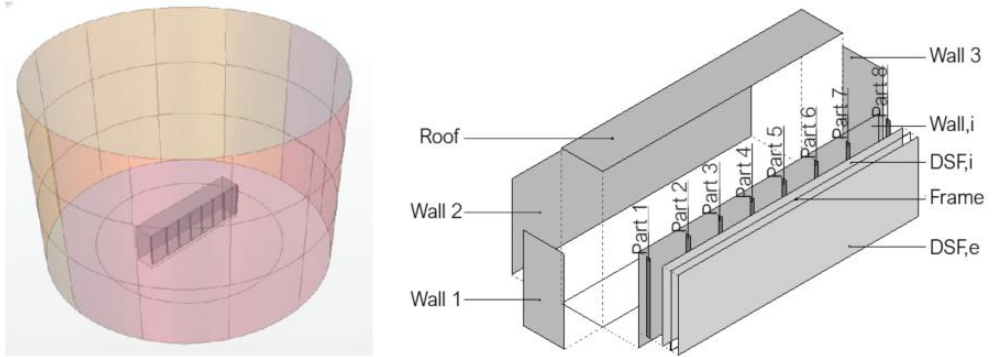


Figure 5.25. Components of the domain (left) and Shaft-Box DSF Building (right).

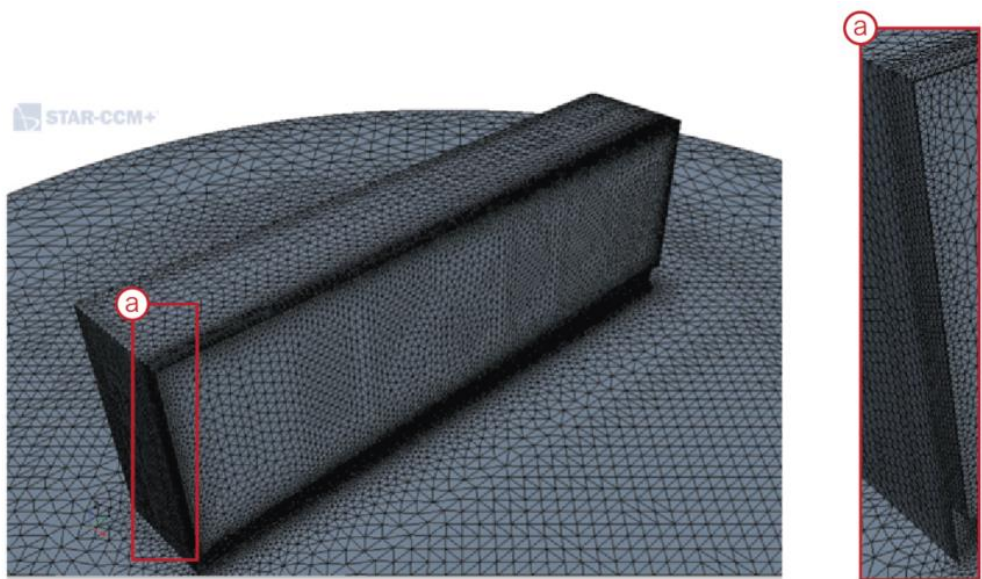


Figure 5.26. Surface meshes referred to the Shaft-Box DSF configuration.

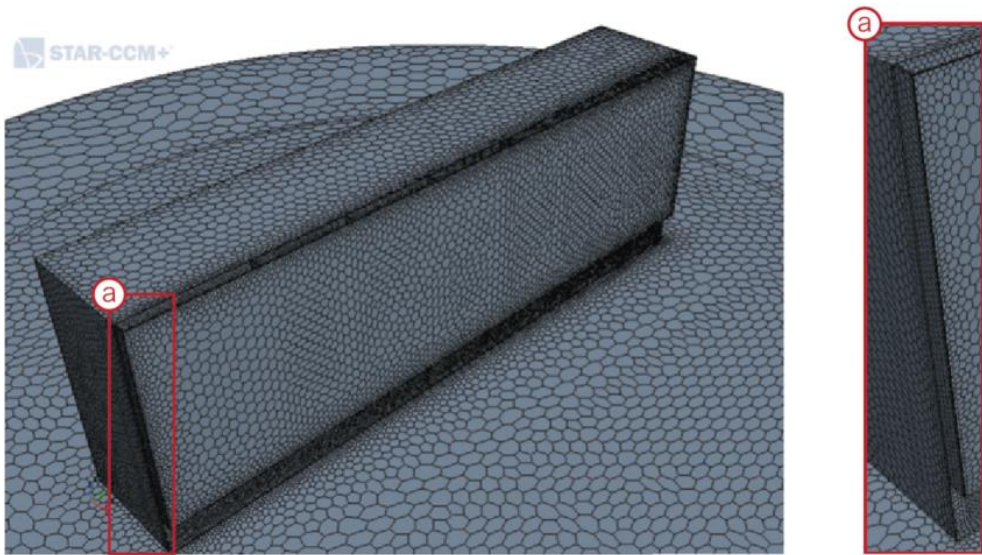


Figure 5.27. Volume meshes referred to the Shaft-Box DSF configuration.

Figure 5.28 shows the velocity profiles estimates for each probe line and various wind directions. According to the outputs, the highest velocities are predicted when the wind comes from the south, with an angle equal to 45° . It is important to underline that the plotted values are referred to estimations related to specific points, placed in the middle of the cavity and, for this reason, only able to describe the velocity profile in the plan.

For better understanding the Shaft-Box performance, further investigations are conducted for the vertical air channels into which the DSF is subdivided. As shown in Figure 5.29, each partition has variable pressure conditions. In the case of extremely low-pressure values, the air ventilation is very weak and associated with low velocities which are not accurately described by the graphs previously plotted. Moreover, the comparison between pressure and velocity levels underlines the generation of an air vortex along the later boundaries of each vertical channel, with the consequent flux acceleration and a decrement of its velocity close to the upper building edge where it exits the DSF.

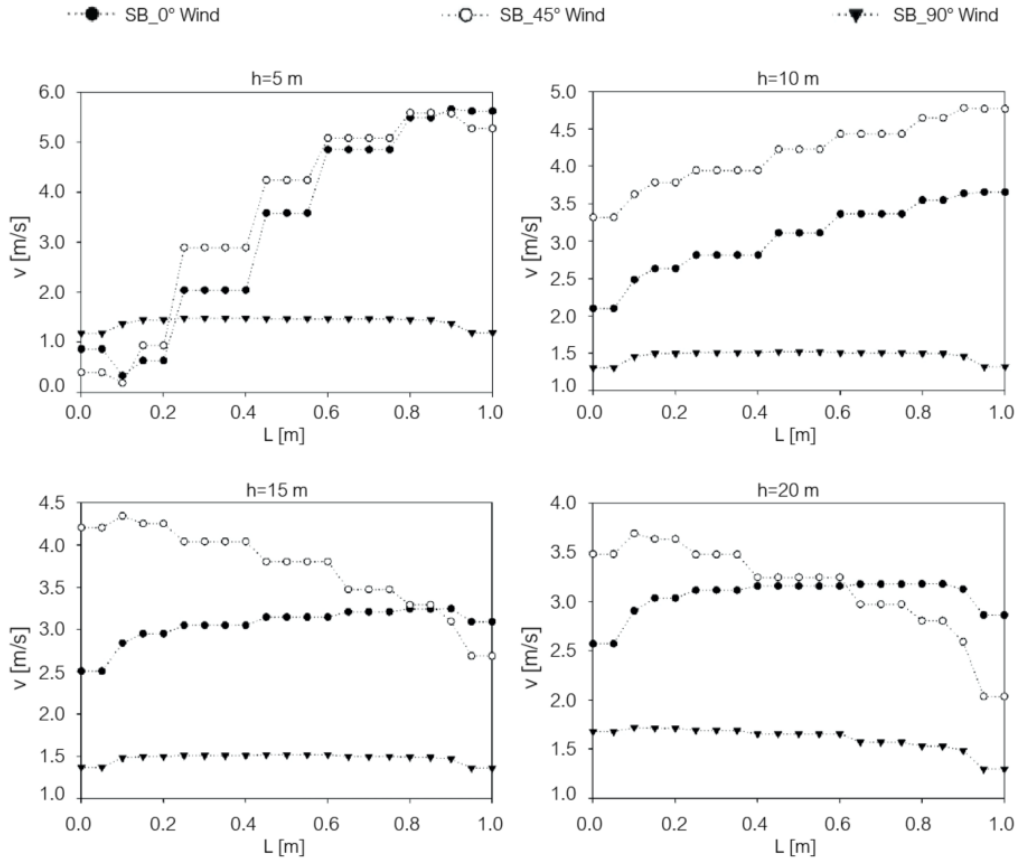


Figure 5.28. Velocity profile comparisons for each probe line and various wind directions referred to the Shaft-Box DSF.

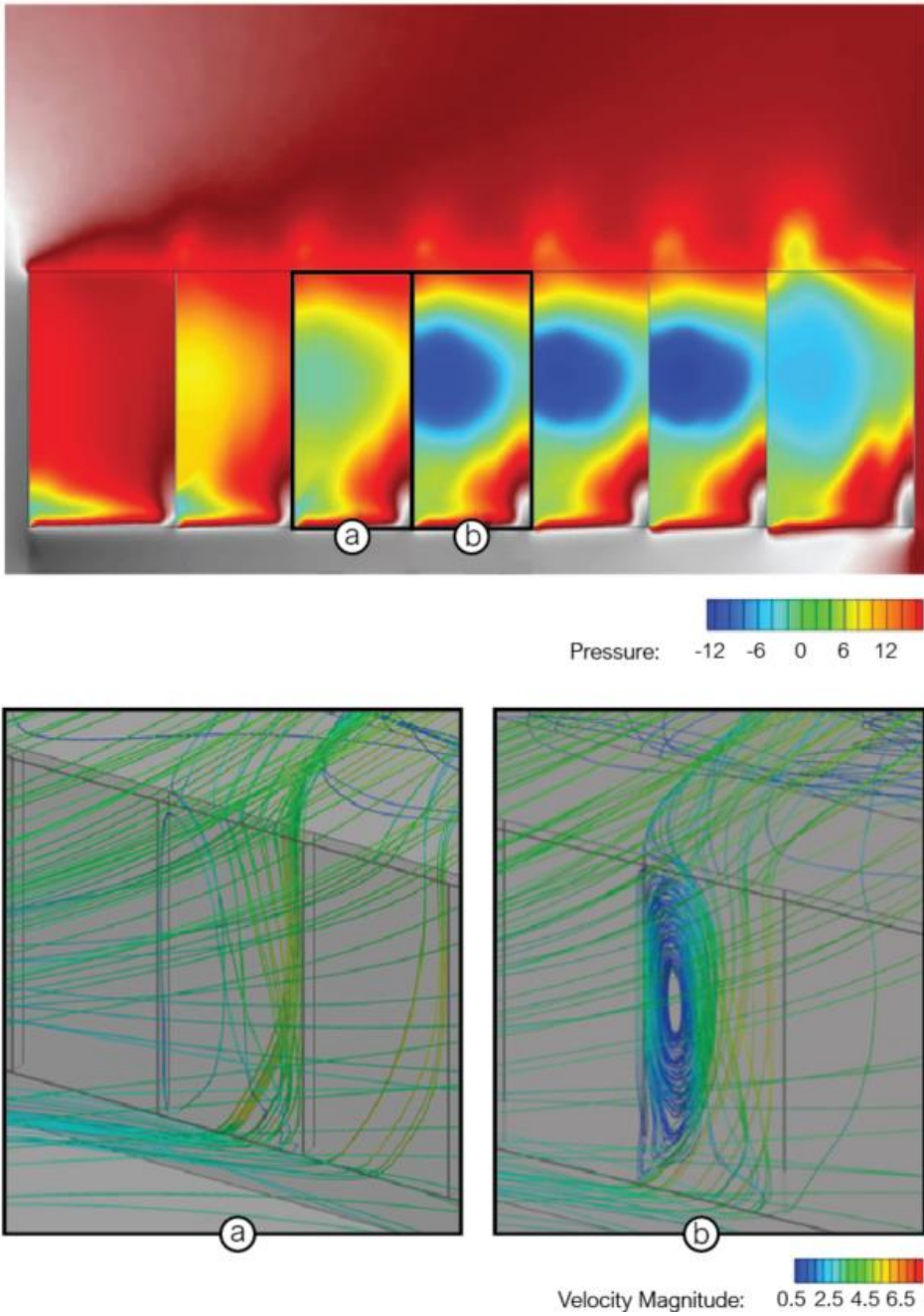


Figure 5.29. Pressure levels and velocity magnitudes estimated for the DSF air channels.

5.3.5. DSF Performance Comparisons

Once the fluid dynamic behaviour of each Double Skin Façade has been evaluated, comparisons between their performances are described in the current paragraph. For each DSF configuration, the velocity profile is depicted from Figure 5.30 to Figure 5.35, on the basis of different wind directions.

Comparing the outputs obtained when the wind impacts directly on the DSF (see Figure 5.30), the Corridor typology shows the lowest velocity values, becoming the less effective solution. In contrast, the Shaft-Box configuration presents the creation of air vortices in correspondence to the inlet openings. This happens especially along the separation surfaces, where the pressure values are lower because of friction losses. Comparing the velocity magnitudes estimated for a wind orthogonal to the DSF elevations, the best configuration is the Multi-Storey, as it can be observed in Figure 5.31.

The Corridor DSF confirms to be the worst even in case of wind from the south (45°) (see Figure 5.32) for which a weakly ventilation is estimated inside the cavity for all the selected heights. The Multi-Storey and the Shaft-Box configurations, instead, show similar performances, ensuring the good ventilation of the cavity. Moreover, Figure 5.33 depicts the vortex distributions with a 3D representation for underling the air movements inside and around the DSF cavity. It is interesting to see the flow separation problems that characterise the Shaft-Box DSF, visible only with a 3D representation.

The last case, which evaluates the effect on DSFs of a wind coming from the south-west (90°), is plotted in Figure 5.34. In this case, the Corridor DSF shows an intense cavity air movement, and the Shaft-Box confirms to be able to ensure the best ventilation of the cavity. To better understand its behaviour, stream traces are plotted in Figure 5.35. They underline the tendency of the air fluxes of creating a flow separation area above the upper edge of the building.

Chapter 5

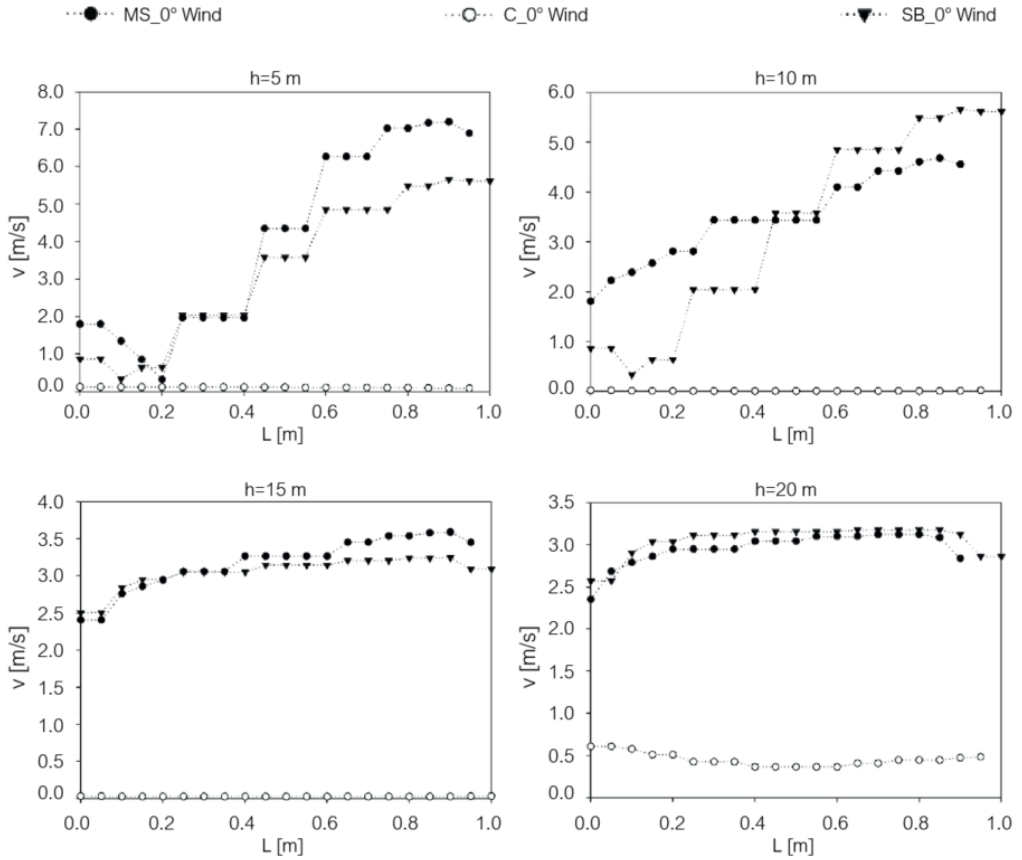


Figure 5.30. Velocity profile comparisons for each probe line various DSF configuration due to a south-east wind (0°).

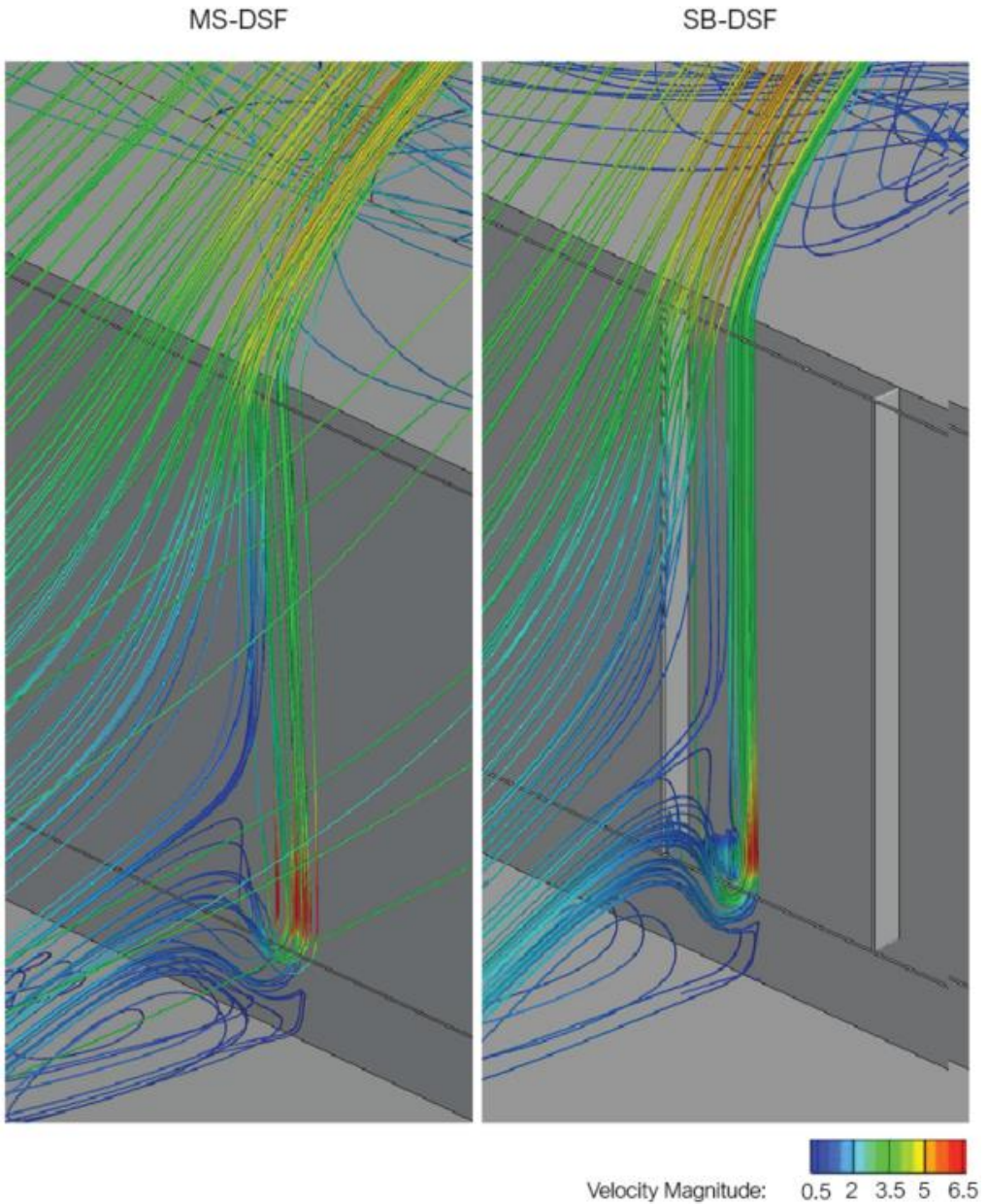


Figure 5.31. Representation of the stream traces estimated for the Multi-Storey, and Shaft-Box DSF referred to the south-east wind.

Chapter 5

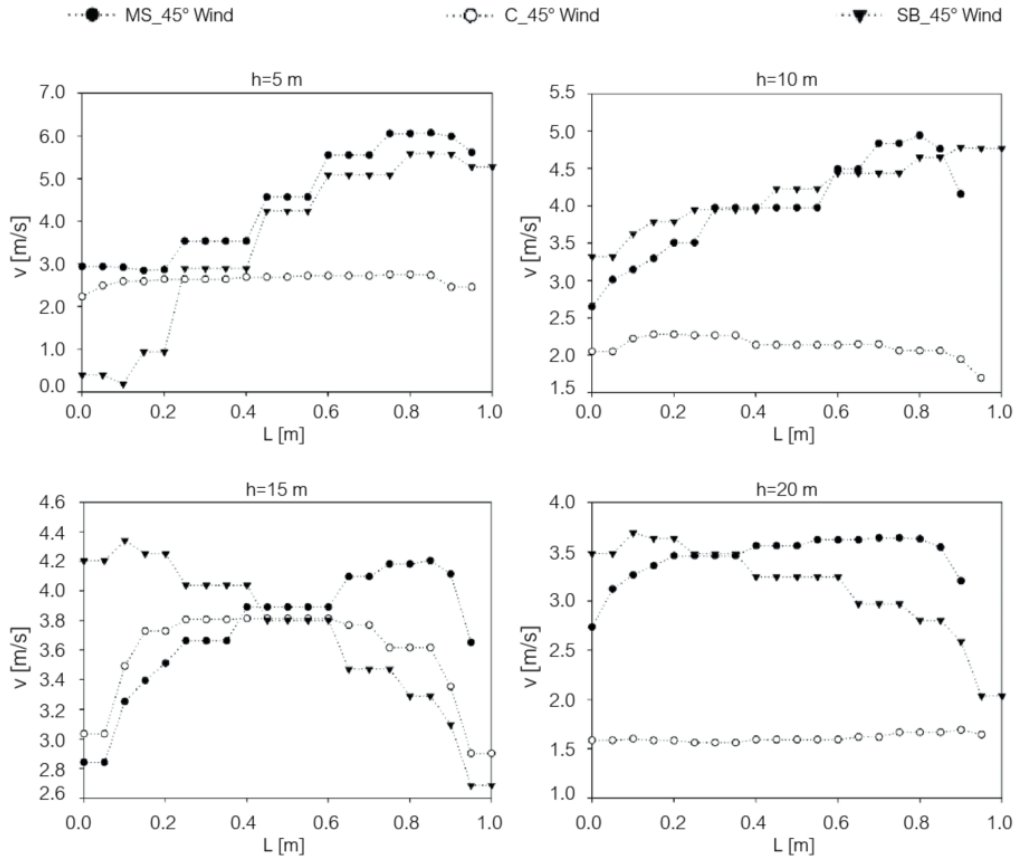


Figure 5.32. Velocity profile comparisons for each probe line various DSF configuration due to a south wind (45°).

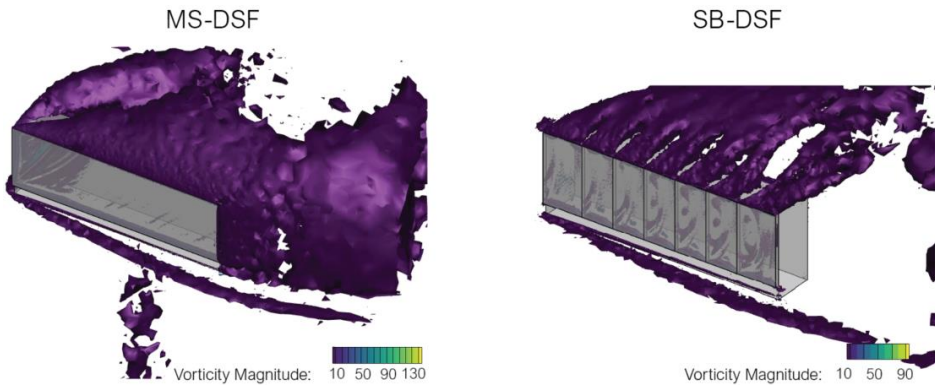


Figure 5.33. Vorticity representation for the Multi-Storey and Shaft-Box DSF associated with the south wind.

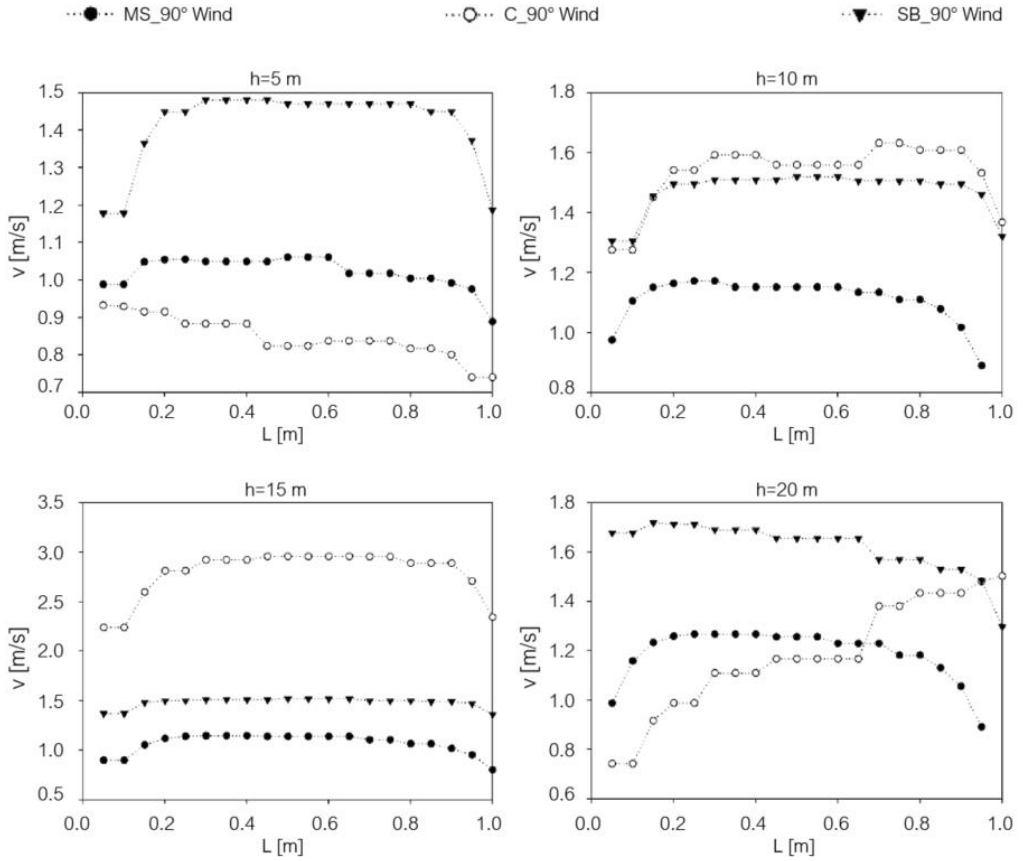


Figure 5.34. Velocity profile comparisons for each probe line various DSF configuration due to a south-west wind (90°).

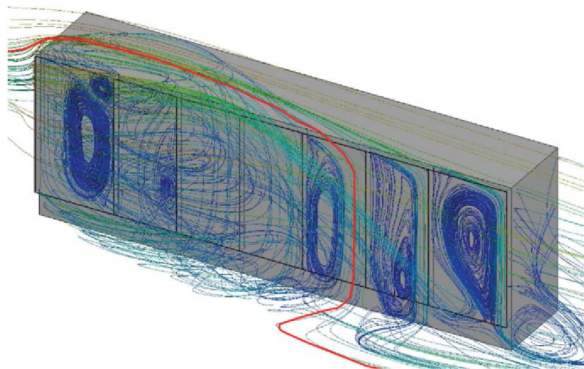


Figure 5.35. Representation of the stream traces inside the Shaft-Box channels due to a south-west wind.

5.4. Modelling of the Reference Building with DSF on Two Elevations

A different stage of the CFD study involves the evaluation of the fluid dynamic performance ensured by the insertion of the DSF system on two different elevations. For this set of simulations, the shape of the building, previously modelled as a simple prism, is enriched by details, as the presence of balconies on the north-west elevation and the pitched roof. The second DSF is inserted on the north-west façade, and a 2 m cavity depth is considered for taking into account the presence of balconies that could obstacle the airflow. Also in this case, various wind directions are adopted for estimating the air velocity inside the cavity, referred to probe lines placed at 5 m, 10 m, 15 m and 20 m (like for the other models). Considering the insertion of the second Double Façade, the north-west wind direction (180°) is added to the previously evaluated ones. Figure 5.36 synthesises the wind directions selected for the following comparisons.

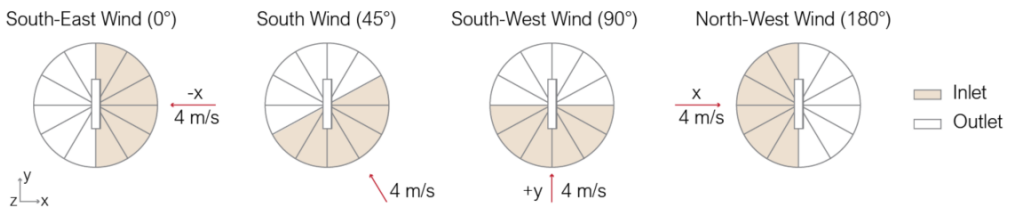


Figure 5.36. Wind directions evaluated for the here presented simulations.

The main components of the domain and the building with DSFs are plotted in Figure 5.37, whereas Figure 5.38 and Figure 5.39 depict, respectively, the surface and volume meshes. The mesh size defined for the model is 0.25 m, selected on the basis of previous analyses. Thus, the model is subdivided into 1003757 cells.

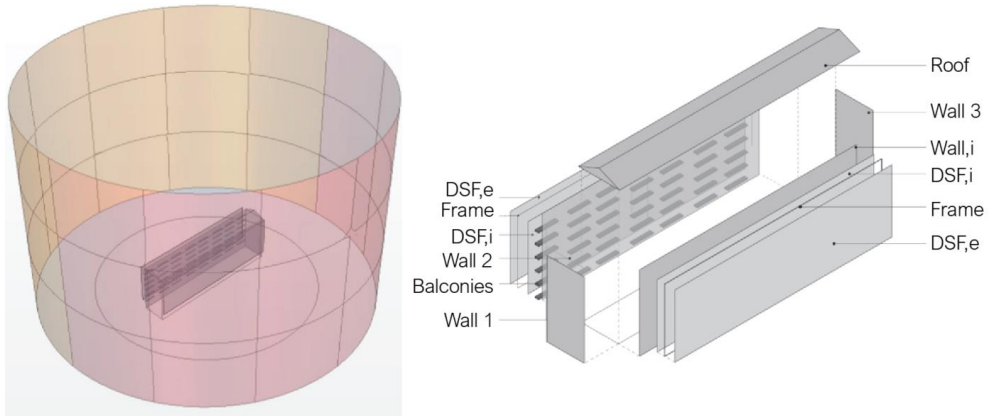


Figure 5.37. Components of the domain (left) and DSF Building (right).

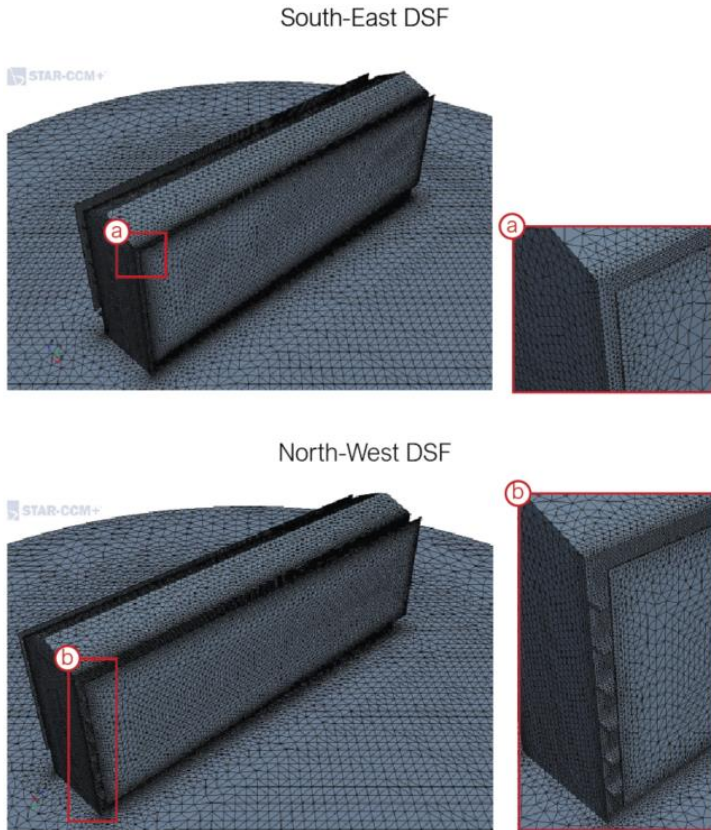


Figure 5.38. Surface meshes referred to the more detailed building with DSF on two elevations.

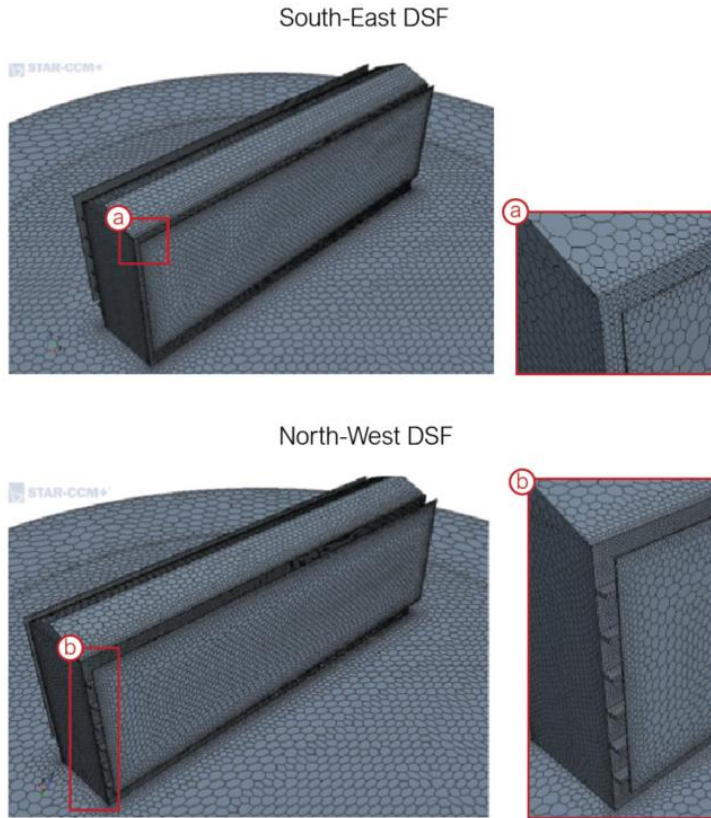


Figure 5.39. Volume meshes referred to the more detailed building with DSF on two elevations.

First, the effectiveness of the north-west DSF is investigated, and its performance is tested considering the above-mentioned wind directions, plotted in Figure 5.40. Then, the behaviour of the two DSFs is compared and depicted in the same graphs, evaluating a wind that impacts, alternatively, on one elevation and the other.

According to the obtained results, the north-west façade allows the proper ventilation of the cavity when the wind impacts directly on its elevation, with an angle equal to 180° . In this case, in fact, the velocity profile estimated for the various probe lines assume higher values than those expected with other directions. Such behaviour underlines that the effectiveness of a DSF system is strictly connected to the direction of the wind, and, for ensuring good performances, it should be

designed according to the local climatic conditions. Moreover, the outputs confirm that a multi-layer façade can be a useful intervention for encouraging the free cooling of existing buildings.

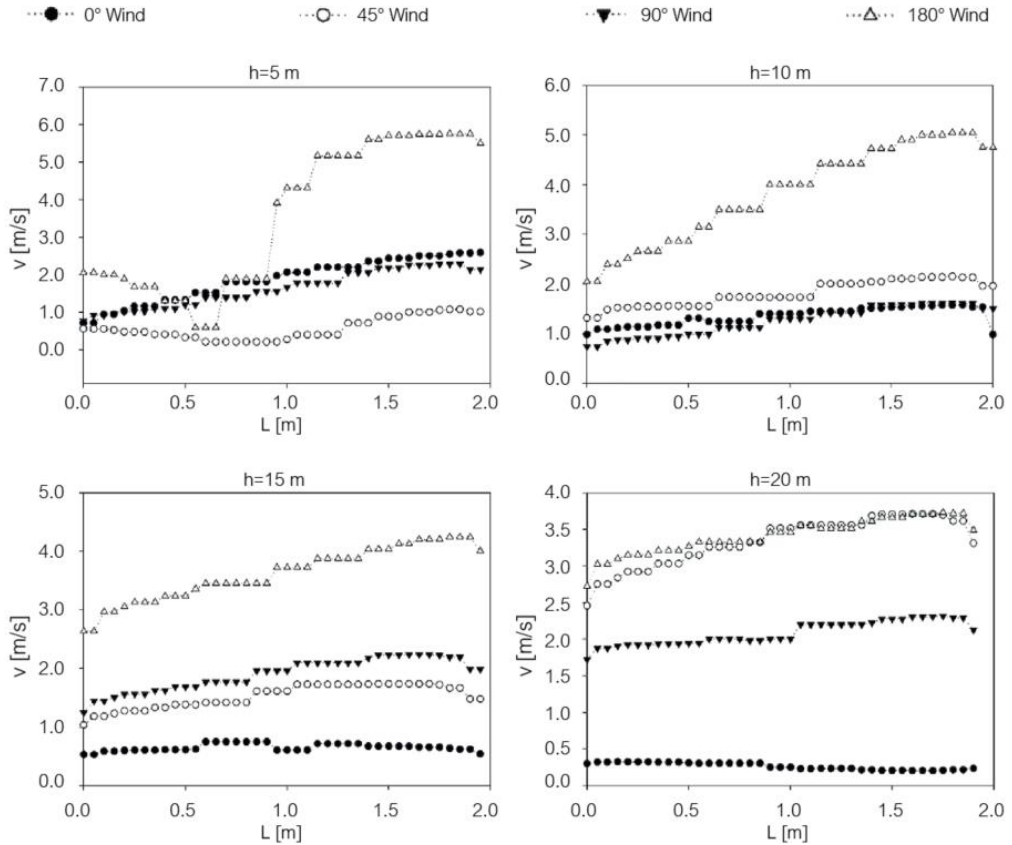


Figure 5.40. The velocity profile, referred to various probe lines and wind directions, for the north-west DSF placed on the real building shape.

A second evaluation is done comparing the behaviour of each DSF, for the south-east (0°) and north-west (180°) wind, as schematised in Figure 5.41. The results, depicted in Figure 5.42, underline that, when the DSF is downwind, the ventilation of the cavity is extremely weak, without benefits on the building cooling side. A different situation is, instead, estimated when the DSF is upwind. The natural ventilation of the cavity, in fact, is profoundly encouraged when the wind impacts directly on it, and this aspect is particularly crucial during the summertime,

avoiding DSF overheating. Moreover, the outputs show that the presence of the balconies on the north-west elevation does not affect the effectiveness of the DSF.

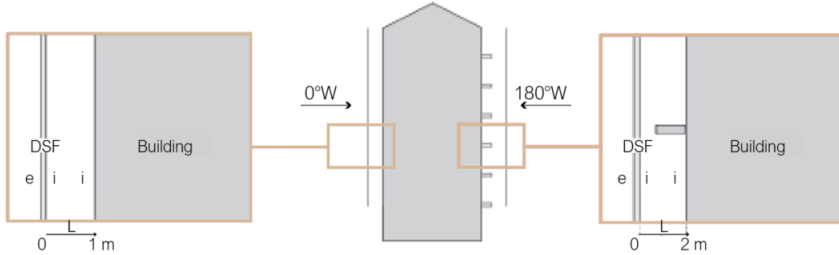


Figure 5.41. Wind directions investigated for testing the effectiveness of the south-east and north-west DSF.

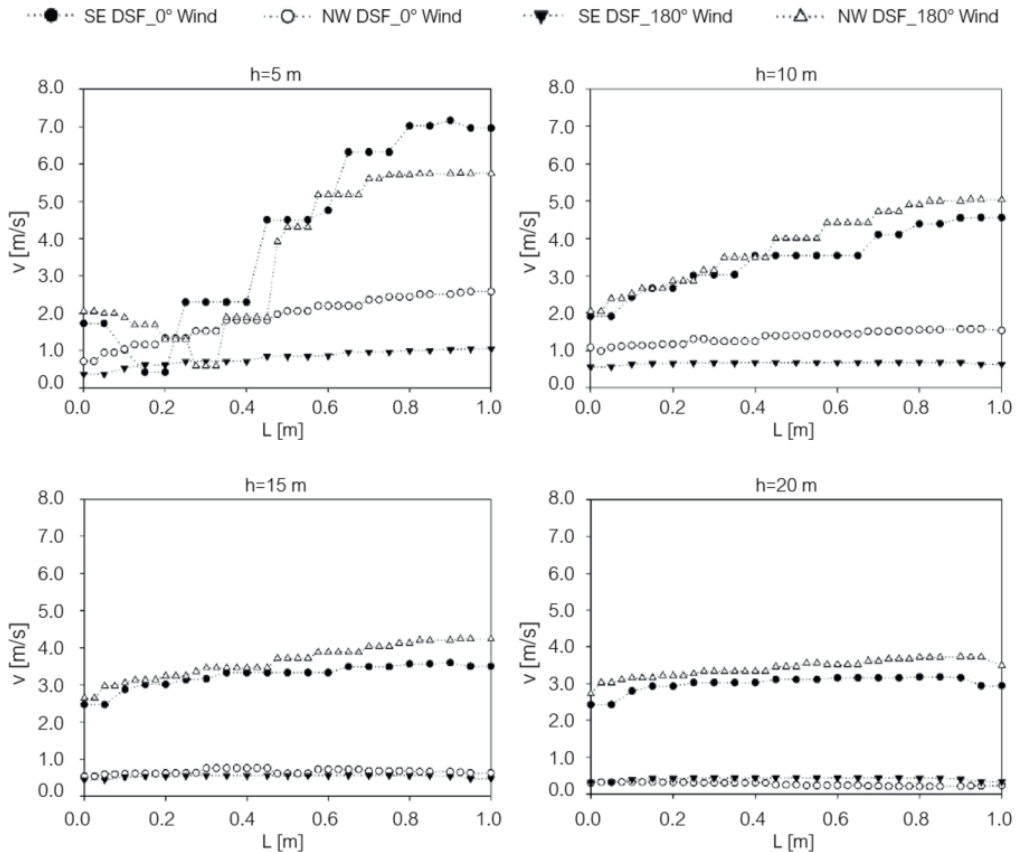


Figure 5.42. The velocity profile, referred to various probe lines and wind directions, for the north-west and south-east DSF placed on the real building shape.

5.5. Evaluation of Optimised DSF Shapes

The last phase of the CFD modelling is centred on the definition and evaluation of optimised DSF shapes, able to improve the fluid dynamic behaviour of these systems. Thus, more aerodynamic profiles are conceived, and multiple inlet/outlet grills are inserted for encouraging the cavity ventilation and reducing friction losses. The effectiveness of the suggested solutions is evaluated with a south-east wind, which impacts directly on the DSF. In detail, the following solutions, schematised in Figure 5.43, are taken into account:

- The insertion of a DSF, on the south-east elevation, with smooth edges, both at the bottom and the top (Case 1).
- The insertion of a DSF with upper and lower smooth edges, on the south-east elevation, with building rounded corners (Case 2).
- The insertion of multiple DSF inlet and outlet grills on Case 2 (Case 3).
- The insertion of Case 3 on both south-east and north-west elevation.

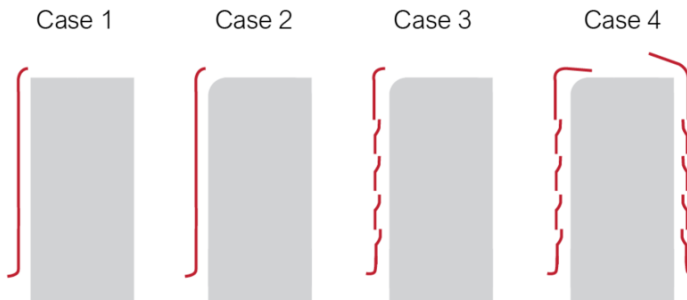


Figure 5.43. The here-evaluated optimised shapes for better DSF performances.

The first two models to be elaborated and compared are Case 1 and Case 2. Figure 5.44 to Figure 5.46 show the components and the surface and volume meshes referred to Case 1, whereas the same model inputs related to Case 2 are depicted from Figure 5.47 to Figure 5.49.

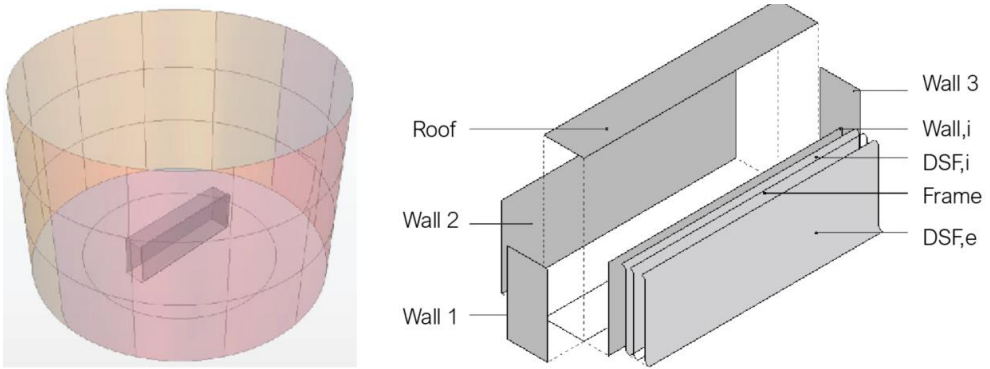


Figure 5.44. Components of the domain (left) and DSF Building (right) for Case 1.

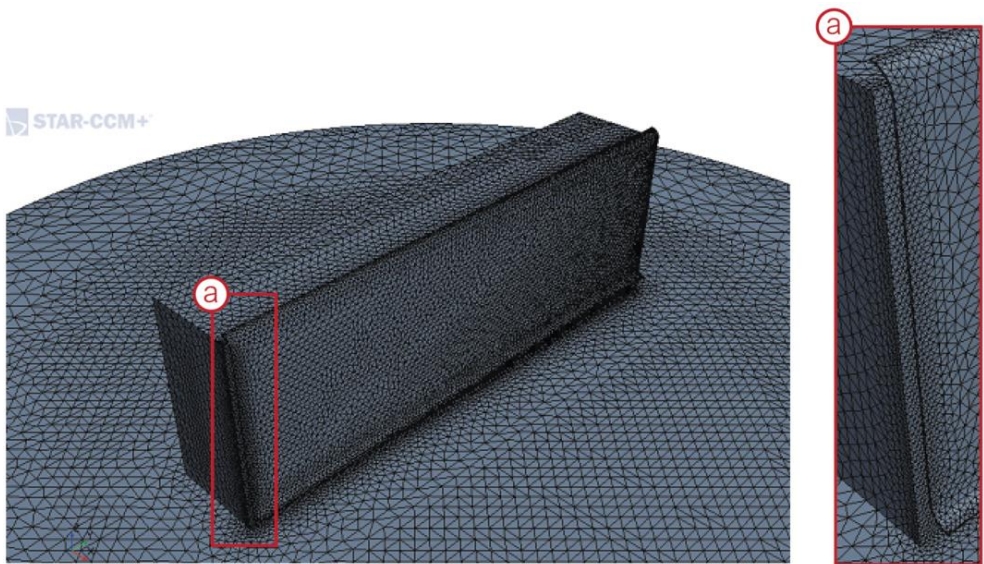


Figure 5.45. Surface meshes referred to Case 1.

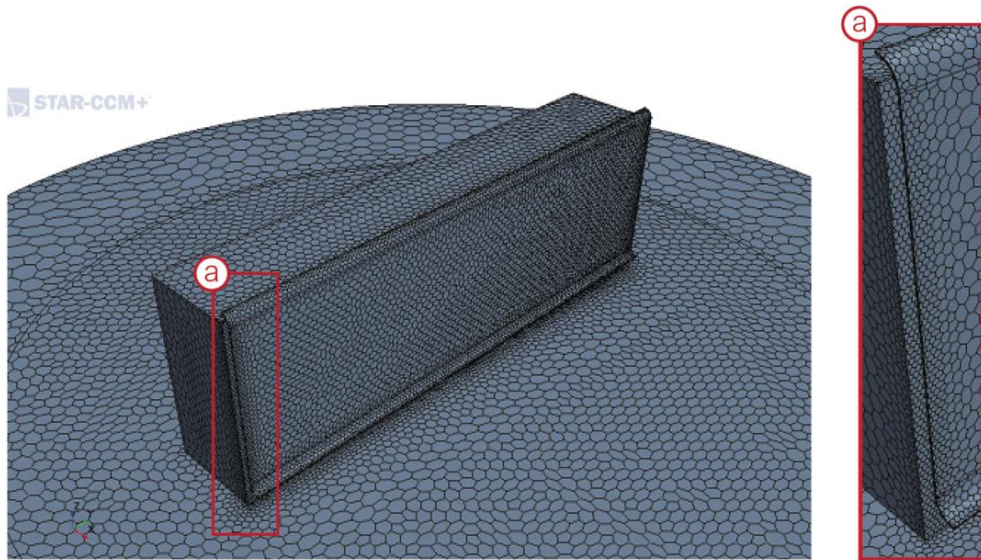


Figure 5.46. Volume meshes referred to Case 1.

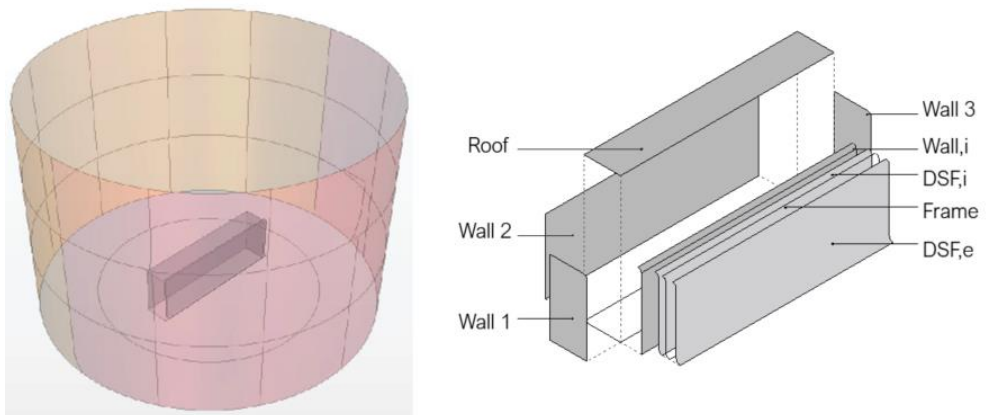


Figure 5.47. Components of the domain (left) and DSF Building (right) for Case 2.

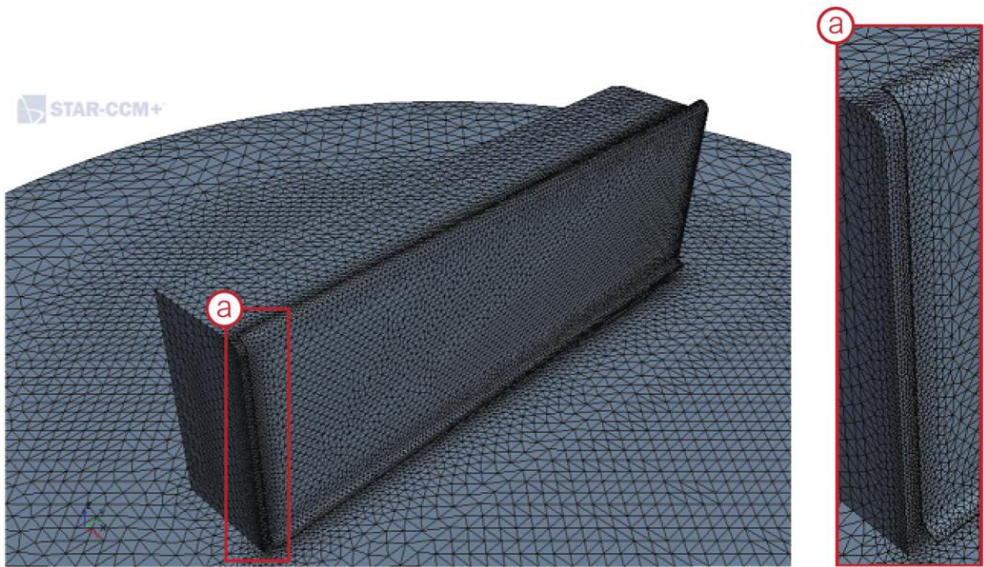


Figure 5.48. Surface meshes referred to Case 2.

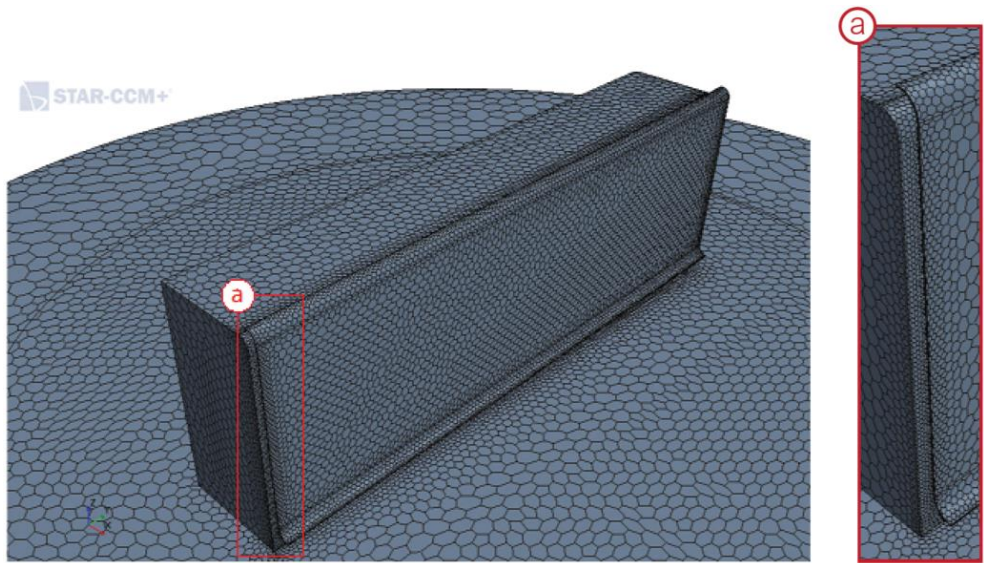


Figure 5.49. Volume meshes referred to Case 2.

The obtained results, expressed in terms of velocity magnitude for several DSF heights, are plotted in Figure 5.51. Comparisons are made with the already analysed Multi-Storey DSF in order to estimate the improvements achievable with

more aerodynamic shapes (see Figure 5.50). The outputs underline that the presence of rounded edges for both the DSF and the building façade allows reaching higher velocities if compared to standard configurations. The reduction of friction losses, in fact, increments the ventilation of the cavity that becomes much more intense when rounded corners are adopted for both building and Double Façade surfaces. These considerations are also confirmed by the investigation of the pressure levels and velocity magnitudes shown, respectively, in Figure 5.52 and Figure 5.53.

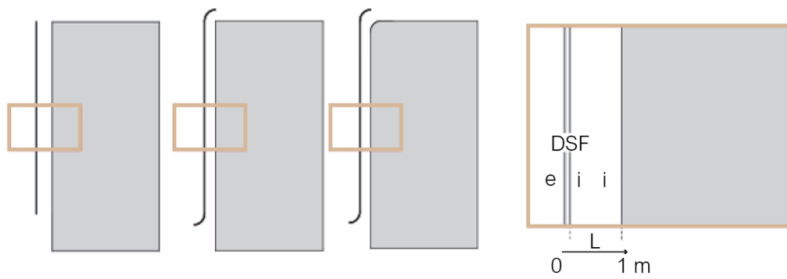


Figure 5.50. Schematisation of the DSF models selected for the comparisons.

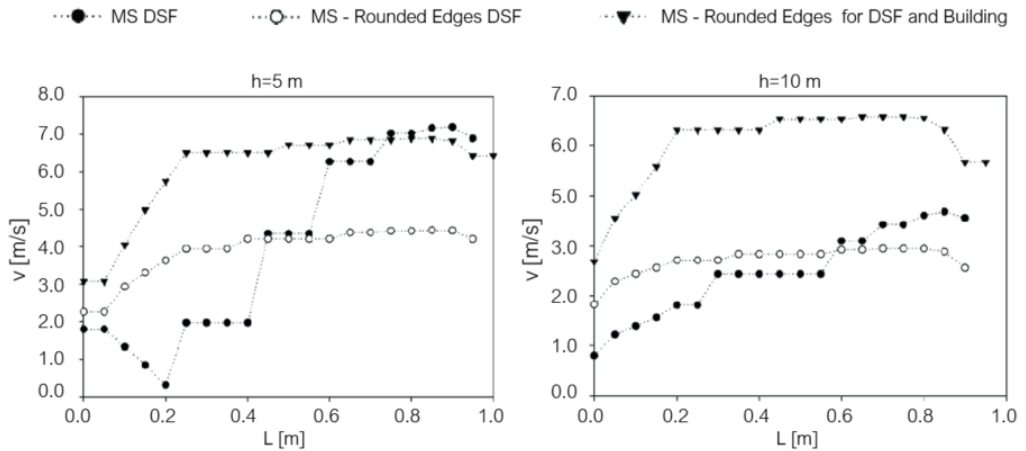


Figure 5.51. The velocity profile, referred to various probe lines, for the standard and optimised DSF (Case 1 and Case2).

Chapter 5

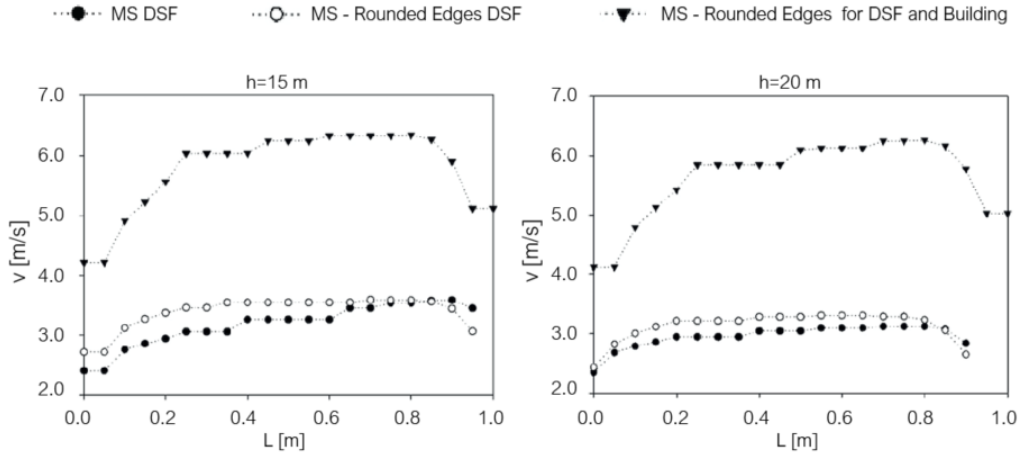


Figure 5.51. (Continued).

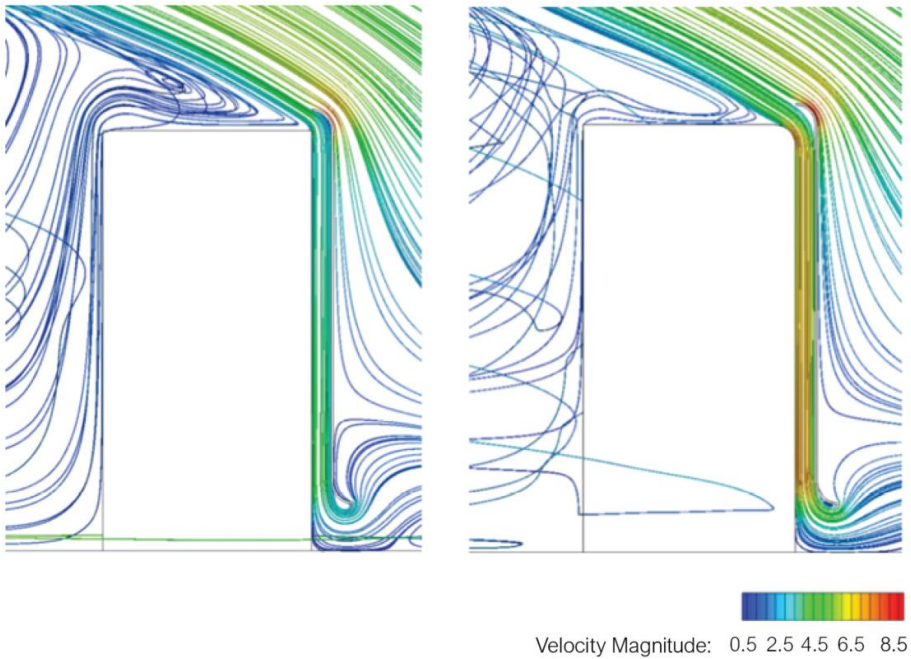


Figure 5.52. Velocity magnitudes estimated for Case 1 (left) and Case 2 (right).

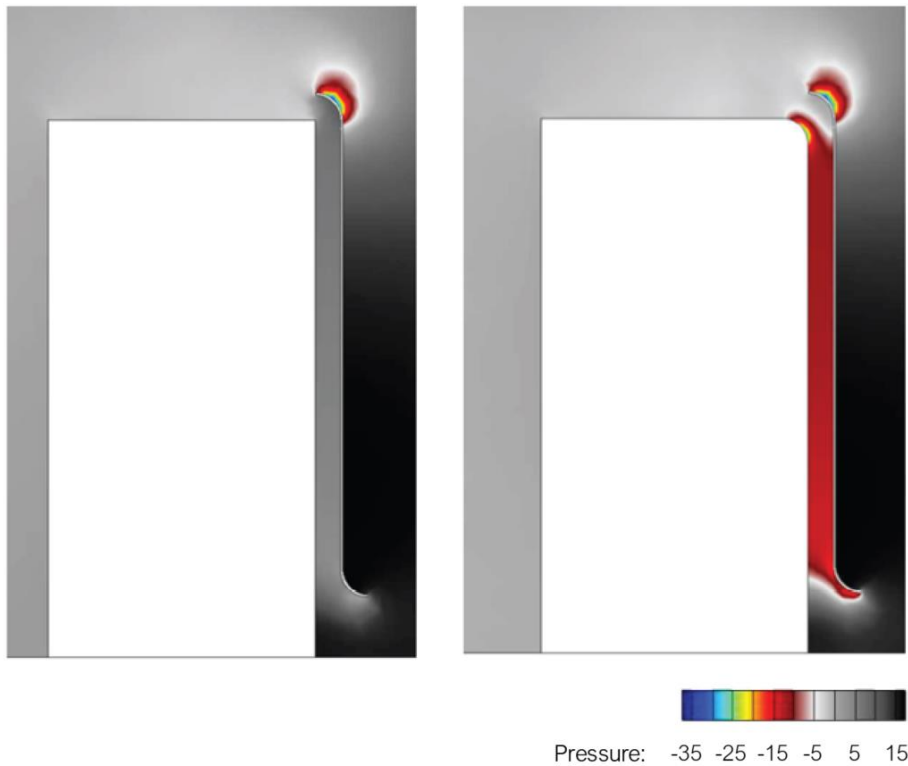


Figure 5.53. Pressure levels estimated for Case 1 (left) and Case 2 (right).

The last two improved solutions to be investigated consider the insertions of multiple grills along the elevation of the outer layer of the DSF to encourage the cavity ventilation. For better estimations, the building is subdivided into various floors that communicate with the cavity for the ventilation of the occupied spaces. Thus, the last two models to be elaborated and compared are Case 3 and Case 4. Figure 5.54 to Figure 5.56 show the components and the surface and volume meshes referred to Case 3, whereas the same model inputs related to Case 4 are depicted from Figure 5.57 to Figure 5.59. Considering the accuracy of these models, the number of cells into which they are subdivided is higher than the previous cases. In fact, 3965961 and 5450085 are the cells for, respectively, Case 3 and 4.

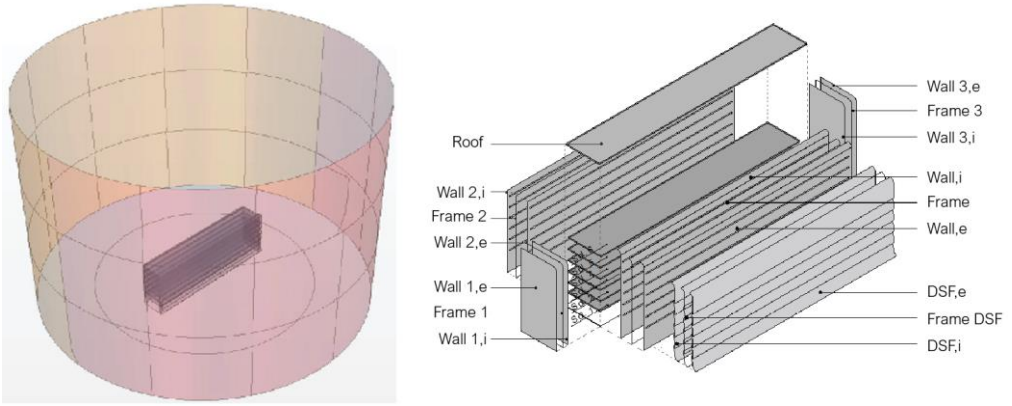


Figure 5.54. Components of the domain (left) and DSF Building (right) for the Case 3.

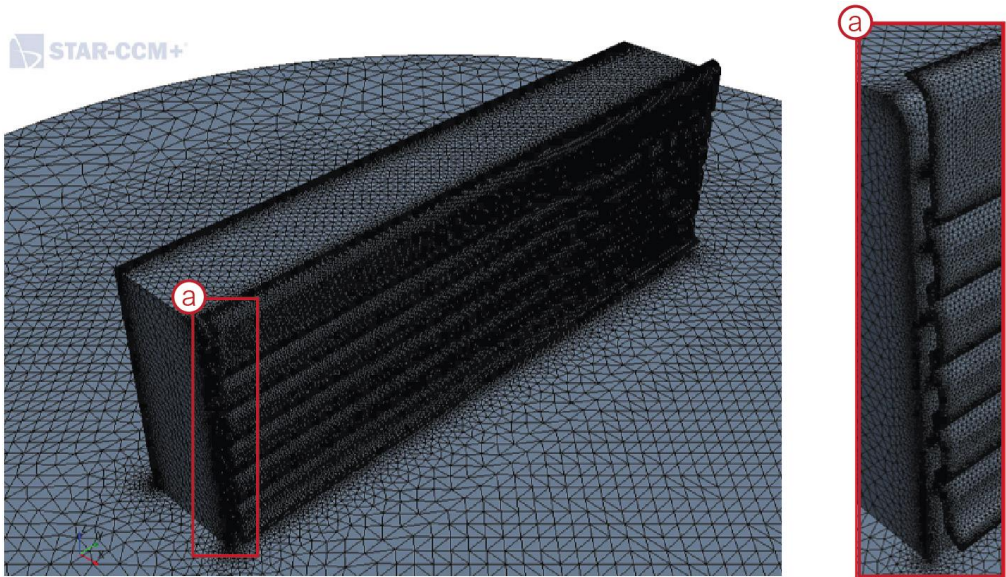


Figure 5.55. Surface meshes referred to the Case 3 model.

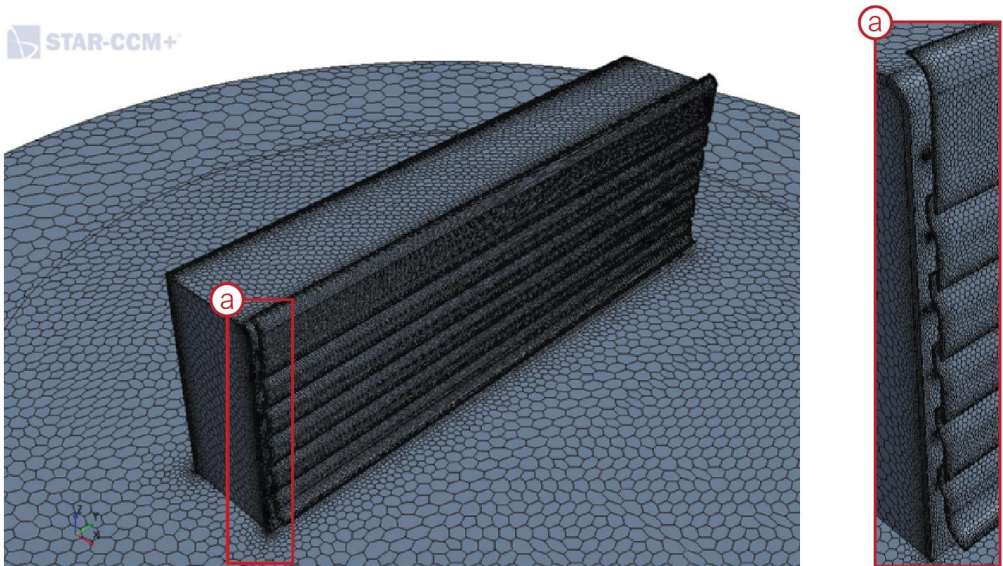


Figure 5.56. Volume meshes referred to the Case 3 model.

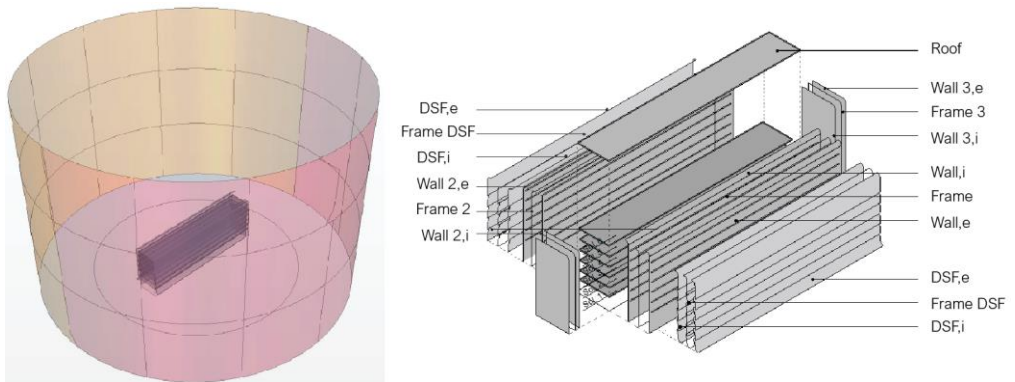


Figure 5.57. Components of the domain (left) and DSF Building (right) for the Case 4.



Figure 5.58. Surface meshes referred to the Case 4 model.

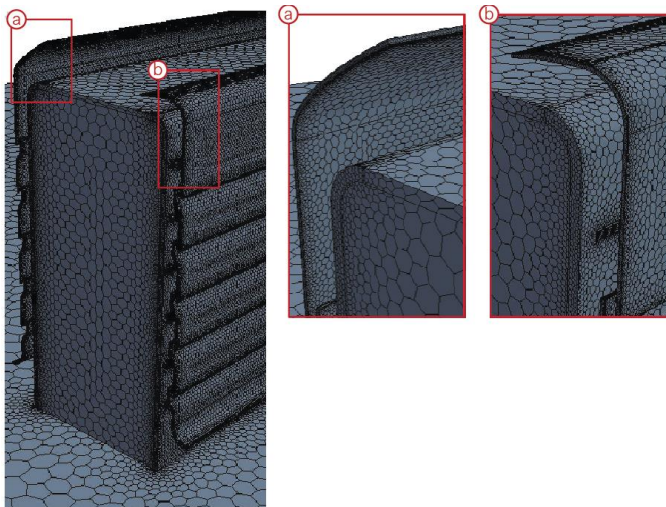


Figure 5.59. Volume meshes referred to the Case 4 model.

The probe lines for these two cases are localised at each floor level. Thus, the velocity profile is estimated at 3.5 m, 6.3 m, 9.3 m, 12.3 m, 15.3 m, and 18.3 m. The obtained results are plotted in Figure 5.60 and Figure 5.61, and

comparisons are made between Case 3, for which the DSF is placed on one elevation, and Case 4 that, instead, presents the system on two façades. The outputs underline that, for both cases, the insertion of multiple grills along the façade increases the ventilation of the cavity. Moreover, the use of aerodynamic profiles for the Double Façade allows reducing velocity losses due to the friction forces generated on the building corner, with benefits on the free cooling of the inner spaces. In conclusion, as shown in Figure 5.61, Case 4 confirms to be the most effective configuration among the various models here analysed, with excellent performances ensured on both elevations.

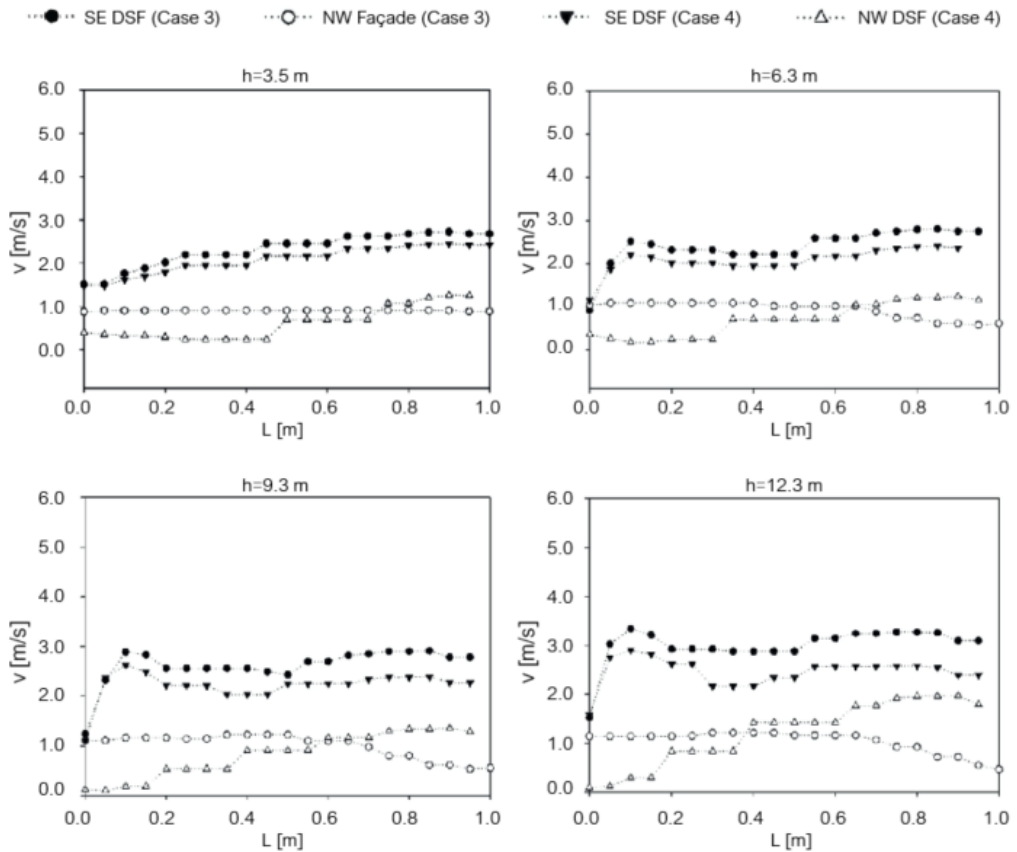


Figure 5.60. The velocity profile, referred to various probe lines, for optimised DSF configurations (Case 3 and Case 4).

Chapter 5

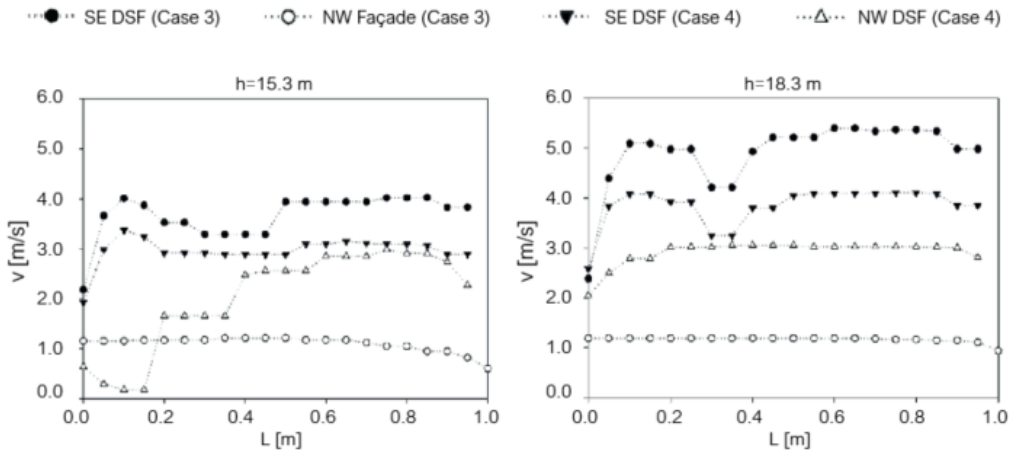


Figure 5.60. (Continued).

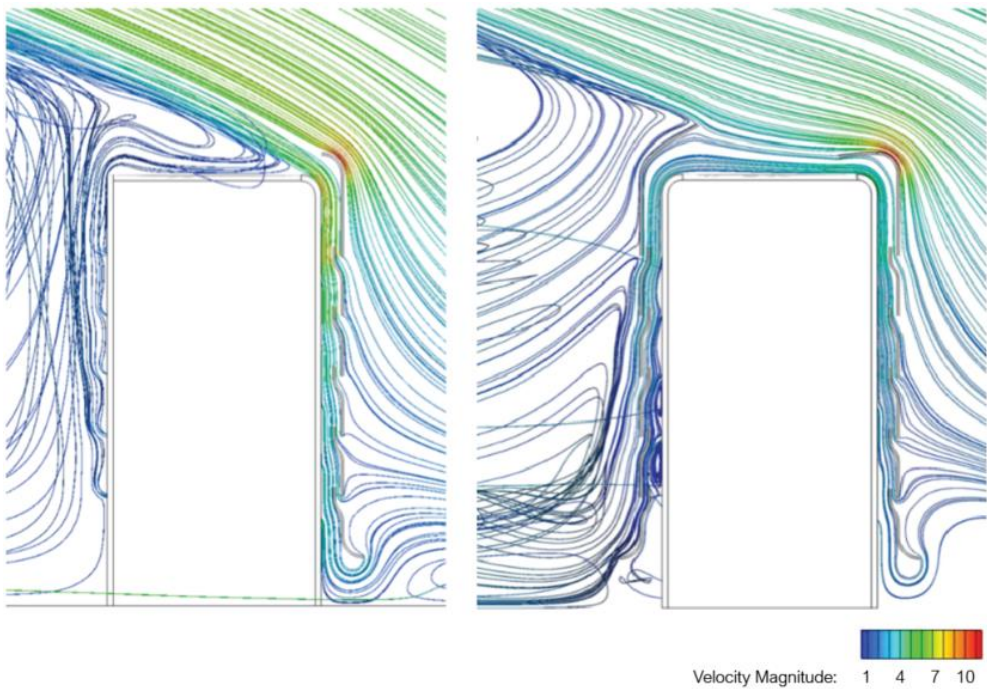


Figure 5.61. Velocity magnitudes estimated for Case 3 (left) and Case 4 (right).

5.6. Conclusions

The performed Computational Fluid Dynamic simulations underline several findings that can be summarised as follows:

- The insertion of the Double Skin Façade on existing building ensures a general improvement of the ventilation. It, in fact, avoids the stagnation pressure phenomenon above the façade, encouraging the free cooling of the occupied spaces.
- Bi-dimensional CFD analyses could be not accurate enough for predicting the effectiveness of such complex systems like DSFs. Comparing the results obtained with 2D and 3D simulations, it is clear that the bi-dimensional case tends to overestimate the velocity profile inside the cavity. In contrast, the three-dimensional modelling guarantees more accurate predictions but higher solving times. Thus, performing sensitivity analyses can be the correct choice for ensuring refined results from one side and adequate calculation times from the other.
- Considering the DSF cavity depth, the results show that the best option which ensures better ventilation rates for every wind condition is the 1 m cavity. Such dimension allows proper ventilation for both the inner and outer DSF layers. Moreover, the continuous cavity airflow avoids the overheating risk and reduces the superficial temperatures estimated for all layers.
- The Multi-Storey Double Skin Façade confirms to be the most versatile and useful configuration. It guarantees better velocity profiles and pressure levels than the Shaft-Box and the Corridor typology. Good performances are also estimated for the Shaft-Box DSF, whereas the Corridor is characterised by general weak ventilation for the presence of horizontal partitions that limit pressure gradients inside each air channel. Besides, the results underline that for being effective, the DSF has to be upwind; otherwise, its benefits are drastically reduced.
- The analysis of optimised shapes for improving the DSF performance puts in evidence that the use of more aerodynamic profiles or incrementing the grills placed along the height of the Double Façade can increase the cavity

Chapter 5

ventilation and remarkably reduce the cooling loads of the building occupied spaces.

The main findings here described confirm the effectiveness of the Double Skin Façade. It, in fact, represents a good option in case of retrofit intervention for the energy improvement of existing buildings thanks to its capability in encouraging the ventilation and free cooling of the inner spaces.

6. Structural Simulations

6.1. Introduction

The chapter aims to evaluate the seismic performance of the reference building and estimate the effectiveness of the suggested retrofit solution. The structural behaviour of the case study, considering its original and improved version, is investigated by means of linear and nonlinear analyses.

The assessment of the seismic performance and vulnerability of existing buildings is a quite diffuse and investigated topic. Various works are centred on comparing different approaches for evaluating their structural behaviour, thus checking the practical applicability of each method, the relative ease of use, and the degree of agreement on the results [106]. Other investigations, instead, intend to apply advanced technologies and smart materials for the retrofit of existing structures in order to improve their performance and protect them from seismic events. Retrofit interventions can interest the whole building, as the insertion of structures with brand new earthquake systems (e.g., the addition of shear walls or cross bracings or energy dissipation systems, the base insulation), or they can be limited to the strengthening of few beams, columns, and beam-to-column joints (e.g., jacketing of frame elements and joints by adopting steel or Fiber Reinforced Polymers wrappings, or high performance concrete coatings) [10]. Figure 6.1 depicts some of the restorative measures commonly used for the seismic retrofit of buildings.

Advanced techniques, able to reduce the damage of conventional seismic resisting structural systems, do not involve the strengthening of the main structure but aim to soften the earthquake-generating forces acting upon it [107]. Among the various options currently evaluated, the use of replaceable structural elements (RSE) seems to be the most interesting. The RSE is based on the mechanism that the structure fails in the relative weak location under loading and concentrating the damage into replaceable elements ensures less repair time than the traditional structure [108]. In case of damage, in fact, the RSEs can be easily replaced, and the whole structure can be quickly rehabilitated. Innovative devices for energy dissipation are based on the use of SMAs. Thanks to their physical and mechanical

features, they can be successfully integrated into structures to provide functions such as sensing, energy dissipation, actuation, and monitoring [109]. In recent years, various prototypes of SMA-based braced solutions have been designed and experimentally tested, and the main findings have underlined the effectiveness of these systems [110] [111] [112]. Other applications of SMA materials evaluate their use as insulation devices [113] [114] [115], or as beam-to-column connectors [116] [117], applied to both steel and RC structures.

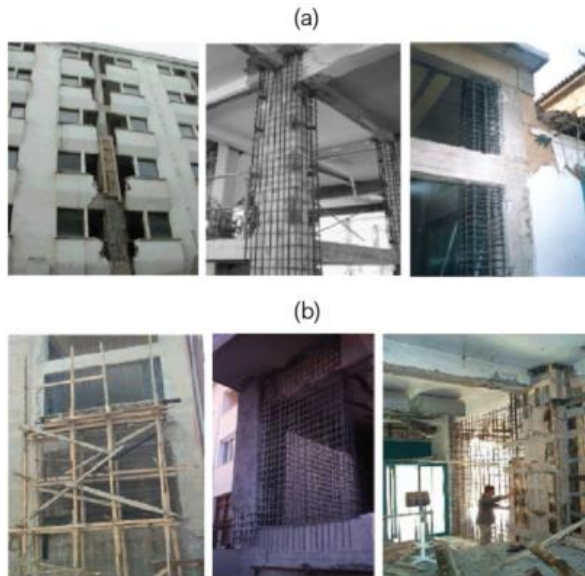


Figure 6.1. Examples of local (a) and global retrofit interventions [118].

The chapter is organised as follows. After this brief introduction about the current tendency in the building restoration, the structural modelling of the reference building is described in Section 6.2. Section 6.3 presents detailed information about the Engineered Double Skin Façade selected for the retrofit intervention with a focus on buckling-restrained braces and the available methods for their design. The main chapter conclusions are then summarised in Section 6.4.

The structural simulations are performed by using the commercial software MidasGEN (version 2020) and following the prescriptions suggested by the Italian (NTC2018) [119] and European (EC8) building code [120].

6.2. Modelling of the Reference Building

The reference structure is a reinforced concrete building, erected in 1983 according to the regulation codes and construction techniques of the time, as already mentioned in Chapter 3. It is composed of two constructions that are separated by a thermal joint. In the present work, each building is supposed to be structurally independent and, for this reason, only one construction is modelled and analysed by means of linear and nonlinear simulations. The building is a 7-storey structure. The garages and the entrances are located on the ground floor, whereas the upper floors host residential apartments (eight for each level). The main dimensions of the building are 30 m x 12 m, thus covering an area of about 360 m² out of each floor. The total height of the building is 21.5 m.

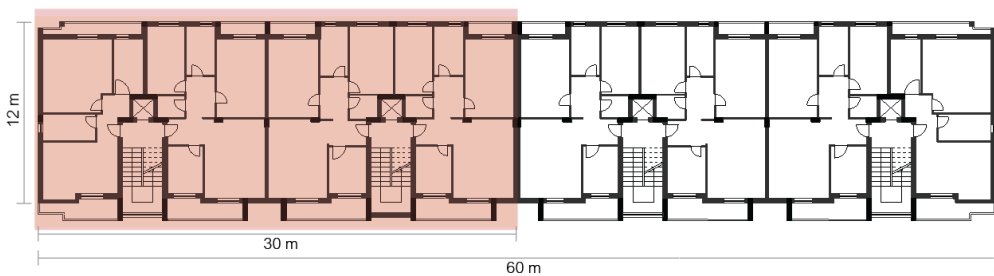


Figure 6.2. Plan of the typical floor with the identification of the selected construction for structural simulations.

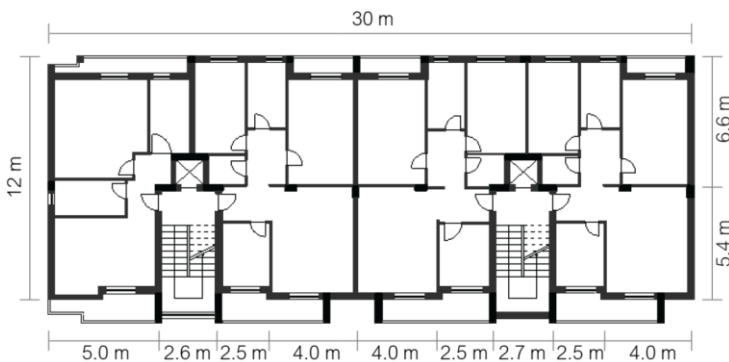


Figure 6.3. Plan of the modelled building.

The inter-storey height is 3.5 m at the ground floor, whereas 2.7 m at the upper floors. The different inter-storey height between the ground floor and the upper levels, added to the absence of the infill panels at the ground floor due to the presence of pilotis, could lead to a possible soft-storey mechanism in case of severe damage and stress concentration.

The longitudinal dimension is subdivided into various spans ranging from 2.5 m to 5.0 m. The building presents two staircases (each stair has two flights), made of reinforced concrete slabs (details are reported in Appendix C, Figure C.11). Beams and columns have been designed for vertical loads only, as usual at that time. The structure laid on deep foundations. The presence of balconies on the north-west elevation is not modelled but only inserted as load. Figure 6.4 depicts the axonometry of the three-dimensional Finite Element Model of the reference building, with and without the infill panels.

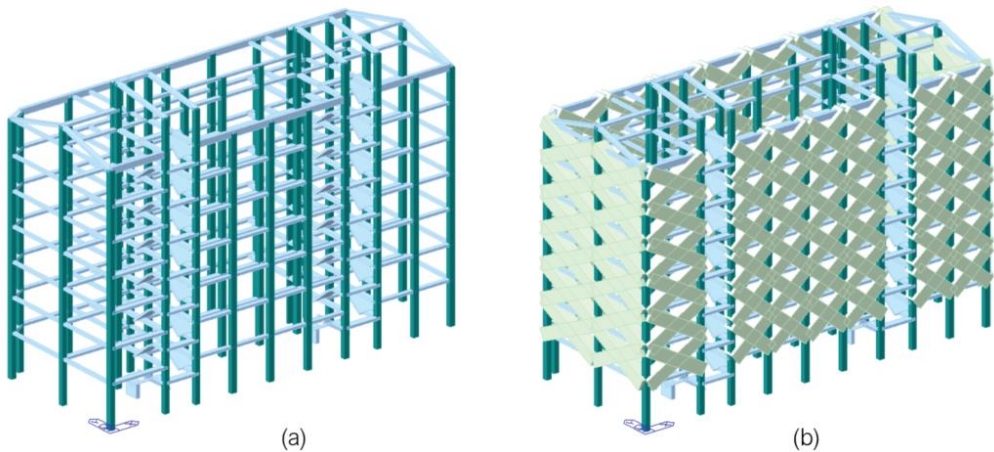


Figure 6.4. Axonometry of the bare frame (a) and infilled (b) model of the case study.

According to the structural details, the used concrete has a strain class equal to C25/30, and the steel of reinforcements is FeB38k. Considering the absence of in situ tests for the characterisation of the real mechanical properties of structural elements, various databases are selected for defining the input settings, ensuring the correct modelling of the case study. The mean concrete compressive strength (F_c) is established on the basis of the experimental campaign carried on by Masi at

al. [121], centred on the creation of an extensive database made up of test results on concrete cores extracted from public buildings, dated different ages. Figure 6.5 and Table 6.1 show the main statistical values of concrete strength coming from the tests.

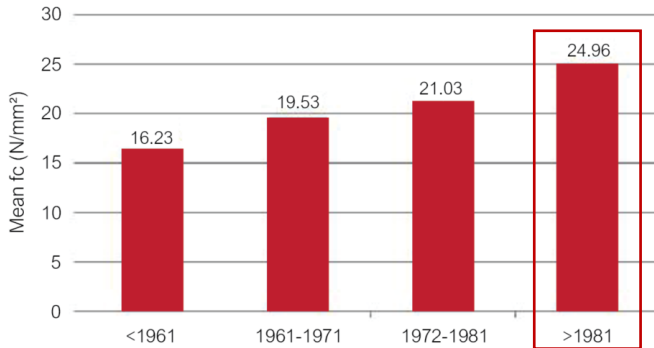


Figure 6.5. Mean values of concrete strength measured for buildings referred to four identified periods (elaborated from [121]).

Table 6.1. Main statistical values of concrete strength for different construction periods (elaborated from [121]).

Statistical Values	Construction Period			
	<1961	1961-1971	1972-1981	>1981
Number of buildings	21	115	112	68
Number of specimens	129	556	553	208
Mean Value (N/mm ²)	16.23	19.53	21.03	24.96
Median Value (N/mm ²)	15.57	18.63	20.26	23.95
Standard Deviation	6.27	7.29	9.06	7.98
Coefficient of variation	0.39	0.37	0.43	0.32

On the basis of the obtained values and the construction period of the reference building, a mean compressive concrete strength equal to 25 MPa is adopted.

The mechanical properties referred to the steel rebars are, instead, defined according to the analyses carried on by Verderame et al. [122], the outcomes of which have been inserted in the software STIL (version 1.0) [123], used for establishing the yield strength (F_y) of the reinforcement steel. The database

identifies for steel rebars dated 1982-1984 and for the Feb38k a mean value equal to 450 MPa, implemented for the following simulations.

The material mechanical properties are evaluated by adopting the appropriate Confidence Factor accounting for the level of knowledge of the existing building (§ 8.5.4 Livelli di Conoscenza e Fattori di Confidenza - NTC2018). The selected Confidence Factor is 1.2, which is referred to a moderate level of knowledge. Thus, the material properties are divided by the Confidence Factor, and the mean F_c and F_y values become, respectively, 21 MPa and 375 MPa. Moreover, the concrete modulus of elasticity is appropriately reduced by 50%, for considering the cracked condition, as suggested by the Italian code in case of existing buildings (§ 7.2.6 Criteri di Modellazione delle strutture e dell'Azione - NTC2018).

The structural and non-structural loads are evaluated on the base of the information synthesised in the technical report, as shown in Appendix C (Figure C.12). The available structural details are also used for defining the geometry and the principle aspects related to the RC frame. Column rebars data are, in fact, extrapolated for both flexural and shear reinforcement (Figure C.9 and Figure C.10, Appendix C), whereas beams reinforcements are calculated, according to the 80's Italian code [124], because only partially defined inside the available documents.

Based on considerations coming from the Italian code (NTC2018 §7.2.6. Criteri di Modellazione delle Strutture e dell'Azione Sismica) and as confirmed by preliminary analyses, the presence of a 4 cm-concrete slab in the stratigraphy of the ceiling allows considering floors able to withstand horizontal loads. Thus, **floor diaphragms** are inserted at each level for simulating this capability. The **foundations** are modelled as simple external constraints, owing to the capacity design that requires them to remain elastic. Thus, the model is fixed base.

The frame elements are modelled by adopting beams, and their flexural and shear inelastic behaviour is taken into account with concentrated plasticity hinges at the beam ends, as schematised in Figure 6.6. Beam elements are also used for modelling the staircases.

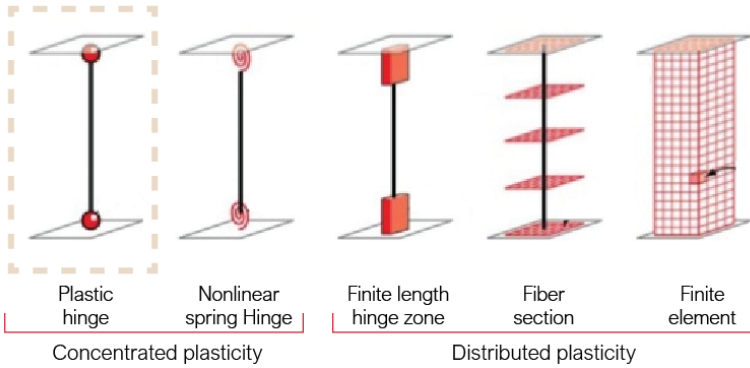


Figure 6.6. Idealised models of beam-column elements with the selected lumped plasticity approach (elaborated from [125]).

In detail, the inelastic behaviour of structural elements is modelled with the degrading Takeda constitutive law [126], depicted in Figure 6.7.

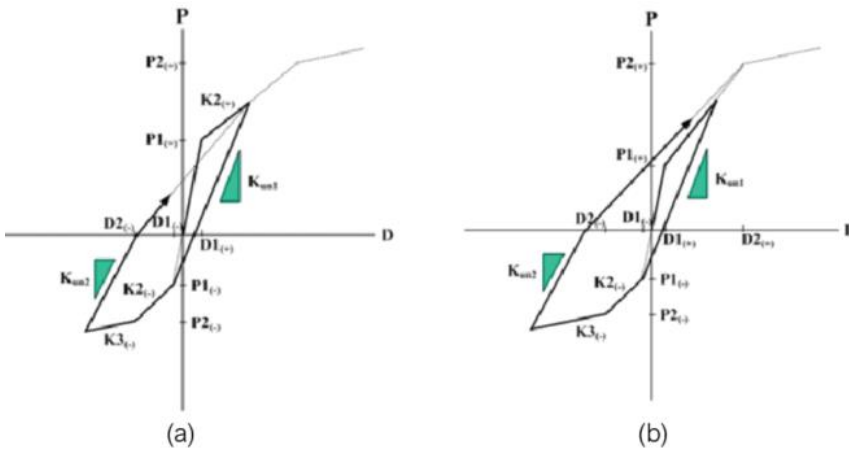


Figure 6.7. Takeda type hysteresis model available in MidasGEN [127]. (a) represents the unloading state prior to yielding in the uncracked zone (small displacement); (b) shows the unloading state to yielding in the uncracked region (large displacement); (c) is the unloading stage after yielding, and (d) represents the inner loop due to the repetition of load reversal.

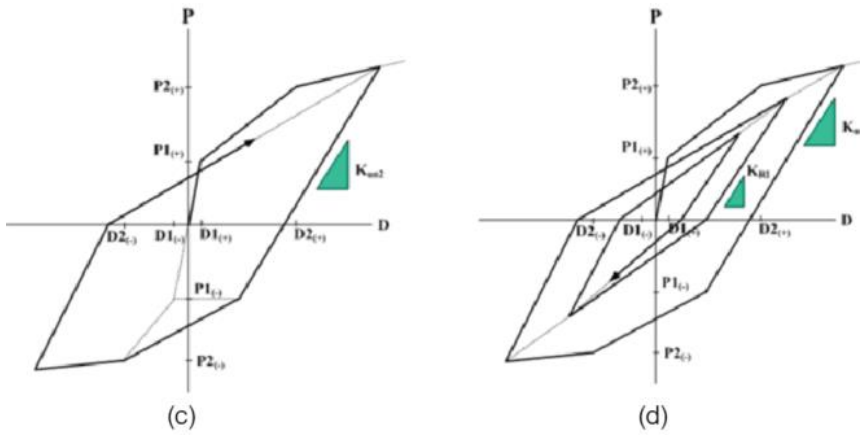


Figure 6.7. (Continued).

The flexural plastic hinge is represented by a trilinear curve followed by a degrading branch, as schematised in Figure 6.8. In contrast, the shear plastic hinge shows a linear behaviour until the ultimate capacity and exhibits a sudden brittle failure once that point is reached. The ultimate shear resistance (V_{max} , ξ_{max}) and the characteristic points referred to the flexural behaviour and describing the cracking (M_{cr} , θ_{cr}), yielding (M_y , θ_y), ultimate (M_u , θ_u), and residual (M_{res} , θ_{res}) condition are calculated on the basis of the Italian and European code. Flexural and shear plastic hinges are inserted for modelling the inelastic behaviour of both columns and beams.

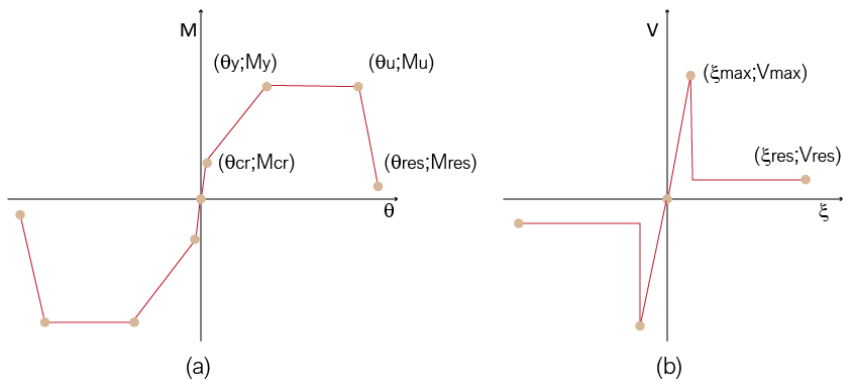


Figure 6.8. Schematisation of the flexural (a) and shear (b) plastic hinge behaviour.

The contribution of the **masonry infill panels** to the response of the reinforced concrete frame is modelled by replacing the panel with an equivalent strut which acts only in compression (Figure 6.9). The equivalent diagonal strut is a consolidated engineering model for infilled frames, also proposed for the design stage from various codes.

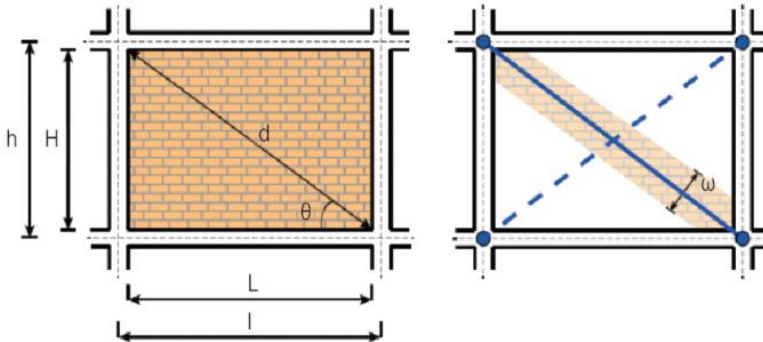


Figure 6.9. Diagonal strut mode for simulating the presence of masonry infills [128].

Several relationships could be adopted for describing the parameters governing the monotonic and cyclic behaviour of the strut, as a function of the mechanical and geometrical characteristics of masonry infills. The Decanini et al. [129] [130] model is selected among the available options, and diagonal elements, properly calculated, are inserted at each level except at the ground floor, where only a few and widely opened partitions are localised, irrelevant for the building structural behaviour.

The resistance of the infill panel is simulated by a fictitious failure compressive stress σ_{br} , taking into consideration the different failure modes, occurred in both conventional tests and real structures in case of seismic action. Four main failure modes are selected, with the corresponding equivalent failure compressive stresses: (a) diagonal tension, $\sigma_{br(1)}$; (b) sliding shear along horizontal joints, $\sigma_{br(2)}$; (c) crushing in the corners in contact with the frame, $\sigma_{br(3)}$, and (d) diagonal compression, $\sigma_{br(4)}$. Equations 6.1 to 6.4 allow the calculation of each failure mechanism, using, as input, the vertical compression strength measured on the masonry specimens (σ_{m0}), the shear strength recorded by means of the diagonal

compression test (τ_{m0}), the sliding resistance in the joints obtained from the triple test (u), and the vertical stress due to working loads (σ_0).

$$\sigma_{br(1)} = \frac{0.6\tau_{m0} + 0.3\sigma_0}{\omega/d} \quad (6.1)$$

$$\sigma_{br(2)} = \frac{(1.2 \sin \theta + 0.45 \cos \theta)u + 0.3\sigma_0}{\omega/d} \quad (6.2)$$

$$\sigma_{br(3)} = \frac{(1.12 \sin \theta \cos \theta)}{K_1(\lambda h)^{-0.12} + K_2(\lambda h)^{0.88}} \sigma_{m0} \quad (6.3)$$

$$\sigma_{br(4)} = \frac{1.16\sigma_{m0} \tan \theta}{K_1 + K_2 \lambda h} \quad (6.4)$$

Once determined the fictitious failure compressive stresses corresponding to the different failure modes, the minimum value ($\sigma_{br,min}$) is used for defining the ultimate lateral strength (H_{mfc}) calculated with Equation 6.5.

$$H_{mfc} = (\sigma_{br})_{min} e \omega \cos \theta \quad (6.5)$$

where ω is the width of the strut, e the thickness of the masonry panel, and θ the angle between the strut and the horizontal axis.

The width of the strut can be calculated using the formulation suggested by Stafford-Smith [131], reported in Equation 6.6. The λh is a non-dimensional parameter depending on the geometric and mechanical characteristics of the frame-infill system (Equation 6.7). K_1 and K_2 are two coefficients, defined on the basis of the λh , as shown in Table 6.2, and d is the length of the equivalent strut.

Table 6.2. Coefficients K_1 and K_2 .

	K_1	K_2
$\lambda h < 3.14$	1.3	-0.178
$3.14 \leq \lambda h < 7.85$	0.707	0.01
$\lambda h \geq 7.85$	0.47	0.04

$$\omega = \left(\frac{K_1}{\lambda h} + K_2 \right) d \quad (6.6)$$

The λh parameter can be defined as:

$$\lambda h = \sqrt[4]{\frac{E_m e \sin(2\theta)}{4E_c I h_m}} h \quad (6.7)$$

where E_m is the elastic equivalent modulus corresponding to the complete cracking stage of the infill, E_c is the elastic modulus of concrete, h and h_m are, respectively, the height of the storey and of the masonry panel, and I is the momentum of inertia of the column.

The last parameter to be calculated is the stiffness of the equivalent strut K_{mfc} at complete cracking condition, and it is given by the following relation:

$$K_{mfc} = \frac{E_m e \omega}{d} \cos^2 \theta \quad (6.8)$$

Thus, the skeleton curve of the lateral force-displacement (H_m - u) relationship can be drawn, as shown in Figure 6.10. The four branches describe the first linear elastic ascending branch (till F-point), the post cracking condition (from F to FC points), the third descending branch referred to the post-peak strength deterioration of the infill, and the horizontal branch representing the infill residual strength.

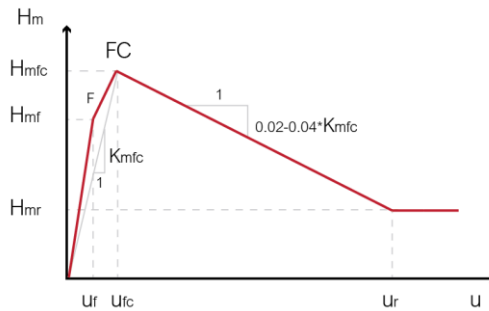


Figure 6.10. Backbone curve for the equivalent strut model.

The presence of openings in the infills reduces the stiffness and ultimate strength of the panel, and, for this reason, they should be carefully taken into account. Thus, reduction factors are employed, as suggested by Decanini et al. [132]. In the specific case, making considerations about the presence of openings

is extremely important considering that, on the longitudinal building elevation, the high percentage of windows leads to a reduced increment in the infilled model in comparison to the bare frame. In contrast, the transversal façade presents few and small windows, thus deeply incrementing the stiffness and ultimate strength of the panel.

Table 6.3 shows the mechanical properties of the masonry, chosen on the main findings and experimental campaign carried on by Hak et al. [133] [134] and referred to the specific infill typology. In detail, the table contains the following information:

- The values of compression strength for the horizontal (f_{wh}) and vertical (f_{wv}) direction.
- The sliding shear resistance of mortar joints (f_{wu}).
- The shear resistance under diagonal compression (f_{ws}).
- The secant modulus of elasticity for horizontal (E_{wh}) and vertical direction (E_{wv}).
- The shear modulus (G).
- The unit weight of the infills (W).

Table 6.3. Mechanical properties of the selected masonry.

f_{wh}	f_{wv}	f_{wu}	f_{ws}	E_{wh}	E_{wv}	G	W
[MPa]	[MPa]	[MPa]	[MPa]	[MPa]	[MPa]	[MPa]	[kN/m ³]
1.11	1.50	0.25	0.31	991	1873	1089	6.87

Once the mechanical characteristics of the equivalent strut have been defined, truss elements are inserted in the bare frame model, and axial plastic hinges are introduced for simulating their nonlinear behaviour. The FEMA formulation [135] is adopted for the infills.

After modelling the reference building, linear and nonlinear analyses are performed for evaluating the structural behaviour. First, the bare frame model is simulated, then the infills are added in order to estimate the building performance in its original configuration. The fundamental periods are, respectively, 2.4 sec for the bare frame and 0.94 sec for the infilled model. In both cases, the modal analysis

shows torsional mechanisms due to vertical and in-plan irregularities. The eccentricity between the centre of mass and the centre of resistance generates the torsional response. Moreover, the presence of a soft floor at the ground level, due to the lack of masonry infills, creates a nonhomogeneous distribution of stiffness and a consequent soft storey mechanism.

Pushover analyses are performed, considering both the uniform response acceleration and the triangular force distribution. The capacity curves, defined in terms of base shear and displacement for each distribution of forces, evaluating both the positive and negative direction, are plotted in Figure 6.11. The comparison between the curves obtained with positive and negative force distributions underlines that the building behaves in the same manner, regardless of their directions. Various considerations can be done, instead, by comparing the bare frame and the infilled model. The insertion of infill panels on the y-direction, in fact, profoundly increases the building stiffness. This huge increment is due to the nearly complete absence of windows on the transversal direction. Thus, the infill contribution allows increasing about two times the initial stiffness if compared to the bare frame configuration. This contribute becomes less intense for the longitudinal direction, where the presence of several openings with appreciable dimensions does not ensure the same entity variation. Moreover, the different post-peak behaviour for the x and y-direction can be explained by evaluating the infill failure. Once the maximum base shear value is reached for the x-direction, the infills present on the first, second and third floor collapse altogether, causing a deep and instantaneous fall of the capacity curves. In contrast, the masonry panels placed in the y-direction gradually collapse, ensuring less intense decrements.

The analysis of the damage distribution shows the formation of shear failures located along the short columns of the staircase and for a few beams situated next to the stairs due to the generation of torsional movements. In general, the building collapse is due to flexural-shear failure mechanisms.

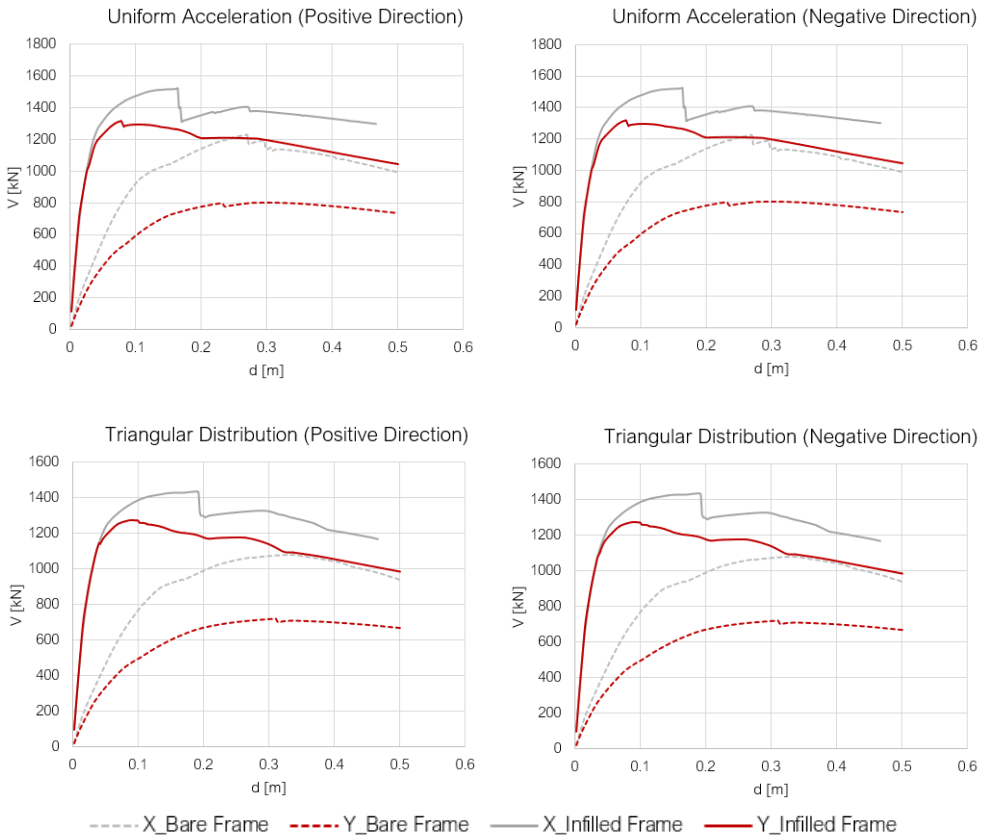


Figure 6.11. Capacity curves due to different force distributions and directions.

The other investigated parameter is the inter-storey drift, evaluated for each force distribution. The literature review suggests several attempts done for correlating the damage of various structural systems to the estimated drifts on the base of experimental and numerical analyses. According to Gobarah [136], the drift ratio limits associated with the severe and collapse damage levels are respectively, 0.8% and 1.0%, in case of nonductile moment resisting frames. A more comprehensive analysis is the one carried on by Hazus [137] that establishes for various typologies of buildings and according to their properties and characteristics, different drift ranges. In case of concrete frame buildings with unreinforced masonry infill walls, classified in Figure 6.12 as “C3”, and with medium height (M), the extensive and complete structural damage appears for drifts higher than, respectively, 0.8% and 1.87%.

Building Properties			Interstorey Drift at				Spectral Displacement (inches)							
Type	Height (inches)		Threshold of Damage State				Slight		Moderate		Extensive		Complete	
	Roof	Modal	Slight	Moderate	Extensive	Complete	Median	Beta	Median	Beta	Median	Beta	Median	Beta
W1	168	126	0.0032	0.0079	0.0245	0.0600	0.40	1.01	1.00	1.05	3.09	1.07	7.56	1.06
W2	288	216	0.0032	0.0079	0.0245	0.0600	0.69	1.04	1.71	0.97	5.29	0.90	12.96	0.99
S1L	288	216	0.0048	0.0076	0.0162	0.0400	1.04	0.85	1.65	0.82	3.50	0.80	8.64	0.95
S1M	720	540	0.0032	0.0051	0.0108	0.0267	1.73	0.70	2.76	0.75	5.84	0.81	14.40	0.98
S1H	1872	1123	0.0024	0.0038	0.0081	0.0200	2.70	0.69	4.30	0.71	9.11	0.85	22.46	0.93
S2L	288	216	0.0040	0.0064	0.0160	0.0400	0.86	1.01	1.38	0.96	3.46	0.88	8.64	0.98
S2M	720	540	0.0027	0.0043	0.0107	0.0267	1.44	0.73	2.30	0.75	5.76	0.80	14.40	0.98
S2H	1872	1123	0.0020	0.0032	0.0080	0.0200	2.25	0.70	3.59	0.70	8.99	0.84	22.46	0.91
S3	180	135	0.0032	0.0051	0.0128	0.0350	0.43	1.06	0.69	1.03	1.73	1.07	4.73	0.89
S4L	288	216	0.0032	0.0051	0.0128	0.0350	0.69	1.11	1.11	1.03	2.77	0.99	7.56	0.98
S4M	720	540	0.0021	0.0034	0.0086	0.0233	1.15	0.81	1.85	0.80	4.62	0.94	12.60	1.00
S4H	1872	1123	0.0016	0.0026	0.0064	0.0175	1.80	0.73	2.88	0.75	7.21	0.90	19.66	0.97
S5L	288	216	0.0024	0.0048	0.0120	0.0280	0.52	1.20	1.04	1.11	2.59	1.08	6.05	0.95
S5M	720	540	0.0016	0.0032	0.0080	0.0187	0.86	0.85	1.73	0.83	4.32	0.94	10.08	0.99
S5H	1872	1123	0.0012	0.0024	0.0060	0.0140	1.35	0.72	2.70	0.75	6.74	0.92	15.72	0.96
C1L	240	180	0.0040	0.0064	0.0160	0.0400	0.72	0.98	1.15	0.94	2.88	0.90	7.20	0.97
C1M	600	450	0.0027	0.0043	0.0107	0.0267	1.20	0.73	1.92	0.77	4.80	0.83	12.00	0.98
C1H	1440	864	0.0020	0.0032	0.0080	0.0200	1.73	0.71	2.76	0.80	6.91	0.94	17.28	1.01
C2L	240	180	0.0032	0.0061	0.0158	0.0400	0.58	1.11	1.10	1.09	2.84	1.07	7.20	0.93
C2M	600	450	0.0021	0.0041	0.0105	0.0267	0.96	0.86	1.83	0.83	4.74	0.80	12.00	0.98
C2H	1440	864	0.0016	0.0031	0.0079	0.0200	1.38	0.73	2.64	0.75	6.82	0.92	17.28	0.97
C3L	240	180	0.0024	0.0048	0.0120	0.0280	0.43	1.19	0.86	1.15	2.16	1.15	5.04	0.92
C3M	600	450	0.0016	0.0032	0.0080	0.0187	0.72	0.90	1.44	0.86	3.60	0.90	8.40	0.96
C3H	1440	864	0.0012	0.0024	0.0060	0.0140	1.04	0.73	2.07	0.75	5.18	0.90	12.10	0.95
PC1	180	135	0.0032	0.0051	0.0128	0.0350	0.43	1.14	0.69	1.14	1.73	1.17	4.73	0.98
PC2L	240	180	0.0032	0.0051	0.0128	0.0350	0.58	1.14	0.92	1.10	2.31	1.10	6.30	0.93
PC2M	600	450	0.0021	0.0034	0.0086	0.0233	0.96	0.87	1.54	0.83	3.85	0.91	10.50	1.00
PC2H	1440	864	0.0016	0.0026	0.0064	0.0175	1.38	0.74	2.21	0.75	5.55	0.91	15.12	0.96
RM1L	240	180	0.0032	0.0051	0.0128	0.0350	0.58	1.20	0.92	1.17	2.31	1.17	6.30	0.94
RM1M	600	450	0.0021	0.0034	0.0086	0.0233	0.96	0.91	1.54	0.89	3.85	0.89	10.50	0.96
RM2L	240	180	0.0032	0.0051	0.0128	0.0350	0.58	1.14	0.92	1.10	2.31	1.15	6.30	0.92
RM2M	600	450	0.0021	0.0034	0.0086	0.0233	0.96	0.89	1.54	0.87	3.85	0.87	10.50	0.96
RM2H	1440	864	0.0016	0.0026	0.0064	0.0175	1.38	0.75	2.21	0.75	5.55	0.84	15.12	0.94
URML	180	135	0.0024	0.0048	0.0120	0.0280	0.32	1.15	0.65	1.19	1.62	1.20	3.78	1.18
URMM	420	315	0.0016	0.0032	0.0080	0.0187	0.50	0.99	1.01	0.97	2.52	0.90	5.88	0.88
MH	120	120	0.0032	0.0064	0.0192	0.0560	0.38	1.11	0.77	1.10	2.30	0.95	6.72	0.97

Figure 6.12. Structural fragility curve parameters according to Hazus [137].

On the base of these considerations and findings coming from similar works in the existing building sector [49] according to which an inter-storey drift equal to 1.0% at the Life Safety Limit State means the failure of the infill panels and severe and extended damages on the existing building, the vulnerability of the case study is evaluated by considering as last point of the capacity curve the one for which an inter-storey drift equal to 1.87% is reached, at least, at one floor.

To analyse the vulnerability of the existing building the Multi Degree of Freedom (MDOF) system is transformed into a Single Degree of Freedom (SDOF) according to prescriptions suggested by the Italian and European codes (NTC2018, EC8). The transformation is obtained by fitting the capacity curve with an equivalent bilinear curve and determining the period, the maximum base shear, and the first mode shape, as depicted in Figure 6.13. For the sake of the brevity, the procedure followed for the creation of the bilinear curve is not here described. Additional details may be found in Section §7.3.4.2. Analisi Non Lineare Statica of the Italian building code NTC2018 [119].

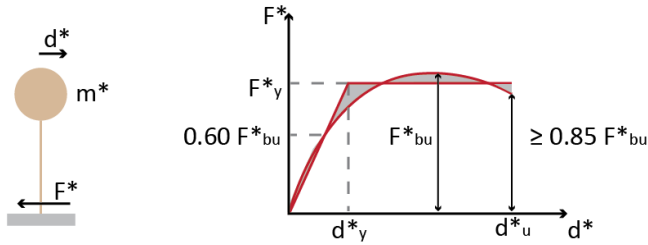


Figure 6.13. The schematisation of the equivalent Single Degree of Freedom (elaborated from NTC2018).

Figure 6.14 shows the bilinear curves, compared to the Acceleration Displacement Response Spectrums (ADRS) at the Damage Limit State (DLS), Life Safety Limit State (LSLS) and Collapse Limit State (CLS). The comparisons are made for each force distribution, only referred to the positive direction. The choice of not representing the negative force distribution is due to an identical structural behaviour for the two directions, as previously mentioned. Moreover, building vulnerability is evaluated only for the infilled model (solid lines in Figure 6.11), selected for being more representative of the expected seismic performance of the case study.

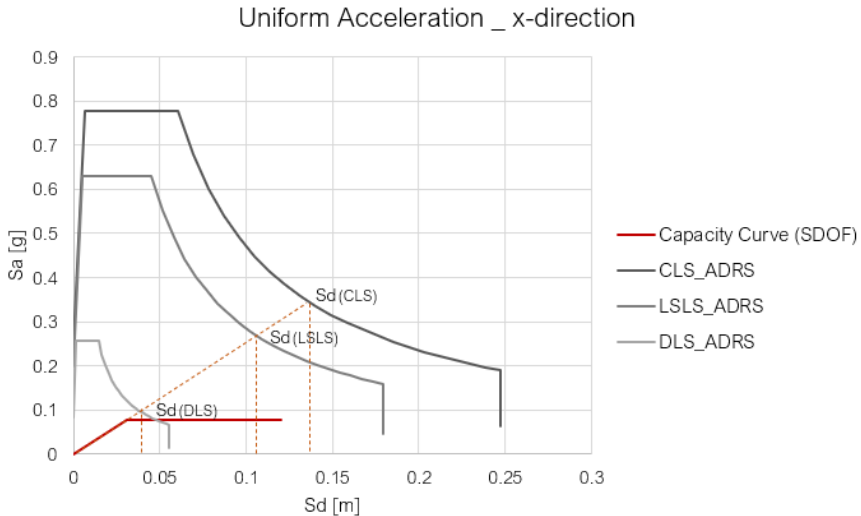


Figure 6.14. ADRS and displacement demands at DLS, LSLS, and CLS for the uniform acceleration force distribution, x-direction.

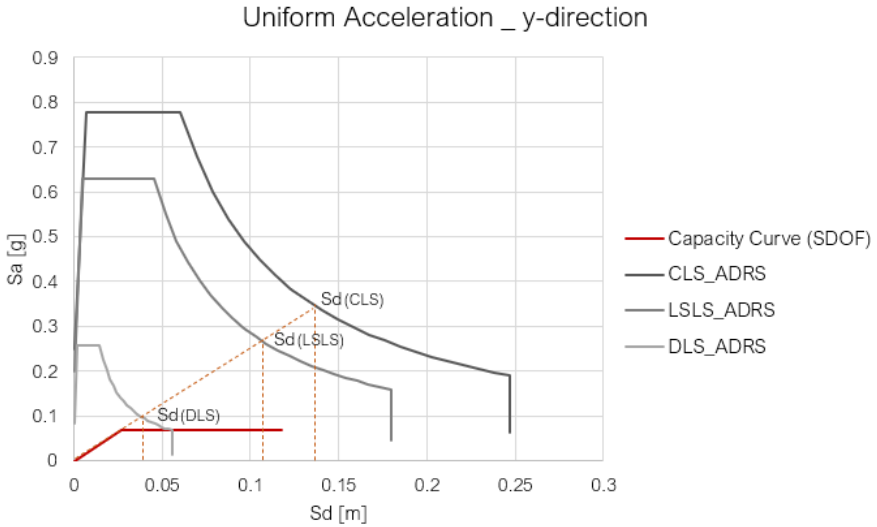


Figure 6.15. ADRS and displacement demands at DLS, LSLs, and CLS for the uniform acceleration force distribution, y-direction.

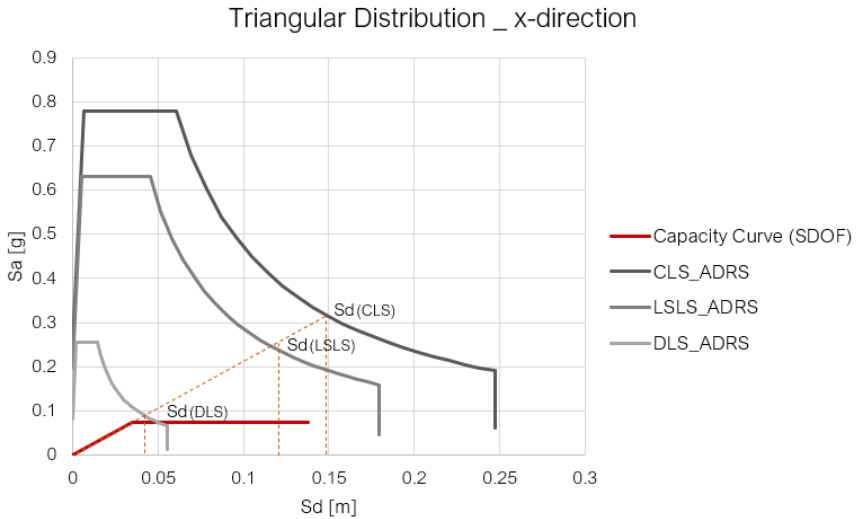


Figure 6.16. ADRS and displacement demands at DLS, LSLs, and CLS for the triangular force distribution, x-direction.

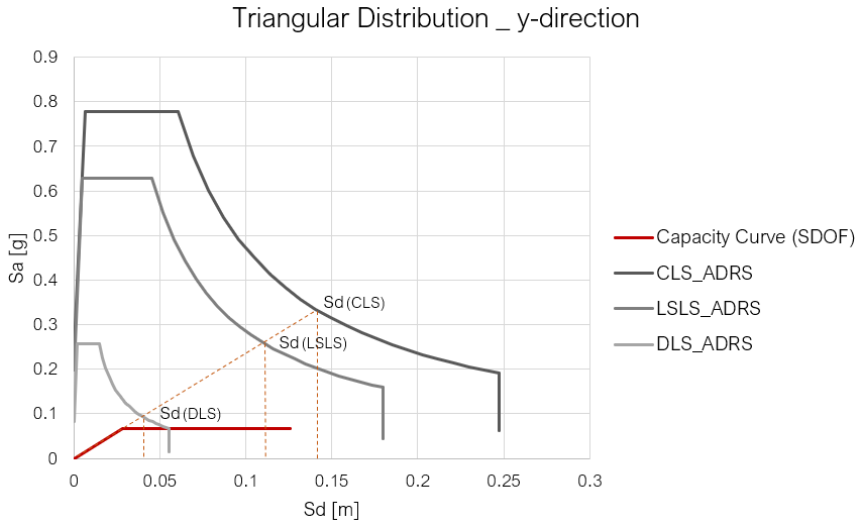


Figure 6.17. ADRS and displacement demands at DLS, LSLS, and CLS for the triangular force distribution, y-direction.

According to the obtained results, the reference building in its existing configuration satisfies, for each force distribution and direction, the displacement demand at the Life Safety Limit State. In contrast, the Collapse Limit State displacement is never verified. On the base of these considerations and even if not strictly required by the European and Italian building code, the case study is structurally retrofitted in order to reduce direct and indirect losses due to earthquake damages, in accordance with the pursued Life Cycle Thinking approach.

6.3. Modelling of the Engineered DSF

In order to improve the building seismic performance, the Engineered Double Skin Façade is inserted on the longitudinal elevations. The choice of introducing the DSF on two façades and not enclosing the whole building is influenced by considerations coming from the energy simulations, previously performed. According to the results, in fact, the use of DSF systems on west and east-oriented elevations allows neglectable improvements from the energy side. Thus, the external skin is localised only along the x-direction with the consequent reduction in terms of materials and costs.

The DSF is designed as a self-supporting braced frame structure and presents a 1 m cavity depth, according to the main findings obtained by energy and CFD analyses. It is made of S275 I-section profiles for beam and columns and Buckling-Restrained Axial Dampers (BRAD) are inserted to protect the structure through energy dissipation. In detail, BRAD braces are introduced into the Double Skin for improving the x-direction performance, whereas they are localised directly inside the building RC frames for the transversal elevation. The dissipative braces are placed in a symmetrical way in order to avoid torsional phenomena of the main structure, and a system of horizontal X braces (elastic braces) is inserted on each floor.

In addition to the global intervention, local retrofit solutions are adopted as the confinement with Fiber Reinforced Polymers (FRP) of the short columns of the staircases and the beams characterised by shear failure. Moreover, the strengthening of beam-column joints is suggested, especially for the y-direction, where the insertion of the BRAD braces could increase the stresses transferred to the connections. The axonometry of the three-dimensional model after the addition of the Double Skin Façade is depicted in Figure 6.18.

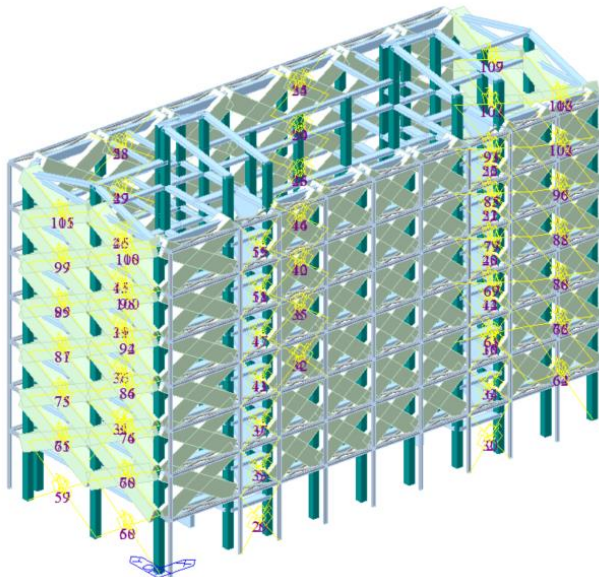


Figure 6.18. Axonometry of the 3D building model after the insertion of the DSF.

The inelastic behaviour of the DSF structural elements is evaluated by inserting plastic hinges for both beams and columns, whereas the nonlinear properties of the seismic devices are opportunely defined by adopting specific general links (yellow elements in Figure 6.18), the so-called “Steel Damper” in MidasGEN. The degrading bilinear model of the steel damper is depicted in Figure 6.19. The use of this general link allows the definition of both the elastic and dissipative contribute of the single brace.

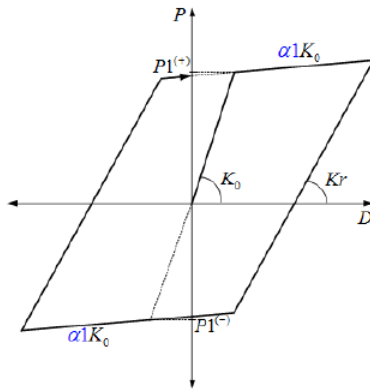


Figure 6.19. Schematisation of the hysteretic model implemented in MidasGen for the Steel Damper [127].

6.3.1. Dissipative Braces: Main Aspects and Design Procedures

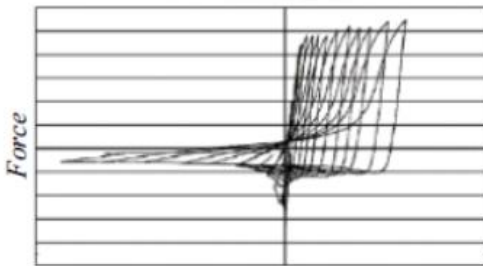
Various options of seismic performance upgrading systems are normally available and the use of energy dissipation devices (friction, viscoelastic and metallic dampers, or buckling-restrained braces) represent an interesting choice, considering their effectiveness and easy replacement. The protection of RC structures from severe earthquakes could be provided by Buckling-Restrained Braces (BRB). The insertion of such devices, in fact, allows the localisation of the damage at specific points of the structure, opportunely designed and verified. BRBs are characterised by stable hysteretic behaviour and, differently from traditional braces, they permit an independent design of stiffness, strength and ductility properties. Figure 6.20 shows a comparison between BRBs and traditional braces.



Traditional brace, buckled in compression

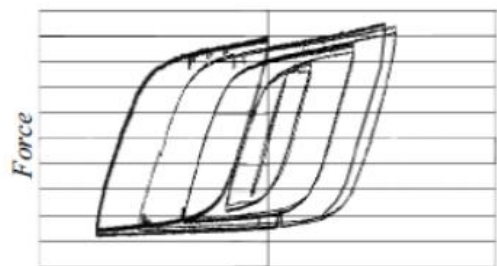


BRB, unbuckled in compression



Displacement

**Hysteresis loop:
poor nonlinear behaviour**



Displacement

**Hysteresis loop:
excellent nonlinear behaviour**

Figure 6.20. Comparisons between traditional braces (left) and buckling-restrained braces (right) [138].

The first studies on the structural performance of BRB devices date back to 1973 when Wakabayashy et al. [138] analysed various system able to inhibit the global buckling of braces in compression. After these preliminary concepts, several developments on BRBs with a steel core confined by a steel casing were made in Japan from the second half of the 1970s to 1990s. The continuous interest in these dissipative devices has allowed their diffusion all over the world. In Italy, BRBs are successfully adopted for the seismic protection of existing buildings, as shown in Figure 6.21.

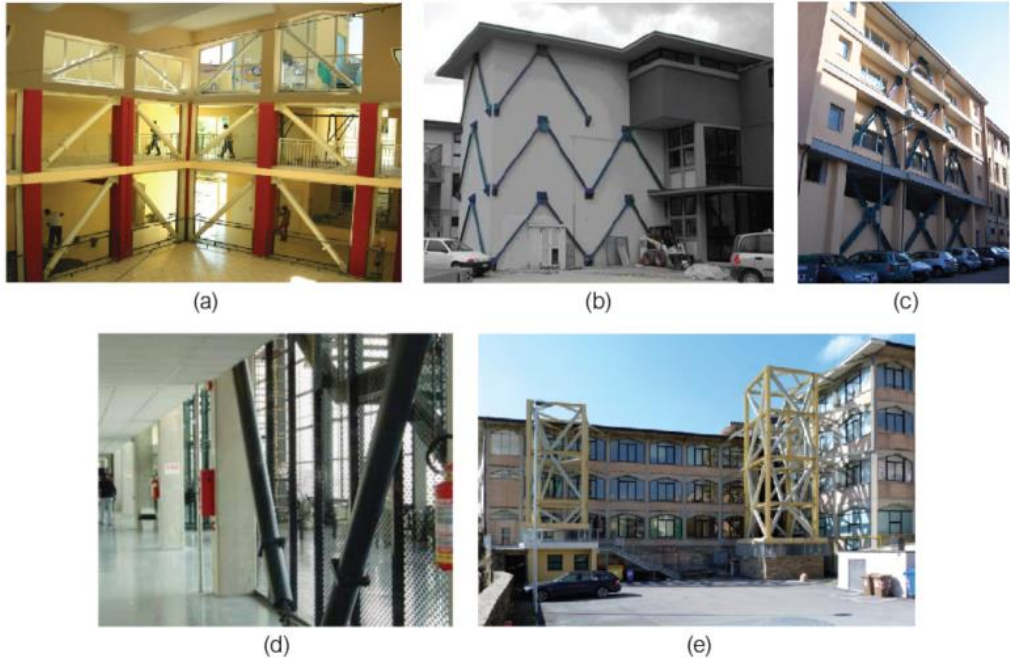


Figure 6.21. Retrofitted and new buildings with BRAD systems: (a) the Cappuccini School [139], (b) the Gentile-Fermi School [140], (c) the Busciolano School [140], (d) The Marche Polytechnic University [141] and (e) the Varano High School [142].

Among the buildings retrofitted by the insertion of BRAD dissipative braces, interesting examples are various school as the Cappuccini School in Ramacca (Figure 6.21a) [139], the Gentile-Fermi School in Fabriano (Figure 6.21b) and the Busciolano School in Potenza (Figure 6.21c) [140]. Moreover, also new prefabricated buildings are designed with BRAD systems for the seismic protection of the main structure, like the recent building of the Marche Polytechnic University (Figure 6.21d) [141]. In most of the cases, the braces are directly connected to the building existing frames. Otherwise, the BRAD systems can be inserted inside dissipative towers connected to the main structure, as it happens for the Varano High School in Camerino (Figure 6.21e) [142].

After this brief introduction about the main aspects of buckling-restrained braces, the comparative of the structural behaviour between elastic and dissipative braces and how they can improve the existing structure performance is presented in Figure 6.22. As it can be seen, the addition of dissipative devices (e.g. BRADs)

into the elastic brace, allows increasing the ductile behaviour of the single element and, consequently, of the whole braced frame system. Moreover, the insertion of dissipative braces, if well designed, ensures good ductility with reduced strength increment, particularly significant especially in the case of building retrofitting.

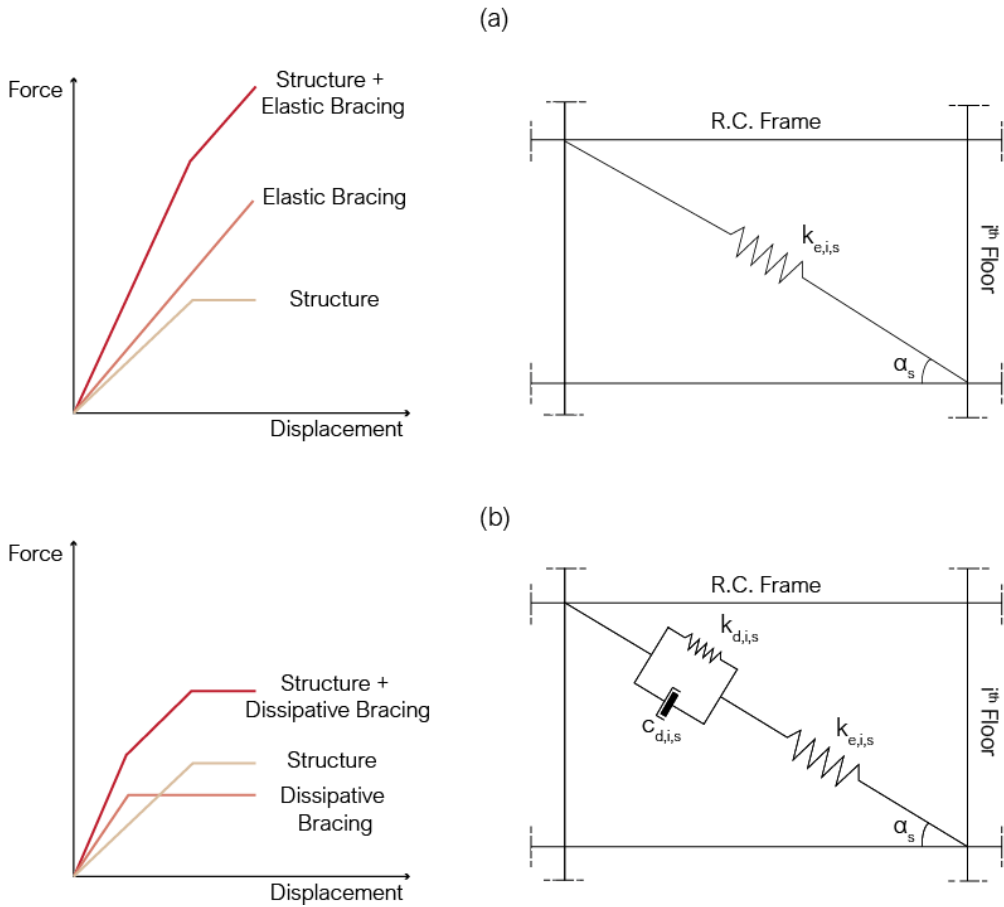


Figure 6.22. Schematisation and comparison between the performance of elastic (a) and dissipative braces (b).

The performance of a buckling-restrained brace is strictly influenced by its elastic and dissipative component. The rheological model, depicted in Figure 6.22, shows that the dissipative link and the elastic brace act in series, and the whole dissipative system is connected in parallel to the main structure. It is essential to underline that the effectiveness of the dissipative brace is related to its inclination

to the horizontal. In this sense, the schematisation proposed by Braga et al. [143], reported in Figure 6.23, defines, for each brace configuration, the specific effectiveness factor (f) according to geometrical aspects, like the angle brace or the length of the selected device.

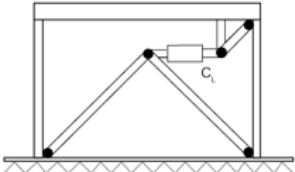
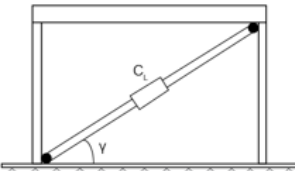
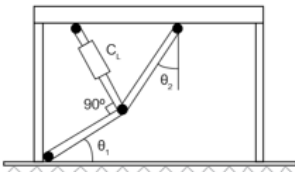
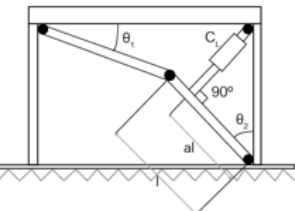
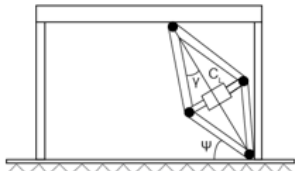
Dissipative Brace Configuration	Effectiveness Factor
<p>(a)</p> 	$f = 1$
<p>(b)</p> 	$f = \cos \gamma$
<p>(c)</p> 	$f = \frac{\sin \theta_2}{\cos(\theta_1 + \theta_2)} + \sin \theta_1$
<p>(d)</p> 	$f = \frac{\alpha \cos \theta_1}{\cos(\theta_1 + \theta_2)} - \cos \theta_2$
<p>(e)</p> 	$f = \frac{\cos \Psi}{\tan \gamma}$

Figure 6.23. Definition of the effectiveness factor, according to the dissipative bracing configuration [143].

Several approaches could be adopted for the design of dissipative braces. The most interesting ones are synthesised in Table 6.4. Fu and Cherry [144] suggest a quasi-static procedure for designing a friction-damped system by introducing a seismic force modification factor, selected according to the specific target spectrum, and able to guarantee particular values of maximum displacement and base share. A second methodology is the one defined by Whittiker et al. [145] which adopts an equivalent lateral force and modal analysis procedure for yielding buildings with damping devices. The methodology is opportunely validated and incorporated in the FEMA 450-NEHRP [146]. Kim and Choi [147] investigate a straightforward design procedure for buckling-restrained structures in order to meet the given target displacement. The approach is based on defining the optimum yield strength of BRBs able to maximise the equivalent damping ratio.

The method investigated by Mazza et al. [148] proposes a displacement-based design procedure for proportioning hysteretic damped braces and for reaching an expected performance level in case of RC existing buildings. The last two selected approaches are the methodologies suggested, respectively, by Bergami and Nuti [149] and Wen et al. [150]. In the first case, the definition of dissipative brace properties is done by evaluating the displacement-based design by using the capacity spectrum method and avoiding nonlinear analyses. The last, instead, integrates multiple response quantities into a single compact format to make easier comparisons of different potential solutions able to satisfy a set of established performance objectives under various levels of seismic hazard.

The quasi totality of the approaches mentioned above is based on simplified methodologies referred to SDOF, and the most common parameter selected for the design procedure is the displacement of the master node placed at the top of the structure. Besides, various optimisation procedures are currently available, and comprehensive analysis of the most common ones is described by Laguardia [140].

Table 6.4. Synthesis of some of the most common approaches available for the design of dissipative bracings (elaborated from [140]).

Year	Authors	Model	Parameter
2000	Fu and Cherry	SDOF	U_{max}, F_{max}
2003	Whittiker et al.	SDOF	U_{max}
2004	Kim and Choi	SDOF	U_{max}
2012	Mazza et al.	SDOF	U_{max}
2013	Bergami and Nuti	MDOF	U_{max}
2013	Wen et al.	SDOF	$U_{max}, T_b, A_t, R_{drift}$

In detail, the design procedure followed in the present work is presented in the following lines. The chosen approach is the one suggested by Ponzo et al. [151] [152] and based on a nonlinear static analysis method, as described in the Italian and European seismic codes. It is an iterative target displacement-based methodology, and it can be subdivided into four main steps, schematised in Figure 6.24.

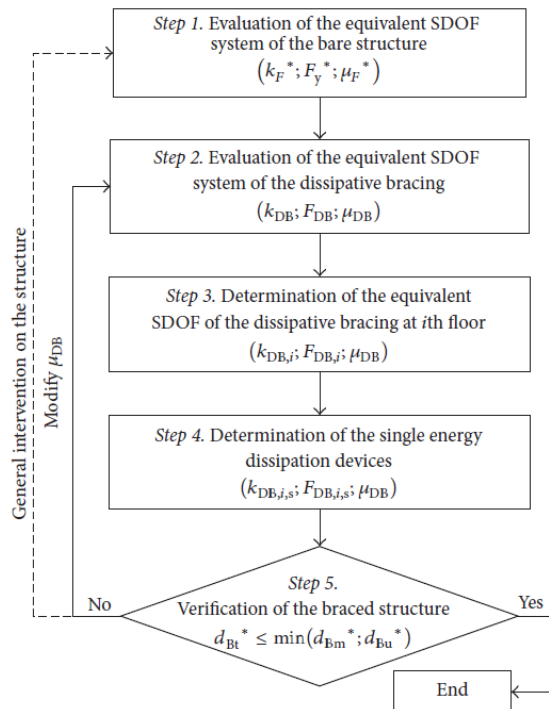


Figure 6.24. Flow chart of the approach followed in the present work for the design of dissipative braces [143].

Step 1 consists in the evaluation of the equivalent SDOF system of the main structure for determining its mechanical characteristics. After performing Pushover analyses and obtaining capacity curves for both directions, the idealised force-displacement of the structure is defined. Thus, the yield force (F_y^*), the yield displacement (d_y^*) or the elastic stiffness (k_F^*), and the ultimate displacement (d_u^*) are calculated.

Step 2 is, instead, centred on the evaluation of the equivalent SDOF system of the dissipative bracing. This stage represents the core of the whole procedure, and the selection of the correct retrofit is evaluated through various iterations until reaching the best configuration. First of all, the maximum displacement d_{Bm}^* of the equivalent SDOF system of the braced structure (existing building + damped bracing) is assumed. If the structure should remain in the elastic range, then $d_{Bm}^* \leq d_y^*$. In case of the main structure is thought for entering the plastic region, then $d_y^* < d_{Bm}^* \leq d_u^*$. Thus, the ductility factor of the equivalent bracing system (μ_{DB}) is evaluated according to the type of the chosen hysteretic device. Knowing that the ultimate displacement of the equivalent bracing d_{DBu} is assumed to be equal to the d_{Bm} , the yielding displacement of the bracing system (d_{DBy}) can be calculated with Equation 6.9.

$$d_{DBy} = \frac{d_{Bm}^*}{\mu_{DB}} \quad (6.9)$$

The next stage is the calculation of the elastic stiffness of the bracing system at the j th step (k_{DB}^j), which could be evaluated according to Equation 6.10. The unknown parameter is the yield force of the damped bracing system (F_{DB}^j). For this reason, an iterative subroutine is necessary until reaching that the obtained results, referred to the j th and $j+1$ step, are lower than the imposed tolerance values.

$$k_{DB}^j = \frac{F_{DB}^j}{d_{DBy}} \quad (6.10)$$

Once the iterative procedure reaches the convergence, all parameters of the equivalent damped bracing are defined, and the trilinear curve which describes the structural behaviour of the system made of the existing structure plus the dissipative braces is obtained by summing in parallel the two contributions. Figure

6.25 depicts the various curves and parameters calculated in the previous steps, evaluated for both short and medium-long period range.

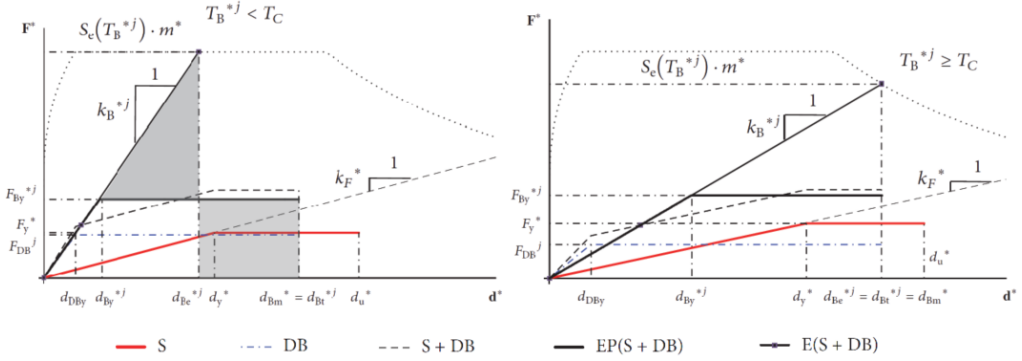


Figure 6.25. Schematisation of the parameters defined in Step 2 for a shot (left) and a medium-long (right) building period. “S” describes the bilinear of the existing structure; “DB” represents the damped bracing system, and “S+DB” is the trilinear obtained by summing the equivalent structure and braces. “EP(S+DB)” describes the equivalent SDOF system of the braced structure, whereas “E(S+DB)” is referred to the elastic braced structure [143].

Step 3 involves the definition of the equivalent dissipative bracing at each storey. Thus, the parameters obtained in the previous stage are distributed along the total height of the building. The distribution of dissipative bracing at each level should be carefully evaluated to guarantee the building regularity in elevation and avoid the risk of excessive inter-storey displacements, as also suggested by the Italian building code. The stiffness of the equivalent bracing at the storey i ($k_{DB,i}$) can be calculated as a function of the single storey existing frame stiffness ($k_{F,i}$) and the ratio (r_k) between k_F^* and k_{DB} which is the elastic stiffness of the bracing systems, as shown in Equation 6.11.

$$k_{DB,i} = r_k * k_{F,i} \tag{6.11}$$

$$r_k = \frac{k_{DB}}{k_F^*} \tag{6.12}$$

$$k_{F,i} = \frac{1}{\Delta s_i} * \sum_i^{n_p} F_i \tag{6.13}$$

where Δ_{s_i} is the inter-storey displacement obtained by means of linear static analyses. By adopting the same considerations, the yield force of the equivalent bracing at the storey i ($F_{DB,i}$) can be calculated as reported in Equation 6.14:

$$F_{DB,i} = r_F * F_{y,i} \quad (6.14)$$

$$r_F = \frac{F_{DB}}{F_y^*} \quad (6.15)$$

$$F_{y,i} = k_{F,i} * d_{y,i} \quad (6.16)$$

$$d_{y,i} = \frac{\Delta_{s_i}}{s_{TOT}} * d_y^* \quad (6.17)$$

where r_F is the ratio between the strength of the equivalent bare structure and the bracing system and $F_{y,i}$ is the yield force of the storey i , calculated with Equation 6.16. The $d_{y,i}$ represents the displacement at the elastic state of the i th floor, whereas the s_{TOT} is the total building displacement defined by means of linear analyses.

Finally, the last stage is focused on the determination of the single energy dissipation device, which is calculated on the base of the characteristics established for the equivalent dissipative devices of each floor. Equation 6.18 and 6.19 allow the calculation of the elastic stiffness of the single dissipative brace ($k_{DB,i,s}$) and its strength ($F_{DB,i,s}$) as a function of the number of braces ($n_{DB,i}$) and their angle with the horizontal (ϕ_s).

$$k_{DB,i,s} = \frac{k_{DB,i}}{n_{DB,i}} * \frac{1}{\cos^2 \phi_s} \quad (6.18)$$

$$F_{DB,i,s} = \frac{F_{DB,i}}{n_{DB,i}} * \frac{1}{\cos \phi_s} \quad (6.19)$$

Once the characteristics of each dissipative brace are known, the last step is their subdivision into the elastic and damping device by considering that they act in series. Thus, the retrofitted structure can be verified through nonlinear analyses for comparing the estimated with the obtained results.

The above-described procedure is adopted for identifying the mechanical characteristics of the dissipative braces designed for the here proposed Engineered DSF. X braces are thus localised on two frames of each façade, in a symmetrical way and at every level, from the building ground floor to the top, in order to ensure the correct stiffness distribution and to avoid torsional phenomena. Moreover, BRAD devices are adequately defined for guaranteeing their activation before the manifestation of brittle failures for non-structural elements.

6.3.2. Static and Dynamic Nonlinear Analyses of the Engineered DSF

Nonlinear analyses are performed to estimate the seismic behaviour of the retrofitted building and to evaluate the effectiveness of the DSF. First, Pushover (PO) simulations are carried on, and comparisons are made between the capacity curves referred to the existing and improved building configuration. Then, Time History analyses are run for verifying the improvements related to the insertion of the suggested solution from a dynamic point of view.

Figure 6.26 shows the PO curves obtained for the case study in the existing (red curves) and retrofitted (beige curves) version. The addition of the system made of the Double Façade with dissipative braces increases the ductile behaviour of the main structure, with benefits on both x and y directions. Moreover, the comparison of the inter-storey drifts estimated for the two models (see Figure 6.27) underlines the effectiveness of the retrofit intervention, able to ensure similar storey displacements at each floor and equal vertical stiffness distribution. By inserting the DSF, in fact, the obtained inter-storey drifts lay under 1%, whereas the existing building exhibits higher values, especially at the ground floor. It is crucial to bear in mind that the here presented comparisons are made assuming as last point of the PO simulations the one for which, in the original configuration, an inter-storey drift equal to 1.87% is reached.

As required by the Italian building code, the capacity curves obtained for the retrofitted model are bilinearised and compared with the ADRS spectrums. The Hazus criterion is adopted, and the PO curves are interrupted when the inter-storey drift assumes, at least at one floor, the value of 1.87%. Also in this case, only the positive direction is evaluated for each force distribution. The bilinear curves, plotted from Figure 6.28 to Figure 6.31, show that the displacement demands for the selected limit states are always verified.

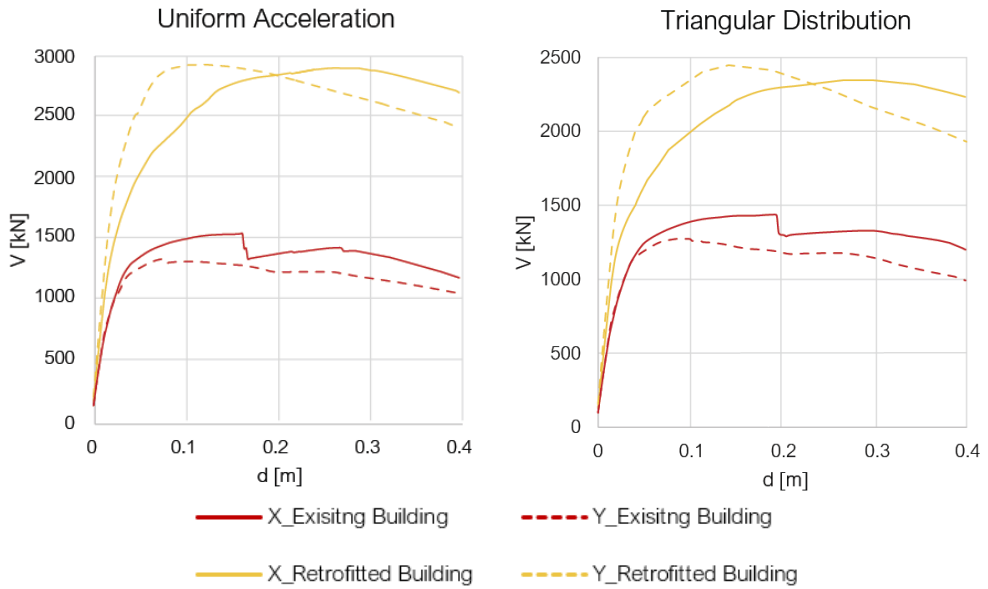


Figure 6.26. PO capacity curves for the case study before and after the insertion of the Engineered DSF.

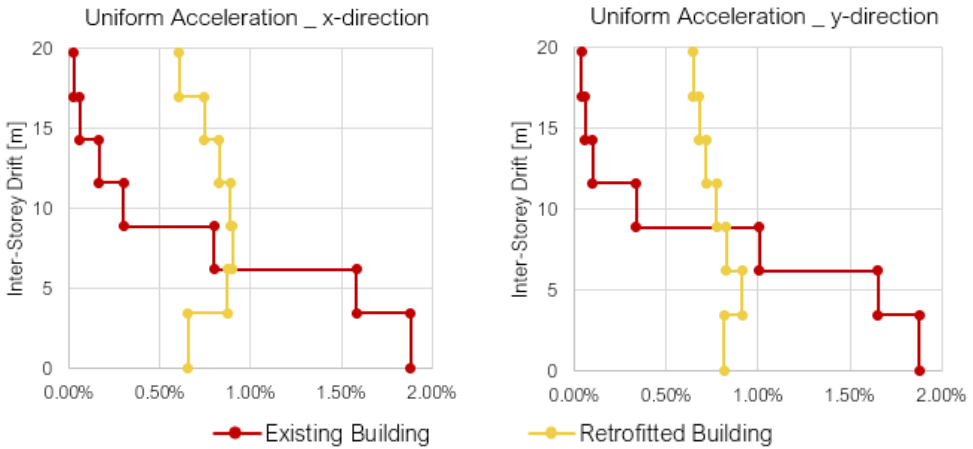


Figure 6.27. Comparisons of the inter-storey drifts estimated for the reference building before and after the insertion of the Engineered DSF.

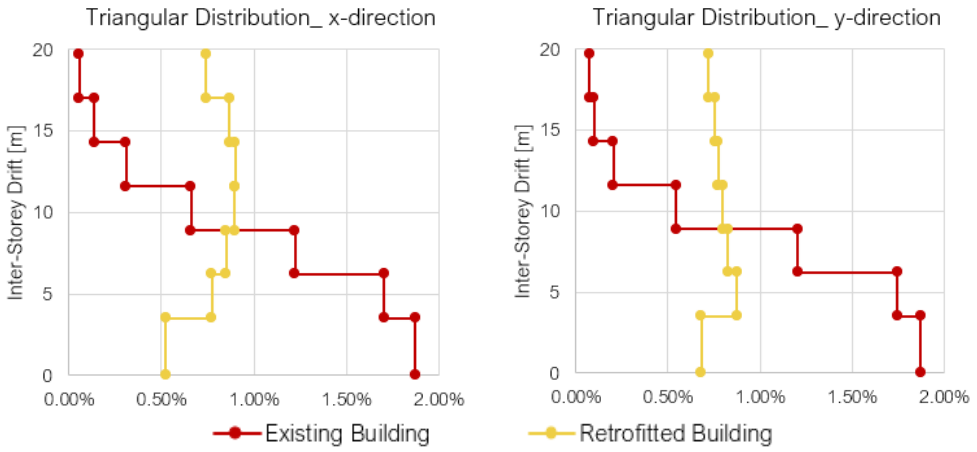


Figure 6.27. (Continued).

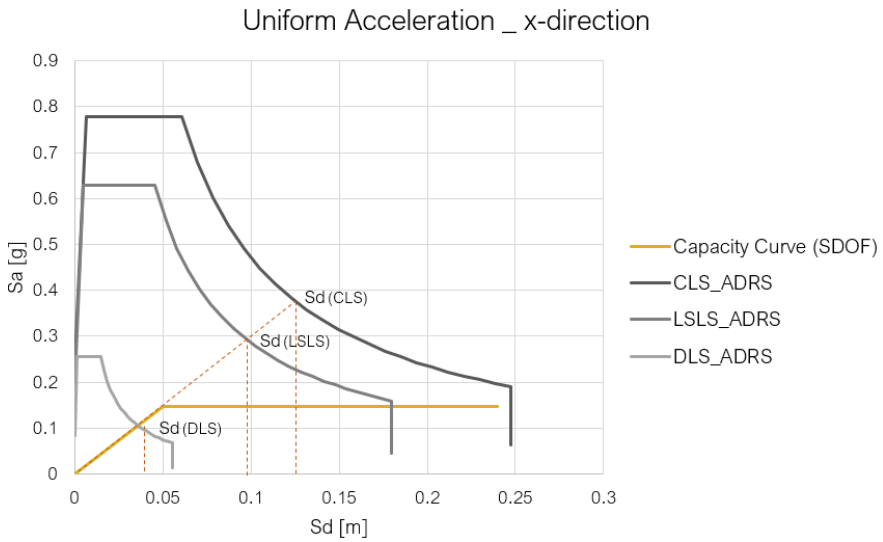


Figure 6.28. ADRS and displacement demands at DLS, LSL, and CLS for the uniform acceleration force distribution, x-direction (Retrofitted building).

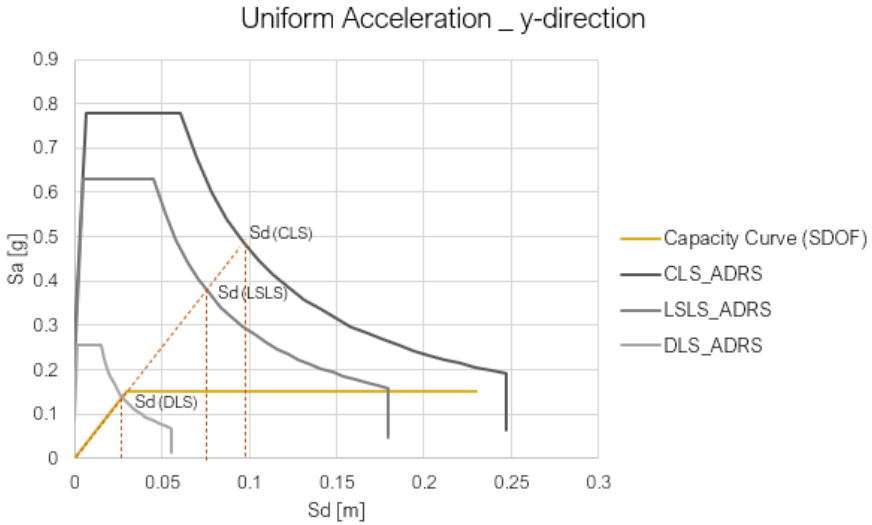


Figure 6.29. ADRS and displacement demands at DLS, LSLs, and CLS for the uniform acceleration force distribution, y-direction (Retrofitted building).

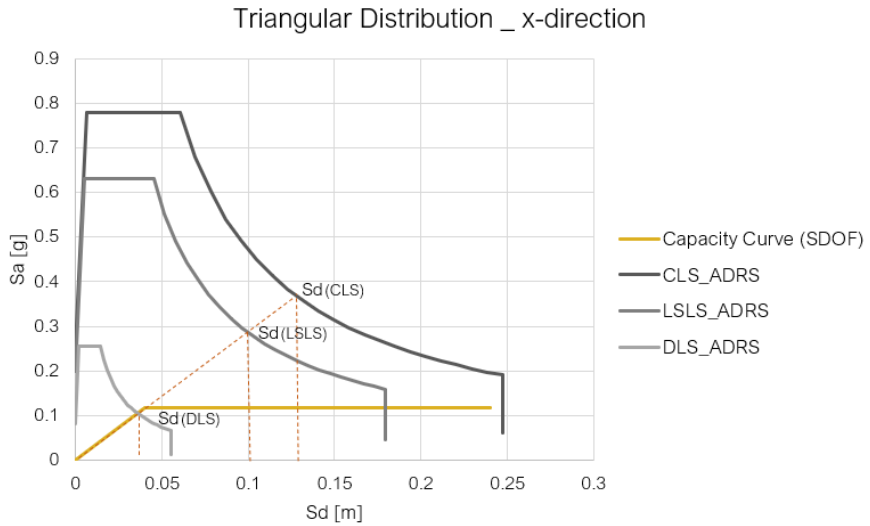


Figure 6.30. ADRS and displacement demands at DLS, LSLs, and CLS for the triangular force distribution, x-direction (Retrofitted building).

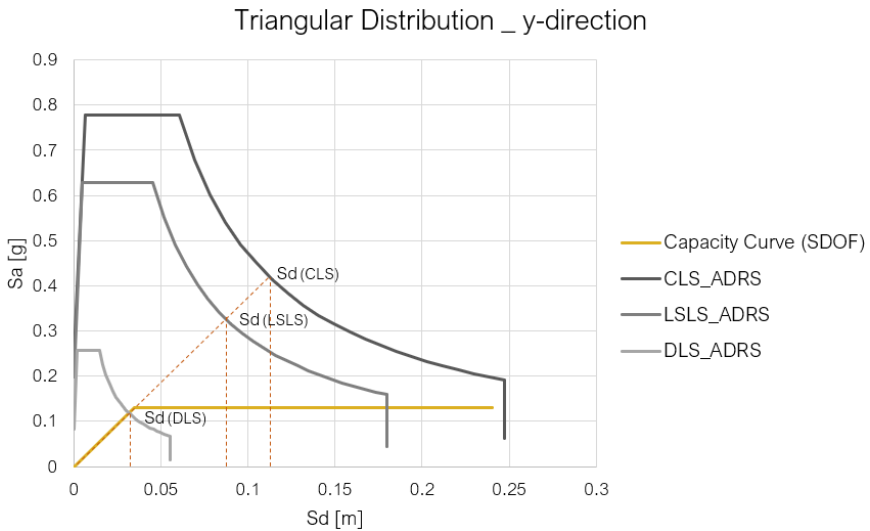


Figure 6.31. ADRS and displacement demands at DLS, LSLS, and CLS for the triangular force distribution, y-direction (Retrofitted building).

Nonlinear Time History analyses are carried out for validating the suggested option and comparing the outputs, expressed in terms of inter-storey drifts, related to the original and improved configuration of the case study. A crucial point of these types of analyses is the selection of appropriate inputs, which are able to correctly describe the seismicity of the site where the structure is located. For the following simulations, seven couples of accelerograms, compatible with the code spectrum of Pescara (soil category C and Topography T1), are obtained by using the software Roxel (version 3.5) [153]. The records are real earthquakes, opportunely scaled to fit Pescara Response Spectrum at, respectively, the Life Safety Limit State and the Damage Limit State. Details and information about the settings and records are described in Appendix F. Figure 6.32 and Figure 6.33 show the DLS and the LSLS Response Spectrum, while Table 6.5 and Table 6.6 summarise the principle aspects of the selected real earthquakes.

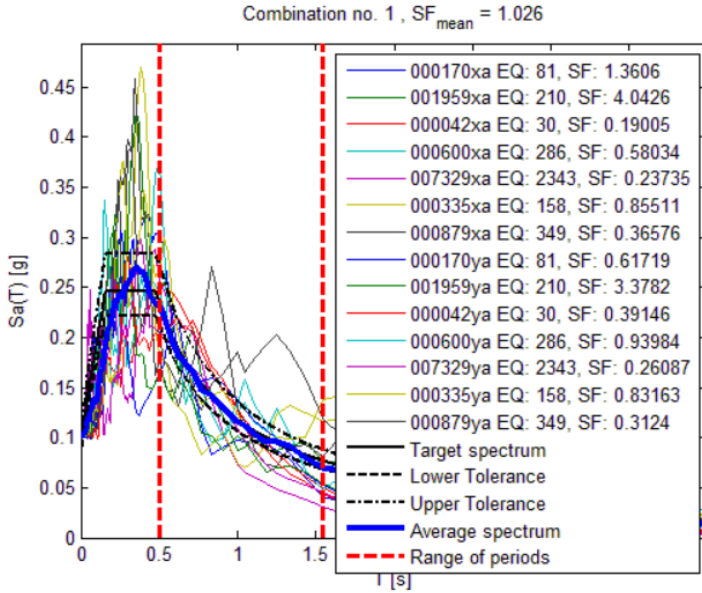


Figure 6.32. Combination of the selected accelerograms at the DLS.

Table 6.5. Presentation of main aspects of the real earthquakes selected from the European strong motion database for the DLS.

Waveform ID	Earthquake Name	Date	Mw	Fault Mechanism	Epicentral Distance [km]	PGA_X [m/s ²]	PGA_Y [m/s ²]	PGV_X [m/s]	PGV_Y [m/s]	ID TH Analyses
170	Basso Tirreno	15/04/1978	6.00	Oblique	18	0.72	1.58	0.06	0.15	Acc 1
1959	Kyllini	16/10/1988	5.90	Strike slip	49	0.24	0.29	0.02	0.02	Acc 2
42	Ionian	04/11/1973	5.80	Thrust	15	5.15	2.50	0.57	0.26	Acc 3
600	Umbria Marche	26/09/1997	6.00	Normal	22	1.69	1.04	0.14	0.12	Acc 4
7329	Faial	09/07/1998	6.10	Strike slip	11	4.12	3.75	0.28	0.35	Acc 5
335	Alkion	25/02/1981	6.30	Normal	25	1.14	1.18	0.11	0.15	Acc 6
879	Dinar	01/10/1995	6.40	Normal	8	2.67	3.13	0.29	0.41	Acc 7

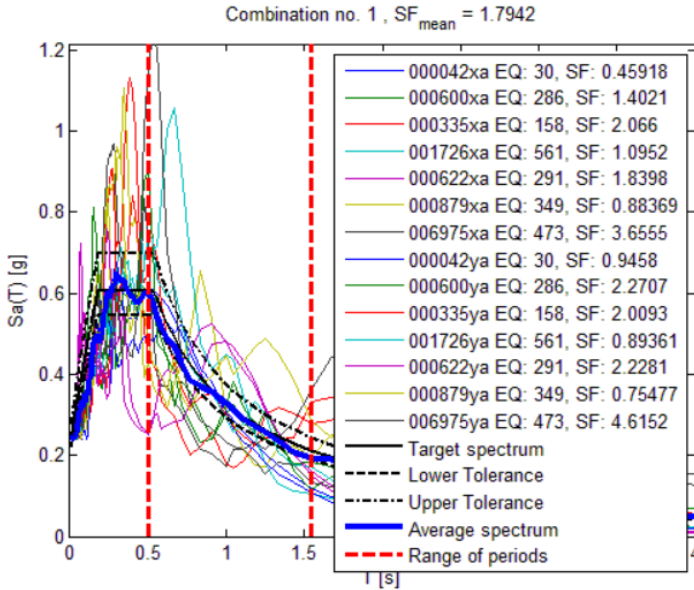


Figure 6.33. Combination of the selected accelerograms at the LSLs.

Table 6.6. Presentation of main aspects of the real earthquakes selected from the European strong motion database for the LSLs.

Waveform ID	Earthquake Name	Date	Mw	Fault Mechanism	Epicentral Distance [km]	PGA_X [m/s ²]	PGA_Y [m/s ²]	PGV_X [m/s]	PGV_Y [m/s]	ID TH Analyses
42	Ionian	04/11/1973	5.80	Thrust	15	5.15	2.50	0.57	0.26	Acc 1
600	Umbria Marche	26/09/1997	6.00	Normal	22	1.69	1.04	0.14	0.12	Acc 2
335	Alkion	25/02/1981	6.30	Normal	25	1.14	1.18	0.11	0.15	Acc 3
1726	Adana	27/06/1998	6.30	Strike slip	30	2.16	2.64	0.28	0.20	Acc 4
622	Umbria Marche (aftershock)	06/10/1997	5.50	Normal	7	1.28	1.06	0.11	0.10	Acc 5
879	Dinar	01/10/1995	6.40	Normal	8	2.67	3.13	0.29	0.41	Acc 6
6975	Izmit (aftershock)	13/09/1999	5.80	Oblique	26	0.65	0.51	0.06	0.07	Acc 7

The chosen input to be investigated in the here presented analyses is the inter-storey drift, as previously done for the Pushover simulations. In the specific case, the parameter is estimated for every direction, both x and y, and for the DLS and LSLs. The outputs are predicted for the reference building, considering its existing configuration (referred as “EB” in the graphs) and the retrofitted version

(referred as “RB” in the charts). Figure 6.34 and Figure 6.35 show the effectiveness of the proposed solution. The insertion of the Engineered Double Skin, in fact, allows better control of the inter-storey drift, avoiding excessive variations of displacements between one floor and the other. The maximum inter-storey drift estimated for the improved version is opportunely reduced, matching with the prescription of the Italian and European building code related to the Damage Limit State (see Figure 6.34). It assumes an averaged value equal to 0.24%, which is lower than the maximum admissible drift set at 0.50% (§7.3.6.1 Elementi Strutturali (ST) - NTC2018). Looking at the Life Safety Limit State, the improved performance is more evident, as it can be observed in Figure 6.35. In this case, the averaged value is reduced from 1.20%, referred to the original building configuration, to 0.75% in case of the retrofit intervention. On the base of these considerations, the seismic performance of the case study can be considered improved.

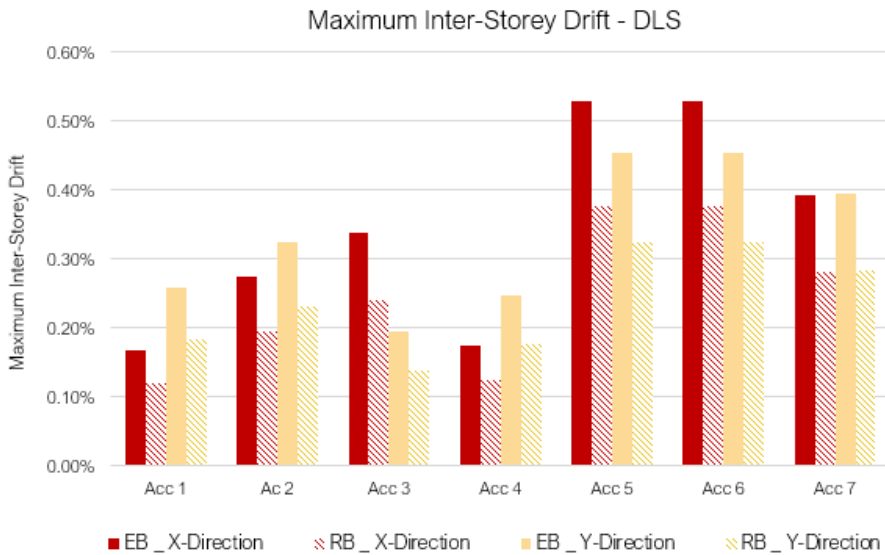


Figure 6.34. Comparisons between maximum inter-storey drifts estimated for the x and y-direction and referred to the selected accelerograms at DLS.

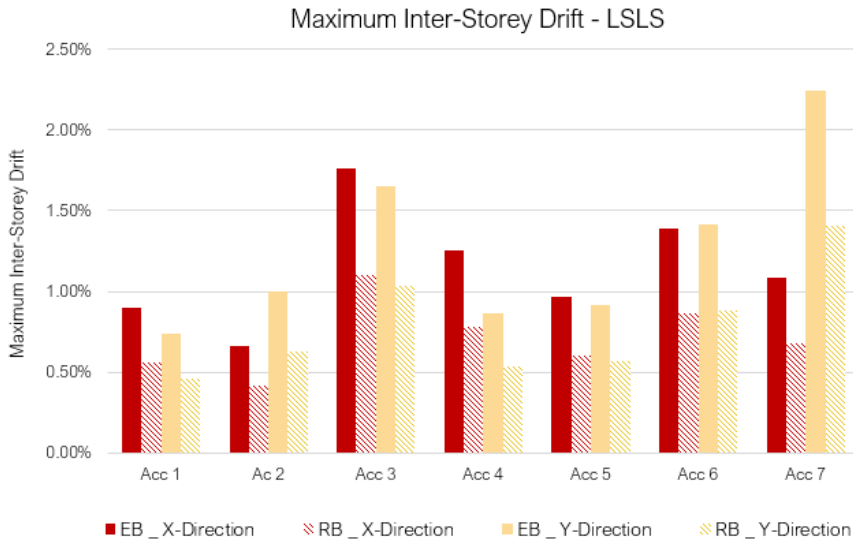


Figure 6.35. Comparisons between maximum inter-storey drifts estimated for the x and y-direction and referred to the selected accelerograms at LSL.

6.4. Conclusions

The performed analyses underline several findings that can be summarised as follows:

- Introducing the Double Skin Façade along with the dissipative braces leads to improve the seismic performance of the main structure by overcoming the deficiencies that commonly characterised the buildings' design in past years. In fact, by carefully choosing the positioning of BRAD devices, it is possible to reduce the vertical and in-plan irregularities, which negatively affect the structural behaviour under horizontal loads.
- Moreover, the suggested solution increases the ductility capacity of the main building. In fact, the ultimate displacement of the pushover control node (assumed as the top displacement) increases by approximately 50% (passing from approximately 12-14 cm to 23-24 cm), depending on the direction and force distribution. Thanks to this increment, the retrofitted structure not only satisfies all requirements defined by the Italian building code, but also verifies the Collapse Limit State, which refers to a more demanding design spectrum.

- Besides the ductility improvement, the insertion of the DSF leads to an increase of the overall stiffness, with higher forces being transferred to the foundation level. More specifically, the base shear for the retrofitted model is approximately twice the one referred to the pre-intervention configuration.
- The insertion of dissipative devices into which concentrating the seismic energy dissipation guarantees the safety of the structure. In addition, damaged BRADs may be easily replaced, with benefits in terms of costs and recovery time. Indeed, it would be possible for the building to resume its functionality shortly after a seismic event.

On the base of the here presented consideration the use of the Engineered Double Skin Façade represents a good option for the retrofit of existing buildings.

7. Life Cycle Analyses

7.1. Introduction

The Life Cycle Sustainability Assessment (LCSA) is the evaluation of all environmental, social and economic negative impacts and benefits in decision-making processes towards more sustainable products throughout their life cycle [154]. The Life Cycle Thinking (LCT) or Life Cycle Perspective (LCP) is the only systematic approach able to evaluate the global impact of products or processes, considering their entire life, from raw material extraction and acquisition to use and end-of-life disposal. Various are the benefits related to the use of LCSA techniques. The LCSA, in fact, can help consumers in determining which products are not only cost-efficient, eco-efficient or socially responsible, but also more sustainable; it supports decision-makers in prioritising resources that have more chances of positive impacts and shows enterprises how to become more responsible for their business by taking into account the full spectrum of implications associated with their products and services [154].

The Life Cycle Analysis is part of ISO 14040:2006 (Environmental management- life cycle assessment - principles and framework) [155] and ISO 14044:2006 (Environmental management - life cycle assessment - requirements and guidelines) [156]. They classify the possible life cycle techniques as follows:

- The Environmental Life Cycle Assessment (ELCA) for measuring the environmental dimension of a product or service.
- The Life Cycle Costing (LCC) which investigates the economic sphere.
- The Social Life Cycle Assessment (SLCA) with the primary objective centred on the evaluation of the social impact of a product or service.

Measuring the environmental dimension of sustainability is widespread, whereas the other two have still limited applications worldwide. Considering their shared background and purpose, ELCA, LCC and SLCA can be combined all together by using the formulation suggested by Klöpffer [157], reported in Equation 7.1.

$$LCSA = ELCA + LCC + SLCA \quad (7.1)$$

The Klöpffer's equation allows to take into account, at the same time, the three sustainability dimensions with only one indicator, represented by the sum of the each investigated area, as depicted in Figure 7.1.

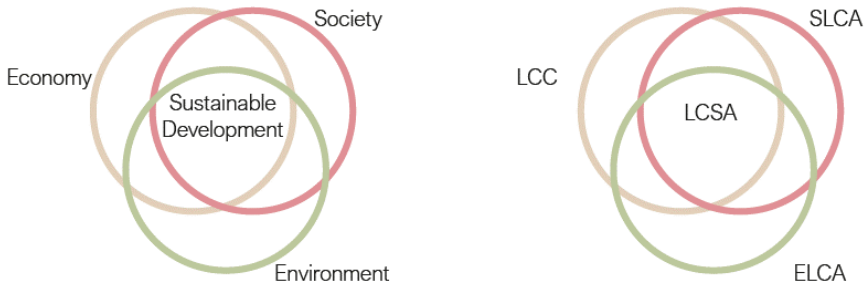


Figure 7.1. The comparison between sustainable development and its pillars (left) and the Life Cycle Sustainable Assessment (right).

As established in the ISO 14040 and 14044 standards, The ELCA (hereafter referred as LCA) is carried out in four phases, which are typically interdependent. These phases, summarised in Figure 7.2, are the goal and scope definition, the inventory of resources use and emissions, the estimation of the impact assessment and the interpretation of the results.

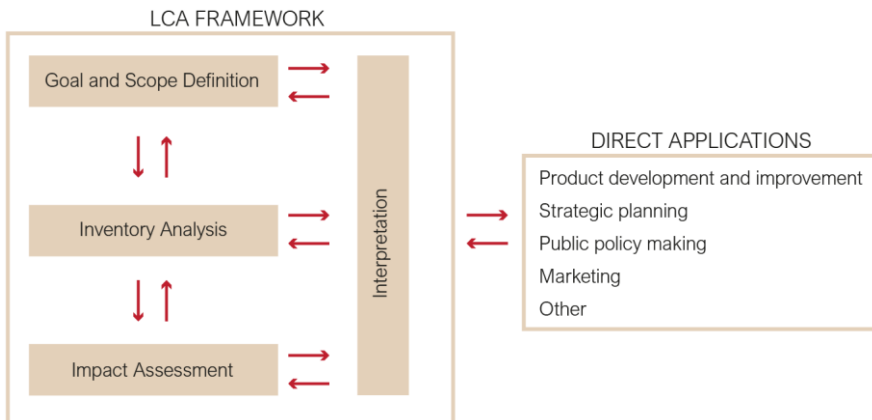


Figure 7.2. Stages of an LCA (elaborated from [155]).

The first phase defines the purpose of the analysis, its application, the products to be used, the system boundaries and the functional units. The second step consists, instead, in the elaboration of a detailed description of all the environmental inflows at each stage of the life cycle. For this step, the global product is subdivided into its components, and the various processes are identified. According to the standards, the results coming from the inventory analysis are classified into impact categories that can be aggregated, considering their effects on the human health, the environmental or the resource depletion (see Table 7.1). The interpretation of the results represents the last stage, and it consists in the identification of all life cycle phases and products with the highest environmental impact.

Table 7.1. List of the impact categories with the corresponding damage sectors.

Impact Categories	Damage Categories		
	Human Health	Resource Depletion	Ecosystem Quality
Climate change			
Resource depletion			
Land use			
Water use			
Human toxic effects			
Ozone depletion			
Photochemical ozone creation			
Ecotoxic effects			
Eutrophication			
Acidification			
Biodiversity			

It is essential to underline that there is not only one way for carried on Life Cycle Assessment analyses but several options that should be adopted and chosen, case by case, on the basis of several factors as products, strategy, systems and available tools. Moreover, there could be several variants of LCAs according to the life cycles selected for the analysis. The Cradle-to-Grave approach is the full life cycle assessment from the resource extraction (“cradle”) to

the use phase and disposal (“grave”). A variation of this approach is the Cradle-to-Cradle analysis for which the end-of-life disposal step coexists with the recycling process of the product. The Cradle-to-Gate assessment considers the partial product life cycle, from resource extraction to the factory gate. Finally, the last possible approach is the Gate-to-Gate that is a partial LCA, focused only on the value-added process in the entire production chain. Figure 7.3 schematises the here-mentioned options.

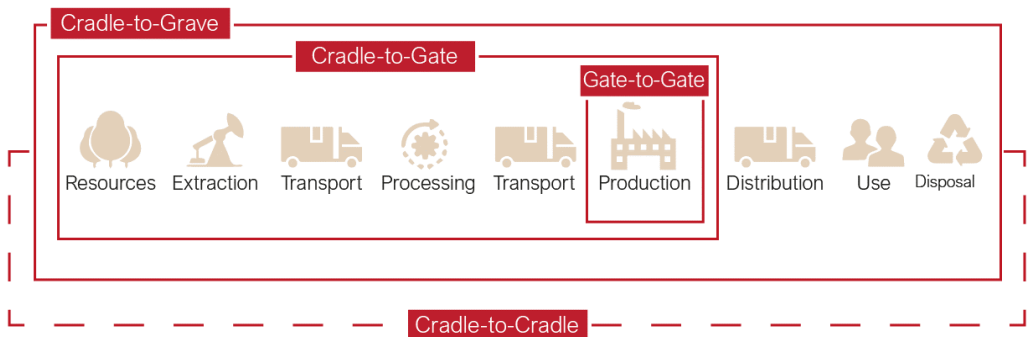


Figure 7.3. Life Cycle Assessment possible approaches.

Nowadays, LCA analyses are commonly performed in all sectors and various programs (e.g., GaBi, SimaPro, openLCA, One Click LCA), both open-source and not, are adopted for the calculations. The main limitation of these analyses could be the absence of specific databases, actualised in time or referred to a location, with effects on the accuracy of the results.

This chapter is addressed to a comparative study about LCA analyses carried on for the selected Double Skin Façades in order to identify the environmental impact due to each configuration and to define the most eco-efficient option. The analyses are performed using the One Click LCA software (trial version). The chapter is structured as follows. After this introduction centred on the description of basic information about the Life Cycle Thinking, and the possible approaches, few examples of the use of LCA analyses applied to the construction sector are shown in Section 7.2. Subsequently, Section 7.3 presents the evaluation of the use of the holistic approach to DSF buildings, whereas Section 7.4 summarises the LCA analyses performed for the DSF typologies selected for the current work. Finally, Section 7.5 draws the main conclusions.

7.2. LCA and Buildings

The application of the LCA to the construction industry started two decades ago, and its interest has recently increased, thanks to its capability in the monitoring of all stages of the product life cycle thus orienting the building design towards directions with the lowest environmental impact. Performing LCA analyses during the project phase, in fact, ensures the reduction of the embodied impacts associated with, for example, the use of energy, water or materials. Two alternatives are generally adopted when LCA analyses are performed for the building sector, and they are:

- The LCA for building materials and component combinations (bottom-up).
- The LCA of the whole construction process (top-down).

According to Rodrigues et al. [158], building materials have the highest values of embodied energy and carbon, if compared to the other processes during the construction of the industry. In particular, more processed materials, such as metals and concrete, contribute more than natural or less processed materials as soil, stone and wood, because of a higher energy use necessary for their generation. Other LCA analyses have been carried on by Adalberth et al. [159] for evaluating which phase among manufacturing, transport, erection, use, renovation, demolition and removal has the most significant impact for a multi-family building located in Sweden. The results underline that the use phase accounts for 70%-90% of the total environmental impact of the building.

The literature review shows that most of the LCA analyses in this sector are mainly centred on the evaluation of various impacts related to new buildings, whereas there are very few works focused on the calculation of the environmental cost of retrofit interventions. Generally, in fact, during the building restoration, the principal aspects which are taken into account are the prices, the structural or energy performance of the intervention and the feasibility of the maintenance process. Even if rare, there are some examples that use LCA analyses for orienting retrofit interventions and selecting the option which performs better in life cycle environmental impact than the building in the original configuration. This is the case of the LCA analyses carried on by Gu et al. [160] for evaluating the impact of several schemes of envelope design, applied to an office building in order to adopt the less impacting strategy. A second example is a study conducted by Vitiello et

al. [161], centred on the evaluation of different straightening solutions applied to a reinforced concrete building located in Italy. In detail, the insertion of FRP sheets on structural elements or above the surface of beams and joints, the RC jacketing of columns, the RC shear walls installation and the base insulation are the options investigated by using the Life Cycle Assessment. The main research finding is that, among all categories, the base insulation has, for the specific case study, the lowest environmental impact, representing the greenest retrofit solution. It is essential to bear in mind that the limited use of LCA analyses for building restoration is also due to their strict dependence to the case study and, for example, to its vulnerability or the seismic hazard of the site.

7.3. LCA and Double Skin Façades

The operational energy of Double Skin Façade building has been mainly investigated, considering various configurations and climatic conditions. The wealth of studies on the operational phase of DSFs are starkly contrasted by extremely limited knowledge about its embodied energy and carbon. Only a few studies provide a detailed evaluation of DSF systems from a Life Cycle Perspective, and most of them are referred to specific conditions or locations, not allowing the replicability of the results. Moreover, the evaluation of the life cycle impact of multi-layer façades is usually cost-oriented for defining the real feasibility of these systems in comparisons to less expensive solutions. LCA analyses are, in fact, carried on by Stribling et al. [162] for calculating the projected payback period due to various Double Façade construction systems, located in three cities different for the climatic zone (London, Las Vegas and Winnipeg). The analysis underlines that the DSF construction costs are higher than other restorative interventions with a consequent longer payback period, estimated from 30 up to 200 years. Cities with extreme conditions ensure a lower payback period thanks to the better DSF performance. The obtained results are also confirmed by the LCA analyses performed by Cakmanus [163] who has evaluated the insertion of a DSF, opportunely shaded and ventilated, for the restoration of an office building in Ankara, underlining the high constructions costs of the system.

An interesting attempt for filling the knowledge gap between operable energy of DSFs and their life cycle performance has been made by Pomponi et al. [164]. Several Cradle-to-Gate Life Cycle analyses have been carried out to estimate the

environmental impact of DSFs used for the restoration of an office building located in London. The primary purpose of the study has been comparing the total environmental impact of the DSF retrofit with a single-skin alternative. Thus, a parametric study has been conducted for testing various DSF configurations. Cavity width, glass composition and coating, source of construction materials, and orientations of the building have been the investigated elements, and the performance of each typology of DSF has been expressed in terms of embodied energy and carbon. In total, the study has evaluated 128 Double Façade options. The outputs have been calculated for all LCA stages identified as follows:

- Product and construction process stages (Winning raw materials, manufacturing/production, construction).
- Use stage (Post-occupancy, maintenance, and repair).
- End of life stage (Disassembly, disposal/recycling).

According to the obtained results, the majority of the options that consider the restoration by inserting DSFs perform exceptionally well when looked at them from a life cycle perspective. In detail, 98% of the DSF configurations has a better life cycle energy performance than the single skin alternative and nearly 83% a better life cycle carbon performance. It is clear that even if multiple façades have, from one side, the greatest construction costs, on the other, they are able to cut down the operational energy load, allowing more appreciable reduction than working directly on the building envelope. However, it is crucial to bear in mind that the effectiveness of the solution is strongly influenced by the design phase and wrong decisions can have adverse effects on the life cycle balances and the real feasibility of the retrofit intervention. In conclusion, even with a higher initial construction cost, the DSF could be considered as a successful means to reduce the life cycle energy consumption of existing buildings as well as a low-carbon technology for their sustainable refurbishment.

7.4. LCA Applied to the Engineered Double Skin Façade

LCA analyses are performed for evaluating the environmental impact related to the Double Skin Façade options investigated in the current work. The primary purpose of the study is orienting the choice towards the most eco-efficient solution for minimising the impact that a such conceived system could have on the

environment. It is essential to underline that the here presented analyses are not referred to the whole life cycle of DSFs but take into account only primary aspects, putting in evidence the estimated differences between one configuration and the others. Moreover, the results are referred to the impacts due to the generation, transportation and disposal of building materials (steel structure and glazed surfaces), ignoring BRAD devices. The calculations are performed with both DesignBuilder and One Click LCA tool. In detail, DesignBuilder is used for estimating the Embodied and Equivalent Carbon, whereas One Click LCA shows results in terms of Global Warming impact category.

The Embodied Carbon represents all the CO₂ emitted in the producing materials. It is estimated to extract and transport raw materials as well as emissions from manufacturing processes. It is used as an indicator for identifying elements which are carbon-intensive and promote alternative options able to reduce the amount of CO₂ realised. The Equivalent Carbon is similar to the Embodied index but it also includes the effects of other greenhouse gases providing an equivalent amount of CO₂ that would cause the same quantity of global warming as the actual greenhouse gases emitted by the processes involved in the material production. The Global Warming potential can be defined, instead, as the parameter which is able to describe changes in local, regional, or global surface temperatures caused by an increased concentration of greenhouse gases in the atmosphere. It is calculated in carbon dioxide equivalents meaning that the greenhouse potential of emission is given in relation to CO₂.

The Global Warming potential is estimated for three main LCA stages. The first considers the emissions generated when raw materials are taken from nature and transported to industrial units for being processed. This phase takes into account the transport impact due to the movement of all raw materials from suppliers to the manufacturer's production plant as well as impacts of the production of fuels and those caused by the material processing. The second stage evaluates the transportation of materials from the production plant to the building site. Finally, the last phase is the deconstruction, and it evaluates the impacts for processing recyclable construction waste flows or for landfilling waste streams that can not be recycled.

Figure 7.4 depicts the comparison, made in terms of Embodied and Equivalent Carbon, associated with each DSF configuration. According to the

results, the lower environmental impact is ensured by the Multi-Storey typology, which has the smallest value of Embodied and Equivalent Carbon. This configuration, in fact, does not present any partition of the cavity and, for this reason, it uses the lowest amount of materials, with a consequent reduced environmental impact. Also the Shaft-Box typology allows a discrete performance. The insertion of vertical partitions increases the CO₂ emissions, conferring higher values if compared to the Multi-Storey typology but lower than the estimations referred to the Corridor and Box-Window DSF. The two last configurations have similar performances and show the highest emissions. In particular, the Box-Window Double Skin, presenting small cells subdivided by horizontal and vertical partitions, has the most significant impact, quantified as the double of the values calculated for the Multi-Storey configuration.

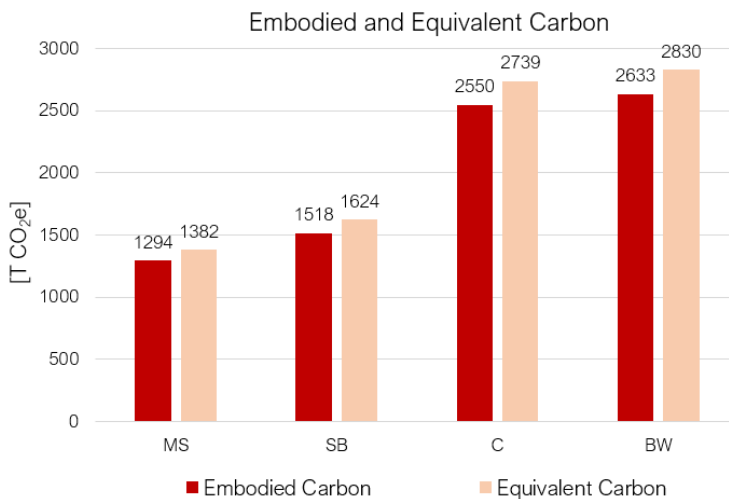


Figure 7.4. Embodied and Equivalent Carbon estimated for the selected DSF options.

Evaluating the Global Warming impact (Figure 7.5 to Figure 7.8), it is clear that, among the various stages, higher CO₂ emissions are related to the material processing, and this is valid for all DSF configurations and structural components. The Multi-Storey DSF (Figure 7.5) shows its most significant emissions for processing glazed surfaces. Also the steel frame component accounts for a high value, whereas ceilings and floors impact in the same way and with a very low amount. The disposal of the structural components does not substantially affect Global Warming. Similar considerations can be made for the Shaft-Box

configuration (Figure 7.6) for which only a few variations appear. The insertion of vertical partitions for subdividing the cavity, in fact, causes higher emissions related to the glazed surfaces and steel frame. A greater impact is estimated, instead, for the Corridor (Figure 7.7) and Box-Window (Figure 7.8) typologies. In both cases, the predicted Global Warming impact is generally much higher than the previous configurations, especially for the emissions referred to the material processing of the floor component that are more than six times bigger than the Multi-Storey and Shaft-Box DSF.

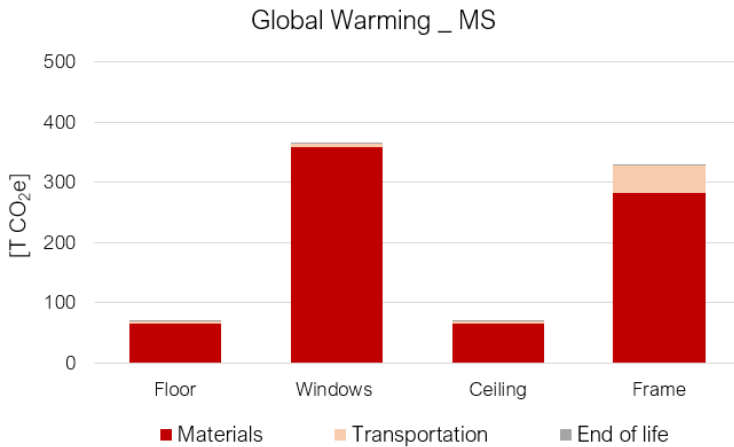


Figure 7.5. Global Warming impact category referred to the Multi-Storey DSF.

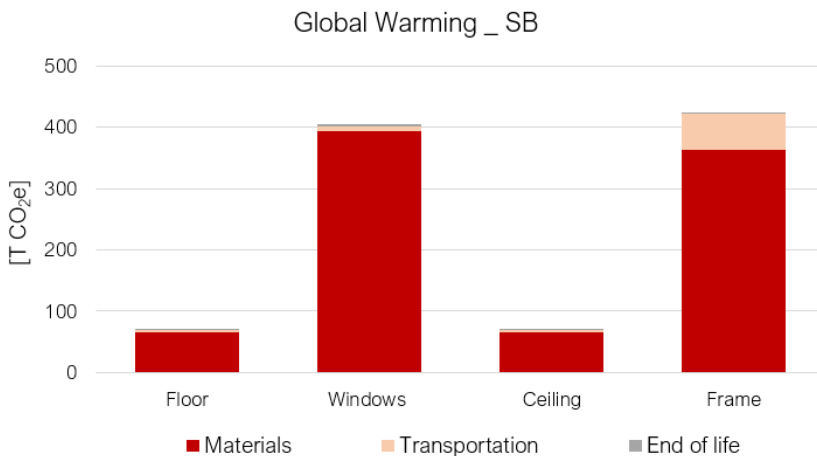


Figure 7.6. Global Warming impact category referred to the Shaft-Box DSF.

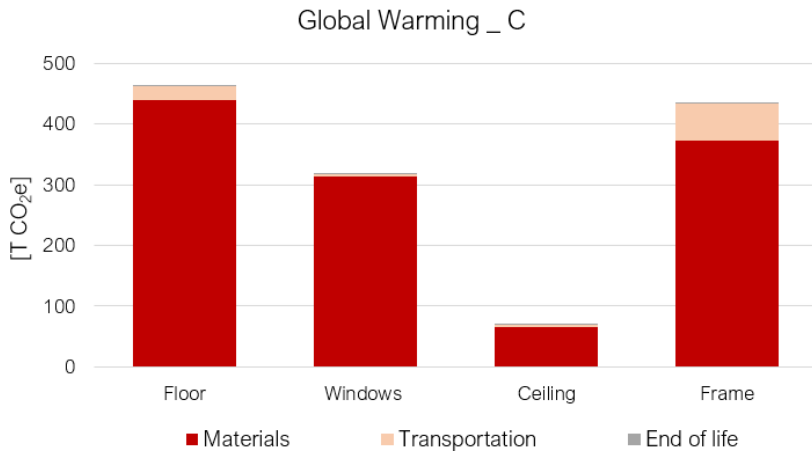


Figure 7.7. Global Warming impact category referred to the Corridor DSF.

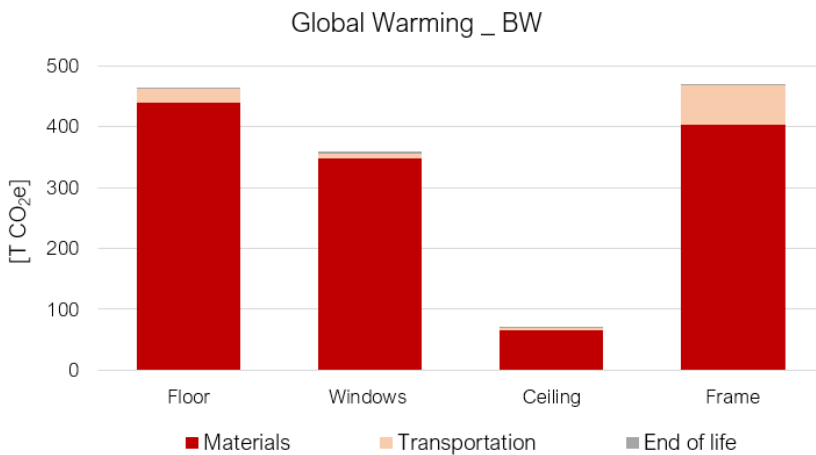


Figure 7.8. Global Warming impact category referred to the Box-Window DSF.

7.5. Conclusions

The performed LCA analyses underline the significant environmental impact of the suggested Double Skin Façades. The insertion of a new layer for the structural and energetic retrofit of existing buildings, in fact, involves a considerable investment, in terms of money and materials. According to the estimations, the amount of CO₂ equivalent emitted for all DSF typologies is much bigger than the one that would be related to commonly adopted retrofit interventions. This is due

to the use of high processing materials as metal and glass. Moreover, the material generation phase has the most significant responsibility for emissions. In contrast, the transportation and the end-of-life stage weakly affect the outputs. For all DSF configurations and components, in fact, the material processing accounts for 86% up to 97% of the total emissions of a single element, evaluating its life cycle. The other stages, in comparisons, seem to be negligible with very low CO₂ emissions.

A second important finding is referred to the LCA performance of each DSF typology. As expected, the Multi-Storey DSF ensures, according to the selected LCA indicators, the lowest environmental impact. The absence of any type of cavity partitions allows the reduction of the used materials with the consequent decrement in terms of environmental impact. Good performances are also estimated with the Shaft-Box façade, whereas the Corridor and Box-Window configurations confirm to be the most impacting due to the relevant number of components.

In conclusion, performing LCA analyses for evaluating the environmental impact of DSF systems could be the unique and reliable method able to orient design choices to more eco-efficient solutions. In this way, the effectiveness of the Double Façade is evaluated not only in terms of operable energy but also considering the other stages not related to the use of the building. Moreover, performing Life Cycle Assessment analyses, environmental or cost-oriented, is the sole option for the correct calculation of the payback period estimated for the whole life cycle of the retrofit solution.

8. Conclusions

In the current dissertation, the holistic renovation of existing buildings by inserting an Engineered Double Skin Façade is proposed. The suggested solution, able to increase the structural service life while pursuing safety, sustainability and resilience was evaluated by means of multisectoral simulations and Life Cycle Thinking approaches. Structural, energy, fluid dynamics and LCA analyses were performed for testing the effectiveness of the DSF and estimating the improvements achievable in case of retrofit interventions. The suggested solution was applied to an existing reinforced concrete building, located in Pescara (Central Italy), which presents evident structural and energetic deficiencies and minor architectural value.

8.1. Major Contributions and Significant Results

The energy simulations have underlined the effectiveness of Double Façades for the retrofitting of existing buildings. By inserting a well designed and oriented DSF, the energy consumption due to the conditioning of the occupied spaces can be drastically reduced. In fact, thanks to its capability of acting as a buffer zone or a ventilated channel, it allows good performances for the whole year. During the wintertime, the external layer increases the thermal properties of the building envelope. In the hottest months, instead, the ventilated cavity encourages the free cooling of the inner spaces, with benefits in terms of energy requirement and inhabitants' comfort conditions. Among the various investigated DSFs, the Multi-Storey configuration ensures better performances, allowing a more significant reduction of building environmental impact than the other typologies. The effectiveness of the solution is also confirmed by considerations about climate change and its effects on building cooling needs, which could be mitigated by inserting the DSF system.

Similar findings have been confirmed by performing CFD simulations. According to the obtained results, the insertion of the Double Façade avoids the air stagnation around the building, and the stuck effect of the cavity increases the inner free cooling. Also in this case, the Multi-Storey DSF is the configuration with

better performances, ensuring the highest velocity profile in comparison to the other typologies. The effectiveness of the Double Façade can be increased by adopting more aerodynamic shapes, able to reduce friction losses and to encourage cavity ventilation. Moreover, another aspect that should be taken into account in the case of CFD simulations of DSF systems is that the use of bidimensional analyses can lead to high uncertainty and low accuracy in the predictions.

Besides the positive results obtained from the energy and fluid dynamics simulations, the preformed structural analyses have confirmed the improvement ensured by the addition of the engineered skin. The Double Façade along with dissipative braces improves the seismic performance of the existing structure, increasing the safety level and overcoming the deficiencies such as vertical or in-plan irregularities. Moreover, the retrofit solution allows incrementing the ductility capacity of the main structure, thus complying to current Italian and European seismic code.

Despite the multiple benefits from the structural and the energy efficiency point of view, highlighted by the aforementioned results, the DSF remains a solution with a non-negligible environmental impact. In fact, the use of highly processed materials, such as steel and glass, negatively affect the overall sustainability. Nonetheless, the adoption of the holistic approach has a lower environmental impact than applying the retrofit solutions separately. More specifically, the lowest environmental impact is associated with the Multi-Storey DSF configuration, thanks to the lower quantity of materials needed.

8.2. Future Directions

Future developments of the study should be focused on various aspects. Further analyses could be carried on in order to estimate the thermal bridging effect on cladding systems and ventilated façades. The evaluation of the nature and magnitude of thermal bridges due to the connection of the external skin with the existing building envelope may be a significant weak point in thermal insulation protection, especially in case of absent specific cares during the design stage or the construction process.

Optimised and more aerodynamic shapes could be suggested and tested for improving the fluid dynamic performance of DSF technologies, and new materials (e.g., ETFE polymers or recycled steel) could be adopted for reducing the environmental impact of the solution. Moreover, responsive structures able to guarantee different seismic safety levels according to the earthquake intensity should be proposed and investigated by means of more advanced structural analyses.

Another interesting aspect which could be analysed involves the evaluation of the effectiveness and fluid dynamic behaviour of DSF systems by adopting a meso-microscale numerical approach based on the definition and prediction of the local flow patterns to be assumed as boundary conditions for the CFD and BES simulations. By using this methodology, the air flux estimations and their effects on the natural ventilation of the building occupied spaces would be more representative of the real conditions and the effect of the microclimate on the DSF performance.

Finally, proper Life Cycle Costing analyses should be carried on for estimating the economic impact and the feasibility of the suggested solution.

References

- [1] Mazzarella L. Energy Retrofit of Historic and Existing Buildings. The legislative and Regularity Point of View. *Energy Build.* 2015;95:23–31.
- [2] The European Environment - State and outlook 2020. Knowledge for the Transition to a Sustainable Europe. *Eur Environ Agency.* 2019;1–499.
- [3] BPIE, Europe's Building under the Microscope, Buildings Performance Institute, Europe 2011.
- [4] Global Status Report 2017. Towards a Zero-Emission, Efficient, and Resilient Buildings and construction Sector. *UN Environ.*
- [5] Directive 2002/91/EC of the European Parliament and of the Council of 16 December 2002 on the Energy Performance of Buildings. *Official Journal of the European Union.* L.1/65,2003 04.1.
- [6] Directive 2010/31/EU of the European Parliament and of the Council of 19 May 2010 on the Energy Performance of Buildings (Recast). *Official Journal of the European Union.* L.153/13,18.6.2010.
- [7] Directive 2012/27/EU of the European Parliament and of the Council of 16 December 2012 on Energy Efficiency, Amending Directives 2009/125/EC and 2010/30/EU and Repealing Directives 2004/8/EC and 2006/32/EC. *Official Journal of the European Union.* L.315/1,14.
- [8] Buildings Performance Institute Europe (BPIE). State of the Building Stock-Briefing. December 2012.
- [9] Belleri A, Marini A. Does seismic risk affect the environmental impact of existing buildings? *Energy Build.* 2016;(110):149–58.
- [10] Passoni C. Holistic Renovation of Existing RC Buildings: A Framework for Possible Integrated Structural Interventions - PhD Thesis. 2016.
- [11] Iotti F. Alte Prestazioni Sismiche in Edifici Condominiali Grazie al Sistema SismaCoat. Web journal, www.ingenio-web.it. 2018.
- [12] SismaCoat. Presentazione del Sistema Brevettato Sismacoat per l'Adeguamento Sismico ed Energetico degli Edifici Esistenti. www.sismacoat.it. 2018.

References

- [13] Ecosism. Ecosism at Klimahouse 2019. <https://www.archiproducts.com/>. 2019.
- [14] Poirazis H. Double Skin Façades: A Literature Review. 2006. 1–252 p.
- [15] Uuttu S. Study of Current Structures in Double-Skin Façades. Helsinki University of Technology; 2001.
- [16] Saelens D. Energy Performance Assessments of Single Storey Multiple-Sin Facades. Catholic University of Leuven; 2002.
- [17] Ding W, Hasemi Y, Yamada T. Natural Ventilation Performance of a Double-Skin Façade With a Solar Chimney. *Energy Build.* 2005;37:411–8.
- [18] Heimrath, Richard, Hengsberger H, Mach T, Streicher W. Best Practice for Double Skin Façades: WP 1 Report “State of the Art.” 2005. 1–151 p.
- [19] Perino M, Blumel E. State-of-the-Art Review Responsive Building Elements. Vol. 2A. 2008. 1–199 p.
- [20] Ahmed MMS, Abel-Rahman AK, Ali AHH, Suzuki M. Double Skin Façade: The State of Art on Building Energy Efficiency. *J Clean Energy Technol.* 2016;4:84–9.
- [21] GhaffarianHoseini A, GhaffarianHoseini A, Berardi U, Tookey J, Li DHW, Kariminia S. Exploring the Advantages and Challenges of Double-Skin Façades (DSFs). *Renew Sustain Energy Rev.* 2016;60:1052–65.
- [22] Fernandez Solla I. Le Corbusier: A French Lesson on “Murs Neutralisants.” 2020;1–11.
- [23] Figini L, Foillini G, Fiocchi A. *Atlante Architettura Contemporanea.* 2020;1–11.
- [24] Boake TM-. *The Occidental Chemical Center.* 2002;1–6.
- [25] *Australian Design Review.* Media-TIC. 2010;1–10.
- [26] Boronat R. Works Visit to The Digital Cube for ITC Activities: Media-Tic, with the Almost-Finished Works, is the New Image of Barcelona Digital. 2010;(January):1–7.
- [27] *Architectenweb Magazine.* GuangZhou TV Tower. :1–10.
- [28] Schofield J. Case Study: Capital Gate, Abu Dhabi. *CTBUH J.* 2012;11–7.

- [29] CTBUH Innovation Award. Al Bahar Towers – External Automated Shading System. 2012;172–7.
- [30] Chan ALS, Chow TT, Fong KF, Lin Z. Investigation on Energy Performance of Double Skin Façade in Hong Kong. *Energy Build.* 2009;41:1135–42.
- [31] Gratia E, De Herde A. The Most Efficient Position of Shading Devices in a Double-Skin Façade. *Energy Build.* 2007;39:364–73.
- [32] Stec WJ, Paassen AHC. Symbiosis of the Double Skin Façade with the HVAC System. *Energy Build.* 2005;37:461–9.
- [33] Joe JW, Choi WJ, Huh JH. Operation Strategies for an Office Building Integrated with Multi-Story Double Skin Façades in the Heating Season. *Proc Build Simul 2011 12th Conf Int Build Perform Simul Assoc.* 2011;2:1913–9.
- [34] Gontikaki M. Optimization of a Solar Chimney Design to Enhance Natural Ventilation in a Multi-Storey Office Building. *Proc 10th Int Conf Enhanc Build Oper , Kuwait ICEBO .* 2010;1–10.
- [35] Abraham SB, Ming TZ. Numerical Analysis on The Thermal Performance of a Building With Solar Chimney and Double Skin Façade in Tropical Country. *IOP Conf Ser Mater Sci Eng.* 2018;453:1–8.
- [36] Stec WJ, Van Paassen AHC, Maziarz A. Modelling the Double Skin Façade with Plants. *Energy Build.* 2005;37:419–27.
- [37] De Gracia A, Navarro L, Castell A, F. Cabeza L. Energy Performance of Ventilated Double Skin Façade with PCM Under Different Climates. *Energy Build.* 2015;91:37–42.
- [38] Johnny AE, Shanks K. Optimization of Double-Skin Facades for High-Rise Buildings in Hot Arid Climates. *Int J Environ Sustain.* 2018;7:88–100.
- [39] Gaillard L, Giroux-Julien S, Ménéz C, Pabiou H. Experimental Evaluation of a Naturally Ventilated PV Double-Skin Building Envelope in Real Operating Conditions. *Sol Energy.* 2014;103:223–41.
- [40] Athienitis AK, Buonomano A, Ioannidis Z, Kapsis K, Stathopoulos T. Double Skin Façades Integrating Photovoltaics and Active Shadings: A Case Study for Different Climates. *Build Integr Renew Energy Syst Conf.* 2017;1–8.

References

- [41] Luo Y, Zhang L, Wang X, Xie L, Liu Z, Wu J, et al. A comparative study on thermal performance evaluation of a new double skin façade system integrated with photovoltaic blinds. *Appl Energy*. 2017;199:281–93.
- [42] Jayathissa P, Luzzatto M, Schmidli J, Hofer J, Nagy Z, Schlueter A. Optimising Building Net Energy Demand With Dynamic BIPV Shading. *Appl Energy*. 2017;202:726–35.
- [43] Moon KS. Structural Design of Double Skin Facades as Damping Devices for Tall Buildings. *Procedia Eng*. 2011;14:1351–8.
- [44] Zhang R, Fu TS. An Integrative Double Skin Façade Damper System For Structural Safety and Energy Efficiency. *Conf Pap ICSD*. 2016;1–17.
- [45] Takeuchi T, Yasuda K, Iwata M. Studies on Integrated Building Façade Engineering with High-Performance Structural Elements. *Conf Pap*. 2006;1–9.
- [46] Scuderi G. Adaptative Exoskeleton for the Integrated Retrofit of Social Housing Buildings. PhD Thesis. 2016;(February).
- [47] Zhai Z, Chen Q, Haves P, Klems JH. On Approaches to Couple Energy Simulation and Computational Fluid Dynamics Programs. *Build Environ*. 2002;37:857–64.
- [48] Passoni C, Belleri A, Marini A, Riva P. Sustainable Restoration of Post-WWII European Reinforced Concrete Buildings. *Conf Pap 16WCEE*. 2017;1–12.
- [49] Labò S. Holistic Sustainable Renovation of Post-World War II Reinforced Concrete Building Under A Life Cycle Perspective by Means Diagrid Exoskeletons. 2017.
- [50] F. Cabeza L, De Gracia A, Castell A, Navarro L, Oro E. Numerical Modelling of Ventilated Façades: A Review. *Renew Sustain Energy Rev*. 2013;22:539–49.
- [51] Kim D-W, Park C-S. Difficulties and Limitations in Performance Simulation of a Double Skin Façade with EnergyPlus. *Energy Build*. 2011;43:3635–3645.
- [52] Erba S, Causone F, Armani R. The Effect of Weather Datasets on Building Energy Simulation Outputs. *Energy Procedia*. 2017;134:545–54.
- [53] Lupato G, Manzn M. Italian TRYs: New Weather Data Impact on Building Energy Simulations. *Energy Build*. 2019;185:287–303.

- [54] Bhandari M, Shrestha S, New J. Evaluation of Weather Datasets for Building Energy Simulation. *Energy Build.* 2012;49:109–18.
- [55] Chiesa G, Grosso M. The Influence of Different Hourly Typical Meteorological Years on Dynamic Simulation of Buildings. *Energy Procedia.* 2015;78:2560–5.
- [56] Ciobanu D, Eftimie E, Jaliu C. The Influence of Measured/Simulated Weather Data on Evaluating the Energy Need in Buildings. *Energy Procedia.* 2014;48:796–805.
- [57] Pernigotto G, Prada A, Baggio P, Gasparella A. Solar Irradiance Modelling and Uncertainty on Building Hourly Profiles of Heating and Cooling Energy Needs. *Conf Pap Int High Perform Build Conf.* 2016;1–11.
- [58] Lupato G, Manzan M, Cirilli S. Comparison of Direct Radiation Split Algorithms for Energy Simulation of Buildings. *Conf Pap.* :1–8.
- [59] Alberto A, Ramos NMM, Almeida RMSF. Parametric Study of Double-Skin Facades Performance in Mild Climate Countries. *J Build Eng.* 2017;12:87–98.
- [60] ANSI/ASHRAE. ASHRAE Guideline 14-2002 Measurement of Energy and Demand Savings. *Ashrae.* 2002;8400:1–170.
- [61] Radhi H. A Comparison of the Accuracy of Building Energy Analysis in Bahrain Using Data from Different Weather Periods. *Renew Energy.* 2009;34:869–75.
- [62] M. C. Peel, B. L. Finlayson and TAM. Updated World Map of the Köppen-Geiger Climate Classification. *Hydrol Earth Syst Sci.* 2007;11:1633–44.
- [63] D.P.R. 26 agosto 1993, n. 412 - Regolamento recante norme per la progettazione, l'installazione, l'esercizio e la manutenzione degli impianti termici degli edifici ai fini del contenimento dei consumi di energia, in attuazione dell'art. 4, comma 4, della legge 9 gennaio 1991, n. 10.
- [64] Decreto del Presidente della Repubblica 26 agosto 1993, n. 412-Regolamento Recante Norme per la Progettazione, l'Installazione, l'Esercizio e la Manutenzione degli Impianti Termici degli Edifici ai fini del Contenimento dei Consumi di Energia.
- [65] American Society of Heating Refrigeration and Air Conditioning Engineers (ASHRAE). International Weather for Energy Calculations (IWEC weather files). Atlanta; 2001.

References

- [66] Murano G, Corrado V, Dirutigliano D. The New Italian Climatic Data and their Effect in the Calculation of the Energy Performance of Buildings. *Energy Procedia*. 2016;101:153–60.
- [67] UNI EN ISO 15927-4. Prestazione Termoisolometrica degli Edifici - Calcolo e Presentazione dei Dati Climatici - Parte 6: Differenze di Temperatura Cumulate (gradi giorno). 2008.
- [68] Grell GA, Dudhia J, Stauffer DR. A Description of the Fifth-generation Penn State/NCAR Mesoscale Model (MM5). NCAR Technical Note NCAR/TN-398+STR. 1994.
- [69] Hong SY, Pan HL. Nonlocal Boundary Layer Vertical Diffusion in a Medium-Range Forecast Model. *Forecast Model Mon Wea Rev*. 1996;124:2322–39.
- [70] Pleim JE, Chang JS. A Non-local Closure Model for Vertical Mixing in the Convective Boundary Layer. *Atmos Environ Part A, Gen Top*. 1992;26:965–81.
- [71] Xiu A, Pleim JE. Development of a Land Surface Model. Part I: Application in a Mesoscale Meteorological Model. *J Appl Meteorol*. 2001;40:192–209.
- [72] Blackadar AK. Modeling the Nocturnal Boundary Layer. *Am Meteorol Soc*. 1976;Proceeding:46–9.
- [73] Besharat F, Dehghan AA, Faghieh AR. Empirical Models for Estimating Global Solar Radiation: a Review and Case Study. *Renew Sustain Energy Rev*. 2013;21:798–821.
- [74] Al Riza DF, Gilani SI ul H, Aris MS. Hourly Solar Radiation Estimation Using Ambient Temperature and Relative Humidity Data. *Int J Environ Sci Dev*. 2011;2:188–93.
- [75] Campbell SG, Norman JM. *An Introduction to Environmental Biophysics*. 1998.
- [76] Tapakis R, Michaelides S, Charalambides AG. Computations of Diffuse Fraction of Global Irradiance: Part 1 – Analytical Modelling. *Sol Energy*. 2016;139:711–22.
- [77] Taylor KE. Summarizing Multiple Aspects of Model Performance in a Single Diagram. *J Geophys Res*. 2001;106:7183–92.
- [78] Corrado V, Ballarini I, Corgnati SP. *Building Typology Brochure – Italy*. 2014. 131 p.

- [79] Elements - Big Ladder Software. <https://bigladdersoftware.com>.
- [80] TABULA WebTool. <http://webtool.building-typology.eu>.
- [81] UNI EN 15251:2008 - Criteri per la Progettazione dell'Ambiente Interno e per la Valutazione della Prestazione Energetica degli Edifici, in Relazione alla Qualità dell'Aria Interna, all'Ambiente Termico, all'Illuminazione e all'Acustica.
- [82] IPCC. <https://www.ipcc.ch>.
- [83] Pachauri RK, Meyer L. Climate Change 2014-Synthesis Report. The Intergovernmental Panel on Climate Change. 2015.
- [84] Silvero F, Lops C, Montelpare S, Rodrigues F. Impact Assessment of Climate Change on Buildings in Paraguay—Overheating Risk under Different Future Climate Scenarios. *Build Simul.* 2019;12:943–60.
- [85] Sanford T, Frumhoff PC, Luers A, Gullett J. The Climate Policy Narrative for a Dangerously Warming World. *Nat Clim Chang.* 2014;4:164–6.
- [86] Berardi U, Jafarpur P. Assessing the Impact of Climate Change on Building Heating and Cooling Energy Demand in Canada. *Renew Sustain Energy Rev.* 2020;121:109681.
- [87] Barbosa R, Vicente R, Santos R. Climate Change and Thermal Comfort in Southern Europe Housing: a Case Study from Lisbon. *Build Environ.* 2015;92:440–51.
- [88] WCRP-CORDEX. <https://cordex.org/domains/cordex-region-euro-cordex>.
- [89] Bubnovà R. Integration of the Fully Elastic Equations Cast in the Hydrostatic Pressure Terrain-Following Coordinate in the Framework of the ARPAGE/Aladin NWP SYstem. *Am Meteorol Soc.* 1995;123:515–35.
- [90] Farda A, Déué M, Somot S, Horányi A, Spiridonov V, Tóth H. Model ALADIN as Regional Climate Model for Central and Eastern Europe. *Stud Geophys Geod.* 2010;54(2):313–32.
- [91] Déqué M, Dreveton C, Braun A, Cariolle D. The ARPEGE/IFS Atmosphere Model: a Contribution to the French Community Climate Modelling. *Clim Dyn.* 1994;10:249–266.
- [92] Horanyi, Ihasz I, Radnoti G. ARPEGE/ALADIN: A numerical Weather Prediction Model for Central-Europe with the Participation of the Hungarian Meteorological Service. *IdoJárás.* 1996;100:277–301.

References

- [93] Huth R, Mládek R, Metelka L, Sedlák P, Huthová Z, Kliegrová S, et al. On the Integrability of Limited-Area Numerical Weather Prediction Model ALADIN over Extended Time Periods. *Stud Geophys Geod.* 2003;47:863–873.
- [94] Pernigotto G, Prada A, Cóstola D, Gasparella A, Hensen JLM. Multi-year and Reference Year Weather Data for Building Energy Labelling in North Italy Climates. *Energy Build.* 2014;72:62–72.
- [95] Cebecauer T, Suri M. Typical Meteorological Year Data: SolarGIS Approach. *Energy Procedia.* 2015;69:1958–69.
- [96] Comminges M, Dugué A. Case Study of a Double Skin Façade: Focus on the Gap Between Predicted and Measured Energy Efficiency – Thermal Storage. *Conference Pap VII Int Congr Archit Envel.* 2015;1–9.
- [97] Kim DW, Park CS. Difficulties and Limitations in Performance Simulation of a Double Skin Façade with EnergyPlus. *Energy Build.* 2011;43:3635–45.
- [98] Vaglio JC. Aerophysics of Double-Skin Facades: Simulation-Based Determination of Pressure Coefficients for Multi-Story Double-Skin Facades. Vol. December, PhD Thesis dissertation. 2015.
- [99] Papakonstantinou KA, Kiranoudis CT, Markatos NC. Numerical Simulation of Air Flow Field in Single-Sided Ventilated Buildings. *Energy Build.* 2000;33:41–8.
- [100] Liddament MW. The Role and Application of Ventilation Effectiveness in Design. *Conf Pap Proc Int Symp Room Air Convect Vent Eff.* 1992;59–75.
- [101] Dama A, Angeli D, Kalyanova Larsen O. Naturally Ventilated Double-Skin Façade in Modeling and Experiments. *Energy Build.* 2017;144:17–29.
- [102] Chen Q, Srebric J. A Procedure for Verification, Validation, and Reporting of Indoor Environment CFD Analyses. *HVAC R Res.* 2002;8:201–16.
- [103] Xu L, Ojima T. Field Experiments on Natural Energy Utilization in a Residential House with a Double Skin Façade System. *Build Environ.* 2007;42:2014–23.
- [104] Pasut W, De Carli M. Evaluation of Various CFD Modelling Strategies in Predicting Airflow and Temperature in a Naturally Ventilated Double Skin Façade. *Appl Therm Eng.* 2012;37:267–74.
- [105] CD-ADAPCO. STAR CCM+ User Guide (Version 4.02). 2008. 1–406 p.

- [106] Lupoi G, Calvi GM, Lupoi A, Pinto PE. Comparison of Different Approaches for Seismic Assessment of Existing Buildings. *J Earthq Eng.* 2004;8:121–60.
- [107] Wang J, Zhao H. High Performance Damage-Resistant Seismic Resistant Structural Systems for Sustainable and Resilient City: A Review. *Hindawi Shok Vib.* 2018;(1–32).
- [108] Chen C, Xilin L, Xiao R. Study on the Shear Wall Structure with Combined Form of Replaceable Components. *Eccomas Proceedia COMPDYN.* 2017;3982–91.
- [109] Menna C, Auricchio F, Asprone D. Applications of Shape Memory Alloys in Structural Engineering. *Shape Mem Alloy Eng.* 2015;Chapter 13:369–403.
- [110] Dolce M, Cardone, Marnetto R. Implementation and Testing of Passive Control Devices Based on Shape Memory Alloys. *Earthq Eng Struct Dyn.* 2000;29:945–68.
- [111] Asgarian B, Morandi S. Seismic Response of Steel Braced Frames with Shape Memory Alloy Braces. *Jpurnal Constr Steel Res.* 2011;67:65–74.
- [112] Auricchio F, Fugazza D, Desroches R. Earthquake Performance of Steel Frames with Nitinol Braces. *J Earthq Eng.* 2006;10:45–66.
- [113] Krumme R, Hayes J, Sweeney S. Structural Damping with Shape-Memory Alloys: One Class of Devices. *SMart Struct Mater.* 1995;2445:225–40.
- [114] Wilde K, Gardoni P, Fujino Y. Base Insulation System with Shape Memory Alloy Device for Elevated High-Way Bridges. *Eng Struct.* 2000;22:222–9.
- [115] Dolce M, Cardone D, Ponzo F. Shaking-Table Tests on Reinforced Concrete Frames with Different Isolation Systems. *Earthq Eng Struct Dyn.* 207AD;36:573–96.
- [116] Desroches R, Taftali B, Ellingwood B. Seismic Performance Assessment of Steel Frames with Shape Memory Alloy Connections. Part I Seismic Demands. *J Earthq Eng.* 2010;14:471–86.
- [117] Youssef MA, Alam MS, Nehdi M. Experimental Investigation on the Seismic Behaviour of Beam-Column joints Reinforced with Superelastic Shape Memory Alloys. *J Earthq Eng.* 2008;12:1205–22.
- [118] Thermou GE, Elnashai AS. Seismic retrofit schemes for RCstructures and local–globalconsequences. *Prog Struct Eng Mater.* 2006;8:1–15.

References

- [119] Aggiornamento delle Norme Tecniche per le Costruzioni (NTC2018)- Ministero delle Infrastrutture e dei Trasporti. 2018 p. 1–372.
- [120] European Standard EN 1998-2005 Eurocode 8: Design of structures for earthquake resistance. Eur Comm Stand.
- [121] Masi A, Digrisolo A, Santarsiero G. Concrete Strength Variability in Italian RC Buildings: Analysis of a Large Database of Core Tests. *Appl Mech Mater.* 2014;597:283–90.
- [122] Verderame GM, Ricci P, Esposito M, Sansiviero FC. Le Caratteristiche Meccaniche degli Acciai Impiegati nelle Strutture in C.A. Realizzate dal 1950 al 1980. AICAP- RELUIS. 2011;1–8.
- [123] Laboratorio Sperimentale del Dipartimento di Ingegneria Strutturale, Facoltà di Ingegneria degli Studi di Napoli Federico II. STIL (v 1.0). www.reluis.it
- [124] Norme Tecniche per l'Esecuzione delle Opere in Cemento Armato Normale, Precompresso e per le Strutture Metalliche. Gazzetta Ufficiale della Repubblica Italiana. 1980 p. 1–161.
- [125] Deierlein GG, Reinhorn AM, Willford MR. Nonlinear Structural Analysis for Seismic Design. *NEHRP Seism Des Tech Br* 4. 2010;1–36.
- [126] Takeda T, Sozen MA, Nielsen NN. R/C Response to simulated Earthquakes. *J Struct Div, ASCE.* 1970;96:2557–73.
- [127] Midas Gen On-line Manual - General Structure Design System. Gen 2020 - Integrated Solution System for Building and General Structures.
- [128] Terrenzi M, Spacone E, Camata G. Collapse Limit State Definition for Seismic Assessment of Code-Conforming RC Buildings. *Int J Adv Struct Eng.* 2018;10:325–337.
- [129] Bertoldi SH, Decanini LD, Gavarini C. Telai Tamponati Soggetti ad Azioni Sismiche. Un Modello Semplificato. Confronto Sperimentale e numerico. Conf Pap 6° Convegno Naz L'ingegneria Sismica Ital. 1993;815–24.
- [130] Decanini LD, Mollaioli F, Mura A, Saragoni R. Seismic Performance of Masonry Infilled RC Frames. Conf Pap 13th WCEE. 2004;Paper 165.
- [131] Stafford Smith B. Lateral stiffness of infilled frames. *J Struct Div ASCE.* 1963;88(ST 6):183–99.
- [132] Decanini L, Liberatore L, Mollaioli F. Strength and stiffness reduction factors for infilled frames with openings. *Earthq Eng Eng Vib.* 2014;13:437–54.

- [133] Morandi P, Hak S, Magenes G. Comportamento Sismico delle Tamponature in Laterizio in Telai in C.A.: Analisi Numeriche su Edifici ed Implicazioni Progettuali. Conf Pap XIV Convegno ANIDIS - L'INGEGNERIA SISMICA Ital. 2011;1–10.
- [134] Morandi P, Hak S, Magenes G. Comportamento Sismico delle Tamponature in Laterizio in Telai in C.A.: Definizione dei Livelli Prestazionali e Calibrazione di un Modello Numerico. Conf Pap XIV Convegno ANIDIS - L'INGEGNERIA SISMICA Ital. 2011;1–10.
- [135] FEMA-273. NEHRP Guidelines for the Seismic Rehabilitation of Buildings. 1997.
- [136] Ghobarah A. On Drift Limits Associated with Different Damage Levels. Proc Int Work Performance-Based Seism Des. 2004;1–12.
- [137] Hazus-MH MR5. Technical Manual. Developed by Department of Homeland Security Federal Emergency Management Agency. Mitigation Division. 2010 p. 1–736.
- [138] D'Aniello M. Steel Dissipative Bracing Systems for Seismic Retrofitting of Existing Structures: Theory and Testing- PhD Thesis. 2007.
- [139] Neri F, La Guzza M, Russo A. L'utilizzo di Controventi Dissipativi per la Protezione Sismica del Plesso Scolastico Cappuccini a Ramacca. Tech Rep. 2002;
- [140] Laguardia R. Una Procedura di Ottimizzazione Multi-Prestazionale per la Riduzione del Rischio Sismico attraverso Sistemi di Controventi Elastici e Dissipativi. PhD-Thesis. 2016.
- [141] Antonucci R, Balducci F, Cappanera F, Castellano MG. Strutture Prefabbricate con controventi Dissipativi: l'Esempio del Nuovo Polo Didattico della Facoltà di Ingegneria dell'Università Politecnica delle Marche di Ancona. Progett Zo Sismica. 2009;1:85–103.
- [142] Balducci A, Castellano MG. Adeguamento Sismico del Liceo Varano di Camerino mediante Sistema a Torri Dissipative. Progett Sismica. 2015;6:69–91.
- [143] Braga F, Buttarazzi F, Dall'Asta A, Walter S. Protezione Sismica di Edifici Esistenti in C.A. con Controventi Dissipativi in Acciaio. 2016. 1–181 p.
- [144] Fu Y, Cherry S. Design of Friction Damped Structures using Lateral Force Procedure. Earthq Eng Struct Dyn. 2000;29:989–1010.

References

- [145] Whittaker A, Constantinou MC, Ramirez OM, Johnson MW, Chrysostomou CZ. Equivalent Lateral Force and Modal Analysis Procedures of the 2000 NEHRP Provisions for Buildings with Damping Systems. *Earthq Spectra*. 2003;19:959–80.
- [146] NEHRP Recommended Provisions for Seismic Regulations for New Buildings and Other Structures (FEMA450). Federal Emergency Management Association. 2003.
- [147] Kim J, Choi H. Behavior and Design of Structures with Buckling-Restrained Braces. *Eng Struct*. 2004;26:693–706.
- [148] Mazza F, Mazza M, Vulcano A. Displacement-based Seismic Design of Hysteretic Damped Braces for Retrofitting In-elevation Irregular RC Framed Structures. *Soil Dyn Earthq Eng*. 2015;69:115–24.
- [149] Bergami AV, Nuti C. A Design Procedure of Dissipative Braces for Seismic Upgrading Structures. *Earthquakes Struct*. 2013;4:85–108.
- [150] Wen J, Guo W, Christopoulos C. Performance Spectra Based Method for the Seismic Design of Structures Equipped with Passive Supplemental Damping Systems. *Earthq Eng Struct Dyn*. 2013;935–52.
- [151] Di Cesare A, Ponzo CF. Seismic Retrofit of Reinforced Concrete Frame Buildings with Hysteretic Bracing Systems: Design Procedure and Behaviour Factor. *Hindawi Shock Vib*. 2017;1–21.
- [152] Ponzo FC, Di Cesare A, Arleo G, Totaro P. Protezione Sismica di Edifici Esistenti con Controventi Dissipativi di Tipo Isteretico: Aspetti Progettuali ed Esecutivi. *Progett Sismica*. 1:37–60.
- [153] Iervolino I, Galasso C, Cosenza E. REXEL: Computer Aided Record Selection for Code-Based Seismic Structural Analysis. *Bull Earthq Eng*. 2010;8:339–362.
- [154] United Nations Environmental Program (UNEP). *Towards a Life Cycle Sustainability Assessment - Making Informed Choices on Products*. 2011. 1–66 p.
- [155] ISO. *EN ISO 14040:2006 Environmental Management - Life Cycle Assessment - Principles and Framework*. International organization for standardization 2006 p. 1–28.

- [156] International organization for Standardization. EN ISO 14044:2006 Environmental Management - Life Cycle Assessment - Requirements and Guidelines. 2006.
- [157] Kloepffer W. Life Cycle Sustainability Assessment of Products. Vol. 13, International Journal of Life Cycle Assessment. 2008. 89–95 p.
- [158] Rodrigues V, Martins AA, Nunes MI, Quintas A, Mata TM, Caetano NS. LCA of Constructing an Industrial Building: Focus on Embodied Carbon and Energy. Energy Procedia. 2018;153:420–5.
- [159] Adalberth K, Almgren A, Petersen EH. Life-Cycle Assessment of Four Multi-Family Buildings. Int J Low Energy Sustain Build. 2001;2:1–21.
- [160] Gu L, Gu D, Lin B, Huang M, Gai J, Zhu Y. Life Cycle Green Cost Assessment Method for Green Building Design. Conf Pap IBPSA 2007 - Int Build Perform Simul Assoc 2007. 2007;1962–7.
- [161] Vitiello U, Salzano A, Asprone D, Di Ludovico M, Prota A. Life-Cycle Assessment of Seismic Retrofit Strategies Applied to Existing Building Structures. Sustainability. 2016;8:1–18.
- [162] Stribling D, Stigge B. A Critical Review of the Energy Savings and Cost Payback Issues of Double Facades. Conf Pap Conf. 2003;1–17.
- [163] Cakmanus I. Optimization of Double Skin Facades for Buildings: an Office Building Example in Ankara-Turkey. Conf Pap Clima 2007 WellBeing Indoors. 2007;1–13.
- [164] Pomponi F, Piroozfar PAE, Southall R, Ashton P, Pirozfar P, Farr ERP. Life Cycle Energy and Carbon Assessment of Double Skin Façades for Office Refurbishments. Energy Build. 2015;109:143–56.
- [165] Silvero F, Lops C, Montelpare S, Rodrigues F. Generation and Assessment of local Climatic Data from Numerical Meteorological Codes for Calibration of Building Energy Models. Energy Build. 2019;25–45.
- [166] Erbs D, Klein S, Duffie J. Estimation of the Diffuse Radiation Fraction for Hourly, Daily and Monthly-Average Global Radiation. Sol Energy. 1982;28:293–302.
- [167] Orgill J, Hollands K. Correlation Equation for Hourly Diffuse radiation on a Horizontal Surface. Sol Energy. 1977;19:357–9.
- [168] Marques Filho EP, Oliveira AP, Vita WA, Mesquita FLL, Codato G, Escobedo

References

- JF, et al. Global, Diffuse and Direct Solar Radiation at the Surface in the City of Rio de Janeiro: Observational Characterization and Empirical Modeling. *Renew Energy*. 2016;91:64–74.
- [169] Boland J, Huang J, Ridley B. Decomposing Global Solar Radiation into its Direct and Diffuse Components. *Renew Energy*. 2013;28:749–56.
- [170] Lemos LFL, Starke AR, Boland J, Cardemil JM, Machado RD, Colle S. Assessment of Solar Radiation Components in Brazil using the BRL Model. *Renew Energy*. 2017;108:569–80.
- [171] Kalyanova O. Double-Skin Facade - Modelling and Experimental Investigations of Thermal Performance. 2008.
- [172] Kalyanova Larsen O, Kvols Heiselberg P, Rasmus Jensen L. Experimental Data and Boundary Conditions for a Double-Skin Facade Building in External Air Curtain Mode. *DCE Tech Memo*. 2014;No. 38:1–24.
- [173] Kalyanova O, Heiselberg P, Felsmann C, Poirazis H, Strachan P, Wijsman A. An Empirical Validation of Building Simulation Software for Modelling of Double-Skin Façade (DSF). *Conf Pap Elev Int IBPSA Conf*. 2009;1107–14.
- [174] Ren K, Hu J, Xiong X, Zhang L, Wei J. Validation of Turbulence Models in STAR-CCM+ by N.A.C.A. 23012 Airfoil Characteristics. *Conf Pap 2009 ASEE Northeast Sect Conf*. 2009;1–11.

List of Figures

Figure 1.1. The final energy use by fuel and sector for the EU Member States [2].	5
Figure 1.2. Breakdown of the energy consumption by end-use for EU households.	6
Figure 1.3. The categorisation of the construction period of the EU Housing stock [3].	7
Figure 1.4. Subdivision of the European building stock per country and EPC class (the sample covers half of the EU Member States) [8].	7
Figure 1.5. Classification of the European building stock according to the dwelling's EPC data (Elaborated from [8]).	8
Figure 1.6. Evaluation of energy consumption, operational cost and carbon emission during the building life cycle, considering, the energy (a) and the energy + seismic (b) retrofit [9].	9
Figure 1.7. Restorative intervention solutions which adopt the holistic approach.	11
Figure 1.8. Schematisation of the Seismic Coat (left) and possible external coatings, (a) Plaster, (b) Brick, and (c) Metal [12].	11
Figure 1.9. Example of the retrofitted building with the ECOSISM Seismic Coat before (a) and after (b) the restoration [12].	12
Figure 2.1. Box-Window DSF schematisation and examples.	17
Figure 2.2. Corridor DSF schematisation and examples.	17
Figure 2.3. Shaft-Box DSF schematisation and examples.	18
Figure 2.4. Multi-Storey DSF schematisation and examples.	18
Figure 2.5. Air fluxes classification method.	19
Figure 2.6. Number of DSF classified according to the analysed criteria.	20

List of Figures

Figure 2.7. Main elevations and a section of the Steiff Toy Factory.	23
Figure 2.8. “Mur neutralisant” and the “Respiration exacte” sketches by Le Corbusier.	24
Figure 2.9. Main elevations of the ICO Center 3.	25
Figure 2.10. Main elevations of the Occidental Chemical Center and the focus on the cavity with the internal blinds.	25
Figure 2.11. The RWE AG Headquarters (a), the Agbar Tower (b) and the Aurora Place (c).	26
Figure 2.12. The Jean-Marie Tjibao Cultural Center and a focus on the metal anchors.	27
Figure 2.13. Possible configurations of the external skin in response to wind conditions.	27
Figure 2.14. The One Peking Road (a) and the Moor House (b).	28
Figure 2.15. North-eastern (left) and south-eastern (right) elevations.	29
Figure 2.16. Schematisation of the ETFE Diaphragm operation.	29
Figure 2.17. South-western elevation with the shading system off (a) and on (b).	29
Figure 2.18. Pictures of the Canton Tower (a), the Capital Gate (b) and the Pearl River (c).	30
Figure 2.19. Pictures of the Shanghai Tower (a), the UnipolSai Tower (b) and the Al Bahar Towers (c).	31
Figure 2.20. Detail of the operation modes of the external shading system.	32
Figure 2.21. Schematic illustration of the simulation cases [18].	34
Figure 2.22. Possible configurations of solar chimney integrated into DSF systems.	35
Figure 2.23. Summer (left) and winter (right) performance of the façade with plants [23].	36

Figure 2.24. PCMs operation: (a) Charge process, (b) discharge process, (c) overheating prevention, (d) free cooling [22].	36
Figure 2.25. Design concept and pictures of the PV façade prototype [24].	37
Figure 2.26. Sketch (left) and operation (right) of the PV façade [25].	38
Figure 2.27. Active solar façade concept (left) and dynamic shading system (right) [27].	39
Figure 2.28. Concept diagram of DSF with low axial stiffness connectors (left) and multiple TMDs inside the cavity (right) (elaborated from [28]).	40
Figure 2.29. DSF damper concept and focus on the connection between the primary building and movable façade [29].	41
Figure 2.30. DSF damper rheological model (a) and analysed configurations: three dampers (b), two dampers (c) and one damper (d) [29].	41
Figure 2.31. Main elements of the Integrated Façade and its structural concept (elaborated from [30]).	42
Figure 2.32. The Tokyo Institute of Technology before (a) and after (b) the restoration.	43
Figure 2.33. Schematisation of the adaptive exoskeleton [47].	44
Figure 2.34. Shear walls (a) and shell structure (b) analysed by the University of Bergamo [47].	44
Figure 2.35. Axonometry of the Diagrid solution and schematisation of the retrofitted building with a standard or responsive exoskeleton [33].	46
Figure 2.36. Main phases of a possible coupling procedure [47].	48
Figure 2.37. Schematisation of the coupling strategies herein described [47].	49
Figure 2.38. Heat transfer mechanism estimated on the building south wall [47].	51
Figure 3.1. The localisation of Pescara (left and middle) and the reference building (right).	53

List of Figures

Figure 3.2. Location of the reference building (red rectangle).	53
Figure 3.3. Views of the reference building. South-east (left) and north-west (right).	54
Figure 3.4. The architectural plan of the ground floor.	54
Figure 3.5. The architectural plan of the typical floor.	55
Figure 3.6. South-east elevation.	55
Figure 3.7. North-west elevation.	55
Figure 3.8. North-east (left) and South-west (right) elevations.	56
Figure 4.1. Köppen-Geiger climate type map of Europe [62].	61
Figure 4.2. MM5 nested domains (red squares) (a) and the grid of the inner domain (b).	65
Figure 4.3. The localisation of weather stations selected for the comparison.	66
Figure 4.4. Normalised Taylor diagram based on annual datasets.	74
Figure 4.5. Normalised Taylor diagram for the spring season.	75
Figure 4.6. Normalised Taylor diagram for the summer season.	75
Figure 4.7. Normalised Taylor diagram for the autumn season.	76
Figure 4.8. Normalised Taylor diagram for the winter season.	76
Figure 4.9. Normalised Taylor diagram based on annual datasets for solar radiation.	77
Figure 4.10. Normalised Taylor diagrams for seasonal datasets for solar radiation: (a) spring, (b) summer, (c) autumn and (d) winter.	78
Figure 4.11. The localisation of Thermal zones on the typical floor.	79
Figure 4.12. The energy model of the case study with balconies (pink elements) and neighbouring buildings (cyan elements).	83

Figure 4.13. The localisation of the case study (red box) and the building selected for the calibration (light brown box).	84
Figure 4.14. Comparison among estimated and collected values for the model calibration.	85
Figure 4.15. The localisation of the thermal zones selected for the winter (blue rectangle) and summer (red box) comfort.	86
Figure 4.16. Monthly mean values referred to the temperature for each climatic dataset.	87
Figure 4.17. Annual energy consumption estimated for the reference building.	88
Figure 4.18. Summer comfort rates for the reference building in the original state.	90
Figure 4.19. Winter comfort rates for the reference building in the original state.	90
Figure 4.20. Schematisation of the investigated DSFs selected for energy simulations.	92
Figure 4.21. Building annual energy consumption estimated with the Climate Network climatic file.	93
Figure 4.22. Building annual energy consumption estimated with the ARTA climatic file.	94
Figure 4.23. Building annual energy consumption estimated with the PVGIS climatic file.	94
Figure 4.24. Building annual energy consumption estimated with the DB climatic file.	95
Figure 4.25. Building annual energy consumption estimated with the CTI climatic file.	95
Figure 4.26. Building annual energy consumption estimated with the MM5-MRF-LSM climatic file.	96
Figure 4.27. Building annual energy consumption estimated with the MM5-PLEIM-XIU climatic file.	96

List of Figures

Figure 4.28. Building annual energy consumption estimated with the MM5-BK climatic file.	97
Figure 4.29. Comfort rates for the typical summer week according to Climate Network climatic file.	98
Figure 4.30. Comfort rates for the typical summer week according to ARTA climatic file.	98
Figure 4.31. Comfort rates for the typical summer week according to PVGIS climatic file.	99
Figure 4.32. Comfort rates for the typical summer week according to DB climatic file.	99
Figure 4.33. Comfort rates for the typical summer week according to CTI climatic file.	100
Figure 4.34. Comfort rates for the typical summer week according to MM5-MRF-LSM climatic file.	100
Figure 4.35. Comfort rates for the typical summer week according to MM5-PLEIM-XIU climatic file.	101
Figure 4.36. Comfort rates for the typical summer week according to MM5-BK climatic file.	101
Figure 4.37. Comfort rates for the typical winter week according to Climate Network climatic file.	102
Figure 4.38. Comfort rates for the typical winter week according to ARTA climatic file.	102
Figure 4.39. Comfort rates for the typical winter week according to PVGIS climatic file.	103
Figure 4.40. Comfort rates for the typical winter week according to DB climatic file.	103
Figure 4.41. Comfort rates for the typical winter week according to CTI climatic file.	104

Figure 4.42. Comfort rates for the typical winter week according to MM5-MRF-LSM climatic file.	104
Figure 4.43. Comfort rates for the typical winter week according to MM5-PLEIM-XIU climatic file.	105
Figure 4.44. Comfort rates for the typical winter week according to MM5-BK climatic file.	105
Figure 4.45. Temperature and Solar Activity trends over the years [82].	107
Figure 4.46. Projected trends of global CO ₂ emissions under various RCP scenarios [85].	108
Figure 4.47. Euro-CORDEX Domain and the coordinates of its corners.	110
Figure 4.48. CORDEX primary information and grid-points with localisation of the selected virtual anemometer (yellow ring) and the reference building (red circle).	111
Figure 4.49. Monthly mean values referred to the temperature.	113
Figure 4.50. Monthly mean values referred to global solar radiation.	113
Figure 4.51. Yearly mean values referred to temperature and global solar radiation.	114
Figure 4.52. Building annual energy consumption estimated for the year 2030.	115
Figure 4.53. Building annual energy consumption estimated for the year 2050.	115
Figure 4.54. Building annual energy consumption estimated for the year 2070.	116
Figure 4.55. Comfort rates for the typical summer week according to the 2030 climatic file.	117
Figure 4.56. Comfort rates for the typical summer week according to the 2050 climatic file.	118

List of Figures

Figure 4.57. Comfort rates for the typical summer week according to the 2070 climatic file.	118
Figure 4.58. Comfort rates for the typical winter week according to the 2030 climatic file.	119
Figure 4.59. Comfort rates for the typical winter week according to the 2050 climatic file.	119
Figure 4.60. Comfort rates for the typical winter week according to the 2070 climatic file.	120
Figure 5.1. Domain and building components of the modelled case study.	125
Figure 5.2. Surface (a) and Volume (b) meshes of the case study model.	126
Figure 5.3. Pressure levels estimated for the reference building before the DSF insertion.	127
Figure 5.4. Velocity magnitudes estimated for the reference building before the DSF insertion.	127
Figure 5.5. Components of the domain (left) and DSF Building (right).	129
Figure 5.6. Surface meshes referred to different mesh sizes.	130
Figure 5.7. Volume meshes referred to different mesh sizes.	131
Figure 5.8. The localisation of the probe lines inserted inside the DSF cavity.	132
Figure 5.9. Velocity profile comparisons for each probe line and mesh size model.	133
Figure 5.10. Pressure levels inside the DSF cavity estimated for various mesh sizes.	133
Figure 5.11. Velocity magnitudes inside the DSF cavity estimated for various mesh sizes.	134
Figure 5.12. Comparison of the selected DSF cavity depth.	135
Figure 5.13. Velocity profile comparisons for each probe line and DSF cavity.	136

Figure 5.14. Pressure levels inside the DSF for the investigated cavity depths.	137
Figure 5.15. Velocity magnitudes inside the DSF for the investigated cavity depths.	137
Figure 5.16. Followed steps for the conversion of the model from 3D to 2D.	138
Figure 5.17. Velocity profile comparisons for each probe line and DSF model.	139
Figure 5.18. Wind directions evaluated for the here presented analyses.	140
Figure 5.19. Velocity profile comparisons for each probe line and various wind directions.	140
Figure 5.20. Velocity profile comparisons for each probe line and various wind directions with a focus on the k and j component for the 45°wind.	141
Figure 5.21. Components of the domain (left) and Corridor DSF Building (right).	142
Figure 5.22. Surface meshes referred to the Corridor DSF configuration.	143
Figure 5.23. Volume meshes referred to the Corridor DSF configuration.	143
Figure 5.24. Velocity profile comparisons for each probe line and various wind directions estimated for the Corridor DSF.	144
Figure 5.25. Components of the domain (left) and Shaft-Box DSF Building (right).	145
Figure 5.26. Surface meshes referred to the Shaft-Box DSF configuration.	145
Figure 5.27. Volume meshes referred to the Shaft-Box DSF configuration.	146
Figure 5.28. Velocity profile comparisons for each probe line and various wind directions referred to the Shaft-Box DSF.	147
Figure 5.29. Pressure levels and velocity magnitudes estimated for the DSF air channels.	148
Figure 5.30. Velocity profile comparisons for each probe line various DSF configuration due to a south-east wind (0°).	150

List of Figures

Figure 5.31. Representation of the stream traces estimated for the Multi-Storey, and Shaft-Box DSF referred to the south-east wind.	151
Figure 5.32. Velocity profile comparisons for each probe line various DSF configuration due to a south wind (45°).	152
Figure 5.33. Vorticity representation for the Multi-Storey and Shaft-Box DSF associated with the south wind.	152
Figure 5.34. Velocity profile comparisons for each probe line various DSF configuration due to a south-west wind (90°).	153
Figure 5.35. Representation of the stream traces inside the Shaft-Box channels due to a south-west wind.	153
Figure 5.36. Wind directions evaluated for the here presented simulations.	154
Figure 5.37. Components of the domain (left) and DSF Building (right).	155
Figure 5.38. Surface meshes referred to the more detailed building with DSF on two elevations.	155
Figure 5.39. Volume meshes referred to the more detailed building with DSF on two elevations.	156
Figure 5.40. The velocity profile, referred to various probe lines and wind directions, for the north-west DSF placed on the real building shape.	157
Figure 5.41. Wind directions investigated for testing the effectiveness of the south-east and north-west DSF.	158
Figure 5.42. The velocity profile, referred to various probe lines and wind directions, for the north-west and south-east DSF placed on the real building shape.	158
Figure 5.43. The here-evaluated optimised shapes for better DSF performances.	159
Figure 5.44. Components of the domain (left) and DSF Building (right) for Case 1.	160
Figure 5.45. Surface meshes referred to Case 1.	160

Figure 5.46. Volume meshes referred to Case 1.	161
Figure 5.47. Components of the domain (left) and DSF Building (right) for Case 2.	161
Figure 5.48. Surface meshes referred to Case 2.	162
Figure 5.49. Volume meshes referred to Case 2.	162
Figure 5.50. Schematisation of the DSF models selected for the comparisons.	163
Figure 5.51. The velocity profile, referred to various probe lines, for the standard and optimised DSF (Case 1 and Case2).	163
Figure 5.52. Velocity magnitudes estimated for Case 1 (left) and Case 2 (right).	164
Figure 5.53. Pressure levels estimated for Case 1 (left) and Case 2 (right).	165
Figure 5.54. Components of the domain (left) and DSF Building (right) for the Case 3.	166
Figure 5.55. Surface meshes referred to the Case 3 model.	166
Figure 5.56. Volume meshes referred to the Case 3 model.	167
Figure 5.57. Components of the domain (left) and DSF Building (right) for the Case 4.	167
Figure 5.58. Surface meshes referred to the Case 4 model.	168
Figure 5.59. Volume meshes referred to the Case 4 model.	168
Figure 5.60. The velocity profile, referred to various probe lines, for optimised DSF configurations (Case 3 and Case 4).	169
Figure 5.61. Velocity magnitudes estimated for Case 3 (left) and Case 4 (right).	170
Figure 6.1. Examples of local (a) and global retrofit interventions [118].	174

List of Figures

Figure 6.2. Plan of the typical floor with the identification of the selected construction for structural simulations.	175
Figure 6.3. Plan of the modelled building.	175
Figure 6.4. Axonometry of the bare frame (a) and infilled (b) model of the case study.	176
Figure 6.5. Mean values of concrete strength measured for buildings referred to four identified periods (elaborated from [121]).	177
Figure 6.6. Idealised models of beam-column elements with the selected lumped plasticity approach (elaborated from [125]).	179
Figure 6.7. Takeda type hysteresis model available in MidasGEN [127]. (a) represents the unloading state prior to yielding in the uncracked zone (small displacement); (b) shows the unloading state to yielding in the uncracked region (large displacement); (c) is the unloading stage after yielding, and (d) represents the inner loop due to the repetition of load reversal.	179
Figure 6.8. Schematisation of the flexural (a) and shear (b) plastic hinge behaviour.	180
Figure 6.9. Diagonal strut mode for simulating the presence of masonry infills [128].	181
Figure 6.10. Backbone curve for the equivalent strut model.	183
Figure 6.11. Capacity curves due to different force distributions and directions.	186
Figure 6.12. Structural fragility curve parameters according to Hazus [137].	187
Figure 6.13. The schematisation of the equivalent Single Degree of Freedom (elaborated from NTC2018).	188
Figure 6.14. ADRS and displacement demands at DLS, LSLS, and CLS for the uniform acceleration force distribution, x-direction.	188
Figure 6.15. ADRS and displacement demands at DLS, LSLS, and CLS for the uniform acceleration force distribution, y-direction.	189

- Figure 6.16. ADRS and displacement demands at DLS, LSLS, and CLS for the triangular force distribution, x-direction. 189
- Figure 6.17. ADRS and displacement demands at DLS, LSLS, and CLS for the triangular force distribution, y-direction. 190
- Figure 6.18. Axonometry of the 3D building model after the insertion of the DSF. 191
- Figure 6.19. Schematisation of the hysteretic model implemented in MidasGen for the Steel Damper [127]. 192
- Figure 6.20. Comparisons between traditional braces (left) and buckling-restrained braces (right) [138]. 193
- Figure 6.21. Retrofitted and new buildings with BRAD systems: (a) the Cappuccini School [139], (b) the Gentile-Fermi School [140], (c) the Busciolano School [140], (d) The Marche Polytechnic University [141] and (e) the Varano High School [142]. 194
- Figure 6.22. Schematisation and comparison between the performance of elastic (a) and dissipative braces (b). 195
- Figure 6.23. Definition of the effectiveness factor, according to the dissipative bracing configuration [143]. 196
- Figure 6.24. Flow chart of the approach followed in the present work for the design of dissipative braces [143]. 198
- Figure 6.25. Schematisation of the parameters defined in Step 2 for a short (left) and a medium-long (right) building period. “S” describes the bilinear of the existing structure; “DB” represents the damped bracing system, and “S+DB” is the trilinear obtained by summing the equivalent structure and braces. “EP(S+DB)” describes the equivalent SDOF system of the braced structure, whereas “E(S+DB)” is referred to the elastic braced structure [143]. 200
- Figure 6.26. PO capacity curves for the case study before and after the insertion of the Engineered DSF. 203
- Figure 6.27. Comparisons of the inter-storey drifts estimated for the reference building before and after the insertion of the Engineered DSF. 203

List of Figures

Figure 6.28. ADRS and displacement demands at DLS, LSLS, and CLS for the uniform acceleration force distribution, x-direction (Retrofitted building).	204
Figure 6.29. ADRS and displacement demands at DLS, LSLS, and CLS for the uniform acceleration force distribution, y-direction (Retrofitted building).	205
Figure 6.30. ADRS and displacement demands at DLS, LSLS, and CLS for the triangular force distribution, x-direction (Retrofitted building).	205
Figure 6.31. ADRS and displacement demands at DLS, LSLS, and CLS for the triangular force distribution, y-direction (Retrofitted building).	206
Figure 6.32. Combination of the selected accelerograms at the DLS.	207
Figure 6.33. Combination of the selected accelerograms at the LSLS.	208
Figure 6.34. Comparisons between maximum inter-storey drifts estimated for the x and y-direction and referred to the selected accelerograms at DLS.	209
Figure 6.35. Comparisons between maximum inter-storey drifts estimated for the x and y-direction and referred to the selected accelerograms at LSLS.	210
Figure 7.1. The comparison between sustainable development and its pillars (left) and the Life Cycle Sustainable Assessment (right).	213
Figure 7.2. Stages of an LCA (elaborated from [155]).	213
Figure 7.3. Life Cycle Assessment possible approaches.	215
Figure 7.4. Embodied and Equivalent Carbon estimated for the selected DSF options.	220
Figure 7.5. Global Warming impact category referred to the Multi-Storey DSF.	221
Figure 7.6. Global Warming impact category referred to the Shaft-Box DSF.	221
Figure 7.7. Global Warming impact category referred to the Corridor DSF.	222
Figure 7.8. Global Warming impact category referred to the Box-Window DSF.	222
Figure A.1. Flow chart of the followed methodology.	264

Figure A.2. Normalised Taylor diagrams on annual and seasonal dataset.	265
Figure A.3. Methodology followed for the estimation of solar radiation and its components.	267
Figure A.4. Annual and seasonal normalised Taylor diagrams on global solar radiation.	268
Figure A.5. Annual and seasonal normalised Taylor diagrams on direct solar radiation.	271
Figure A.6. Architectural maps and thermal zones of the case study.	272
Figure A.7. Annual average comfort rates according to the adaptive and static thermal comfort, considering the original and the energy-efficient version.	276
Figure A.8. Annual heating and cooling requirement in the original and improved version.	277
Figure A.9. Temperature distribution for the years 1990, 2030, 2050 and 2070 according to the selected RCPs.	278
Figure A.10. Temperature frequency, according to the selected datasets.	279
Figure A.11. Annual average comfort rates according to the adaptive and static approach.	280
Figure B.1. Architectural plan and section of the ReLUIS case study.	282
Figure B.2. Schematisation of the existing building (a) with the insertion of the DSF on one (b) or two elevations (c).	283
Figure B.3. Energy requirement for the cold climate with north-west and south-east DSF exposition.	284
Figure B.4. Energy requirement for the hot climate with north-west and south-east DSF exposition.	285
Figure B.5. Possible building configurations.	286
Figure B.6. Schematisation of the case study in the pre-intervention configuration (a), with the insertion of a north (b) or south DSF (c), or on two (d) and four (e) elevations.	286

List of Figures

- Figure B.7. The annual energy requirement of a detached building for cold climates (Bergamo). 287
- Figure B.8. The annual energy requirement of a detached building for mild climates (Pescara). 287
- Figure B.9. The annual energy requirement of a detached building for hot climates (Messina). 288
- Figure B.10. Schematisation of the case study in the pre-intervention configuration (a), with the insertion of a north (b) or south DSF (c) and on two (d) elevations. 288
- Figure B.11. The annual energy requirement of an internal building for cold climates (Bergamo). 289
- Figure B.12. The annual energy requirement of an internal building for mild climates (Pescara). 289
- Figure B.13. The annual energy requirement of an internal building for hot climates (Messina). 289
- Figure B.14. Schematisation of the case study in the pre-intervention configuration (a), with the insertion of a north (b) or south DSF (c), or on two (d) and three (e) elevations. 290
- Figure B.15. The annual energy requirement of a semi-detached (west corner) building for cold climates (Bergamo). 290
- Figure B.16. The annual energy requirement of a semi-detached (west corner) building for mild climates (Pescara). 291
- Figure B.17. The annual energy requirement of a semi-detached (west corner) building for hot climates (Messina). 291
- Figure B.18. Schematisation of the case study in the pre-intervention configuration (a), with the insertion of a north (b) or south DSF (c), or on two (d) and three (e) elevations. 292
- Figure B.19. The annual energy requirement of a semi-detached (east corner) building for cold climates (Bergamo). 292

Figure B.20. The annual energy requirement of a semi-detached (east corner) building for mild climates (Pescara).	292
Figure B.21. The annual energy requirement of a semi-detached (east corner) building for hot climates (Messina).	293
Figure B.22. Inlet airflow rate.	295
Figure B.23. Outlet airflow rate.	295
Figure B.24. Axonometry of the FEM model in the pre-intervention configuration.	296
Figure B.25. Pushover curves with modal and uniform force distribution.	297
Figure B.26. Schematisation of the BRAD system (a) and the structural model of the building with the exoskeleton (b).	298
Figure B.27. Capacity and Demand Spectrum of the building with and without DSF.	298
Figure C.1. North-east (left) and south-west (right) elevations.	300
Figure C.2. South-east elevation.	300
Figure C.3. North-west elevation.	301
Figure C.4. Typical plans of the residential district (red box is the case study).	301
Figure C.5. Building section and the detail of the balcony.	302
Figure C.6. The localisation of column and beam for structural details.	302
Figure C.7. Shear and flexural reinforcements details of some beams.	303
Figure C.8. Shear and flexural details of beams placed on the roof.	304
Figure C.9. Shear reinforcement details of columns.	305
Figure C.10. Flexural reinforcement details of columns.	305
Figure C.11. Plans and shear and flexural details of the stairs.	306

List of Figures

Figure C.12. Stratigraphy of infills and slabs.	307
Figure E.1. Plan of the Cube (left) with photos of the southern (middle) and northern (right) façade [101].	312
Figure E.2. Schematisation of the investigated DSF configurations and models.	313
Figure E.3. Representation of domain components (left) and DSF case study (right).	314
Figure E.4. Surface meshes (a) and volume meshes (b) of the CFD model.	314
Figure E.5. The localisation of the probe lines inside the DSF cavity.	315
Figure E.6. Velocity magnitude results for various probe lines.	316
Figure E.7. Representation of domain components (left) and the improved DSF configuration (right).	317
Figure E.8. Surface meshes (a) and volume meshes (b) of the improved CFD model.	318
Figure E.9. The localisation of the probe lines inside the original and improved version of DSF cavity.	318
Figure E.10. Velocity magnitude results for various probe lines, referred to the DSF base case and its improved version.	319
Figure E.11. Representation of domain components (left) and the improved DSF configuration (right) for the 3D simulation.	321
Figure E.12. Surface meshes (a) and volume meshes (b) of the improved 3D CFD model.	321
Figure E.13. Velocity magnitude results for various probe lines, referred to the improved DSF configuration for the 2D and 3D models.	322
Figure F.1. The set of accelerograms referred to the Damage Limit State (DLS).	323
Figure F.2. Record of the Basso Tirreno (15/04/1978) earthquake, x-component (DLS).	324

- Figure F.3. Record of the Basso Tirreno (15/04/1978) earthquake, y-component (DLS). 324
- Figure F.4. Record of the Kyllini (16/10/1988) earthquake, x-component (DLS). 325
- Figure F.5. Record of the Kyllini (16/10/1988) earthquake, x-component (DLS). 325
- Figure F.6. Record of the Ionian (04/11/1973) earthquake, x-component (DLS). 326
- Figure F.7. Record of the Ionian (04/11/1973) earthquake, y-component (DLS). 326
- Figure F.8. Record of the Umbria Marche (26/09/1997) earthquake, x-component (DLS). 327
- Figure F.9. Record of the Umbria Marche (26/09/1997) earthquake, y-component (DLS). 327
- Figure F.10. Record of the Faial (09/07/1998) earthquake, x-component (DLS). 328
- Figure F.11. Record of the Faial (09/07/1998) earthquake, y-component (DLS). 328
- Figure F.12. Record of the Alkion (25/02/1981) earthquake, x-component (DLS). 329
- Figure F.13. Record of the Alkion (25/02/1981) earthquake, y-component (DLS). 329
- Figure F.14. Record of the Dinar (01/10/1995) earthquake, x-component (DLS). 330
- Figure F.15. Record of the Dinar (01/10/1995) earthquake, y-component (DLS). 330
- Figure F.16. The set of accelerograms referred to the Life Safety Limit State (LSLS). 331

List of Figures

- Figure F.17. Record of the Ionian (04/11/1973) earthquake, x-component (LSLS). 331
- Figure F.18. Record of the Ionian (04/11/1973) earthquake, y-component (LSLS). 332
- Figure F.19. Record of the Umbria Marche (26/09/1997) earthquake, x-component (LSLS). 332
- Figure F.20. Record of the Umbria Marche (26/09/1997) earthquake, y-component (LSLS). 333
- Figure F.21. Record of the Alkion (25/02/1981) earthquake, x-component (LSLS). 333
- Figure F.22. Record of the Alkion (25/02/1981) earthquake, y-component (LSLS). 334
- Figure F.23. Record of the Adana (27/06/1998) earthquake, x-component (LSLS). 334
- Figure F.24. Record of the Adana (27/06/1998) earthquake, y-component (LSLS). 335
- Figure F.25. Record of the Umbria Marche (aftershock) (06/10/1997) earthquake, x-component (LSLS). 335
- Figure F.26. Record of the Umbria Marche (aftershock) (06/10/1997) earthquake, y-component (LSLS). 336
- Figure F.27. Record of the Dinar (01/10/1995) earthquake, x-component (LSLS). 336
- Figure F.28. Record of the Dinar (01/10/1995) earthquake, y-component (LSLS). 337
- Figure F.29. Record of the Izmit (aftershock) (13/09/1999) earthquake, x-component (LSLS). 337
- Figure F.30. Record of the Izmit (aftershock) (13/09/1999) earthquake, y-component (LSLS). 338

List of Tables

Table 2.1. Main DSF ventilation modes.	20
Table 2.2. Comparison between heat transfer coefficients, surface temperatures and energy requirement calculated with and without the coupling procedure [47].	50
Table 4.1. Weather datasets used in the energy simulations.	63
Table 4.2. Decision matrix for determining the atmospheric transmittance.	68
Table 4.3. Empirical correlation models suggested by various authors.	69
Table 4.4. Coefficient of the correlation model for each constrain.	71
Table 4.5. Description of building envelope components.	80
Table 4.6. Input parameters used for simulations. For each thermal zone, the occupation density (people/m ²), the minimum fresh air (l/s-person), the target illuminance (Lux), and the occupation schedule are shown.	82
Table 4.7. Operative Temperature range for comfort categories.	89
Table 5.1. Synthesis of the main settings adopted for the investigated models.	132
Table 6.1. Main statistical values of concrete strength for different construction periods (elaborated from [121]).	177
Table 6.2. Coefficients K_1 and K_2 .	182
Table 6.3. Mechanical properties of the selected masonry.	184
Table 6.4. Synthesis of some of the most common approaches available for the design of dissipative bracings (elaborated from [143]).	198
Table 6.5. Presentation of main aspects of the real earthquakes selected from the European strong motion database for the DLS.	207
Table 6.6. Presentation of main aspects of the real earthquakes selected from the European strong motion database for the LSLS.	208

List of Tables

Table 7.1. List of the impact categories with the corresponding damage sectors.	214
Table A.1. Input parameters implemented for simulations: occupation density (m ² /person), minimum fresh air (L/s*person), target illuminance (lx) and occupation schedules.	273
Table A.2. Building envelope components in the original and energy-efficient version.	274
Table B.1. The cooling requirement, according to the wind direction.	294
Table D.1. Annual energy consumption estimated with the DB climatic file.	308
Table D.2. Annual energy consumption estimated with the ARTA climatic file.	308
Table D.3. Annual energy consumption estimated with the Climate Network climatic file.	309
Table D.4. Annual energy consumption estimated with the CTI climatic file.	309
Table D.5. Annual energy consumption estimated with the PVGIS climatic file.	309
Table D.6. Annual energy consumption estimated with the MM5-MRF-LSM climatic file.	310
Table D.7. Annual energy consumption estimated with the MM5-BK climatic file.	310
Table D.8. Annual energy consumption estimated with the MM5-PLEIM-XIU climatic file.	310
Table D.9. Annual energy consumption estimated with the 2030 climatic file.	311
Table D.10. Annual energy consumption estimated with the 2050 climatic file.	311
Table D.11. Annual energy consumption estimated with the 2070 climatic file.	311

Appendix A

Results obtained from previous research, centred on the evaluation of the impact of climatic files for energy simulations, are herein reported. These outputs have been used for defining and testing a scientifically validated procedure for the generation of local climatic data from numerical meteorological codes.

This approach has also been applied for the creation of future climatic files, necessary for estimating the impact of climate changes on existing buildings and orienting energy-efficient solutions.

The first stage involves the intercomparison between weather datasets obtained from different sources. The weather data sources used correspond to the Fifth Mesoscale Model (MM5), the HadRM3P and RCA4 regional models through the Coordinated Regional Climate Downscaling Experiment (CORDEX) and the International Weather for Energy Calculations (IWECC).

The evaluation is made considering the correlation coefficient (R), the centred root-mean-square difference (RMSD) and the standard deviation (σ). This stage aims to figure out the accuracy of these climate models to describe the pattern of the analysed climate parameters and the climatology of the city under study. To this purpose, the datasets are compared with observed meteorological data collected from a weather station.

In the second stage, some standard methodologies to estimate the diffused and direct component of the global solar radiation are analysed, aiming to solve the problem of missing separated components and to evaluate the accuracy of the selected correlation models.

The third stage consists of creating weather data files to be used in the building simulation software, to quantify the influence of measured/simulated meteorological data on the evaluation of building energy performance. A set of forecasting data is also elaborated for evaluating the building energy requirement and comfort condition due to climate change effects, considering the case study in the original and improved version.

The results obtained by these analyses have been published as two papers in Q1 scientific journals (*Energy & Buildings* and *Building Simulation*) reported

among the references as [84] and [165]. For the sake of the brevity, only the principle results are presented in the following lines.

COMPARISON OF CLIMATIC FILES

Figure A.1 summarises the methodology followed for the generation and comparison of climatic files.

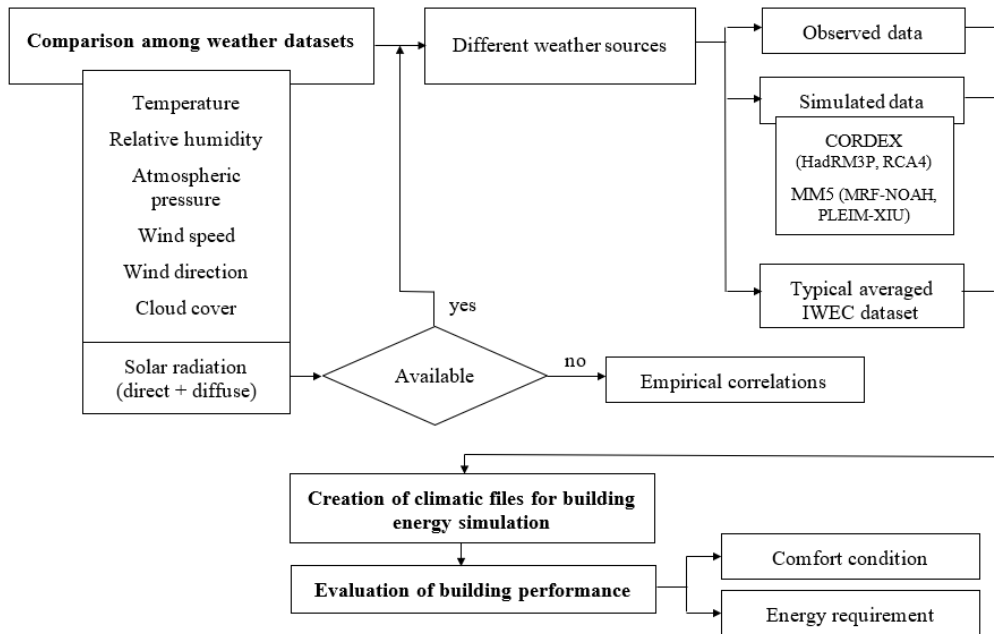


Figure A.1. Flow chart of the followed methodology.

The studied site location is the city of Asunción in Paraguay, for which observed data regarding six climate parameters (temperature, atmospheric pressure, relative humidity, wind speed and direction and cloud cover) from the mast in the Silvio Pettrossi Airport are available for the 2009 year. These values are compared with those obtained from other sources like MM5, the HadRM3P and RCA4 regional models through CORDEX and IWEC (referred as DB).

Normalised Taylor diagrams are elaborated for plotting correlations among simulated and recorded values, considering both annual and seasonal (Figure A.2) time scales.

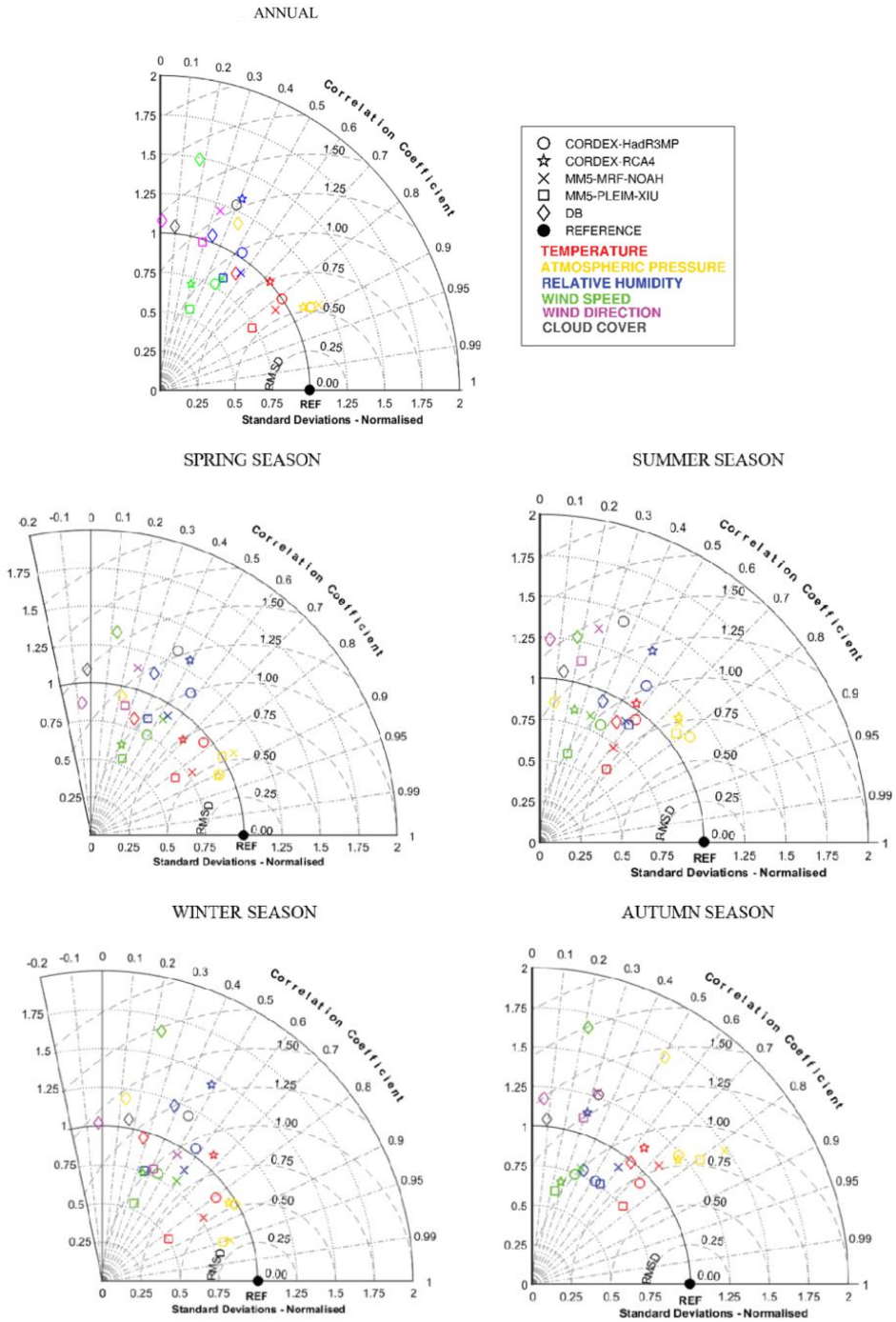


Figure A.2. Normalised Taylor diagrams on annual and seasonal dataset.

Appendix A

In general, it can be seen that the performance of the models varies according to the simulated parameter. In most cases, the parameters having lower RMSD and higher correlations are the temperature and the atmospheric pressure (red and yellow markers) since they are located nearest the reference point.

The other parameters are scattered throughout the quadrant with most data points within the 1.5 RMSD circle and correlations between 0.2 and 0.6, excluding the datasets of DB which have, most of the times, the highest RMSD and lowest correlation, and even negative values (spring and winter season).

Regarding the standard deviation, generally, the data points fell into the area between the circles of 0.75 and 1.25, underling how models can represent the time distribution of the simulated parameters with a good approximation.

According to Figure A.2, the DB (diamond marker) dataset delivers the lowest correlation patterns for all the parameters, being the poorest performance model since its markers are always the farthest from the reference point.

Another essential aspect which has been investigated is the solar radiation which is not often recorded by meteorological stations but has a significant impact on building energy simulations. Moreover, it is an essential climatic parameter for the creation of weather data files. For all these considerations, a derived estimation of this parameter and its components for Asunción is described and adopted.

This estimation is made considering the sun angles and position, the latitude and longitude of the site location, and the extra-terrestrial radiation on a horizontal surface. The methodology has been firstly applied to the city of São Martinho da Serra (Brazil), for which solar radiations data are available and validated through a quality control process. Moreover, this source has also been used to create and test several correlation models for the estimation of solar radiation data.

Even though these correlation models can be applied to any location in the world, it is important to note that Asunción and São Martinho da Serra are in the same climatic area, in the same hemisphere and 750 km far from each other.

The methodology followed for decomposing the global solar radiation into its direct and diffuse components can be summarised by the flow chart here inserted (Figure A.3).

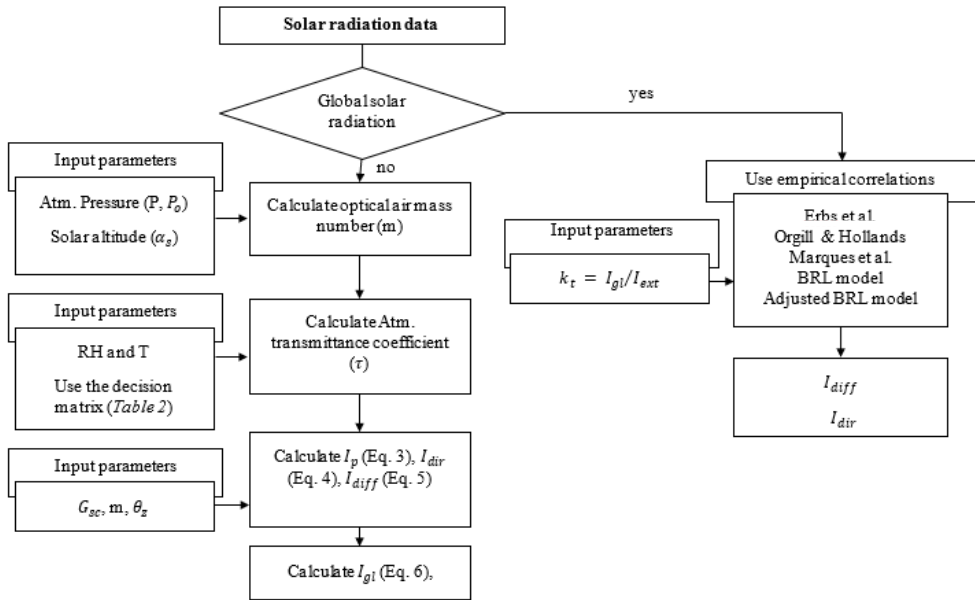


Figure A.3. Methodology followed for the estimation of solar radiation and its components.

First, global solar radiations obtained from regional climate models and recorded by the meteorological station have been compared in order to evaluate the accuracy of each model in the estimation of this parameter. Then, several empirical correlations to determine the fraction of the hourly radiation on a horizontal plane which is diffused were used.

The correlation model, which better agreed with São Martinho da Serra observations was considered the suitable one to be used to create the weather data files for Asunción. Also in this case, the comparison results are depicted through Taylor diagrams.

Figure A.4 shows annual and seasonal Taylor diagrams where the plotted parameter is the global solar radiation, whereas Figure A.5 depicts the comparison among the selected correlations applied to the Brazilian city. In detail, five empirical correlations have been used, and they correspond to those developed by Erbs et al. [166], Orgill and Hollands [167], Marques et al. [168], and the BRL model proposed by Ridley et al. [169] and its modified version [170].

Appendix A

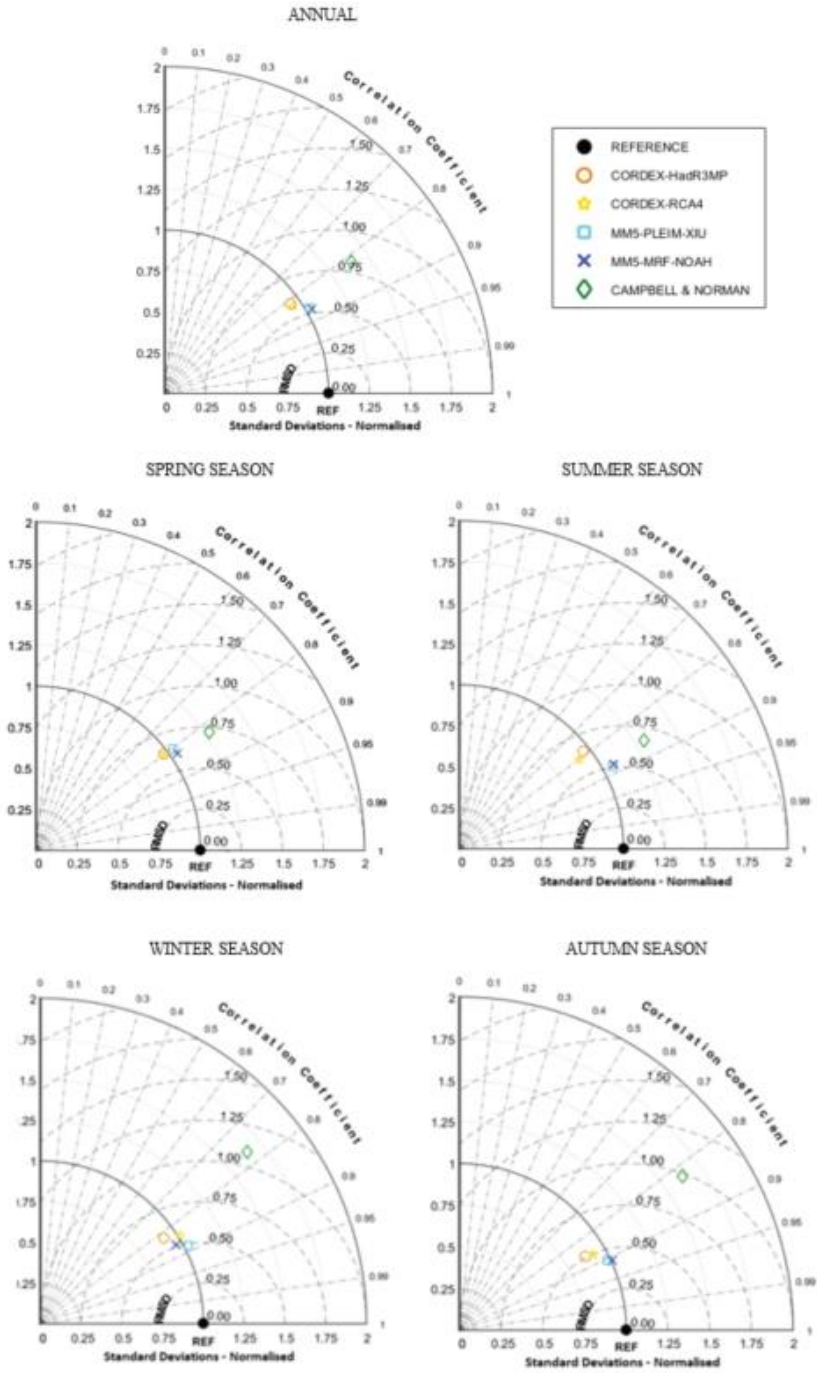


Figure A.4. Annual and seasonal normalised Taylor diagrams on global solar radiation.

The regional climate models, both MM5 and CORDEX, are in general able to describe the variation of global solar radiation during the seasonal and annual periods. In detail, the MM5 datasets (square and x markers) agree best with observations for all seasons, considering that both MRF-NOAH and PLEIM-XIU are always the closest to the reference point, particularly during the coldest seasons. In fact, MM5-MRF-NOAH records the lowest distance from the reference in autumn, with a 0.43 RMSD value and a correlation equal to 0.91.

In the same way, CORDEX is able to describe the seasonal variability of global radiation. Nevertheless, the models deliver slightly lower correlations and higher RMSD values than those of MM5. When compared to each other, CORDEX-RCA4, which has a lower RMSD (0.50) and higher correlation coefficient (0.87), is more accurate than CORDEX-HadRM3P, that has values equal to 0.51 and 0.86, respectively.

The model developed by Campbell & Norman [75] could be useful when measured, or simulated data for global solar radiation are unavailable (even if it is not as accurate as the regional climate models). In general, the model tends to estimate variations that were much greater than observations, delivering slightly better results in the warmer seasons, recording its best value in summer and becoming less accurate in winter.

The trend analysed for seasonal datasets is also confirmed by annual data. The MM5 models describe the global solar radiation for the annual dataset slightly better; MRF-NOAH with a 0.53 RMSD value and correlation equal to 0.87 and PLEIM-XIU with a 0.54 RMSD value and 0.86 correlation. CORDEX models deliver slightly lower correlation and higher RMSD values. Campbell and Norman's model improves its accuracy when the annual dataset is considered, with values of RMSD, R and σ equal to 0.82, 0.82 and 1.39, respectively.

Evaluating the accuracy of empirical correlation models, it can be seen that, in general, they estimate very short-time variability of the parameter, especially during colder seasons, where the markers fall further from the reference point ($\sigma \cong 0.43$ for colder seasons and $\sigma \cong 0.82$ for warmer seasons).

Regarding correlation coefficients, the values for spring and summer season are always lower than 0.70, while for the winter and autumn season, they decrease to 0.40 for all empirical models. The correlation model delivering the best results in

all seasons corresponds to the one suggested by Marques et al., which has RMSD and correlation coefficients equal to 0.83 and 0.64 for spring, 0.82 and 0.62 for summer, 0.98 and 0.30 for autumn and 0.95 and 0.35 for winter, respectively.

The adjusted BRL model and the original one deliver very similar results, and the adjusted BRL model is able to describe the variation of direct solar radiation slightly better than the original one. In fact, the adjusted BRL model has a slightly higher correlation coefficient in every season, especially for spring and winter seasons.

Analysing the results based on an annual dataset, the same trend in the seasonal case is observed. The correlation model estimating the direct component of solar radiation slightly better was the one developed by Marques, et al., delivering values of RMSD, R and σ equal to 0.90, 0.52 and 0.81, respectively.

In synthesis, the analyses carried out in this section show the accuracy of regional climate models (MM5 and CORDEX) in estimating global solar radiation values. Thus, the regional climate models driven by reanalysis data might be an option when measured data for global solar radiation are unavailable.

The results also underline that the estimation of this parameter using the model defined by Campbell & Norman, which considers the observed data of temperature, atmospheric pressure and relative humidity, but is not as accurate as MM5 and CORDEX regional climate models.

In regards to the analysis of empirical models for the decomposition of global solar radiation, measured or just estimated, into its direct component, in general, all the correlation models delivered similar results. The model developed by Marques et al. was slightly better at describing the time variability of the parameter during the seasons and the whole year.

For this reason, it was employed to determine the direct and diffused components of solar radiation to create the weather data files used in the energy simulations, as described in the next sections.

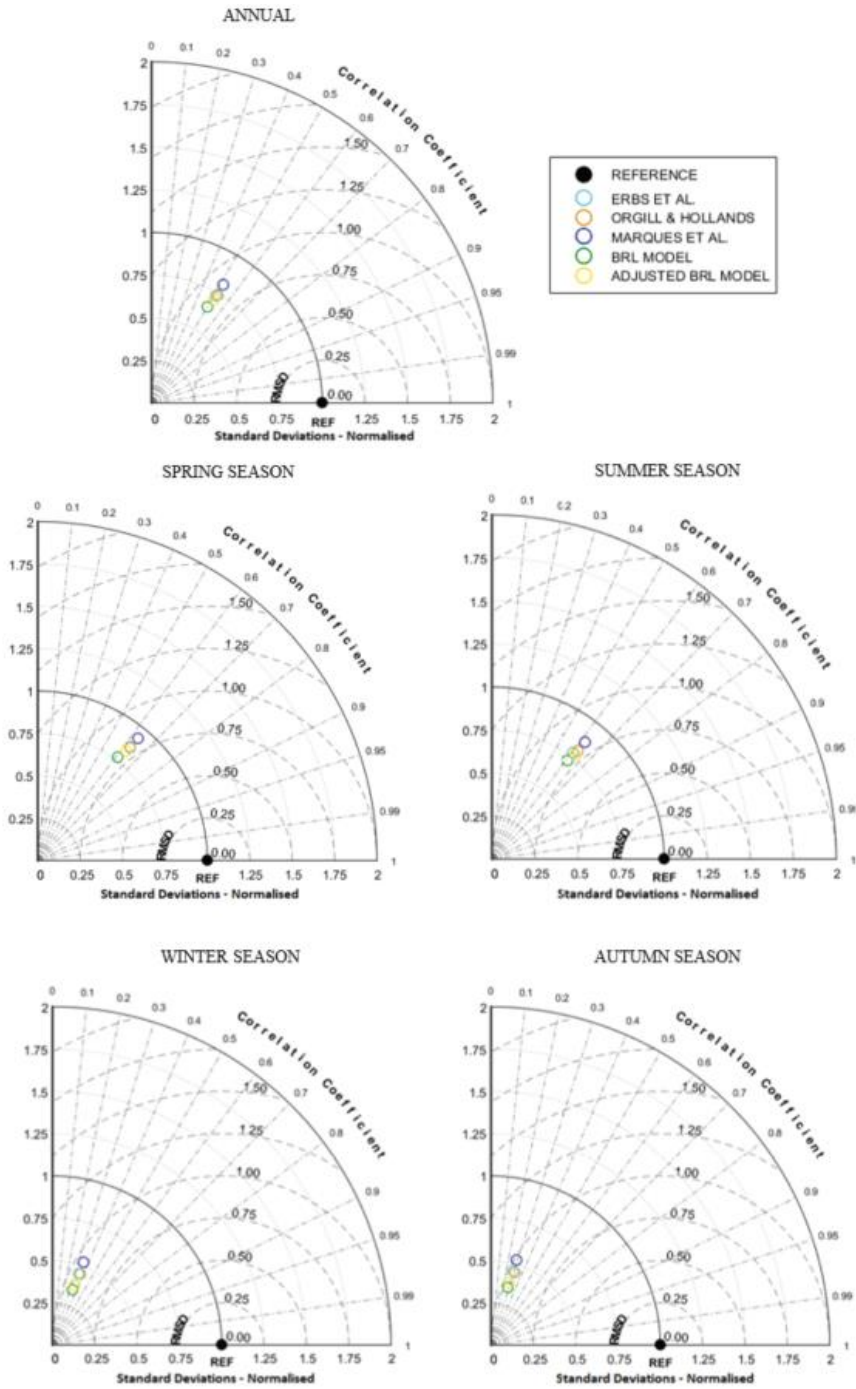


Figure A.5. Annual and seasonal normalised Taylor diagrams on direct solar radiation.

CASE STUDY DESCRIPTION

The case study consists of a historical building located in the Historic Centre of Asunción. It is a two-storey structure and, according to the area (188.8 m²) and geometry, corresponds to a single-family dwelling. The ground floor is composed of four thermal zones (lounge, circulations, bathroom, dining room and a kitchen) and the first floor has three thermal zones (two bedrooms and one lounge) (Figure A.6). The main thermal zone under analysis and for which the results are depicted corresponds to Bedroom 2 (19 m²), a thermal zone on the first floor and with east orientation.

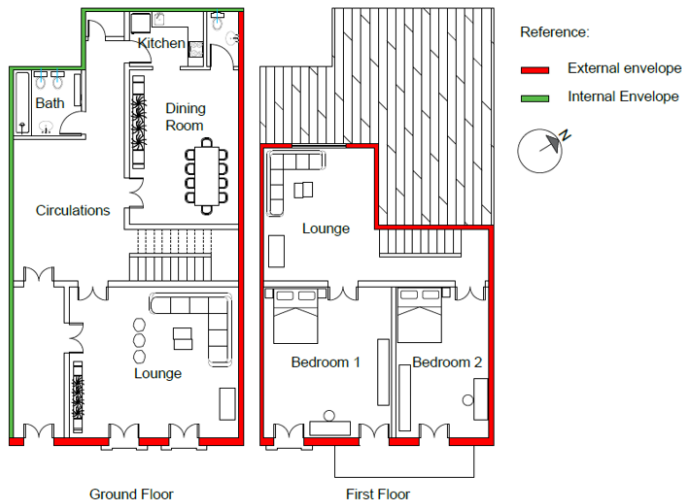


Figure A.6. Architectural maps and thermal zones of the case study.

For dynamic simulations, the metabolic factor is set to 1 for all thermal zones, the values used for insulation clothing are 0.5 clo for the summer season and 1 clo for the winter season. The input parameter values, varying according to each thermal zone, are shown in Table A.1.

For the thermal comfort evaluation, the selected building is considered without any heating or cooling system. However, a natural ventilation strategy is inserted, where the minimum natural ventilation rate is defined using minimum fresh air requirements (Table A.1).

Table A.1. Input parameters implemented for simulations: occupation density ($m^2/person$), minimum fresh air ($L/s*person$), target illuminance (lx) and occupation schedules.

Thermal zone	Lounge	Circulations	Kitchen & dining	Bedroom	Bathroom
Occupation density	53.32	64.50	59.12	43.59	53.37
Fresh air	4	4	14	4	10
Illuminance	200	100	300	100	150
Internal gains	3.9	1.57	30.28	3.58	1.67
Schedule					

The windows operation schedule defines the operation of natural ventilation. Thus, for summer season windows are open, and the natural ventilation is allowed only when the outdoor temperature is lower than the indoor temperature and higher than 20 °C. For the winter season, windows are open only when the operative temperature is higher than the comfort temperature calculated from the CEN 15251:2014 adaptive comfort model.











Regarding the window shading (exterior venetian blinds), the aperture operation is scheduled for the winter season: 100% open from 8 a.m. to 6 p.m. and fully closed the rest of the day. For the summer season, the shading is on when solar radiation reaches the medium solar setpoint of 189 W/m^2 , aiming to reduce thermal discomfort due to direct solar radiation but taking advantage of natural daylight.

First, the building is simulated in its original state with the various data files previously created. Subsequently, its energy-efficient version is analysed to figure out how climate change effects can influence the design and correct setting of energy retrofit solutions.

The thermal properties of the building envelope in the original state and the improved solutions are summarised in Table A.2.

Appendix A

Table A.2. Building envelope components in the original and energy-efficient version.

Building component	Material [outer to inner]	<i>s</i> (m)	λ (W/(m·K))	<i>c</i> (J/(kg·K))	ρ (kg/m ³)	<i>U</i> (W/(m ² ·K))	<i>M_s</i> (kg/m ²)
Configurations in the original state							
W1 – Façade SE orientation							
30cm Wall  outer inner (a)(b)(c)	(a) Sand-lime plaster	0.015	1.15	1000	1800	1.95	459
	(b) Solid brick burned	0.270	0.85	840	1500		
	(c) Sand-lime plaster	0.015	1.15	1000	1800		
	(a)(b)(c)						
W2 – NE orientation							
20cm Wall  outer inner (a)(b)(c)	(a) Sand-lime plaster	0.015	1.15	1000	1800	2.53	309
	(b) Solid brick burned	0.170	0.85	840	1500		
	(c) Sand-lime plaster	0.015	1.15	1000	1800		
	(a)(b)(c)						
W3 – NE, NW and SW							
15cm Wall  outer inner (a)(b)(c)	(a) Sand-lime plaster	0.015	1.15	1000	1800	2.93	234
	(b) Solid brick burned	0.120	0.85	840	1500		
	(c) Sand-lime plaster	0.015	1.15	1000	1800		
	(a)(b)(c)						
F1 – Calcareous Floor							
(a) (b) (c) 	(a) Calcareous tile	0.010	2.21	840	2550	2.92	277
	(b) Soil-sand screed	0.015	1.15	1000	1800		
	(c) Granular subbase	0.100	1.80	840	2240		
R1 – Pitched Roof Tile							
(a) (b) 	(a) High density wood	0.025	0.29	1340	850	4.20	40
	(b) Ceramic clay tile	0.010	0.84	800	1900		
G1 – Glazing							
outer inner (a) 	(a) Single clear glazing	0.006	0.90	880	2500	5.78	5
Configurations of the energy efficient version ^{1,2}							
W2a – NE orientation							
29.5cm Wall  outer inner (a) (b) (c) (d) (e)	(a) Thin clay plaster	0.015	0.35	2100	3000	0.45	368
	(b) Glass wool felt	0.080	<i>R_f</i> =1.80	840	175		
	(c) Sand-lime plaster	0.015	1.15	1000	1800		
	(b) Solid brick burned	0.170	0.85	840	1500		
	(e) Sand-lime plaster	0.015	1.15	1000	1800		
W3a – NE, NW and SW							
24.5cm Wall  outer inner (a) (b) (c) (d) (e)	(a) Thin clay plaster	0.015	0.35	2100	3000	0.46	293
	(b) Glass wool felt	0.080	<i>R_f</i> =1.80	840	175		
	(c) Sand-lime plaster	0.015	1.15	1000	1800		
	(b) Solid brick burned	0.120	0.85	840	1500		
	(e) Sand-lime plaster	0.015	1.15	1000	1800		
R1a – Pitched Roof Tile							
(a) (b) (c) (d) (e) 	(a) Ceramic clay tile	0.010	0.84	800	1900	0.43	1281
	(b) High density wood	0.025	0.29	1340	850		
	(c) Air gap	1.000	<i>R_f</i> =0.15	1000	1200		
	(d) Glass wool felt	0.080	<i>R_f</i> =1.80	840	175		
	(e) Plasterboard	0.030	0.25	1000	900		
G1a – Double Glazing							
outer inner (a)(b)(c) 	(a) Single clear glazing	0.006	0.90	2500	880	2.76	10
	(b) Air gap	0.010	<i>R_f</i> =0.15	1000	1200		
	(c) Single clear glazing	0.006	0.90	2500	880		

1. To calculate the thermal parameters of the roof R1a, an equivalent constant thickness was used for the air gap.

2. For some constructive elements were considered their thermal resistance (*R_f*) instead their thermal conductivity.

DYNAMIC ENERGY SIMULATIONS

After generating climatic files, dynamic energy simulations were carried out. Figure A.7 depicts the results of the annual thermal comfort evaluation, while Figure A.8 shows the annual energy requirements of the thermal zone under analysis, using the different climatic files and considering both, the building original state and the energy-efficient version (there referred as the improved state).

In general, the results agree with the outputs previously analysed, where it was concluded that the MM5 datasets tend to underestimate the temperature parameter and to simulate shorter time variability for most of the climate parameters. In fact, the results of dynamic simulations record the lowest overheating rates and the highest heating needs. Nonetheless, all the models delivered similar outputs in the annual assessment.

In the thermal comfort evaluation, the results for the CORDEX datasets, both HadRM3P and RCA4, deliver similar results. In regards to the CORDEX-HadRM3P dataset, the highest overheating rates are recorded, which agrees with the previous results. Similar results are also seen in the MM5 datasets where just minor differences are found comparing the results for MRF-NOAH and PLEIM-XIU.

Regarding the results employing the DB dataset, minor differences are detected in the annual thermal comfort assessment when compared with the outputs using the other datasets. This is due to the inaccuracy of the models in describing the temperature pattern changes according to the months since they alternately underestimate or overestimate it. This involves changes in the distribution of overheating or underheating rates. In addition, when considering the annual results, the values tend to offset each other through the days resulting in a reasonable estimation of the total comfort rates.

Considering the energy efficient version, significant improvements in the building thermal performance are estimated if compared to the original state. The use of thermal insulation in walls and roofs is quite effective in decreasing the discomfort rate of the building.

Appendix A

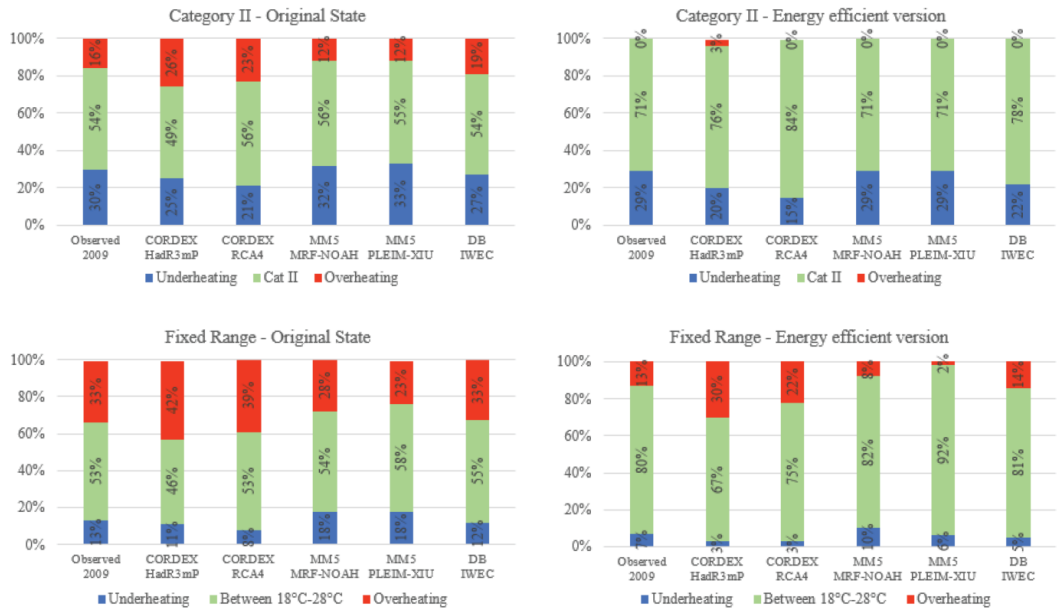


Figure A.7. Annual average comfort rates according to the adaptive and static thermal comfort, considering the original and the energy-efficient version.

In Figure A.8, the annual simulation underlines the ability of the climate models to estimate the total annual energy requirement for both the original and the improved state, especially in the case of MM5-MRF-NOAH, which delivered results with an excellent approximation regarding the observed situation.

Nonetheless, both MM5 datasets tended to slightly overestimate the heating needs, which agrees with the thermal assessment analysis, considering that they delivered the highest underheating rates. The datasets exceeding the cooling requirements correspond to those of CORDEX and DB.

Considering the improved state, the energy demand of the thermal zone decreased exponentially, showing the effectiveness of the energy-efficient version of the building, and confirming the recorded trend among all models. Thus, the annual energy requirement is also well estimated with different weather datasets.

It is clear that the differences among the weather datasets, detected in the statistic intercomparison of hourly values, are not reflected in the annual energy simulation results. This is due to the inability of models to estimate the temperature

pattern throughout the year, affecting the distribution of heating and cooling energy needs.

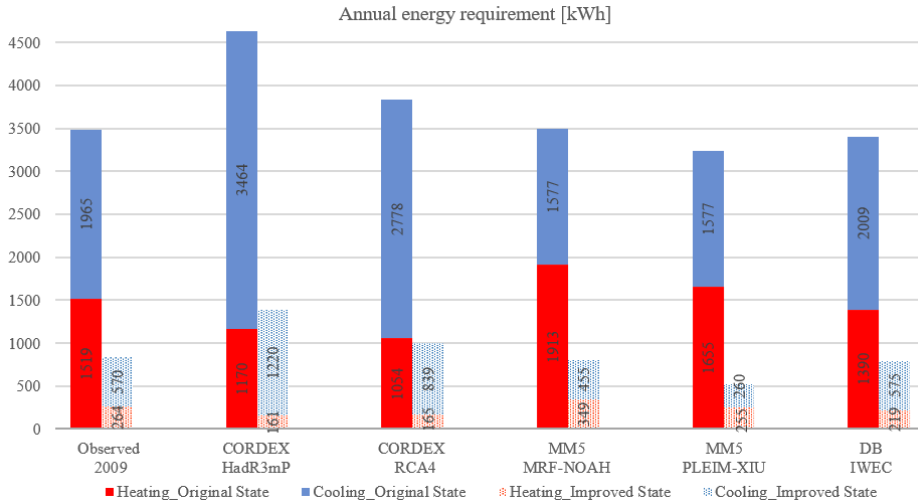


Figure A.8. Annual heating and cooling requirement in the original and improved version.

IMPACT ASSESSMENT OF CLIMATE CHANGE

Energy dynamic simulations are also performed for evaluating the impact of climate change on the case study, before and after the energy improvement. Low and high Representative Concentration Pathways (RCP) climate scenarios for 2030, 2050 and 2070 are employed with a CORDEX climate model.

The RCP 4.5 and RCP 8.5 scenarios have been selected as the best and worst scenario, respectively. The RCP 8.5 is consistent with a future with no policy changes to reduce emissions, and the RCP 4.5 is compatible with a future with relatively ambitious emission reductions.

Figure A.9 depicts the temperature distribution according to the datasets obtained by the RCP 4.5 and RCP 8.5 for the time horizons and the city under analysis. Comparing the percentage of the time during the year in which a specific temperature is presented, the scenario that considers a future with significant emissions reductions clearly projects a limitation in terms of temperature increase (RCP 4.5). Thus, no substantial increases in temperature can be noted when comparing the circles of the historical (grey lines) and the 2030 (yellow) datasets.

Appendix A

With this climate scenario, the increase in temperature starts to be noted with the 2050 and 2070 weather datasets, since the circles tend to turn to the left, which indicates the occurrence of higher temperatures.

In the same line, the trend of temperature increase is better appreciated with the RCP 8.5 since the differences among each weather dataset are accentuated, and the circles tend to turn to the left according to the considered time horizon, indicating the occurrence of higher temperatures.

The historical dataset, referred to the 1990 year, shows for the temperature recorded that the highest percentage of occurrences is 23°C. This trend is maintained for the estimation coming from the RCP 4.5 scenario related to the year 2030. For the years 2050 and 2070, the highest percentage corresponds to a temperature of 26 °C. For the RCP 8.5, the 2030 and 2050 weather datasets estimate a temperature of 24 °C as the highest percentage of the occurrence. Considering the year 2070, the highest rate of incidents for temperatures is also 26 °C.

Nonetheless, the 2070-year forecasts estimate maximum temperature values equal to 38 °C and 40 °C, for the RCP 4.5 and RCP 8.5 climate scenarios, respectively.

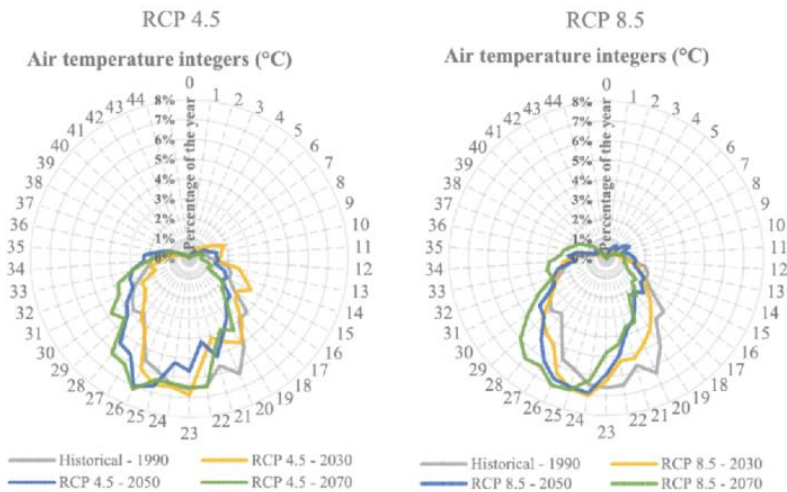


Figure A.9. Temperature distribution for the years 1990, 2030, 2050 and 2070 according to the selected RCPs.

Considering the temperature parameter (Figure A.10), a general increase is projected, where the tendency that the number of hours with higher temperatures will increase and the number of hours with lower temperatures will decrease is outlined.

Nonetheless, both RCP climate scenarios estimate that the highest number of hours during the year will have a temperature value between the acceptable range (18 – 28 °C). With the RCP 8.5 scenario, a significant increase in temperatures is highlighted. The temperatures, in fact, are outside of the comfort range, especially for the 2070-year.

Taking as a base the observed data of the 2009 year, the number of hours with temperatures higher than 28 °C will increase considering climate change effects by the year 2070 in around 20% and 34% for the RCP 4.5 and RCP 8.5, respectively.

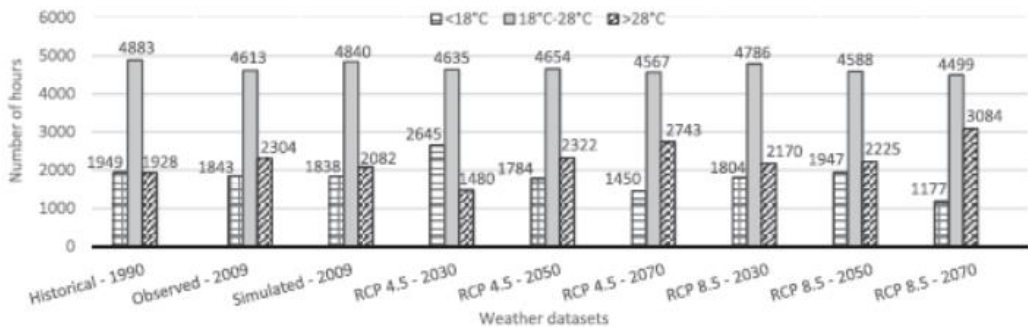


Figure A.10. Temperature frequency, according to the selected datasets.

Figure A.11 depicts the results of the annual thermal comfort evaluation of the case study employing different weather datasets and considering both the original state and the energy-efficient version of the building. Through the analysis of the results using different forecasting scenarios, the projected increase in temperature leads to a consequent increment of the overheating rates with a parallel decrease of the underheating percentage.

In order to analyse the differences between the employed thermal comfort approach, it can be said that when considering a fixed temperature comfort range,

independent of the outdoor conditions, the overheating rates are more significant for both, the original and the energy-efficient version of the building.

In fact, even with the improved version, the overheating rates for both climate scenarios are very significant from the year 2030, indicating the imminent need to use HVAC systems to achieve better comfort conditions, which will lead to higher building energy consumption. Nonetheless, the overheating rates in the original state of the building are significantly bigger, indicating that, if no retrofit measures are considered, the building will have uncomfortable conditions most of the year, mainly from the 2050 and considering the RCP 8.5 scenario.

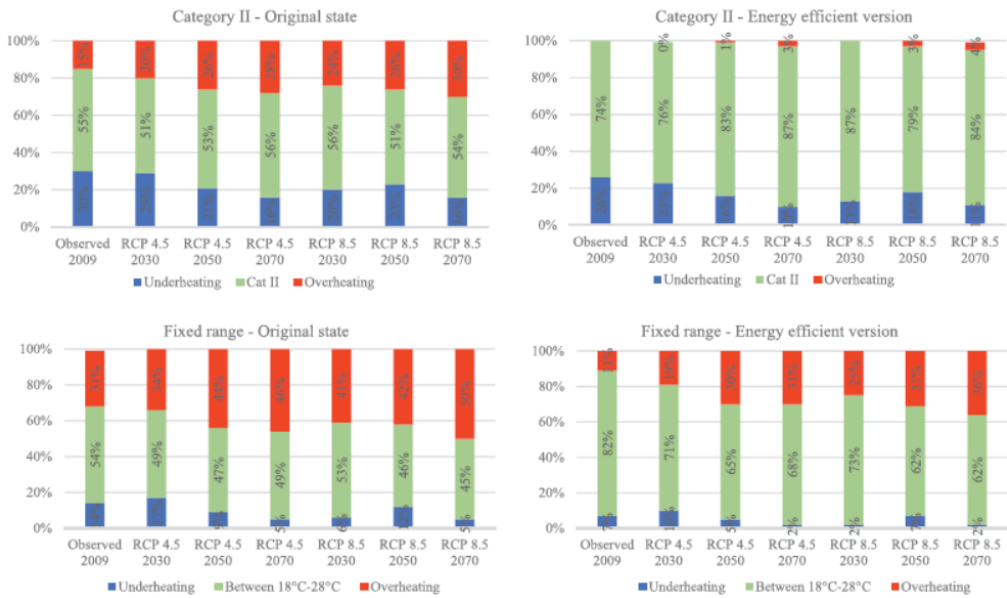


Figure A.11. Annual average comfort rates according to the adaptive and static approach.

Analysing the observed 2009 dataset and the case study in the original state, a high number of values are outside of the acceptable comfort range, both for the fixed and adaptive approach. In the energy-efficient version, a consistent reduction of the operative temperature outside the acceptable range is recorded, assuming as upper and lower limits the two comfort conditions. Thus, the introduction of passive energy efficiency measures to improve the thermal performance of the building can ensure a restraint on the variability of the operative

temperatures through the years, and to collaborate for the steadiness of comfort conditions inside the building.

In conclusion, the projected temperature rise due to climate changes will lead to a consequent increment of the discomfort rates, which will be even worse if no energy retrofit measures are adopted. Furthermore, the overheating rates on buildings can profoundly increase if no emission reduction policies are introduced, considering both the adaptive and the static thermal comfort approach. In fact, considering the RCP 8.5 scenario, the discomfort rate reaches in 2070 30% and 50% respectively for the adaptive and static method, and these percentages could be reduced to 4% and 36% introducing energy efficiency measures.

From the analysis of discomfort rates estimated for the case study in the original and energy-efficient version, the results allow asserting that the strategy implemented contributes for reducing the overheating phenomena significantly and enables to maintain comfortable indoor conditions, contributing to the improvement of occupant wellbeing. In this way, through the retrofit measures, the building has a better capacity to face climate change effects and ensure proper conditions for the inhabitants.

Appendix B

Preliminary analyses are carried out on a simple building, adopted as a case study for 3.3 Task of the ReLUIS Project. The selected building has a rectangular shape with sizes equal to 22 x 11.5 m, and it is made of four levels above ground for a total high equal to 12.2 m. Figure B.1 shows the architectural plan (typical floor) and a section of the building.

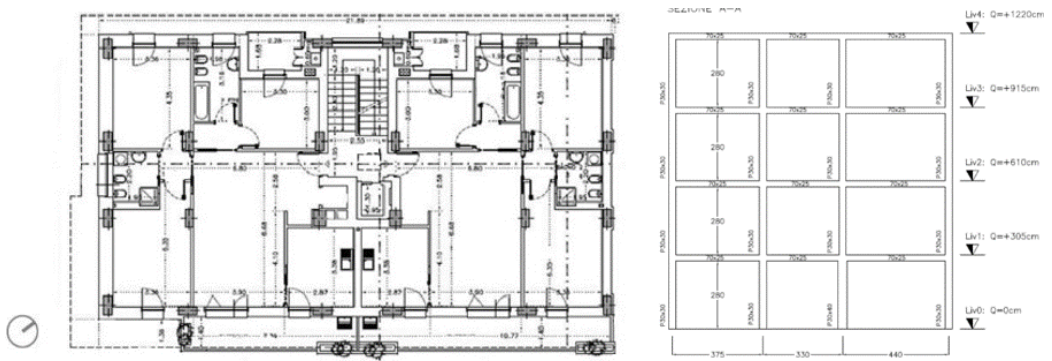


Figure B.1. Architectural plan and section of the ReLUIS case study.

The building has a reinforced concrete frame structure, infills made of hollow bricks and hollow-core concrete slabs. The used concrete has a strain class equal to C20/25, and the steel of reinforcements is FeB32k.

The transmittance values are equal to 1.20 W/m²K and 1.40 W/m²K, respectively for external infills, composed of two layers of hollow bricks (12 + 8 cm), and concrete slabs. For glazed surfaces, the U value is assumed as 3.7 W/m²K with a ratio between the transparent and opaque layers equal to 15%. The considered HVAC system, in accordance with the age of the building, presents low energy efficiency and 0.8 and 2.5 are assumed as values respectively for the heating and cooling equipment.

The building is realistic but not real and, for this reason, it is located in different Italian cities according to the type of analysis that is performed:

- L'Aquila is selected for structural simulations considering the high PGA value (0.260 g).

- Bergamo, Messina, Pescara and Ancona are chosen for energy simulations because representative of different climatic zones.

Energy and structural simulations are carried out to evaluate the performance of the reference building and to estimate the improvement achievable through the insertion of the engineered DSF.

DYNAMIC ENERGY SIMULATIONS

Various energy analyses are carried out for investigating the performance of a Multi-Storey DSF which is considered in a first stage passive and then active. Preliminary simulations are performed for evaluating the best shading system, placing the DSF, alternatively, on one and two elevations, and assuming several cavity depths (1 m, 1.5 m, and 2 m). The case study is localised in both hot and cold climates.

Shading systems with different size and typology are also inserted for each configuration, and the influence of louvres with dimension equal to 0.5 m, 1.0 m and 2.0 m and blinds with low reflectivity slats is evaluated. Figure B.2 presents a simplification of the energy models performed for this first stage.

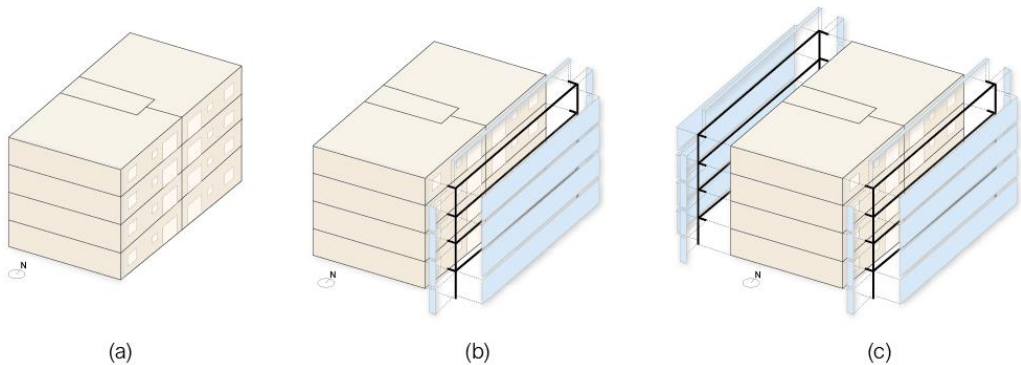


Figure B.2. Schematisation of the existing building (a) with the insertion of the DSF on one (b) or two elevations (c).

The energy performances are evaluated supposing two different Italian locations, Messina (hot climate) and Bergamo (cold weather), and the investigated parameter is the energy required for the heating and cooling of the inner spaces.

The results here reported are subdivided for climate conditions and referred to the pre- and post-retrofit intervention. The building in its existing configuration represents the zero point for the evaluation of the improvement obtained with the suggested solution. For the sake of brevity, the outputs of the energy-efficient versions (Figure B.3 and Figure B.4) are presented in terms of decrement/increment of the total energy requirement, expressed in percentage, compared to the pilot case in its pre-intervention status.

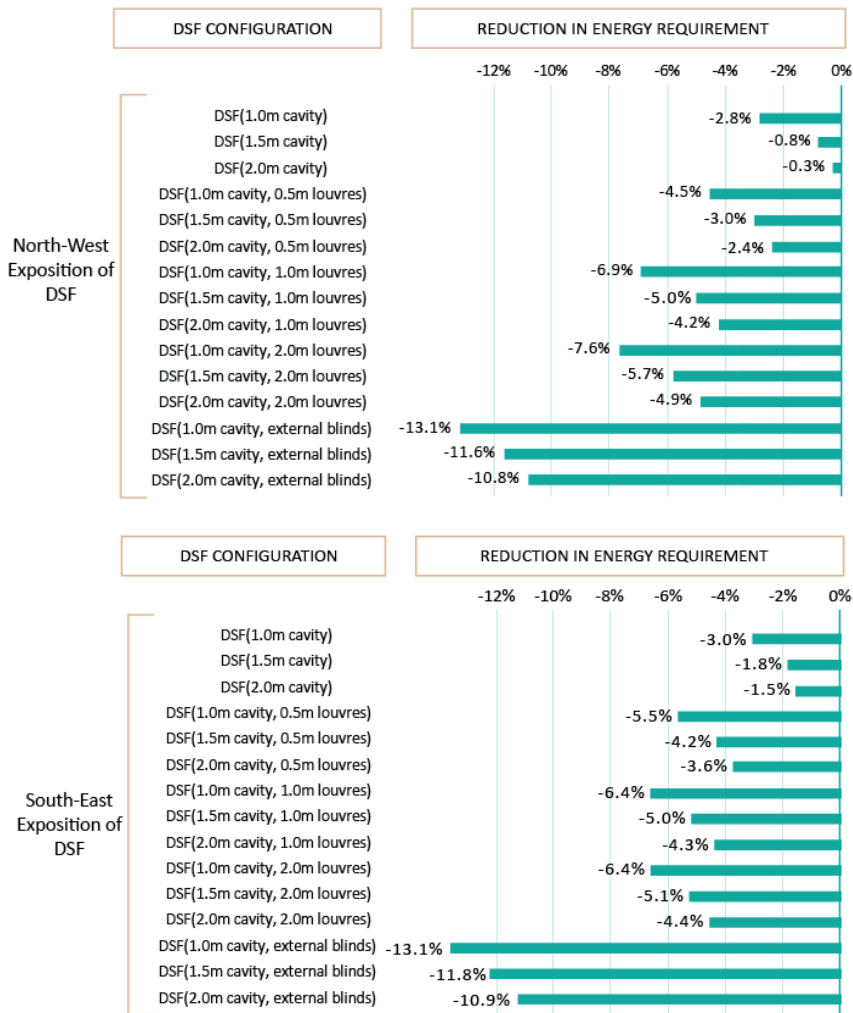


Figure B.3. Energy requirement for the cold climate with north-west and south-east DSF exposition.

Appendix B

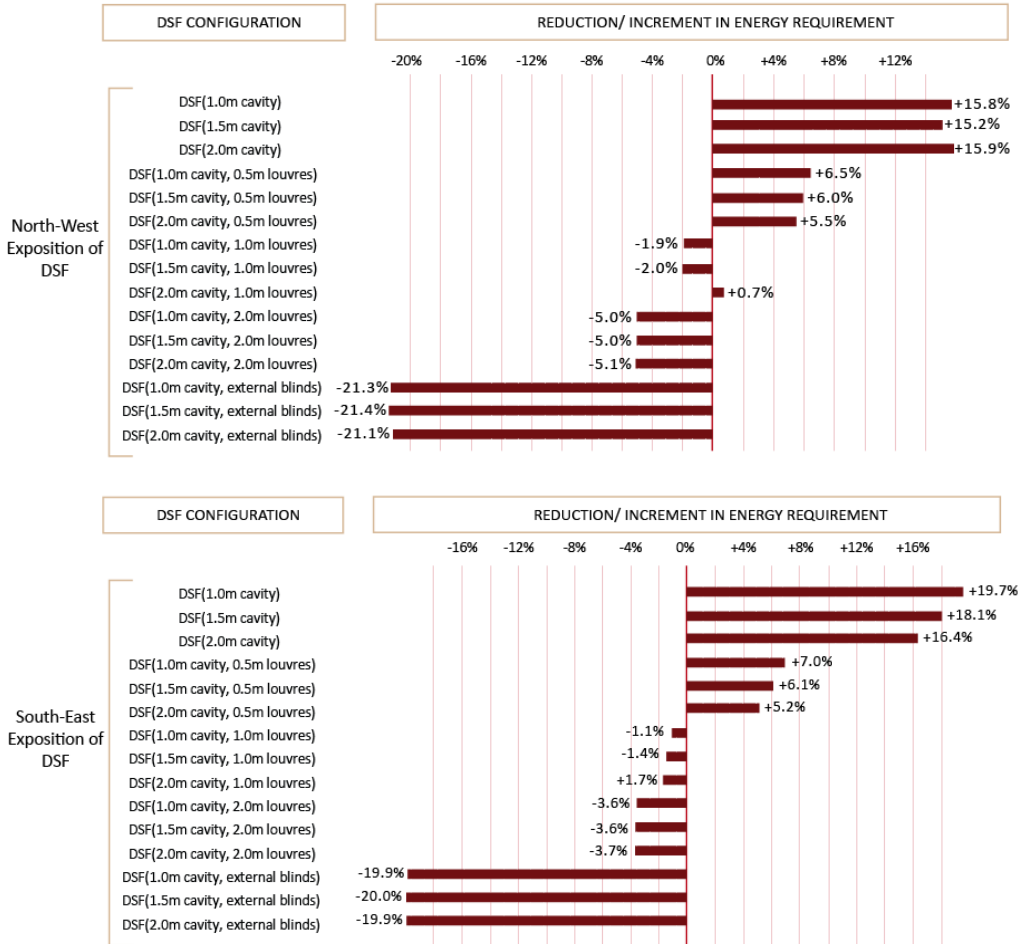


Figure B.4. Energy requirement for the hot climate with north-west and south-east DSF exposition.

The obtained results underline how the insertion of the shading system can drastically improve the performance for all DSF configurations, and this is recorded for both cold and hot climates. Moreover, the use of external blinds with low reflectivity slats confirms to be the best option, conferring more significant decrement and being more efficient in the reduction of the cavity overheating risk during the summer period.

Once the best shading system has been defined, detailed analyses are performed, considering the insertion of the Double Skin Façade on the same

reference building but exploring various options that it can assume, as depicted in Figure B.5:

- Detached building.
- Internal building.
- Semi-detached building (west corner).
- Semi-detached building (east corner).

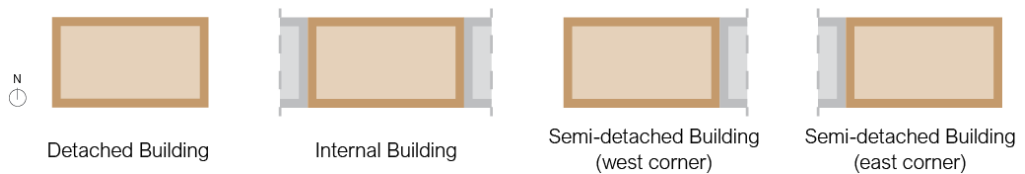


Figure B.5. Possible building configurations.

In the internal or semi-detached case, adiabatic blocks are inserted for simulating the presence of adjacent buildings and avoiding heat transfer from one construction to the other. For these analyses, the case study is considered oriented along the east-west directrix, whereas previously, the main axis direction was inclined towards the East-West directrix of around 53° . This choice is made for evaluating the performance of DSF exposed to north and south, avoiding any possible alterations due to imperfect orientations.

DETACHED BUILDING

The results presented in the following lines are referred to the case study considered as a detached building and the DSF is inserted, respectively, on one elevation (case b and c), two elevations (case d) or all façades (case e).

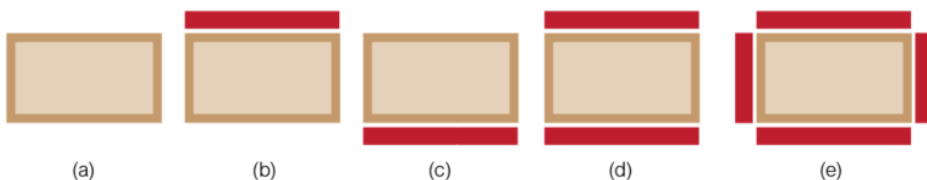


Figure B.6. Schematisation of the case study in the pre-intervention configuration (a), with the insertion of a north (b) or south DSF (c), or on two (d) and four (e) elevations.

Appendix B

The outputs are referred to the energy requirement, both cooling and heating, associated with different climate conditions and due to the insertion of the DSF on one or more elevations. Figure B.7 depicts the results for cold climate, whereas Figure B.8 and Figure B.9 show, respectively, those estimated for mild and hot weathers.

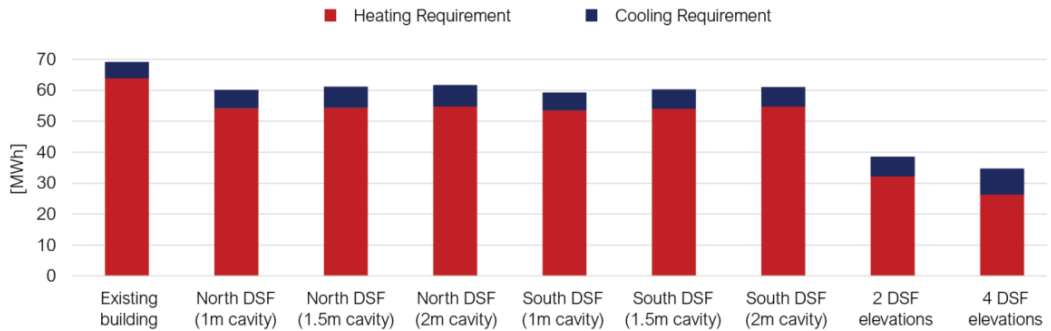


Figure B.7. The annual energy requirement of a detached building for cold climates (Bergamo).

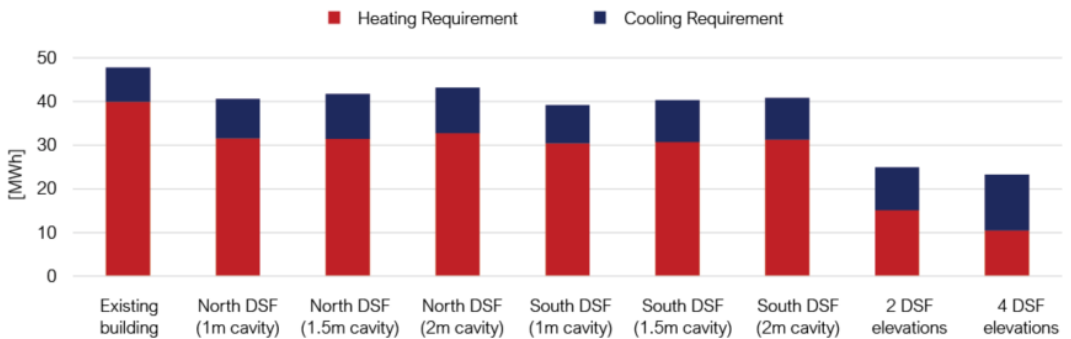


Figure B.8. The annual energy requirement of a detached building for mild climates (Pescara).

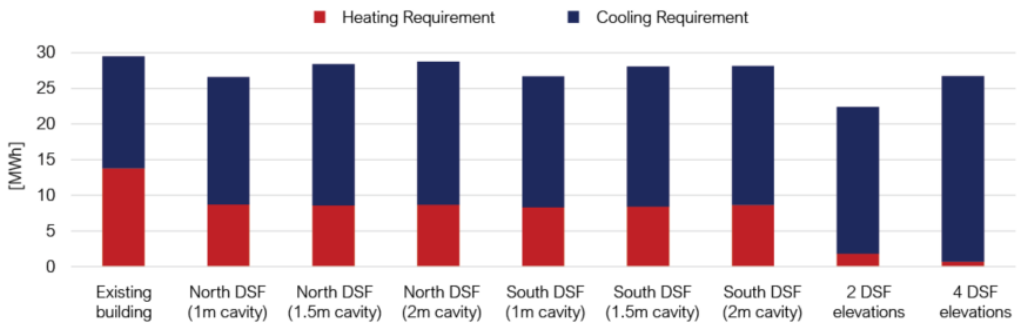


Figure B.9. The annual energy requirement of a detached building for hot climates (Messina).

INTERNAL BUILDING

The results presented in the following lines are referred to the case study considered as an internal building with a DSF inserted, respectively, on one elevation (case b and c), and two façades (case d).

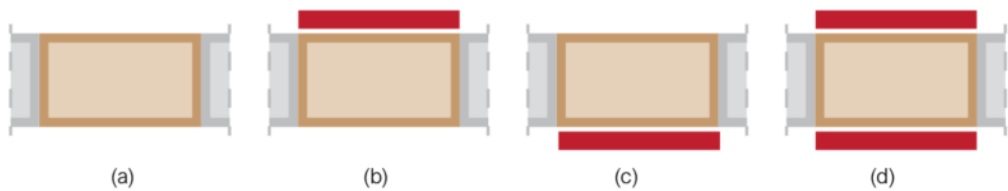


Figure B.10. Schematisation of the case study in the pre-intervention configuration (a), with the insertion of a north (b) or south DSF (c) and on two (d) elevations.

The outputs are referred to the energy requirement, both cooling and heating, associated with different climate conditions and due to the insertion of the DSF on one or more elevations. Figure B.11 depicts the results for cold climate, whereas Figure B.12 and Figure B.13 show, respectively, those estimated for mild and hot weathers.

Appendix B

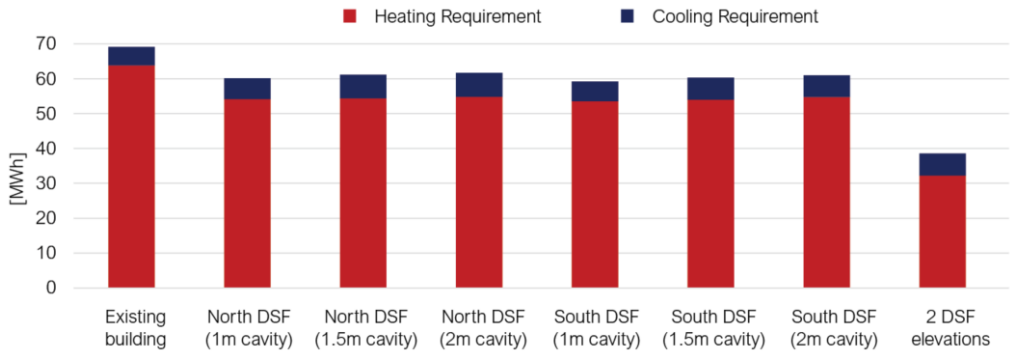


Figure B.11. The annual energy requirement of an internal building for cold climates (Bergamo).

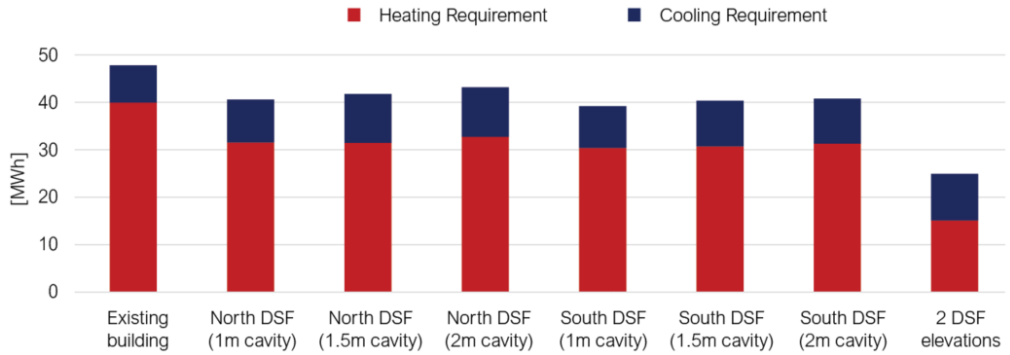


Figure B.12. The annual energy requirement of an internal building for mild climates (Pescara).

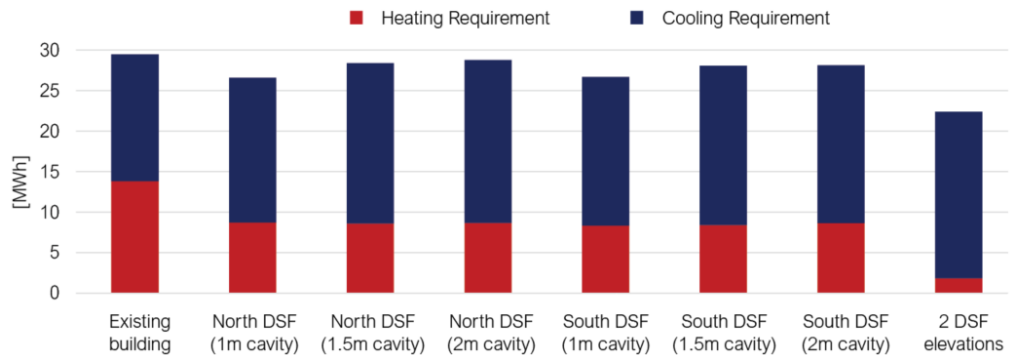


Figure B.13. The annual energy requirement of an internal building for hot climates (Messina).

SEMI-DETACHED BUILDING (WEST CORNER)

The results presented in the following lines are referred to the case study considered as a semi-detached building (west corner) with a DSF inserted, respectively, on one elevation (case b and c), and two (case d) or three (case) façades.

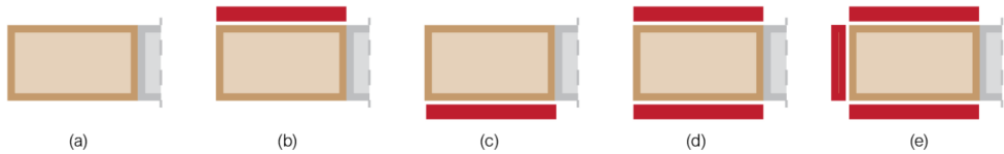


Figure B.14. Schematisation of the case study in the pre-intervention configuration (a), with the insertion of a north (b) or south DSF (c), or on two (d) and three (e) elevations.

The outputs are referred to the energy requirement, both cooling and heating, associated with different climate conditions and due to the insertion of the DSF on one or more elevations. Figure B.15 depicts the results for cold climate, whereas Figure B.16 and Figure B.17 show, respectively, those estimated for mild and hot weathers.

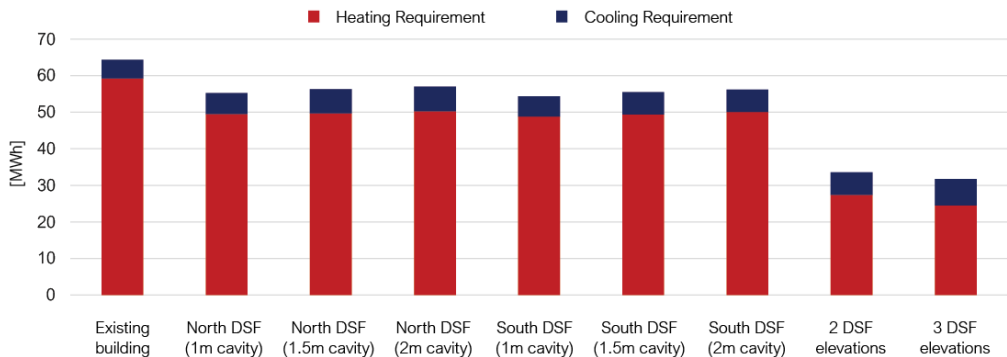


Figure B.15. The annual energy requirement of a semi-detached (west corner) building for cold climates (Bergamo).

Appendix B

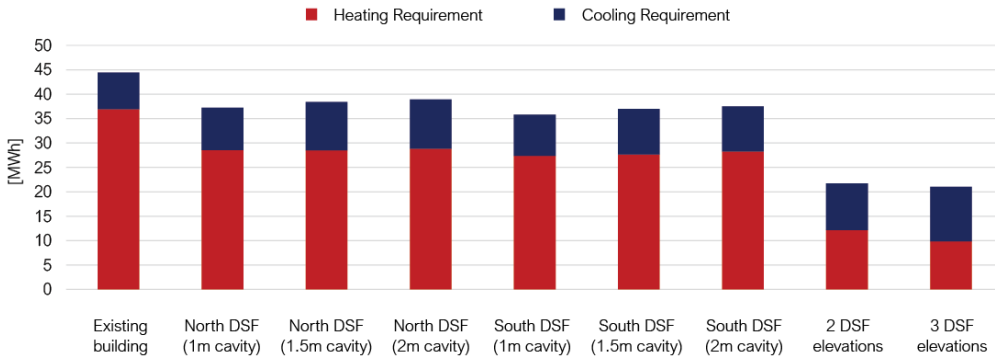


Figure B.16. The annual energy requirement of a semi-detached (west corner) building for mild climates (Pescara).

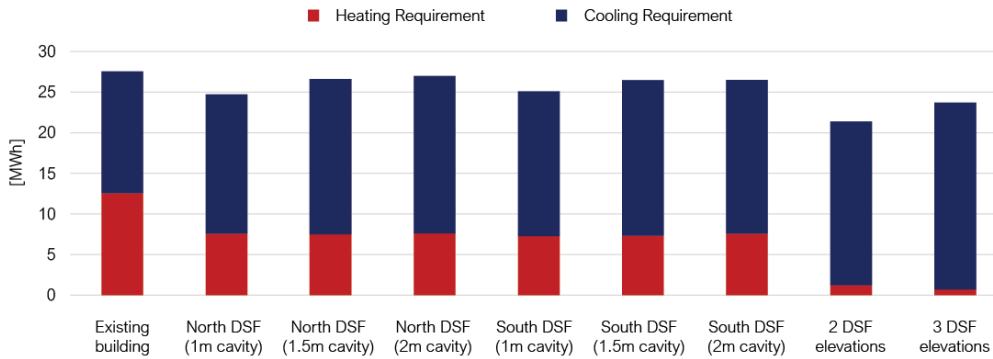


Figure B.17. The annual energy requirement of a semi-detached (west corner) building for hot climates (Messina).

SEMI-DETACHED BUILDING (EAST CORNER)

The results presented in the following lines are referred to the case study considered as a semi-detached building (east corner) with a DSF inserted, respectively, on one elevation (case b and c), and two (case d) or three (case e) façades.

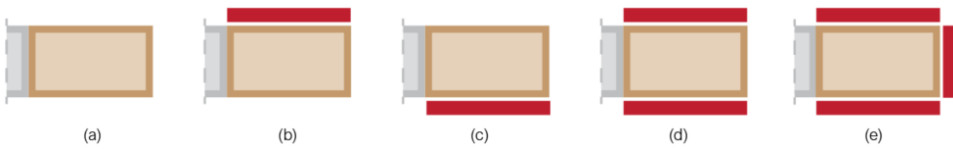


Figure B.18. Schematisation of the case study in the pre-intervention configuration (a), with the insertion of a north (b) or south DSF (c), or on two (d) and three (e) elevations.

The outputs are referred to the energy requirement, both cooling and heating, associated with different climate conditions and due to the insertion of the DSF on one or more elevations. Figure B.19 depicts the results for cold climate, whereas Figure B.20 and Figure B.21 show, respectively, those estimated for mild and hot weathers.

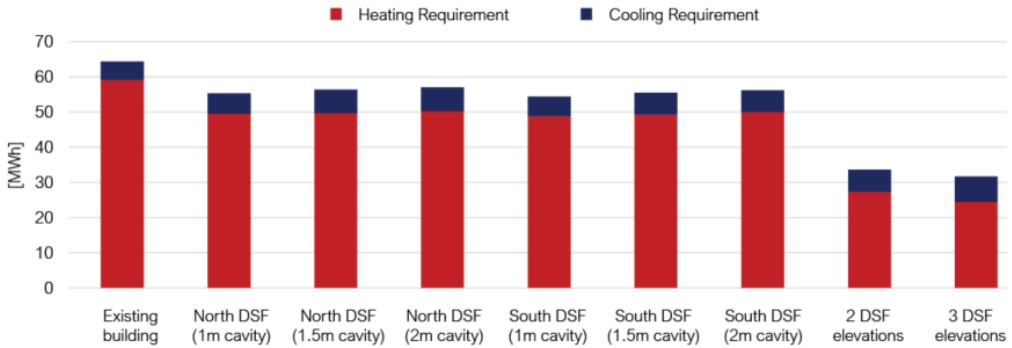


Figure B.19. The annual energy requirement of a semi-detached (east corner) building for cold climates (Bergamo).

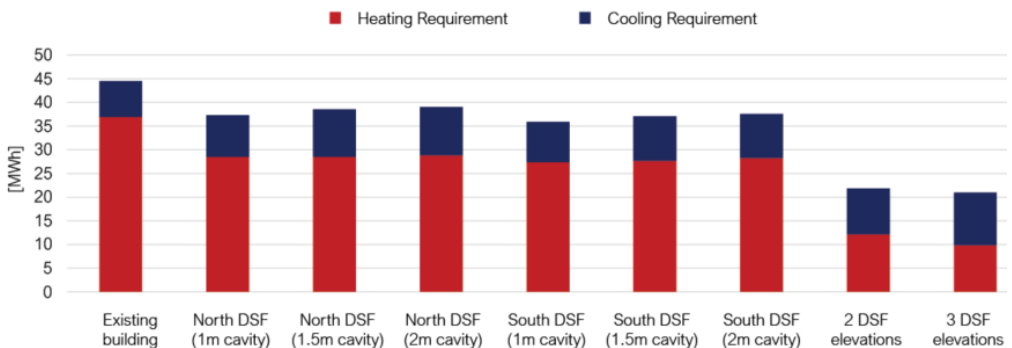


Figure B.20. The annual energy requirement of a semi-detached (east corner) building for mild climates (Pescara).

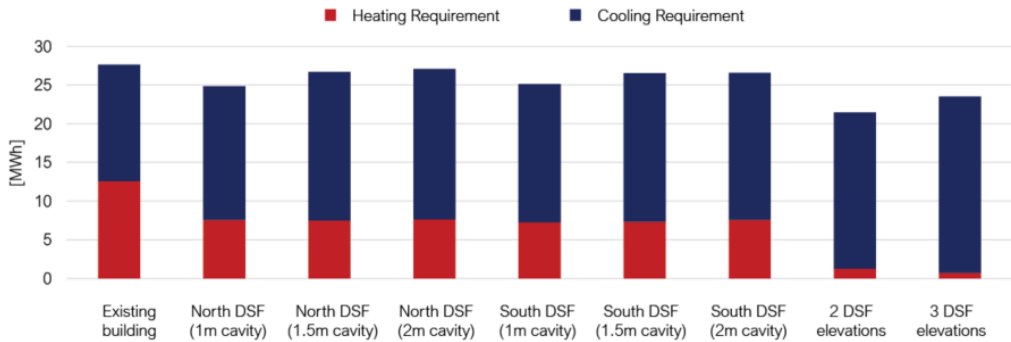


Figure B.21. The annual energy requirement of a semi-detached (east corner) building for hot climates (Messina).

Based on the obtained results, the following findings can be noted:

- The insertion of a DSF on the north elevation ensures, for all climate conditions and cavity depths, a decrement in terms of building energy requirement up to 16% and the highest reduction is recorded with the 1 m cavity depth. The same trend, even better, is also confirmed by the DSF inserted on the south elevation. Also in this case, the 1 m cavity depth represents the best option, allowing higher decrements.
- With DSF on two elevations (both north and south), the annual energy requirement can be drastically reduced notably if the building is located in cold or mild climates with a decrement equal to 48-51% in comparison to the pre-intervention configuration. For hot weathers, the reduction is not so accentuated, reaching only 20%.
- In the case of semi-detached buildings, placing the DSF on three elevations does not create more significant improvements than the previous configurations. In contrast, if it encloses the whole building, assuming an exoskeleton asset possible with a detached building, the energy requirement is drastically reduced up to 50% for both cold and mild climates. For hot weathers, instead, such configuration increases the overheating of the cavity and, for this reason, the decrement in terms of annual energy requirement is only equal to 9%.

These preliminary results underline the effectiveness of the insertion of a multi-layer façade for the energy restoration of existing buildings. The here analysed passive DSF is particularly efficient for the heating requirement reduction whereas, even if opportunely shaded, the overheating of the cavity impacts on the cooling need and this increment is more evident in hot climates. For this reason, further analyses are performed considering the DSF as an active system, and a comparative study is carried on for estimating the reduction in terms of building cooling requirement according to different wind directions. For these analyses, the case study is located in Ancona (Italy), and the investigated parameter is referred to a weekly simulation period.

The Multi-Storey Double Skin Façade is naturally ventilated and placed on the south elevation. The 1 m cavity, enclosed by the inner and the outer layers of the DSF, has inlet and outlet vents that allow the natural ventilation. They are located respectively on the bottom and the top of the external DSF layer, whereas the inner one presents internal grills for ensuring adequate ventilation of the occupied zone. These grills, both the internal and external ones, allow the air continually to enter the cavity and the whole building during the hottest period. In the wintertime, instead, they are closed to seal the cavity, and the ventilation is not permitted to decrease the transmittance of the façade and reduce the heat losses.

The analyses are carried out for the typical summer week (19-25 August), identified by the weather data translator as being representative of the summer period. The simulations consider as main wind directions two cases: the first case analyses the possibility of a wind which impacts directly on the DSF, coming from the south (180°), and the second one studies the opposite condition, with a northern wind (0°). Table B.1 shows the building cooling requirement associated with the selected wind directions.

Table B.1. The cooling requirement, according to the wind direction.

Wind Direction	Cooling Requirement [kWh]
South Wind	605
North Wind	662

Appendix B

According to the energy simulations, the southern wind, impacting directly on the DSF, can reduce the building cooling requirement of 10%. The airflow that enters and goes out from the vents is higher with a 180° wind direction, and the difference between the two configurations reaches 2 m³/s during specific daily hours (Figure B.22 and Figure B.23).

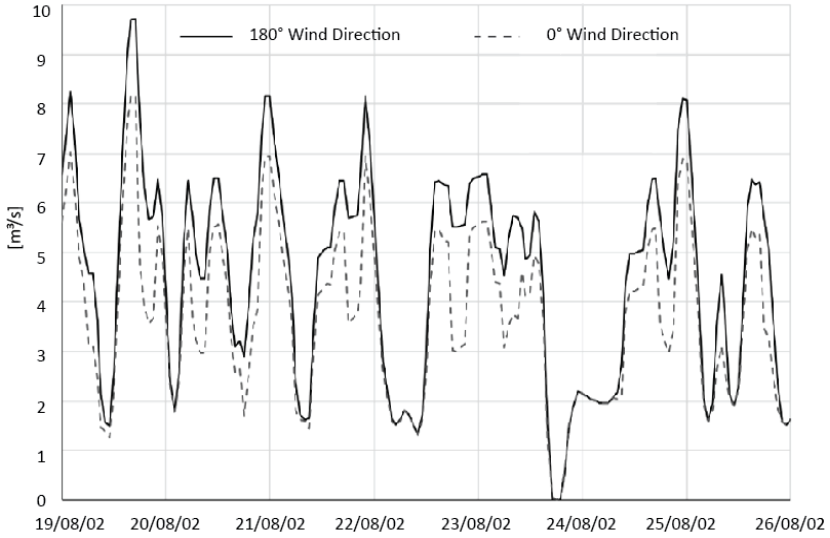


Figure B.22. Inlet airflow rate.

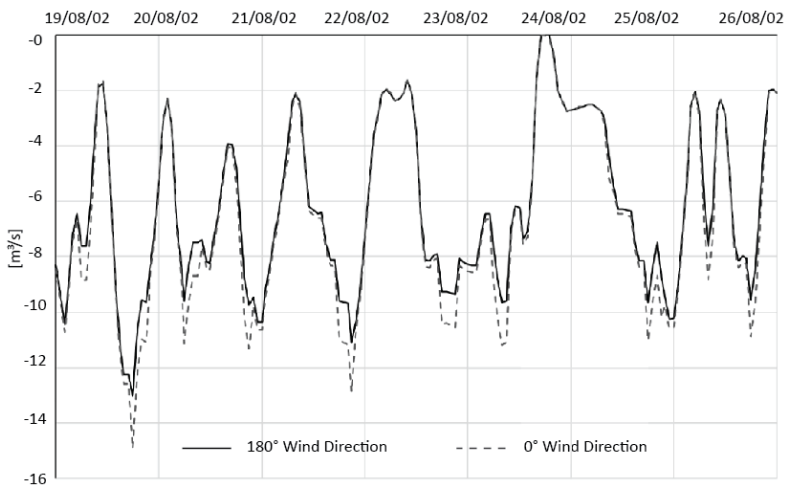


Figure B.23. Outlet airflow rate.

The energy simulations highlight that the most efficient condition for a building with a Double Skin Façade is reached when the wind impacts directly on the grills of the DSF cavity, ensuring the highest amount of natural ventilation, both in the cavity and in the whole building, with a consequent reduction of the cooling need of the occupied zones.

LINEAR AND NONLINEAR STRUCTURAL SIMULATIONS

In addition to energy simulations, structural linear and nonlinear analyses are carried on to evaluate the seismic performance of the case study, before and after the insertion of the engineered DSF. A FEM model is generated (Figure B.24), and beam elements are used for modelling beams, columns and staircase. The mechanical properties of the structural materials are appropriately reduced (70% columns and 50% beams) for considering the cracked condition.

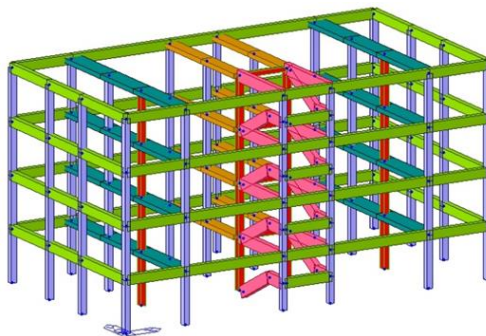


Figure B.24. Axonometry of the FEM model in the pre-intervention configuration.

Zero-length plastic hinges are inserted, and two different force distributions are considered for pushover analyses, as suggested by the Italian code (NTC2018): a modal and uniform distribution of forces, for both directions (positive and negative).

Figure B.25 depicts the capacity curves of the existing structure defined in terms of spectral acceleration-displacement for each distribution of forces. The positive and negative curves overlap each other in any direction and force distribution. Analysing the capacity curves obtained from the simulations, it is evident that the structure has a high seismic vulnerability, especially along the

minor side (y-side). The structural capacity is 54 % of the ultimate limit state earthquake demand. The collapse is due to flexural stresses of the elements, both columns and beams, and, also, shear failures appear along the short columns of the staircase.

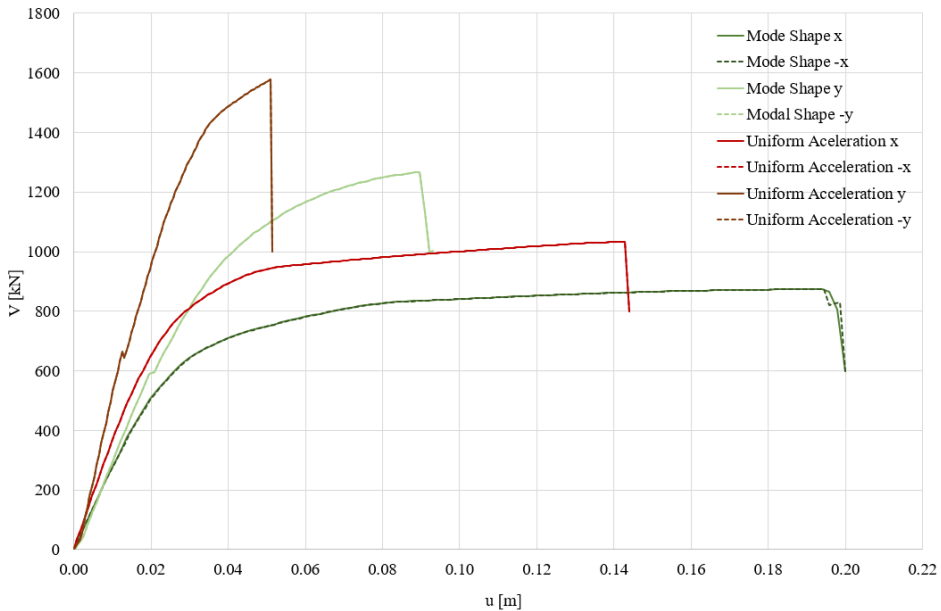


Figure B.25. Pushover curves with modal and uniform force distribution.

According to the preliminary results, the Engineered Double Skin Façade is introduced (Figure B.26b). In detail, Buckling-Restrained Axial Dampers (BRAD) are inserted into the Double Skin in order to protect the structure through energy dissipation. The BRADs (Figure B.26a) are modelled using plastic hinges which simulate the dynamic behaviour of the devices.

A frame of dissipative braces is localised above all sides of the building in a symmetrical way in order to avoid torsional phenomena of the main structure, and a system of horizontal X braces is inserted on the last floor. In addition, the short columns located around the staircase are confined with Fiber Reinforced Polymers for avoiding increasing shear failures.

The insertion of the Double Skin Façade and the improvement of the existing building with this new technology is deeply studied through several pushover

analyses. For the sake of brevity, Figure B.27 depicts the results obtained for only one force distribution (the uniform one) in the y-direction, chosen for being the weakest side of the building.

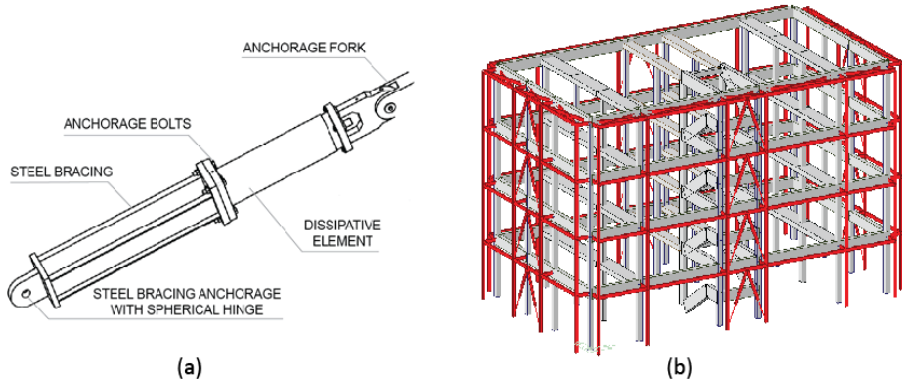


Figure B.26. Schematisation of the BRAD system (a) and the structural model of the building with the exoskeleton (b).

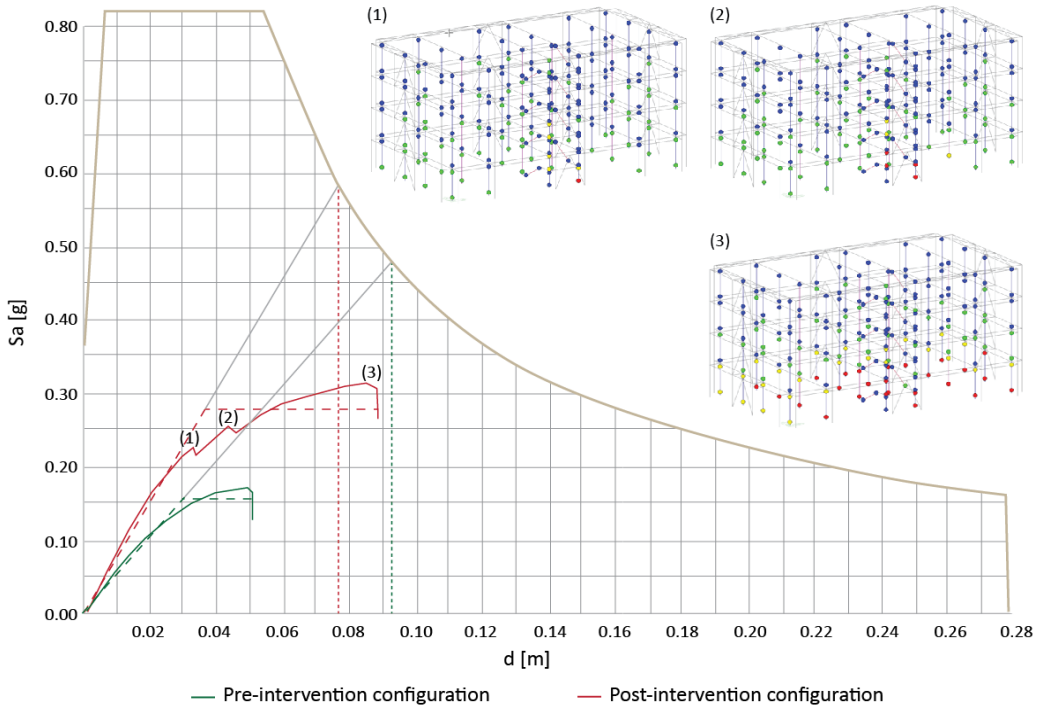


Figure B.27. Capacity and Demand Spectrum of the building with and without DSF.

Appendix B

The obtained results show that the insertion of the Double Skin Façade and the BRAD dampers improves the global performance and the overall flexibility of the structure, reducing the seismic vulnerability of the whole building.

In conclusion, the effectiveness of such a solution has been tested on a simple case study and validated through the application of a holistic approach. As seen, it represents a good option for the rehabilitation of existing buildings with poor architectural quality and insufficient structural and energetic performances, guaranteeing its conversion in more eco-efficient and resilient building stock.

Appendix C

The original documents about structural details are here reported. Figure C.1 to Figure C.5 show architectural elevations, the typical plan of the whole residential complex (a red box encloses the case study), and a section with the focus on the balcony. Figure C.6 depicts the localisation of beams and columns, whereas Figure C.7 and Figure C.8 present shear and flexural details of a few beams placed on the typical floor and the roof, respectively. Shear reinforcement information of columns are collected in Figure C.9, and the table with the flexural one is shown in Figure C.10. The last two figures depict details of the stairs (Figure C.11) and stratigraphies of slabs and wall (Figure C.12), both internal and external.

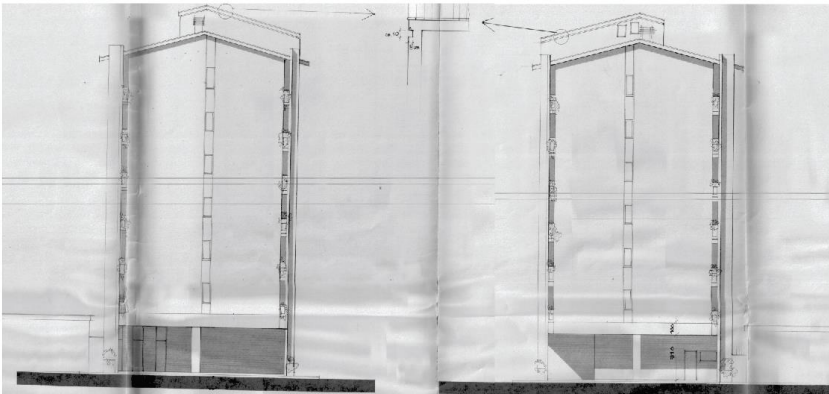


Figure C.1. North-east (left) and south-west (right) elevations.

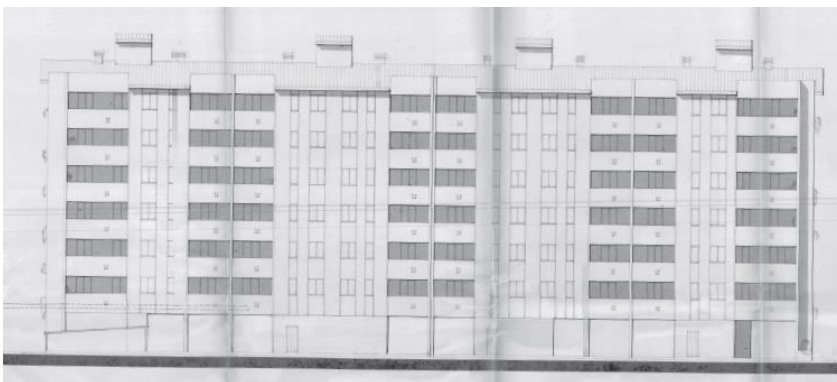


Figure C.2. South-east elevation.

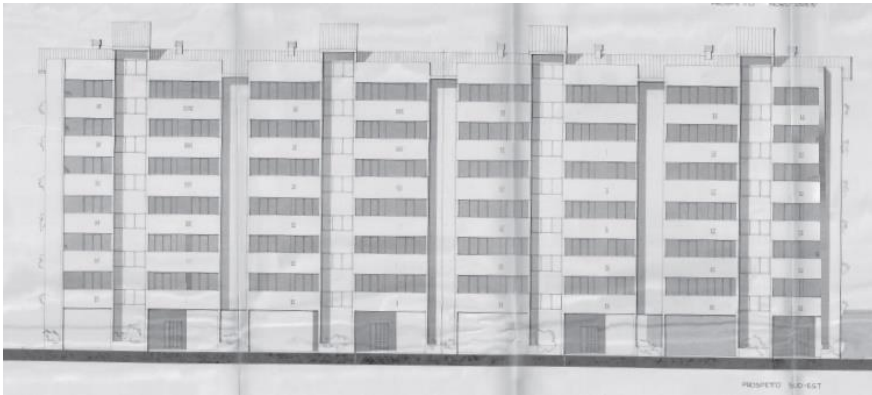


Figure C.3. North-west elevation.

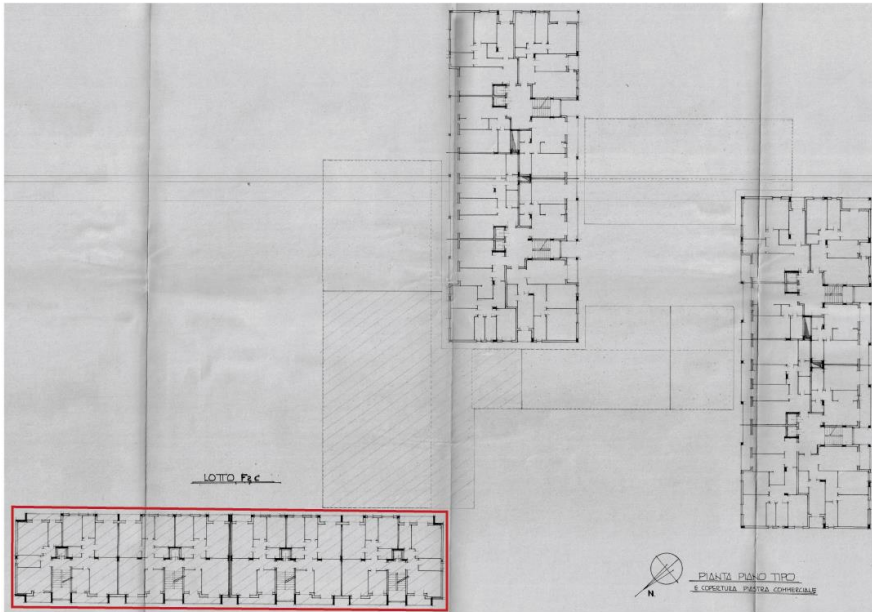


Figure C.4. Typical plans of the residential district (red box is the case study).

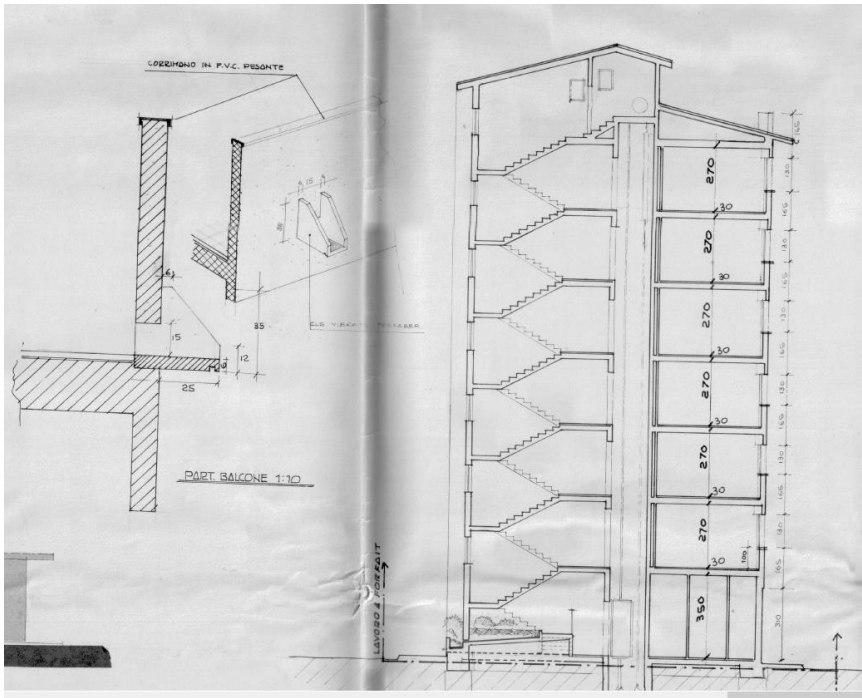


Figure C.5. Building section and the detail of the balcony.

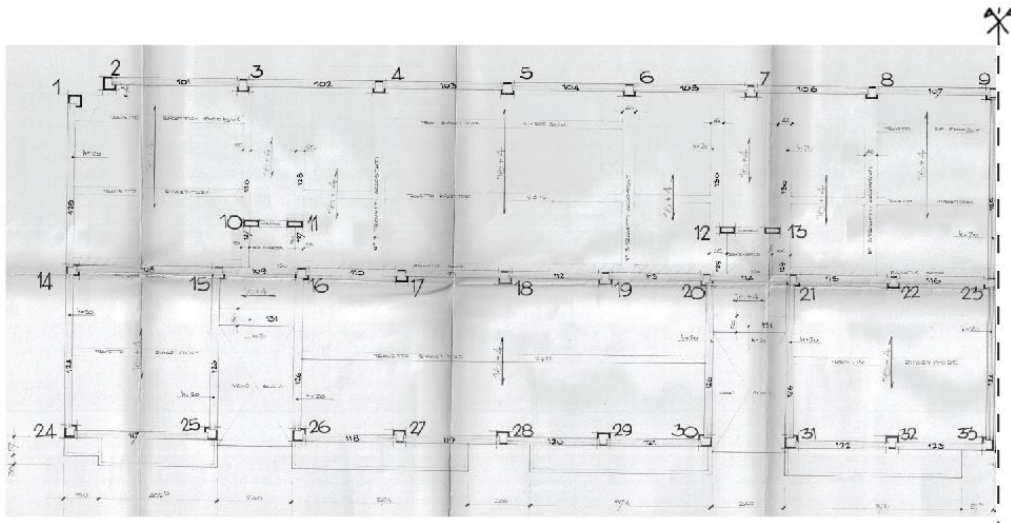


Figure C.6. The localisation of column and beam for structural details.

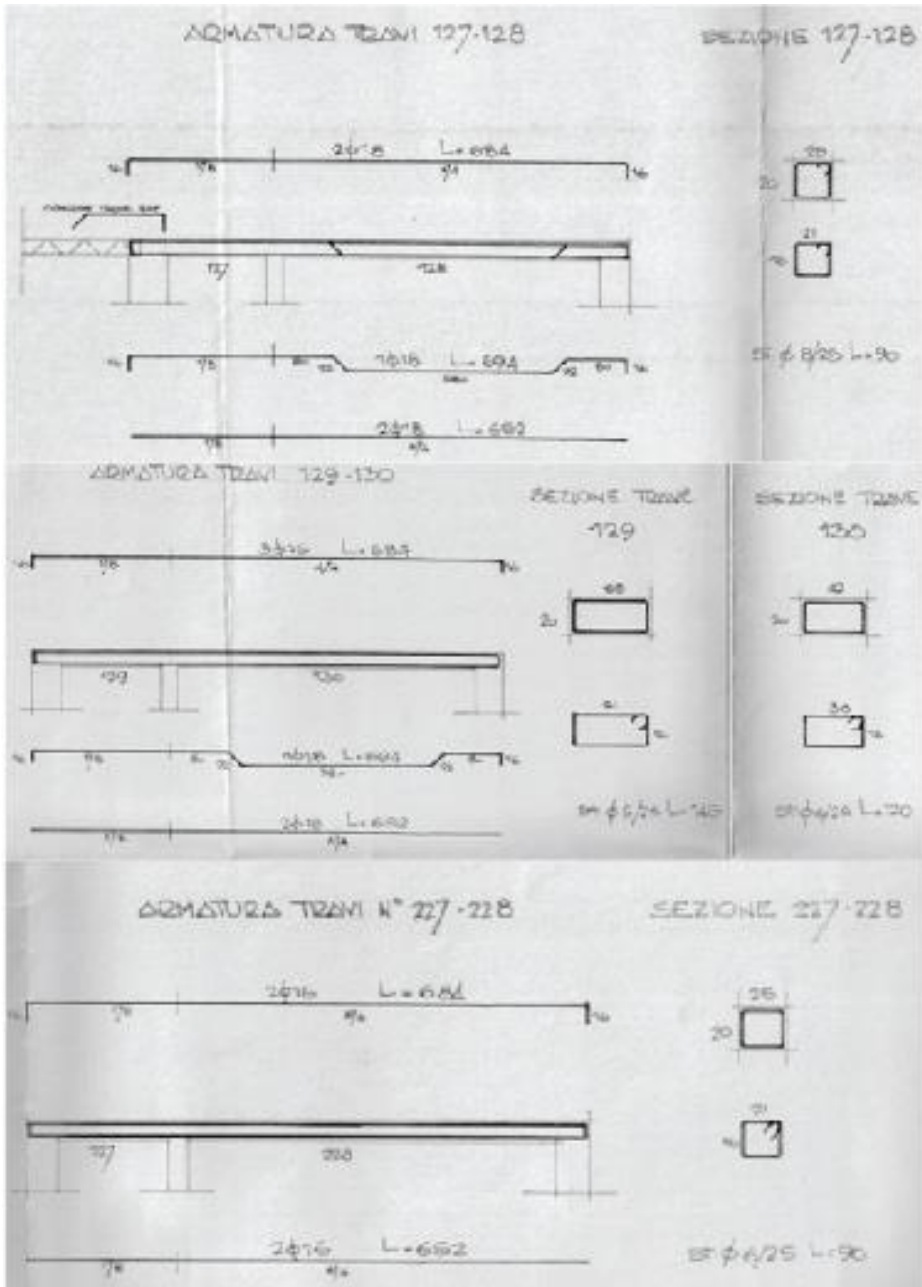


Figure C.7. Shear and flexural reinforcements details of some beams.

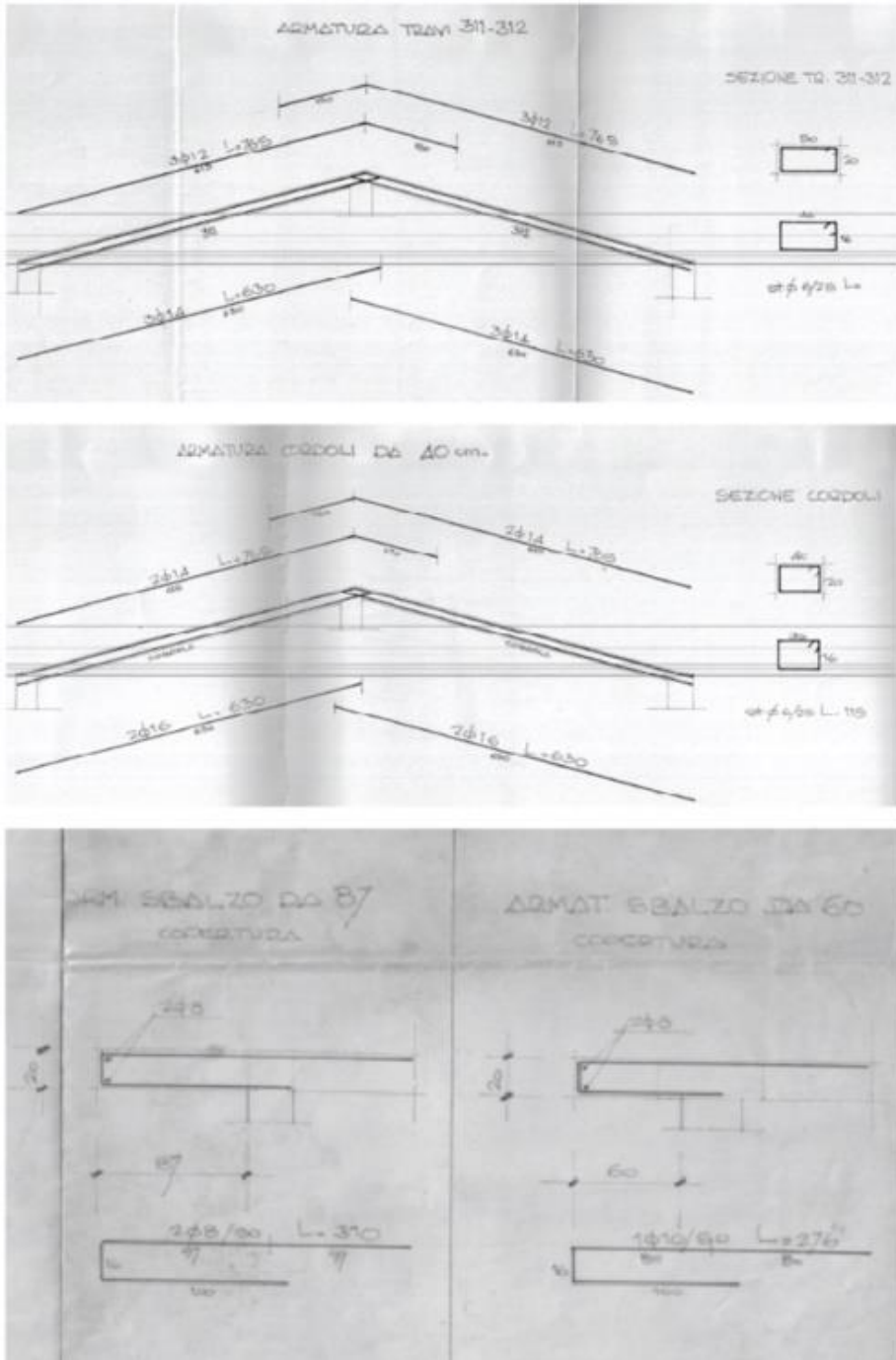


Figure C.8. Shear and flexural details of beams placed on the roof.

Appendix C

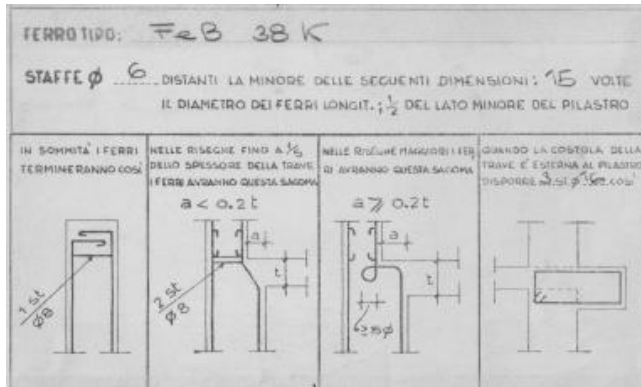


Figure C.9. Shear reinforcement details of columns.

4° Piano	1-9-32.	2-3-4-5-6-7-8.	10-11-12-13.	16-17-18-19-20-21-22.	24-27-28-29-32.	75.	15.	1A.	23.	26-30-31.	33.
SOTTOTETTO			50x70	10x10			10x10	10x10	10x10	10x10	
			4φ12	1φ12			1φ12	1φ12	1φ12	1φ12	
PIANO 6°	10x10	10x10	50x70	10x10	10x10	10x10	10x10	10x10	10x10	10x10	10x10
	1φ12	1φ12	6φ12	1φ14	1φ12	1φ12	1φ14	1φ14	1φ14	1φ12	1φ12
PIANO 5°	10x10	10x10	50x70	10x10	10x10	10x10	10x10	10x10	10x10	10x10	10x10
	1φ12	1φ14	6φ12	1φ14	1φ14	1φ14	1φ16	1φ14	1φ14	1φ14	1φ14
PIANO 4°	10x10	10x10	50x70	10x10	10x10	10x10	10x10	10x10	10x10	10x10	10x10
	1φ14	1φ14	6φ12	1φ16	1φ14	1φ16	1φ16 + 2φ12	1φ16	1φ16	1φ14	1φ14
PIANO 3°	10x10	10x10	50x70	10x10	10x10	10x10	10x10	10x10	10x10	10x10	10x10
	1φ14	1φ16	6φ12	1φ16 + 2φ14	1φ16	1φ16 + 2φ14	1φ16 + 2φ14	1φ16 + 2φ14	1φ16 + 2φ14	1φ16	1φ16
PIANO 2°	10x10	10x10	50x70	10x10	10x10	10x10	10x10	10x10	10x10	10x10	10x10
	1φ12	1φ16 + 2φ12	6φ12	1φ16 + 1φ14	1φ16 + 2φ12	1φ16 + 1φ14	1φ16 + 2φ14	1φ16 + 1φ14	1φ16 + 1φ14	1φ16 + 2φ12	1φ16 + 2φ12
PIANO 1°	10x10	10x10	50x70	10x10	10x10	10x10	10x10	10x10	10x10	10x10	10x10
	1φ16	1φ16 + 2φ14	6φ12	1φ16 + 1φ14	1φ16 + 1φ12	1φ16 + 2φ14	2φ16	1φ16 + 1φ14	1φ16 + 1φ14	1φ16 + 1φ12	1φ16 + 2φ14
POSTICCO	10x10	10x10	50x70	10x10	10x10	10x10	10x10	10x10	10x10	10x10	10x10
	1φ16	2φ16	6φ12	2φ16	1φ16 + 1φ14	2φ16	2φ16	2φ16	2φ16	1φ16 + 1φ14	6φ16
FONDAZIONI											

Figure C.10. Flexural reinforcement details of columns.

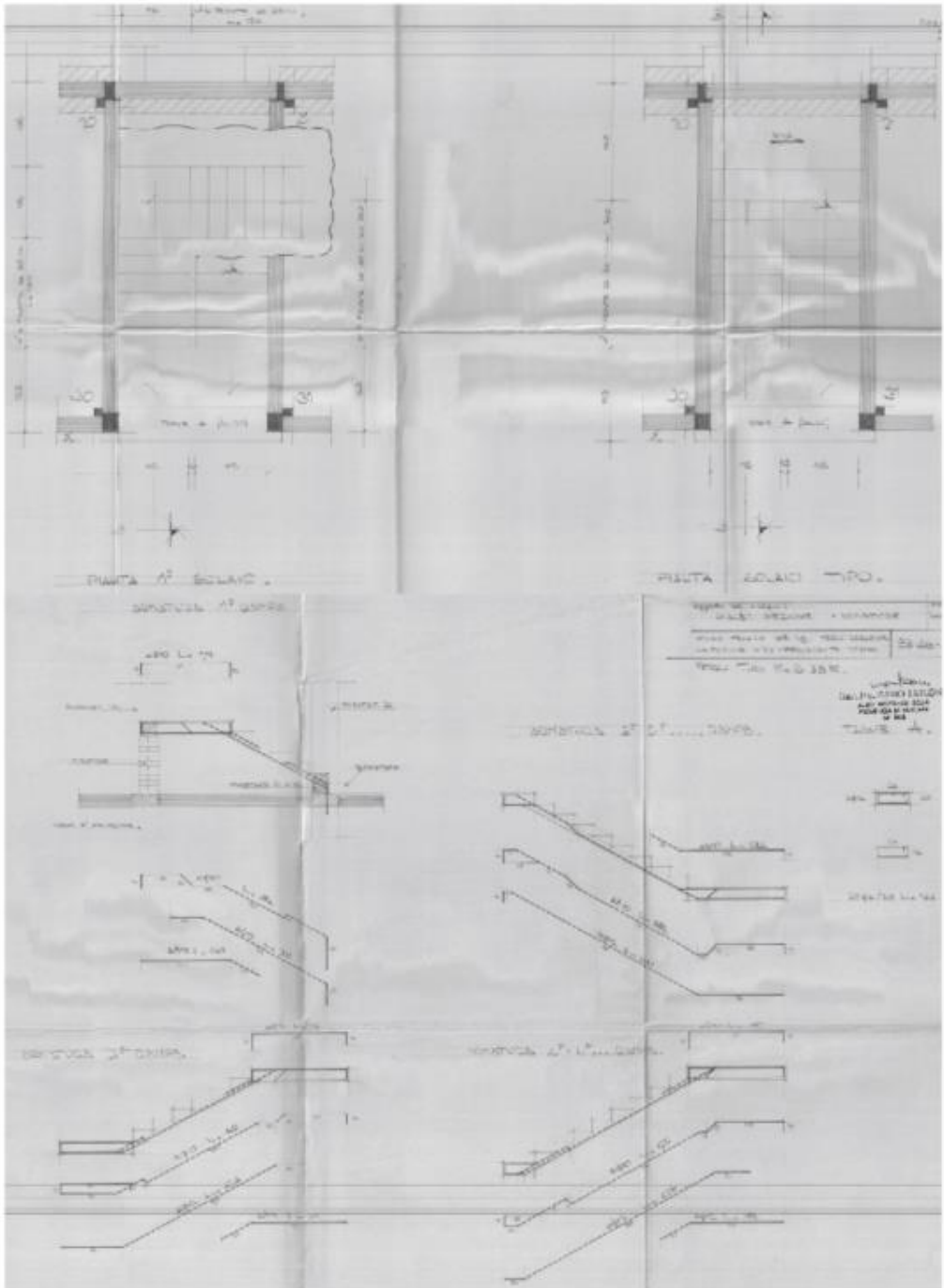


Figure C.11. Plans and shear and flexural details of the stairs.

ANALISI DEI CARICHI

1° SOLAIO DI COPERTURA:	
TIPO: 16+4	
peso proprio	225 Kg/m ²
int. + pavimento	Kg/m ²
massetto p. pend.	Kg/m ²
TEGOLE	100 Kg/m ²
TOTALE f =	325 Kg/m ²
SOPRACCARICO S =	150 Kg/m ²

2° SOLAIO - PLASFONE	
TIPO: 16+4	
peso proprio	225 Kg/m ²
intonaco + pav.	30 Kg/m ²
mass. di pomice	Kg/m ²
tramezzi	Kg/m ²
	Kg/m ²
TOTALE f =	255 Kg/m ²
SOPRACCARICO S =	100 Kg/m ²

3° SOLAIO - PIANO TIPO	
TIPO: 16+4	
peso proprio	225 Kg/m ²
intonaco + pav.	100 Kg/m ²
mass. di pomice	Kg/m ²
tramezzi	100 Kg/m ²
	Kg/m ²
TOTALE f =	425 Kg/m ²
SOPRACCARICO S =	200 Kg/m ²

4° BAUCONI E SCALE	
peso proprio	250 Kg/m ²
int. + pavimento	100 Kg/m ²
ringhiera	50 Kg/m ²
	Kg/m ²
TOTALE f =	400 Kg/m ²
SOPRACCARICO S =	100 Kg/m ²

5° MURATURA PORTANTE:	
FORMATA DA:	
+ fila di _____	Kg/m ²
_____	Kg/m ²
intonaco su _____ F	Kg/m ²
_____	Kg/m ²
_____	Kg/m ²
_____	Kg/m ²
TOTALE f =	Kg/m ²
PER UN'ALTEZZA DI _____ m. SONO	
f =	Kg/ml

6° MURATURA DI TOMPAGNO:	
FORMATA DA:	
+ fila di MULTICOR (13cm)	Kg/m ²
+ 1 FILA FORATINI (8cm)	150 Kg/m ²
intonaco su _____ F. +	50 Kg/m ²
_____	Kg/m ²
_____	Kg/m ²
TOTALE f =	200 Kg/m ²
PER UN'ALTEZZA DI _____ m SONO	
f =	550 Kg/ml

7° MURATURA DI TOMPAGNO:	
FORMATA DA:	
+ fila di _____	Kg/m ²
_____	Kg/m ²
intonaco su _____ F.	Kg/m ²
_____	Kg/m ²
_____	Kg/m ²
TOTALE f =	Kg/m ²
PER UN'ALTEZZA DI _____ m SONO	
f =	Kg/ml

N.B. IL PESO PROPRIO DEI SOLAI È COMPRESIVO DELL'INCIDENZA DELLE TRAVI VALUTATO IN 20 Kg/m² CIRCA. IL PESO DELLE MURATURE È RIDOTTO DEL 15% PER TENER CONTO DELLE APERTURE

Figure C.12. Stratigraphy of infills and slabs.

Appendix D

The outputs obtained from dynamic simulations with various climatic files are reported in terms of energy consumption due to the heating and cooling of the occupied spaces.

Table D.1. Annual energy consumption estimated with the DB climatic file.

Configuration	Heating Consumption [kWh/m ²]	Cooling Consumption [kWh/m ²]	Total
Original State	107.86	3.71	111.57
MS-DSF	58.96	1.36	60.32
SB-DSF	71.09	0.94	72.04
C-DSF (frontal grills)	73.79	0.79	74.58
C-DSF (lateral grills)	73.79	0.79	74.58
BW-DSF	75.43	0.70	76.12

Table D.2. Annual energy consumption estimated with the ARTA climatic file.

Configuration	Heating Consumption [kWh/m ²]	Cooling Consumption [kWh/m ²]	Total
Original State	95.60	6.47	102.06
MS-DSF	52.19	4.33	56.52
SB-DSF	63.10	3.70	66.80
C-DSF (frontal grills)	64.68	3.56	68.24
C-DSF (lateral grills)	64.68	3.60	68.28
BW-DSF	66.57	3.43	70.00

Appendix D

Table D.3. Annual energy consumption estimated with the Climate Network climatic file.

Configuration	Heating Consumption [kWh/m ²]	Cooling Consumption [kWh/m ²]	Total
Original State	97.60	7.55	105.15
MS-DSF	52.67	4.10	56.76
SB-DSF	63.90	3.35	67.25
C-DSF (frontal grills)	64.69	3.18	67.87
C-DSF (lateral grills)	64.69	3.35	68.04
BW-DSF	66.95	3.16	70.11

Table D.4. Annual energy consumption estimated with the CTI climatic file.

Configuration	Heating Consumption [kWh/m ²]	Cooling Consumption [kWh/m ²]	Total
Original State	102.42	5.58	108.00
MS-DSF	57.08	2.86	59.94
SB-DSF	67.58	2.00	69.58
C-DSF (frontal grills)	68.37	1.86	70.23
C-DSF (lateral grills)	68.37	1.74	70.11
BW-DSF	70.44	1.59	72.03

Table D.5. Annual energy consumption estimated with the PVGIS climatic file.

Configuration	Heating Consumption [kWh/m ²]	Cooling Consumption [kWh/m ²]	Total
Original State	98.99	4.60	103.60
MS-DSF	46.25	1.93	48.19
SB-DSF	60.04	1.16	61.21
C-DSF (frontal grills)	61.94	1.08	63.02
C-DSF (lateral grills)	61.94	1.10	63.04
BW-DSF	64.51	0.96	65.47

Table D.6. Annual energy consumption estimated with the MM5-MRF-LSM climatic file.

Configuration	Heating Consumption [kWh/m ²]	Cooling Consumption [kWh/m ²]	Total
Original State	90.99	2.07	93.06
MS-DSF	55.21	1.32	56.53
SB-DSF	61.68	0.91	62.60
C-DSF (frontal grills)	61.00	0.87	61.87
C-DSF (lateral grills)	61.00	0.87	61.87
BW-DSF	63.55	0.80	64.34

Table D.7. Annual energy consumption estimated with the MM5-BK climatic file.

Configuration	Heating Consumption [kWh/m ²]	Cooling Consumption [kWh/m ²]	Total
Original State	99.47	2.39	101.86
MS-DSF	60.80	1.42	62.22
SB-DSF	66.49	1.02	67.50
C-DSF (frontal grills)	67.20	0.94	68.13
C-DSF (lateral grills)	67.20	0.94	68.13
BW-DSF	68.36	0.87	69.22

Table D.8. Annual energy consumption estimated with the MM5-PLEIM-XIU climatic file.

Configuration	Heating Consumption [kWh/m ²]	Cooling Consumption [kWh/m ²]	Total
Original State	117.22	1.53	118.75
MS-DSF	74.11	0.93	75.04
SB-DSF	81.52	0.61	82.13
C-DSF (frontal grills)	82.05	0.57	82.63
C-DSF (lateral grills)	82.05	0.57	82.63
BW-DSF	83.64	0.53	84.16

Appendix D

Table D.9. Annual energy consumption estimated with the 2030 climatic file.

Configuration	Heating Consumption [kWh/m ²]	Cooling Consumption [kWh/m ²]	Total
Original State	65.41	19.25	84.66
MS-DSF	31.19	6.28	37.46
SB-DSF	45.54	4.76	50.30
C-DSF (frontal grills)	45.33	4.71	50.03
C-DSF (lateral grills)	45.33	4.77	50.09
BW-DSF	47.91	4.52	52.43

Table D.10. Annual energy consumption estimated with the 2050 climatic file.

Configuration	Heating Consumption [kWh/m ²]	Cooling Consumption [kWh/m ²]	Total
Original State	59.11	19.06	78.17
MS-DSF	27.19	6.09	33.28
SB-DSF	40.13	4.51	44.64
C-DSF (frontal grills)	41.12	4.52	45.64
C-DSF (lateral grills)	41.12	4.59	45.70
BW-DSF	43.81	4.31	48.12

Table D.11. Annual energy consumption estimated with the 2070 climatic file.

Configuration	Heating Consumption [kWh/m ²]	Cooling Consumption [kWh/m ²]	Total
Original State	52.57	22.53	75.10
MS-DSF	22.68	8.27	30.95
SB-DSF	40.13	4.51	44.64
C-DSF (frontal grills)	35.68	6.45	42.13
C-DSF (lateral grills)	35.68	6.52	42.20
BW-DSF	38.16	6.22	44.38

Appendix E

Preliminary CFD analyses are carried on for testing the performance of a DSF building with simpler shape and smaller size than the thesis case study. The main focus of the here presented simulations is verifying the physical hypotheses adopted for the modelling of various DSF systems. For reaching this purpose, the obtained results are compared with CFD analyses and experimental campaigns assessed by the Department of Civil Engineering of the Aalborg University, in collaboration with the Department of Sciences and Methods for Engineering of the University of Modena and Reggio Emilia [101] [171] [172] [173].

The study, assumed as reference for the following simulations, is centred on comparing CFD estimations with recorded values of Double Skin Façade full-scale test facility, hereafter referred as the “Cube”. Figure E.1 shows the configuration of the test cell with the schematisation the internal zones (on the left), the pictures of the south façade with the DSF (in the middle) and the north elevation (on the right). The Cube dimensions are 6 m x 6 m x 6 m and the DSF cavity depth is equal to 0.70 m.



Figure E.1. Plan of the Cube (left) with photos of the southern (middle) and northern (right) façade [101].

Initially, a bidimensional model is elaborated, and comparisons are made among the obtained results with the measured and CFD values for the model validation. Then, a different DSF opening configuration and a three-dimensional model are generated for improving the effectiveness of the solution. Figure E.2 schematises the investigated options. The software used for the simulations is Star-CCM+ (version 13).

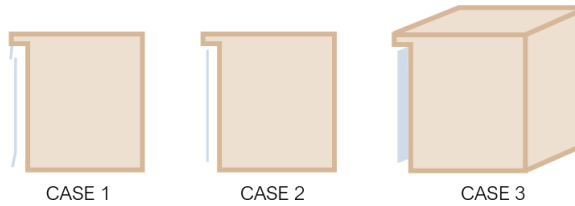


Figure E.2. Schematisation of the investigated DSF configurations and models.

CASE 1: MODELLING OF THE 2D DSF FOR ITS VALIDATION.

The model geometry and principle inputs are defined according to the data obtained from the technical documentation of the Cube. Figure E.3 shows the surfaces used for describing both the domain and the building. Polyhedral and prism layer meshes are used for discretising the model surfaces, and variable mesh sizes are inserted to improve the accuracy of predictions of specific areas (e.g., the DSF cavity) without increasing the model computational cost. The total number of cells is 7493, and the following settings are selected for the surface meshing:

- Base Size = 0.4 m
- Number of Prism Layer = 5
- Prism Layer Stretching = 1.2
- Prism Layer Thickness = 0.1 m

The same meshes are also chosen for the generation of the volume ones, and both of them are depicted in Figure E.4. Uniform temperature conditions are imposed at all glazed surfaces of the façades, as well as at its ground and ceiling. The used temperature values are extrapolated by the measurement campaign carried out for the reference test cell for which the buoyancy is supported by a moderate upward wind differential pressure (named as Case D in the reference) [101]. The recorded temperature values are, respectively, 14.6 °C for the air temperature, 29.5 °C for the inner layer of the DSF and 28.6 °C for the inner building surface. The unsteady Reynolds-Averaged Navier-Stokes (U-RANS) model is selected for the numerical simulations. In detail, the turbulence is considered by means of the two-equation $k-\omega$ model, chosen for its capability in obtaining good performances in case of boundary layers under adverse pressure gradients [174]. The all y^+ hybrid approach is used to determine the relationship

between the first cell centre and the wall, solving the problem of mesh resolution insufficiency near the wall.

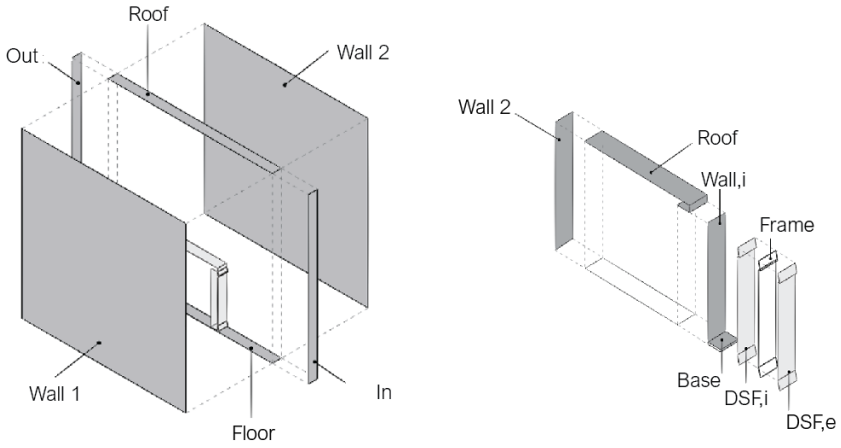


Figure E.3. Representation of domain components (left) and DSF case study (right).

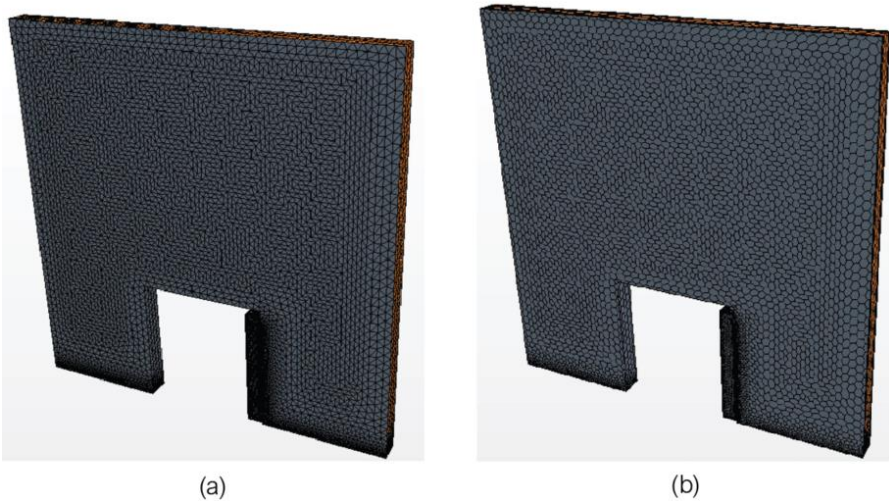


Figure E.4. Surface meshes (a) and volume meshes (b) of the CFD model.

The DSF, located on the south elevation, is naturally ventilated. Thus, the air fluxes inside the cavity are ensured by the natural convection, which should be accurately settled for the CFD simulations. In the specific case, two main assumptions are made: the pressure value on domain borders is fixed at zero (pressure outlet), and the reference density inside the physics continuum is defined according to the gas for the temperature and pressure level of the domain. The last consideration involves the settings of the analysis, which are:

- The time step is equal to 0.05 seconds.
- The maximum physical time is set to 20 minutes

The investigated output is the velocity profile (expressed in m/s), evaluated at different DSF heights, selected for being the same heights at which the anemometers are placed for the experimental campaign. Various probe lines are, in fact, inserted inside the cavity at 0.95 m, 1.91 m, 2.50 m, 4.36 m, 4.70 m, 5.15 m, as schematised in Figure E.5. The results, referred to each probe line, are plotted in Figure E.6.

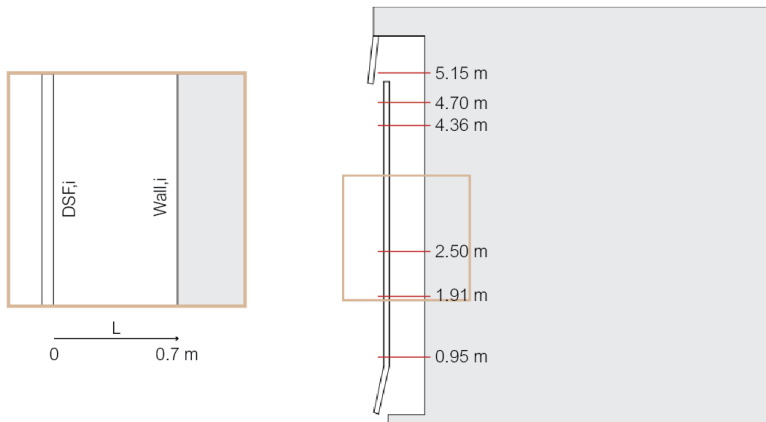


Figure E.5. The localisation of the probe lines inside the DSF cavity.

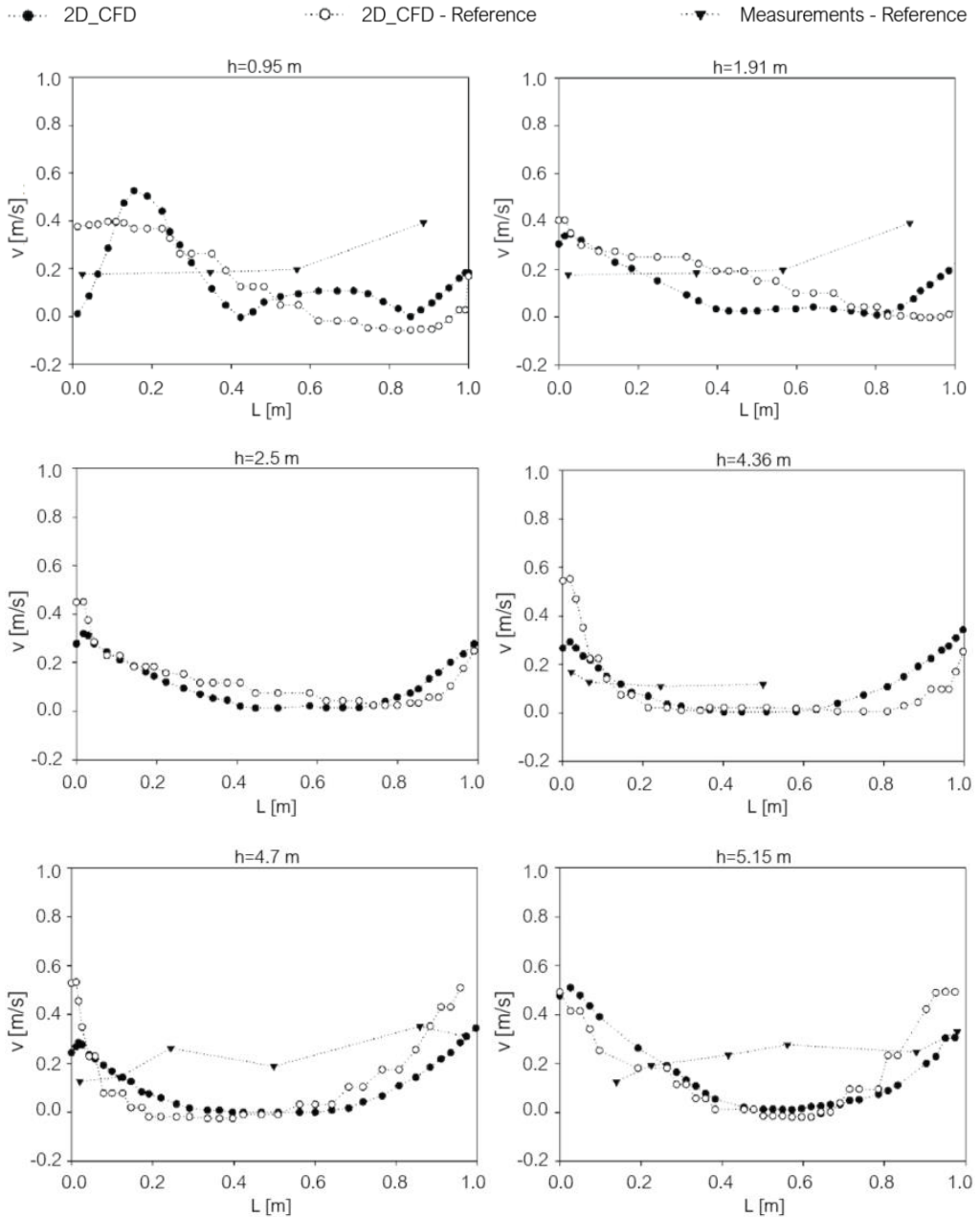


Figure E.6. Velocity magnitude results for various probe lines.

The velocity magnitudes obtained by the CFD analyses here performed (full circle marker) are in good accordance with the estimated outputs (empty circle marker) adopted as reference for the comparisons. Moreover, both results underline a significant variation if compared to the measured values (triangle marker), and this is mostly due to the sensitivity of sensors located inside the perturbed area, which confer high uncertainty to the records. According to the outputs, the model can be considered able to predict the correct fluid dynamic behaviour of the DSF.

CASE 2: MODELLING OF THE IMPROVED DSF (2D).

The second stage of the study is testing a different configuration of Double Façade in which the inlet and outlet openings are not partial but fully open. The simulation settings and hypotheses adopted for the previous model are also confirmed in this case. The same criteria are followed for the model surface definition and meshing (see Figure E.7 and Figure E.8) and for the analysis settings. The total number of cells used for discretising the domain and building is 71376.

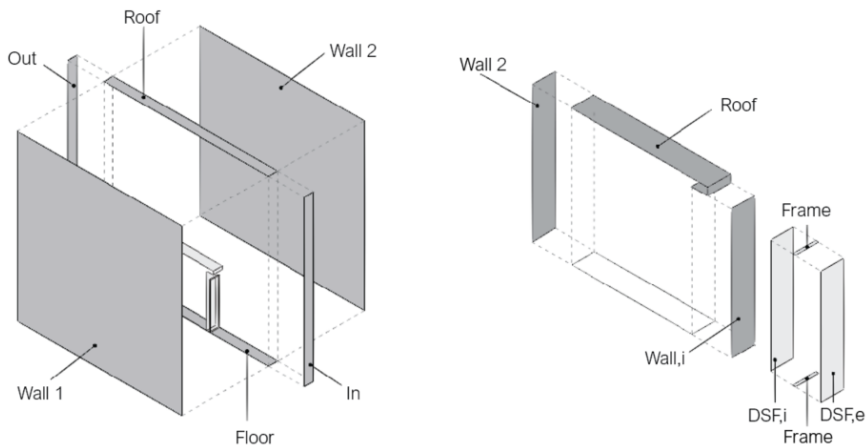


Figure E.7. Representation of domain components (left) and the improved DSF configuration (right).

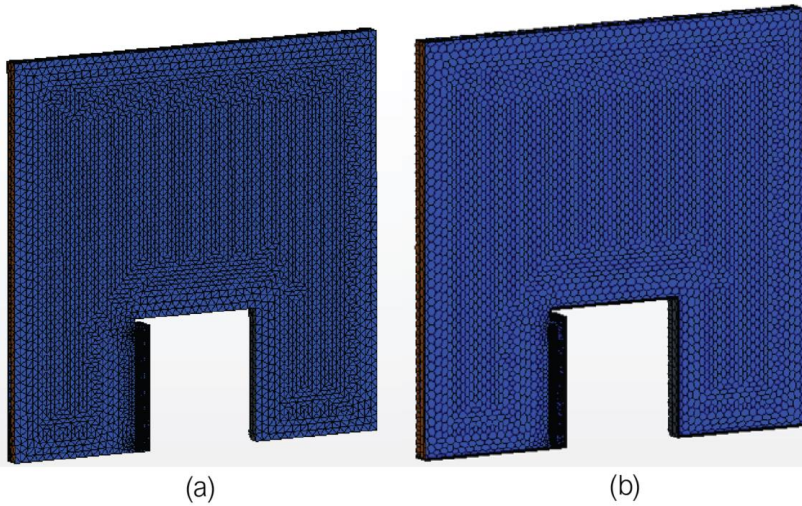


Figure E.8. Surface meshes (a) and volume meshes (b) of the improved CFD model.

The time step used for the simulation is 0.1 seconds, whereas the maximum physical time is 20 minutes. The results are presented in terms of velocity magnitude, extrapolated for various probe lines depicted in Figure E.9.

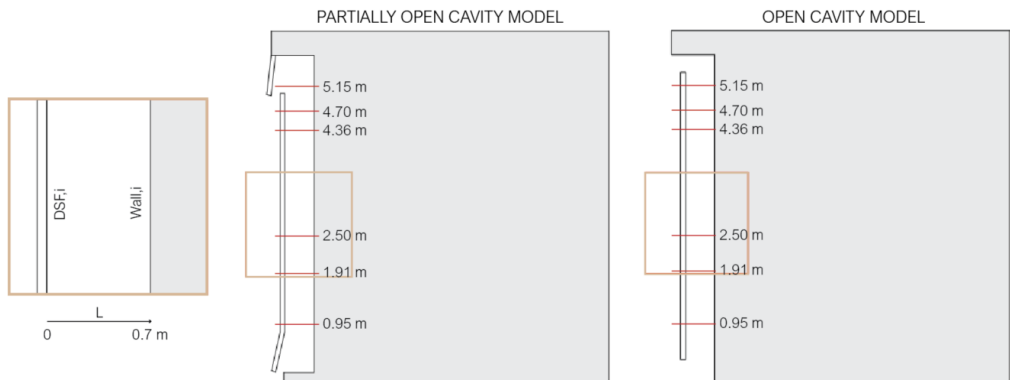


Figure E.9. The localisation of the probe lines inside the original and improved version of DSF cavity.

Appendix E

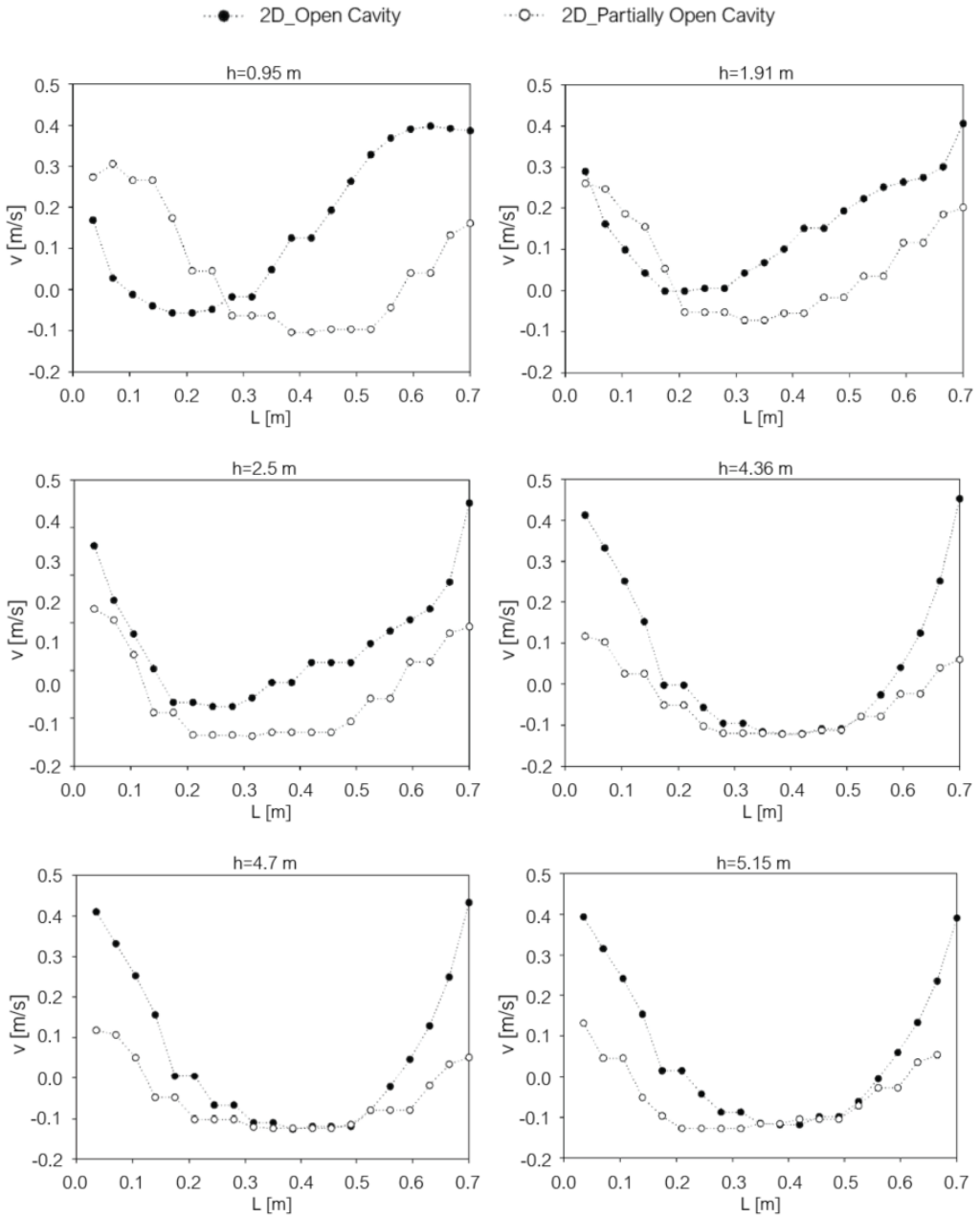


Figure E.10. Velocity magnitude results for various probe lines, referred to the DSF base case and its improved version.

The obtained results, plotted in Figure E.10, underline that higher velocities are estimated for the completely open cavity than the base case. This phenomenon is due to the presence, in the first case, of not aerodynamic profiles which causes velocity losses.

CASE 3: MODELLING OF THE IMPROVED DSF (3D).

After testing the effectiveness of the improved version of DSF case study, a 3D model is elaborated in order to quantify the impact of lateral openings on the cavity air fluxes. The previously adopted assumptions are also confirmed in this case, and the scale factor between building and domain is set to 10%. The total model cells are 657736, whereas the settings inserted for the surface meshing are:

- Base Size = 0.4 m
- Number of Prism Layer = 5
- Prism Layer Stretching = 1.2
- Prism Layer Thickness = 0.1 m

Figure E.11 and Figure E.12 depict, respectively, the components of the domain and building and the generated surface and volume meshes. The simulation settings adopted for the analysis are the same of the previous cases. The only variation is referred to the time step, which is fixed at 0.01 seconds for solving model convergence problems.

The obtained results, expressed in terms of velocity magnitude regarded each probe line, are presented in Figure E.13 and compared with the 2D configuration. According to the outputs, there are no significant variations between the estimations coming from the 2D (full circle marker) and 3D (empty circle marker) models. In fact, the 2D model is able to describe the air fluxes inside the DSF cavity with good accuracy and less computational cost than the three-dimensional simulation which, instead, is much more complex and with higher solving times.

Appendix E

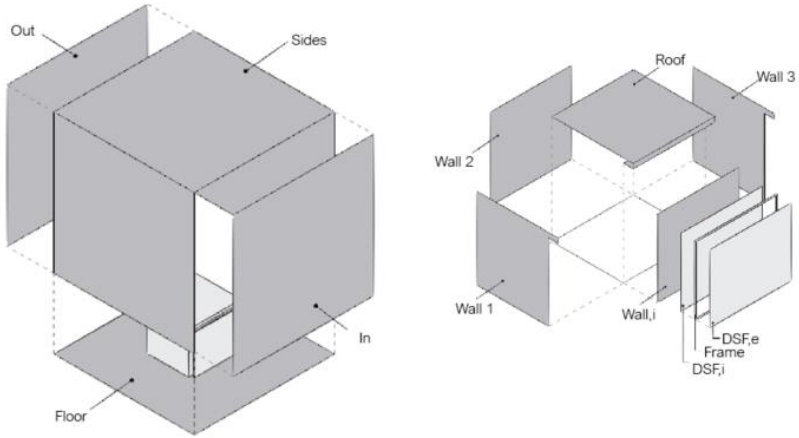


Figure E.11. Representation of domain components (left) and the improved DSF configuration (right) for the 3D simulation.

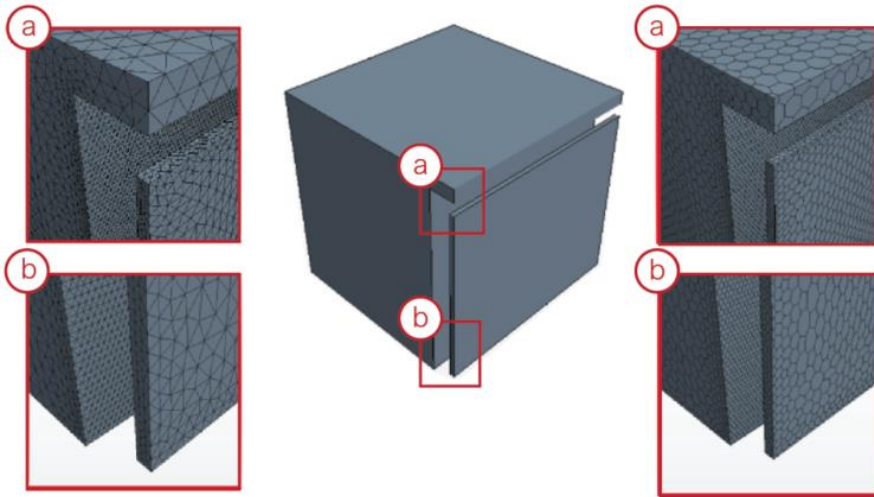


Figure E.12. Surface meshes (a) and volume meshes (b) of the improved 3D CFD model.

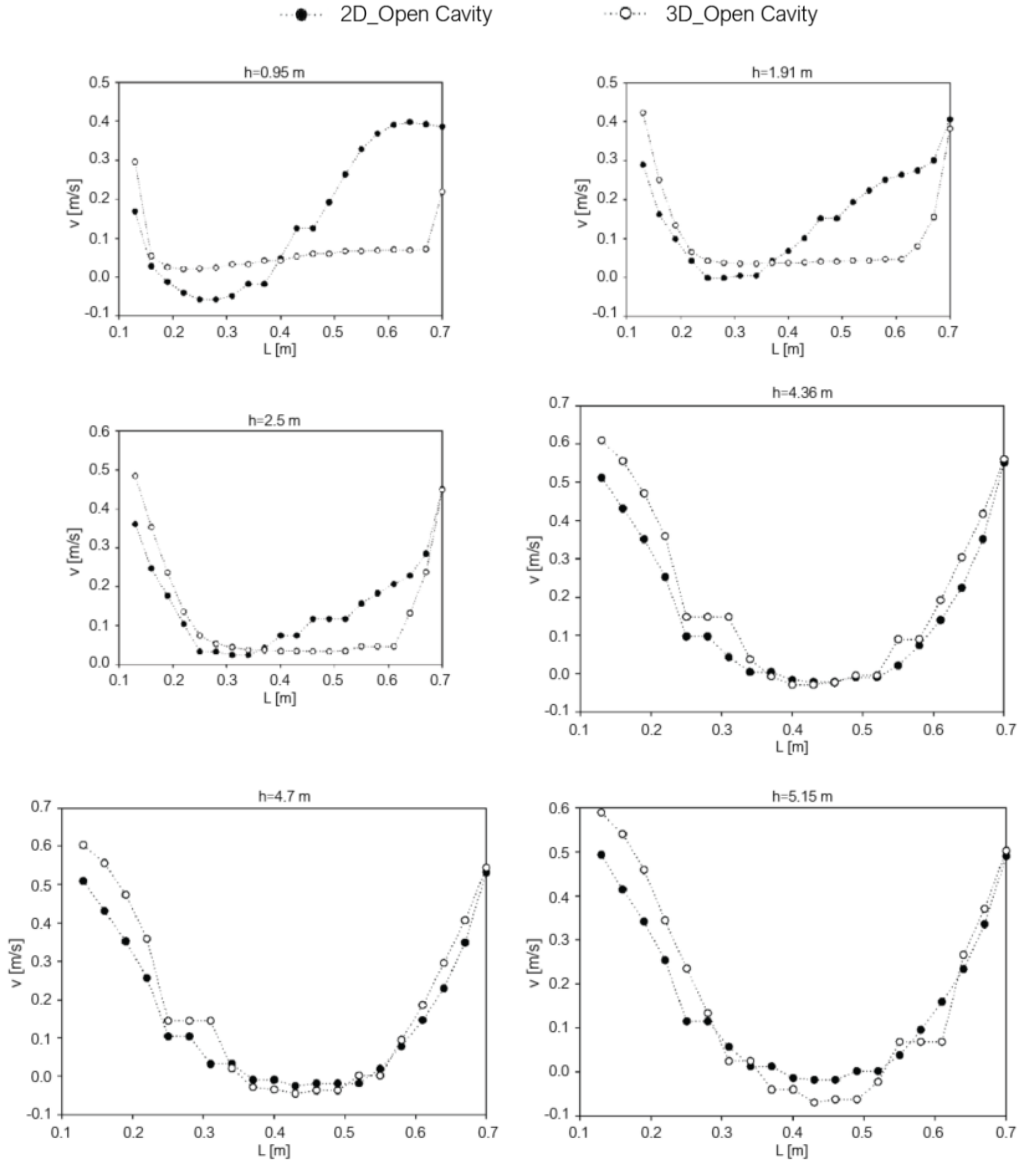


Figure E.13. Velocity magnitude results for various probe lines, referred to the improved DSF configuration for the 2D and 3D models.

Appendix F

The properties of the considered seven records used for the Time History analyses are here reported. The records are real earthquakes, scaled to fit Pescara Response Spectrum at the Life Safety Limit State and Damage Limit State. The Program Rexel (Version 3.5) was used for the selection of the records. The obtained records are referred to a maximum scale factor equal to 1.8 for the LSL and 1.3 for the DLS, and upper and lower tolerance, respectively, equal to 15% and 10%. For each couple of record, the x and y-component are plotted. The first set of accelerograms are referred to the DLS (from Figure F.1 to Figure F.15), whereas the second one to the LSL (from Figure F.16 to Figure F.30).

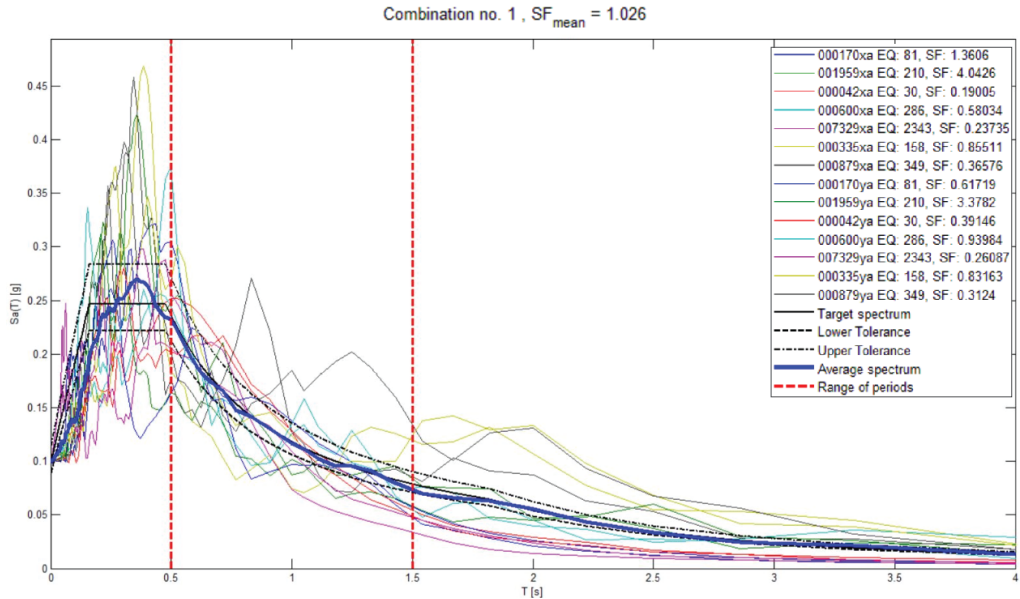


Figure F.1. The set of accelerograms referred to the Damage Limit State (DLS).

Appendix F

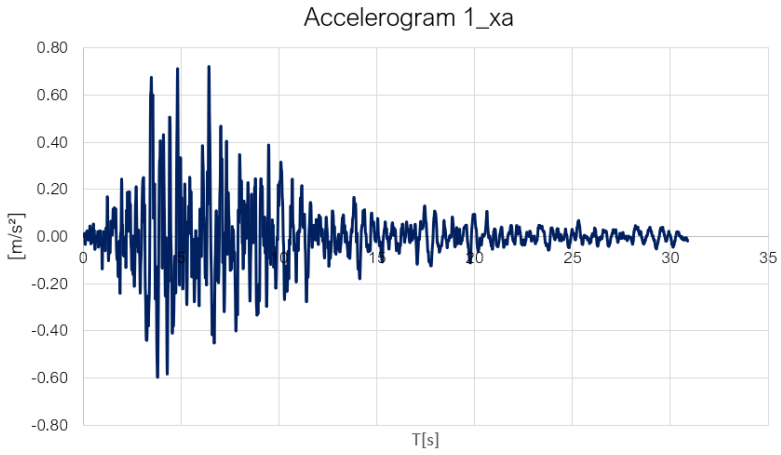


Figure F.2. Record of the Basso Tirreno (15/04/1978) earthquake, x-component (DLS).

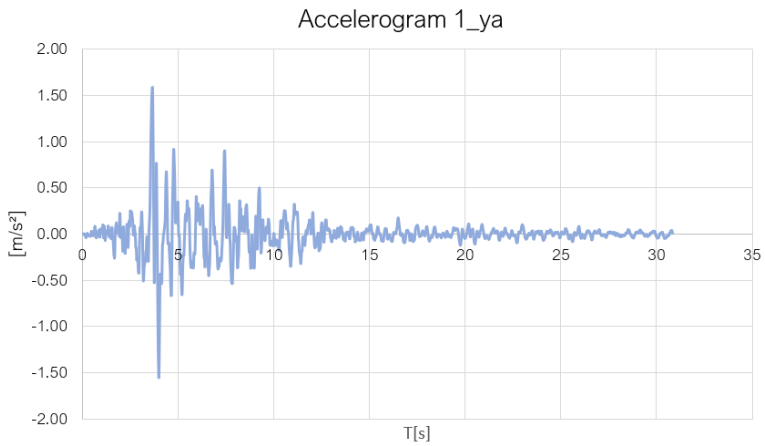


Figure F.3. Record of the Basso Tirreno (15/04/1978) earthquake, y-component (DLS).

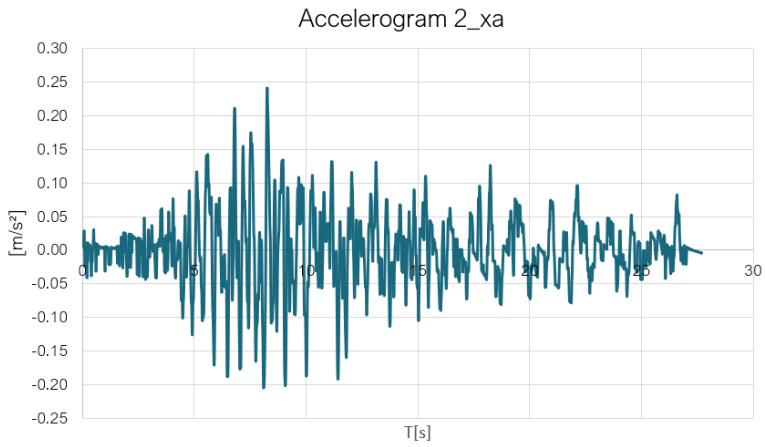


Figure F.4. Record of the Kyllini (16/10/1988) earthquake, x-component (DLS).

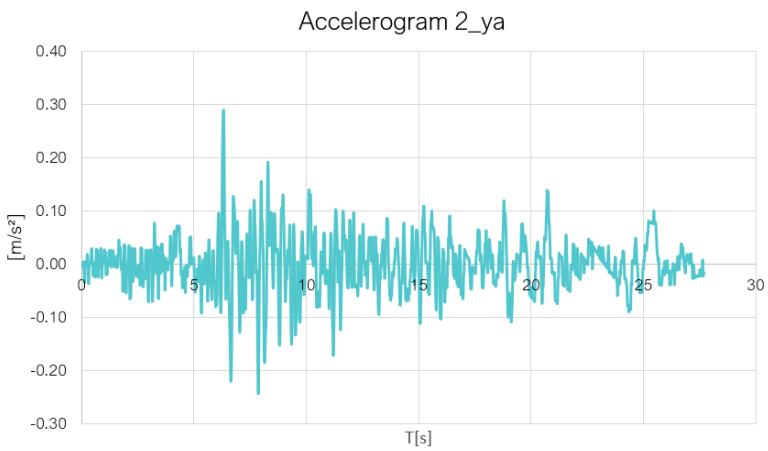


Figure F.5. Record of the Kyllini (16/10/1988) earthquake, x-component (DLS).

Appendix F

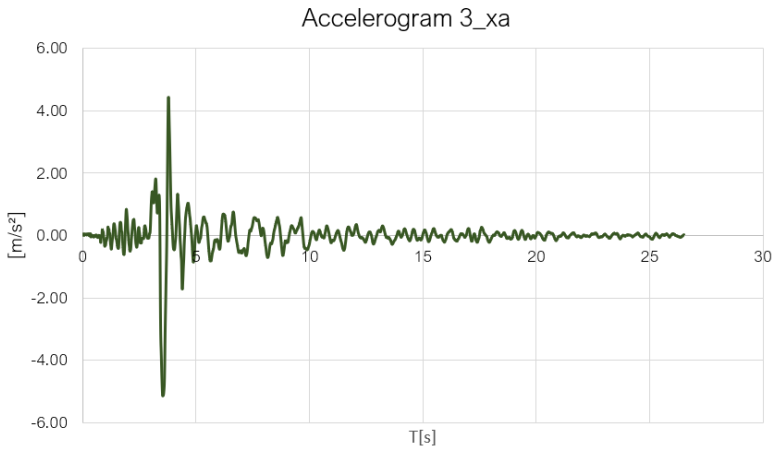


Figure F.6. Record of the Ionian (04/11/1973) earthquake, x-component (DLS).

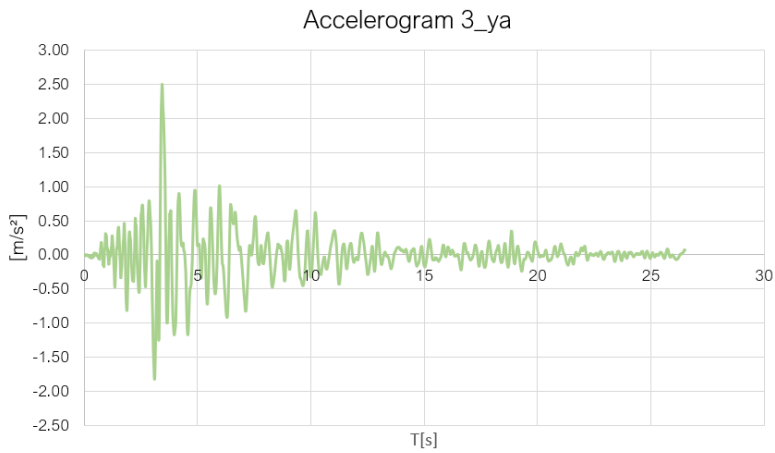


Figure F.7. Record of the Ionian (04/11/1973) earthquake, y-component (DLS).

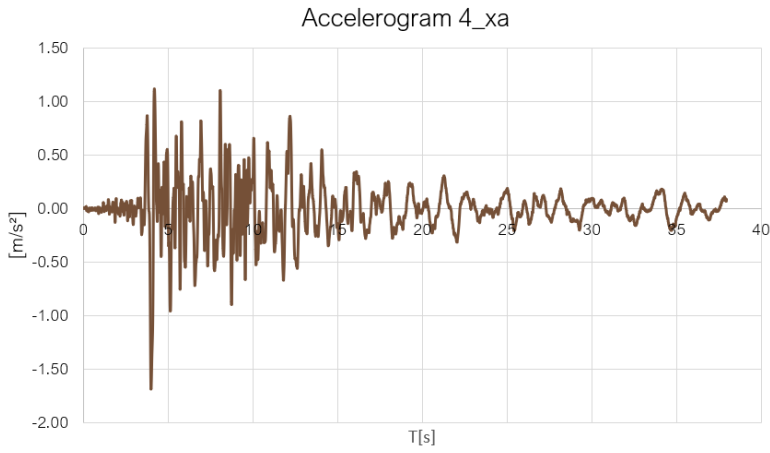


Figure F.8. Record of the Umbria Marche (26/09/1997) earthquake, x-component (DLS).

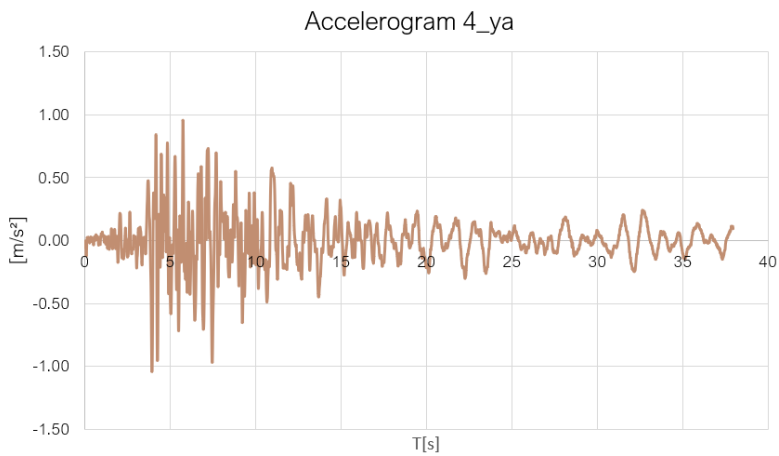


Figure F.9. Record of the Umbria Marche (26/09/1997) earthquake, y-component (DLS).

Appendix F

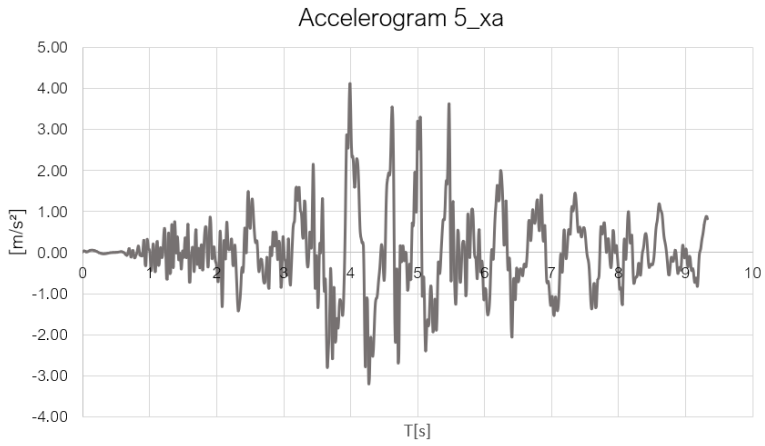


Figure F.10. Record of the Faial (09/07/1998) earthquake, x-component (DLS).

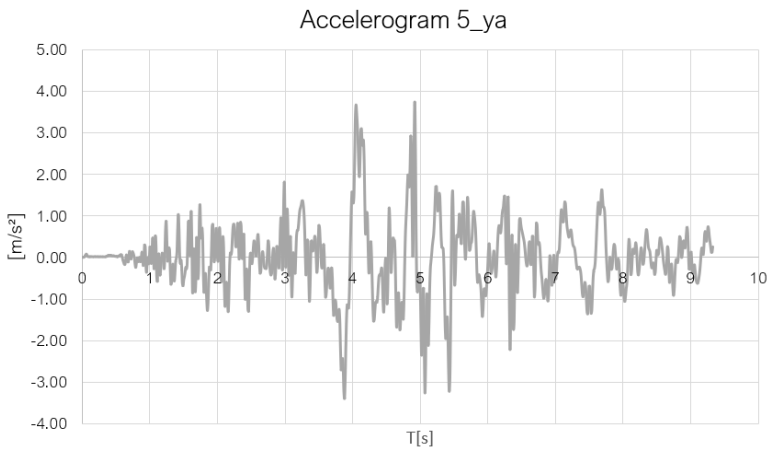


Figure F.11. Record of the Faial (09/07/1998) earthquake, y-component (DLS).

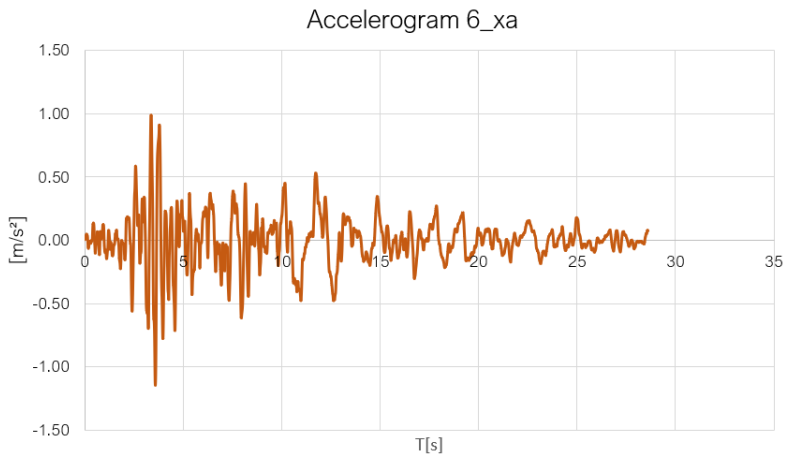


Figure F.12. Record of the Alkion (25/02/1981) earthquake, x-component (DLS).

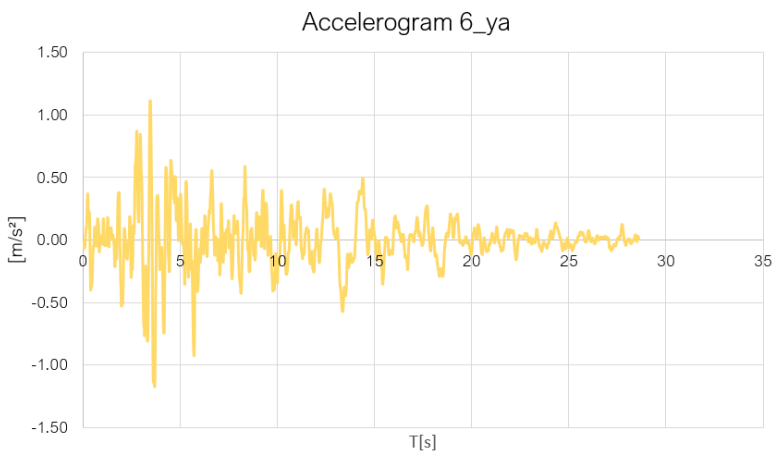


Figure F.13. Record of the Alkion (25/02/1981) earthquake, y-component (DLS).

Appendix F

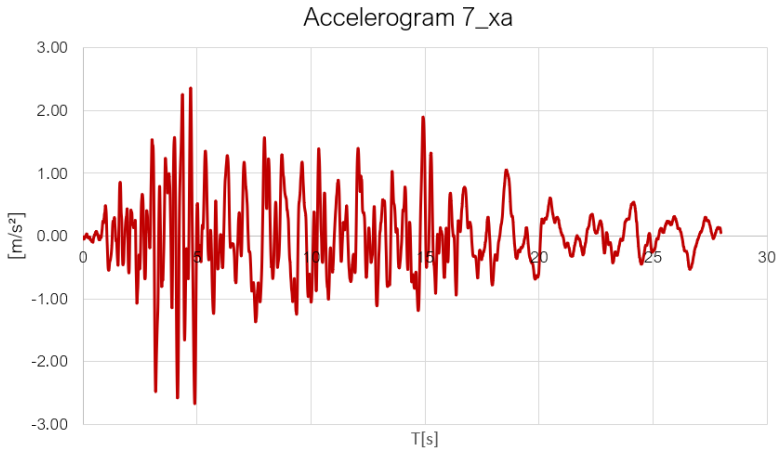


Figure F.14. Record of the Dinar (01/10/1995) earthquake, x-component (DLS).

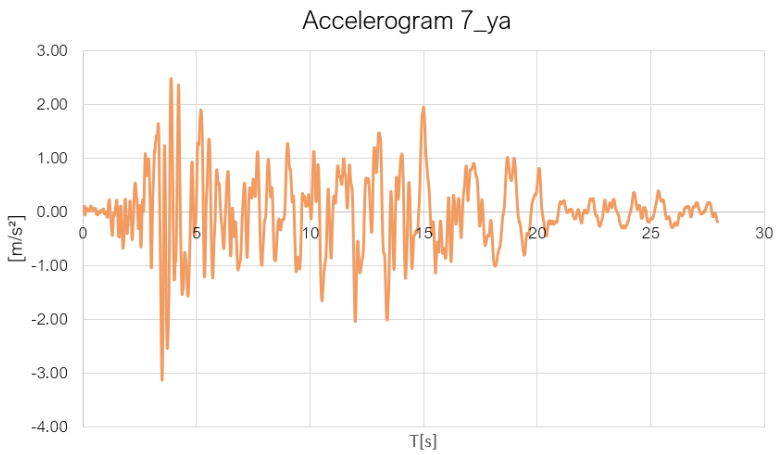


Figure F.15. Record of the Dinar (01/10/1995) earthquake, y-component (DLS).

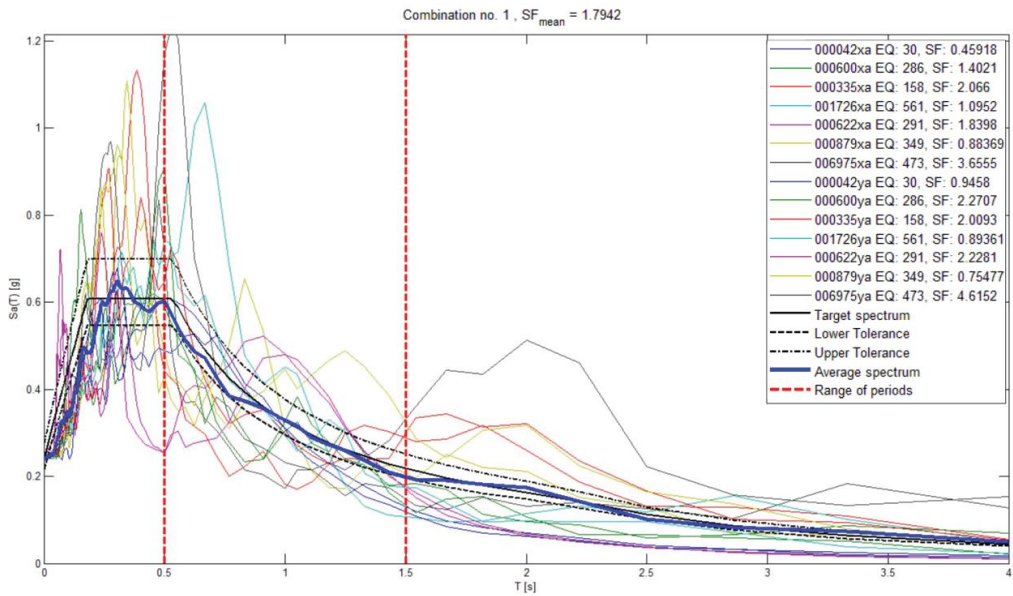


Figure F.16. The set of accelerograms referred to the Life Safety Limit State (LSLS).

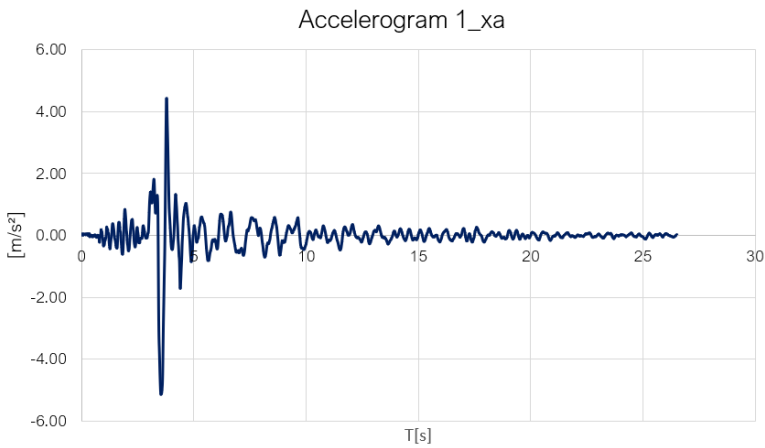


Figure F.17. Record of the Ionian (04/11/1973) earthquake, x-component (LSLS).

Appendix F

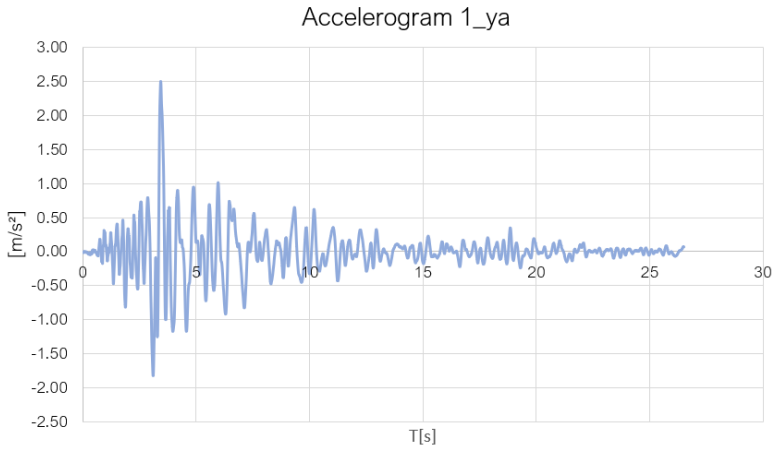


Figure F.18. Record of the Ionian (04/11/1973) earthquake, y-component (LSLS).

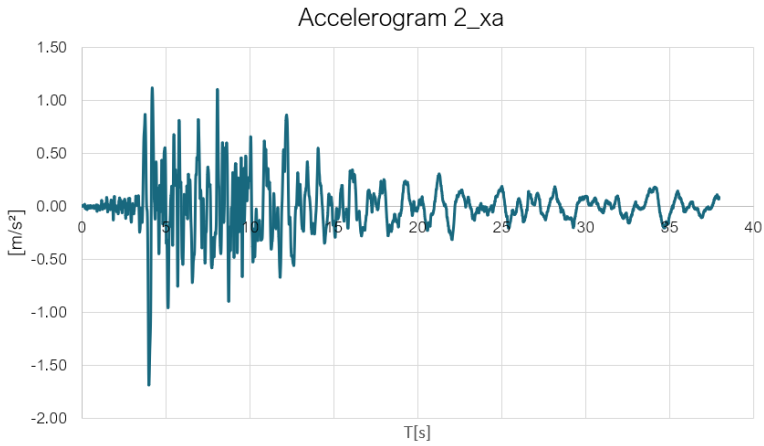


Figure F.19. Record of the Umbria Marche (26/09/1997) earthquake, x-component (LSLS).

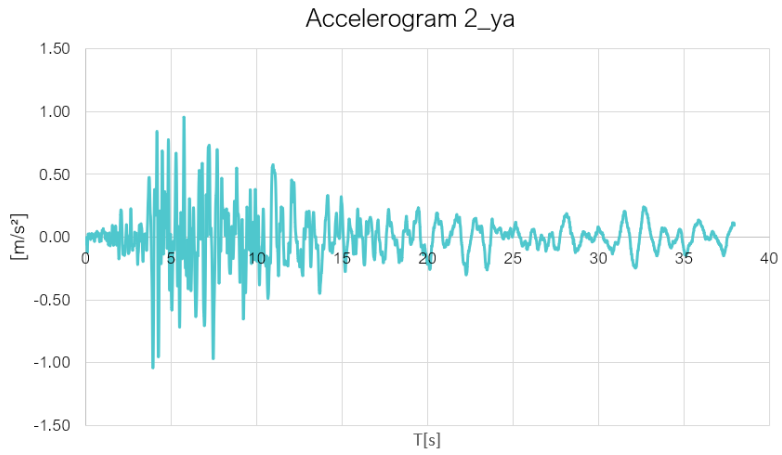


Figure F.20. Record of the Umbria Marche (26/09/1997) earthquake, y-component (LSLS).

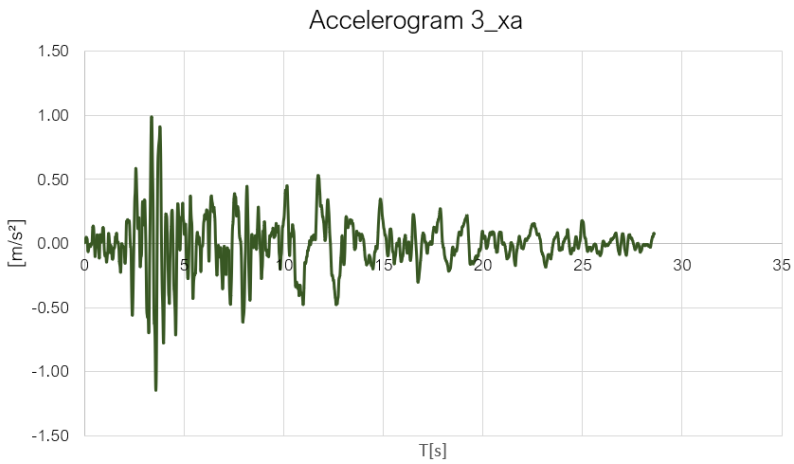


Figure F.21. Record of the Alkion (25/02/1981) earthquake, x-component (LSLS).

Appendix F

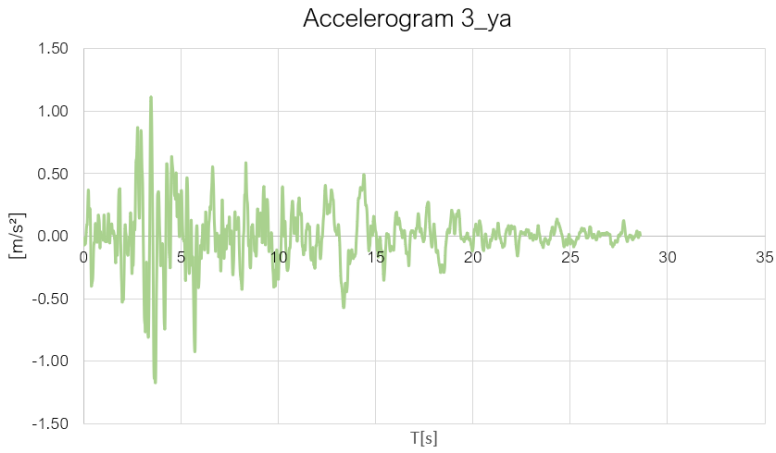


Figure F.22. Record of the Alkion (25/02/1981) earthquake, y-component (LSLS).

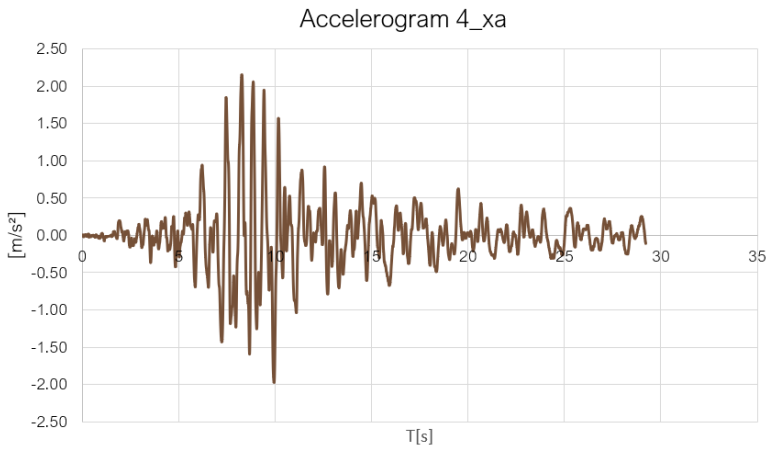


Figure F.23. Record of the Adana (27/06/1998) earthquake, x-component (LSLS).

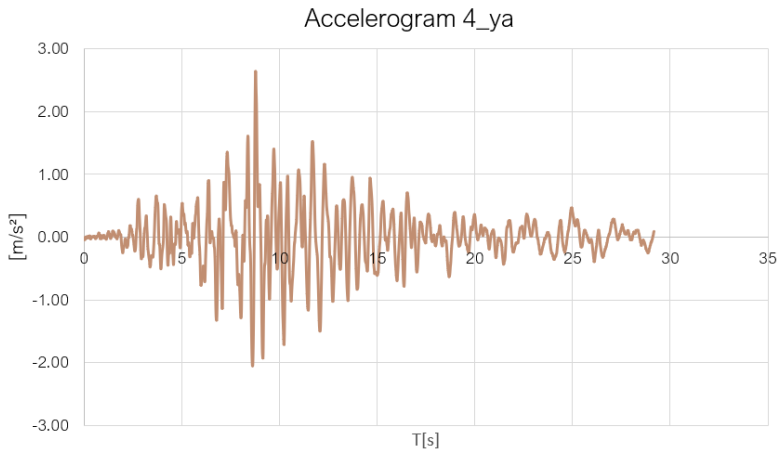


Figure F.24. Record of the Adana (27/06/1998) earthquake, y-component (LSLS).

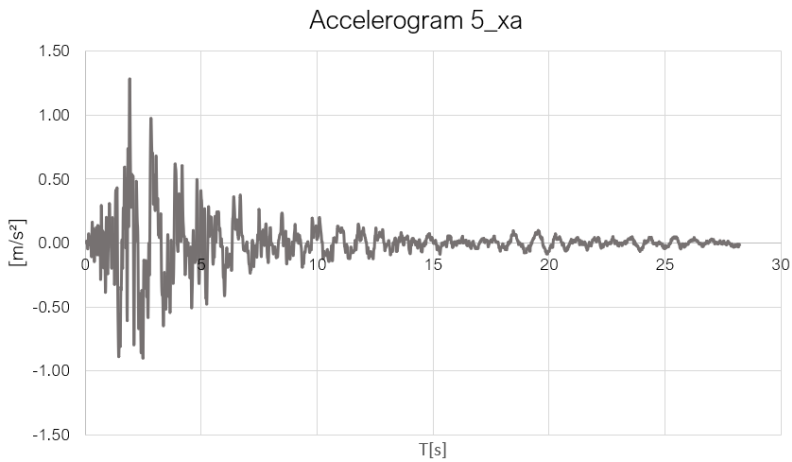


Figure F.25. Record of the Umbria Marche (aftershock) (06/10/1997) earthquake, x-component (LSLS).

Appendix F

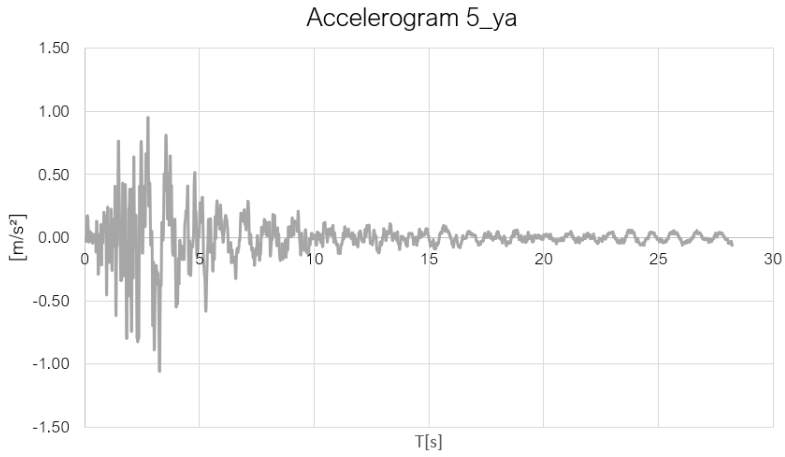


Figure F.26. Record of the Umbria Marche (aftershock) (06/10/1997) earthquake, y-component (LSLS).

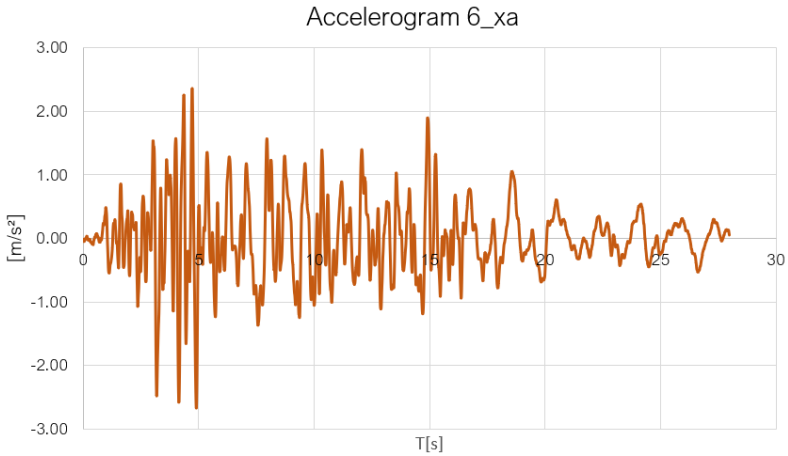


Figure F.27. Record of the Dinar (01/10/1995) earthquake, x-component (LSLS).

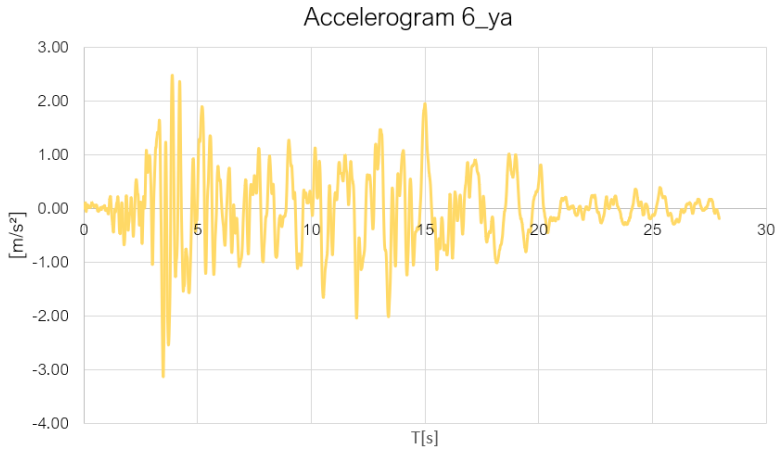


Figure F.28. Record of the Dinar (01/10/1995) earthquake, y-component (LSLS).

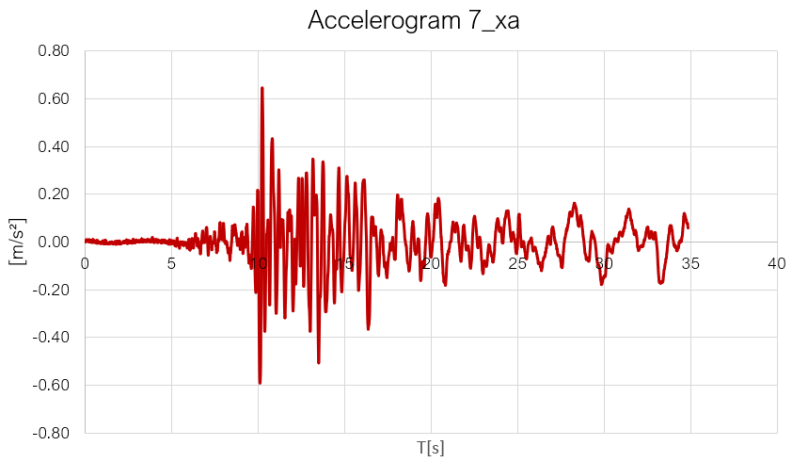


Figure F.29. Record of the Izmit (aftershock) (13/09/1999) earthquake, x-component (LSLS).

Appendix F

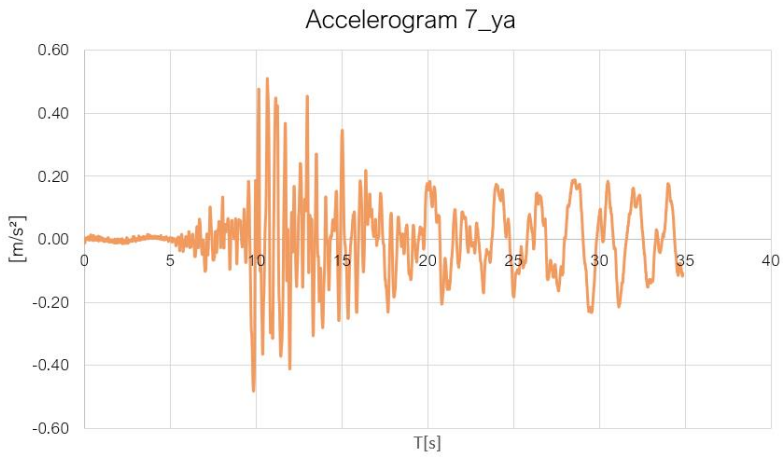


Figure F.30. Record of the Izmit (aftershock) (13/09/1999) earthquake, y-component (LSLS).

La borsa di dottorato è stata cofinanziata con risorse del Programma Operativo Nazionale Ricerca e Innovazione 2014-2020 (CCI 2014IT16M2OP005), Fondo Sociale Europeo, Azione I.1 “Dottorati Innovativi con caratterizzazione Industriale”.



UNIONE EUROPEA
Fondo Sociale Europeo



*Ministero dell'Istruzione,
dell'Università e della Ricerca*

